

Lehrstuhl für Computerunterstützte Klinische Medizin
der Medizinischen Fakultät Mannheim, Universität Heidelberg
Direktor Prof. Dr. rer. nat. Lothar R. Schad

Development and Evaluation of an Actuator System based on Centrifugal Force for Magnetic Resonance Elastography

Inauguraldissertation
zur Erlangung des Doctor scientiarum humanarum (Dr. sc. hum.)
der
Medizinischen Fakultät Mannheim
der Ruprecht-Karls-Universität
zu Heidelberg

vorgelegt von
Wiebke Neumann

aus
Berlin

2018

Dean: Prof. Dr. med. Sergij Goerd
Supervisor: Prof. Dr.-Ing. Frank G. Zöllner

Development and evaluation of an actuator system based on centrifugal force for magnetic resonance elastography

Magnetic resonance elastography (MRE) serves as an important diagnostic tool. It represents one of numerous approaches to monitor tissue stiffness. The most fundamental challenges that MRE face are posed by two linking factors: Constructing a mechanical device that induces tissue motion to the depth of interest and meaningfully resolving said movement in the complex magnetic resonance imaging (MRI) signal. This work aims to address these challenges by improving the quantification of tissue stiffness through the development of a new actuation system for MRE.

Firstly, a 3D printed pneumatic turbine vibrator was developed to induce sinusoidal mechanical waves. It used an eccentrically rotating mass generating a centrifugal force in the turbine. Contrary to conventionally used acoustic pressure drivers, the pneumatic turbine was capable of producing wave amplitudes in the range of appropriate shear waves in human tissue - especially at higher frequencies due to the centrifugal force increasing quadratically in relation to the rotational frequency. A technical assessment showed that the turbine generated vibrations in the range of 30 Hz to 150 Hz. The extent of artifacts caused by the materials brought into the field of view was restricted to the proximity of the actuator. It did not affect image quality in the region of interest. The turbine was MR-safe and an in-house certification according to §3 MPG was conducted, which enabled in-house clinical in vivo studies. The actuation system was additionally extended to a dual turbine actuator in order to investigate if the attenuation of shear waves could be further compensated by using two wave sources.

Secondly, a motion encoding sequence was developed to meaningfully encode the tissue motion in the MRI signal. It was a spin-echo echo-planar-imaging sequence (SE-EPI) and contained a motion encoding gradient (MEG) adjustable for actuation frequencies ranging from 40 Hz to 120 Hz. To accurately reconstruct the wave velocities, i.e tissue elasticity, a trigger was implemented that synchronized the motion encoding sequence to the mechanical waves.

Thirdly, the actuator system was evaluated regarding its performance for MRE image acquisition in a clinical MRI scanner. Silicone-based tissue elasticity mimicking phantoms were developed as test objects with known elasticity. Their shear moduli were in the range of 1.47 kPa to 7.29 kPa, which corresponds to the range of human soft tissue elasticities. A prostate phantom and an anthropomorphic abdominal phantom were manufactured. MR images were acquired with the SE-EPI sequence and were sufficient in terms of signal to noise ratio (liver: $SNR = 71.5$) and contrast to noise ratio (liver: $CNR = 16.5$). The phantoms may also be used for multi-modal imaging; besides MRI, computed tomography (liver: 106 ± 6 HU) and ultrasound imaging by adding scatter particles is feasible. The actuator did not interfere with the imaging procedure and could be integrated into existing clinic equipment. Three actuation set-ups were evaluated: a single, a large surface and a dual source actuation. For each, the strength of the MEG was varied from $5 \frac{mT}{m}$ to $20 \frac{mT}{m}$ for actuation frequencies ranging from 50 Hz to 80 Hz. The dual source actuation demonstrated a more uniform penetration of a larger volume of interest, especially in the peripheral region of the abdominal phantom. The obtained elasticity maps showed elasticity values (liver: 1.12 ± 0.16 kPa, filling material: 4.37 ± 0.52 kPa) in accordance to the results obtained by rheometric testing of the silicone samples.

Additionally, an in vivo MRE examination was conducted, which served as a proof-of-principle for the successful implementation of the first developed MRE actuator system in our clinic. For both liver and prostate MRE, the actuator was well tolerated by the volunteer. Since the developed actuation technique is non-invasive, its incorporation into routine MRI protocols will facilitate patient acceptance, while its short additional set-up time will also increase clinical acceptance. MRE is a unique technique for the identification of various pathologies and the quantification of the shear modulus has the potential to become a further independent parameter for MRI diagnostics in a variety of clinical applications.

Entwicklung und Evaluierung eines auf Zentrifugalkraft basierenden Aktorsystems für die Magnetresonanz-Elastographie

Die Magnetresonanz-Elastographie (MRE) dient als wichtiges diagnostisches Instrument. Es stellt einen von zahlreichen Ansätzen zur Überwachung der Gewebesteifigkeit dar. Die grundlegendsten Herausforderungen der MRE ergeben sich aus zwei Faktoren: Die Konstruktion einer mechanischen Vorrichtung, die eine dynamische Gewebebewegung im Körperinneren induziert, und sinnvolles Kodieren der Bewegung im komplexen Signal der Magnetresonanztomographie (MRT). Diese Arbeit zielt darauf ab, die Methode der Quantifizierung der Gewebesteifigkeit zu verbessern, indem sie ein neues Aktorsystem für die MRE entwickelt.

Zunächst wurde ein 3D-gedruckter pneumatischer Turbinenvibrator entwickelt, welcher sinusförmige mechanische Wellen erzeugt. Dieser verwendete eine exzentrisch rotierende Masse, die eine Zentrifugalkraft in der Turbine erzeugt. Im Gegensatz zu konventionell eingesetzten Schalldrucktreibern war die pneumatische Turbine in der Lage, Scherwellen mit geeigneter Wellenamplitude im menschlichen Gewebe zu erzeugen - insbesondere bei höheren Frequenzen, da die Zentrifugalkraft gegenüber der Drehfrequenz quadratisch ansteigt. Der Aktor erzeugte Vibrationen im Bereich von 30 Hz bis 150 Hz. Das Ausmaß der Artefakte, die durch die eingebrachten Materialien im Field-of-view verursacht werden, waren auf die absolute Umgebung des Aktors beschränkt und hatte keinen Einfluss auf die Bildqualität in der Region-of-Interest. Es wurde eine interne Zertifizierung nach §3 MPG durchgeführt; eine Voraussetzung für interne klinische in vivo Studien. Das Aktorsystem wurde erweitert: zwei Turbinen wurden synchron in Reihe geschaltet, um zu untersuchen, ob die Dämpfung von Scherwellen durch den Einsatz von zwei Wellenquellen kompensiert werden kann.

Außerdem wurde eine Bewegungs-kodierende Aufnahmesequenz entwickelt, die Gewebebewegung im MRI Signal darstellt. Die Sequenz basierte auf einer *spin-echo echo-planar-imaging* (SE-EPI) Sequenz und enthielt einen Bewegungs-kodierenden Gradienten (*motion encoding gradient* (MEG)), der Vibrationsfrequenzen von 40 Hz bis 120 Hz kodierte. Um die Wellengeschwindigkeiten und damit die Gewebeelastizität zu rekonstruieren, wurde ein Trigger implementiert, der die Sequenz mit den mechanischen Wellen synchronisiert.

Zusätzlich wurde das Aktorsystem in Bezug auf die MRE Bildgebung an einem klinischen Scanner bewertet. Gewebeelastizität-imitierende Phantome wurden als Testobjekte mit bekannter Elastizität entwickelt. Der Schermodul der silikonbasierten Materialien lag laut rheometrischer Untersuchung zwischen 1,47 kPa und 7,29 kPa und ist im Bereich der menschlichen Weichteilelastizität. Es wurden ein Prostataphantom und ein anthropomorphes abdominelles Phantom hergestellt. MR Bilder wurden mit der SE-EPI Sequenz aufgenommen, die in Bezug auf das Signal-zu-Rauschen-Verhältnis (Leber: $SNR = 71,5$) und das Kontrast-zu-Rauschen-Verhältnis (Leber: $CNR = 16,5$) ausreichend Signal für die MRE Bildgebung gaben. Neben der MRT ist die Computertomographie- (Leber: 106 ± 6 HU) und die Ultraschallbildgebung durch Hinzufügen von Streupartikeln möglich. Es wurden drei Anregungsarten evaluiert: eine Einzel-, eine Großflächen- und eine Doppelquellenanregung. Für jede wurde die Stärke des MEG von $5 \frac{mT}{m}$ bis $20 \frac{mT}{m}$ für Vibrationsfrequenzen von 50 Hz bis 80 Hz variiert. Die Doppelquellenanregung zeigte eine gleichmäßigere Wellenausbreitung in einem größeren Volumen, insbesondere im peripheren Bereich des abdominalen Phantoms. Die rekonstruierten Elastizitätskarten ergaben Elastizitätswerte (Leber: $1,12 \pm 0,16$ kPa, Füllmaterial: $4,37 \pm 0,52$ kPa) im Bereich der rheometrisch ermittelten Messergebnisse von Silikonproben.

Abschließend wurde eine in vivo MRE Machbarkeitsstudie durchgeführt, die eine erfolgreiche Implementierung des ersten entwickelten MRE Antriebssystems in unserer Klinik demonstriert. Die kurze zusätzliche Einrichtzeit erleichtert die Einbindung in Routineprotokolle und erhöht die klinische Akzeptanz. MRE ist eine Technik zur Identifizierung verschiedener Pathologien - die Quantifizierung des Schermoduls hat das Potenzial, ein weiterer unabhängiger Parameter für die MRT Diagnose in einer Vielzahl von klinischen Anwendungen zu werden.

Contents

1	Introduction	1
2	Theoretical Background	5
2.1	Fundamentals of Elasticity	5
2.2	Characteristics of Soft Tissue Elasticity	10
2.3	A Brief Overview of Organs of Interest	13
2.4	Fundamentals of Magnetic Resonance Imaging	19
2.5	Fundamentals of Magnetic Resonance Elastography	24
2.6	MRE Hardware	30
2.7	Technical Compliance	34
3	Materials and Methods	37
3.1	Actuator Development and Evaluation	38
3.1.1	The Passive Driver	38
3.1.2	A Dual Turbine Design for Coupled Actuation	46
3.1.3	The Active Driver	47
3.1.4	In-house Certification of the Actuator	51
3.2	Linking the Actuator to the MRI System	52
3.2.1	The Scanner Systems	52
3.2.2	The MRE Sequence by Siemens	53
3.2.3	Developing a Motion Encoding Sequence	54
3.2.4	Triggering the MRE Sequence with the Actuator	55
3.3	MRE Image Acquisition	56
3.3.1	Material Studies	57
3.3.2	Design of Anthropomorphic Tissue-Mimicking Phantoms	62
3.3.3	MR Elastography - Phantom Studies	66
3.3.4	MR Elastography - In Vivo Studies	69
4	Results	71
4.1	Actuator Development and Evaluation	71
4.1.1	The Passive Driver	71

4.1.2	The Active Driver	80
4.1.3	In-house Certification of the Actuator	84
4.2	Linking the Actuator to the MRI System	86
4.2.1	A Motion Encoding Sequence for MRE	86
4.2.2	Triggering the MRE Sequence with the Actuator	87
4.3	MRE Image Acquisition	90
4.3.1	Material Studies - Rheometric Evaluation of Silicones	90
4.3.2	Design of Anthropomorphic Tissue-Mimicking Phantoms	93
4.3.3	MR Elastography - Phantom Studies	96
4.3.4	MR Elastography - In Vivo	105
5	Discussion	107
5.1	Actuator Development and Evaluation	107
5.2	Linking the Actuator to the MRI System	113
5.3	MRE Image Acquisition	120
6	Summary and Outlook	131
	List of Figures	135
	List of Tables	137
	Acronyms	139
	Notation	141
	References	143
	Appendices	167
	A Technical Evaluation	169
	B Technical Documentation	171
	C Material Studies	191
	D MR Elastography	197
	Publications	199

Introduction 1

Detecting changes in tissue stiffness serves as an important diagnostic tool [1, 2, 3, 4, 5, 6]. Physicians have long been palpating suspicious lesions to detect diseases and manual self-examination is often the first way of detecting breast or testicular cancer [7, 8]. It is easy to palpate superficial tissues. However, it is much more difficult to palpate if the diseased tissue is further away from the body surface. For this reason, numerous approaches to monitor stiffness inside the body have been developed, one example is the magnetic resonance elastography (MRE) [9]. This work aims to improve a method for the quantification of tissue stiffness by developing a new actuation system for MRE.

The presence of hard tissue is the prerequisite of disease detection through palpation. Changes in stiffness result from microstructural changes in tissues that affect its apparent macroscopic mechanical properties [10, 11, 12, 13]. For example, clinicians can palpate macroscopic abnormal stiffness in superficial lymph nodes and abdominal organs. Although palpation is an established tool, it is highly subjective as the clinician can neither quantify tissue stiffness nor detect changes within deep, dense or heterogeneous tissue [7, 14]. To quantify those changes, the mechanical parameters such as Young's modulus or shear modulus serve as a measure for elasticity. They may vary by orders of magnitude within soft tissues depending on their physiological state [7, 15, 16, 17].

MRE can quantify tissue stiffness during magnetic resonance imaging (MRI) examinations and may be used as a discriminator for benign or cancerous tissue [6, 18]. It can employ non-invasive actuation techniques and it only requires a short additional set-up time to incorporate MRE in a routine MRI examination, which facilitates clinical and patient acceptance. MRE may serve as an objective additional diagnostic marker that detects cancer invisible to other imaging techniques and monitors the progression of disease - in the future, it may also replace invasive biopsies [3, 6, 19, 20, 21, 22, 23].

MRE imaging employs the principles of mechanical wave propagation. In a soft medium, these waves spread more slowly than in a stiffer medium [24, 25]. Snapshots of the waves at consecutive times allow the determination of wave propagation velocities. Elasticity values can then be reconstructed based on the information of wave velocities.

It is possible to encode the wave propagation with MRI, which can acquire complex signals of the hydrogen distribution in the human body with a specific magnitude and phase. In most cases, only the magnitude of these signals is used to reconstruct anatomical images, while the phase information is ignored. However, the phase information can be exploited to encode the motion of tissue, as the phase depends on the magnetic field B and local changes in B lead to a phase offset of the complex signal. In other words, superimposed magnetic field gradients can encode the motion of particles due to the changes in the phase of the signal. If a tissue moves in this magnetic field, micrometer displacements become measurable. Thus, MRE imaging of the in vivo mechanical response of soft tissue has emerged as a virtual palpation tool yielding quantifiable tissue stiffnesses [15, 26, 27].

The most fundamental challenge of MRE is posed by two linking factors. Firstly, a mechanical device has to be constructed that induces tissue movement to the depth of interest. Secondly, the mechanical responses to said movement has to be meaningfully resolved in the complex MR signal [9]. Various actuators have been designed that generate sinusoidal mechanical waves; the most prominent one being an acoustic pressure driver [21, 28, 29, 30]. There, varying acoustic pressures are generated outside the scanner room and fed to an air cushion attached to the patient in the scanner room. This system struggles to maintain sufficient amplitude at higher actuation frequencies. In addition, it cannot easily synchronize multiple drivers, since the tubing between the source of wave generation outside the scanner room and the application of the wave inside the scanner room can cause unknown phase lags in the acoustic waves. Both are important factors for a reliable wave induction in deep-lying tissues, such as the prostate, as large amplitudes of the mechanical waves need to be applied at the surface to overcome damping in deep-lying organs. The use of multiple drivers has been shown to increase the spatial resolution of the obtained elasticity maps through wave interference effects [31, 32].

During this work, a novel actuation system for sinusoidal mechanical wave generation based on the principle of centrifugal force was developed: the pneumatic turbine vibrator. The generated centrifugal force increases quadratically for increasing frequencies, thus yielding mechanical waves whose amplitude increases at higher frequencies, contrary to conventionally used acoustic pressure drivers. The design is similar to that of the industrially used compressed air vibrators, which are common in the bulk material handling sector. An eccentric weight, also called unbalance, within these pneumatic turbines generates a dynamic harmonic vibration. This results in a centrifugal force with its amplitude depending on the driving frequency of the turbine as well as on the weight and dimensions of the unbalance. However, due to the turbine material and centrifugal force range, commercial compressed air vibrators can neither be operated safely within high magnetic fields nor are the generated vibrations in the required range of mechanical wave actuation forces. This work pursues three objectives to bring the new actuator into clinical MRE application.

The first aim was to develop and evaluate a 3D printed pneumatic vibrator that was MR-safe and yielded the range of wave amplitudes needed to encode waves in MRE for deep tissue. The design was also extended to a dual turbine actuator to investigate if the attenuation of shear waves could be compensated by using two wave sources. Besides the assessment of the technical parameters of the actuator, it was also certified for clinical in-house in vivo studies. The second aim was to develop a motion encoding sequence for MRE imaging. In order to synchronize the mechanical waves of the actuator to the motion encoding gradient of the sequence, a synchronization trigger needed to be implemented. This was important as the wave velocities, i.e. tissue elasticity, can only be accurately reconstructed if the wave propagation can be imaged at multiple controlled time points.

The third aim was to implement the actuator system consisting of the mechanical actuator and the sequence on the MRI scanner and evaluated its performance for MRE image acquisition. For this reason, tissue elasticity mimicking phantoms were developed as test objects with known elasticity for the MRE evaluation. Additionally, an in vivo MRE examination was conducted, which served as a proof-of-principle of the successful implementation of the first developed MRE actuator system in our clinics.

Theoretical Background 2

The following chapter introduces the fundamental concept of elasticity and describes the mechanical characteristics of human soft tissue elasticity with emphasis on the two organs liver and prostate. The main principle for quantifying tissue elasticity in MRI is based on the encoding, acquisition and reconstruction of mechanical waves propagating through the human body at subsequent time points. Therefore, their principles are described in the following. The last part describes the fundamentals of MR elastography in terms of image acquisition and conceptual hardware developments.

2.1 Fundamentals of Elasticity

If a given material is subjected to a force, it will react to this force with a deformation due to a dislocation of the atoms in the material. The kind of deformation depends on the mechanical properties of the material. In general, there are four different types of deformation. For one, the deformation of the material may be reversible or irreversible. For another, the material may exhibit a time independent or time dependent reaction when subjected to a force.

A reversible deformation is characterized by a restoration of the initial shape of the material after the force is released. For example, a spring can be elongated or compressed to a certain degree. After its release, it will return to its initial shape. An irreversible deformation, on the other hand, cannot be restored. This characteristic may be useful for energy absorption, e.g. in crash elements during car accidents. Overall, any kind of reversible deformation is denoted as an elastic deformation, any type of irreversible deformation is described as a plastic deformation.

Additionally, the material may undergo a time independent or dependent deformation. A time independent deformation is an immediate reaction of the material to a given force. On the contrary, a time dependent deformation is characterized by a delayed reaction of the material and is denoted with the prefix *viscos*.

The following section introduces a description of outer forces and the resulting deformations in materials. Later, the time independent elastic behavior of material is described, followed

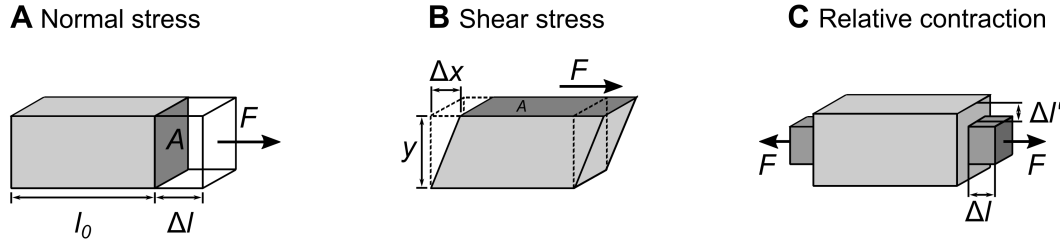


Figure 2.1 – Schematic relation of displacements, stresses and strains. **A:** A force F applied perpendicularly to an area A results in a change of length Δl of the material and is denoted as normal stress σ . **B:** A force F applied in parallel to an area A results in an angular change $\frac{\Delta x}{y}$ and is denoted as shear stress τ . **C:** Poisson's ratio measures the relative contraction $\Delta l'$ to the applied loading with respect to the relative expansion Δl of the material.

by a short overview on time dependent elastic, i.e. visco-elastic, behavior of materials such as polymers or biological soft tissues.

The overview about the mechanical properties of materials is primarily based on [33] and further on [34], [35], and [36] unless cited otherwise.

Displacements, stresses and strains

An elastic solid undergoes a deformation as a result of an applied loading. It restores to its original state if the external force is no longer applied. The deformations can be quantified by knowing the displacements of material points in the body. A displacement field can be found at all points inside a continuous elastic material as established by the continuum hypothesis. A linear relationship connects the stresses and strains of the material and is similar to Hooke's spring law.

The stress normalizes a given force to a certain area. If the force F is applied perpendicularly to the area A , the stress

$$\sigma = \frac{F_{\perp}}{A} \quad (2.1.1)$$

is denoted as normal stress and given in units of 1 N m^{-2} , which is equivalent to 1 Pa (Fig. 2.1).

If the force is applied in parallel to an area, a shear stress as defined in

$$\tau = \frac{F_{\parallel}}{A} \quad (2.1.2)$$

is applied (Fig. 2.1).

The strain describes the change in length or angular distortion within the material due to an applied loading. A normal stress causes a normal strain ϵ , a proportional deformation, which is defined as the difference Δl between the length l_1 when the load is applied and the original

length l_0 before the material is subject to the load:

$$\varepsilon = \frac{l_1 - l_0}{l_0} = \frac{\Delta l}{l_0}. \quad (2.1.3)$$

The strain ε is dimensionless as it is a relation between two lengths. A shear stress causes a shear strain γ , defined as the angular change of a right angle for small Δx as:

$$\gamma = \frac{\Delta x}{y}. \quad (2.1.4)$$

Time independent elasticity

On an atomic level, a deformation may be represented by expanding springs connected between single atoms in the material. The strain components are related to the displacement fields and an elasticity tensor can be developed. In three dimensions, it is described by

$$\sigma = \vec{C} \varepsilon \quad (2.1.5)$$

with \vec{C} being a tensor of rank 4 with 81 unknowns including all material parameters necessary to characterize the material.

However, this model may be simplified using certain assumptions. For small displacements from the equilibrium position of symmetric systems as in a homogeneous isotropic materials, such as a one-dimensional rod, a linear elastic behavior mathematically described by Hooke's law is valid. For uni-axial normal stress, Hooke's law yields

$$\sigma = E\varepsilon \quad (2.1.6)$$

with E being the elastic modulus, also called Young's modulus, given in units of 1 Pa.

The elastic modulus is thus a measure of the stiffness of a solid material in the linear regime. A stiff material needs more force to be deformed, as it is having a larger elastic modulus, compared to a soft material having a smaller elastic modulus. The elastic modulus is the proportionality constant in Hooke's law and is obtained as the slope of a stress-strain-diagram. After exceeding a critical elongation, a time independent elasticity may no longer be assumed and the material will not return to its initial shape.

Regarding a purely shear loading, the shear stress is defined as

$$\tau = G\gamma \quad (2.1.7)$$

with G being the shear modulus, a constant for the stiffness of a material with respect to shear deformation, also given in units of 1 Pa.

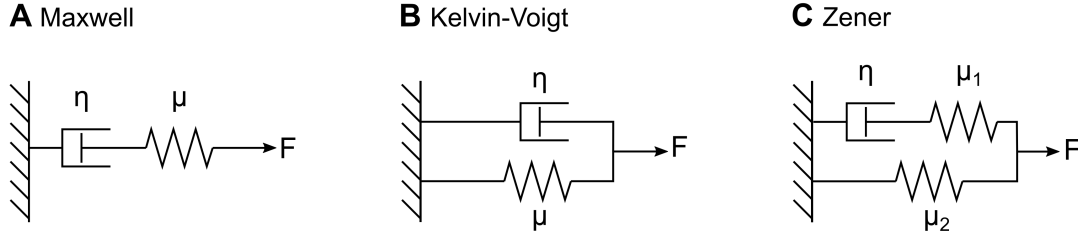


Figure 2.2 – Graphical representation of three principal visco-elastic models. **A:** In the Maxwell model, a dash pot is set in series with a spring. **B:** In the Kelvin-Voigt model, a dash pot is in parallel to a spring. **C:** The Zener model, also known as the standard linear solid, sets a a spring with a spring constant μ_1 in series with a dash pot of viscosity η . This is then placed in parallel with another spring with a different spring constant μ_2 .

Considering only isotropic material, whose elastic properties are identical in all spatial directions, the elastic modulus and shear modulus are interdependent:

$$G = \frac{E}{2(1 + \nu)} \quad (2.1.8)$$

with ν being Poisson's ratio. It is a dimensionless measure for the relative contraction perpendicular to the applied loading with respect to the relative expansion of the material in the direction parallel to the applied loading, also termed lateral contraction coefficient (Fig. 2.1). Most materials have a Poisson's ratio ranging between 0.0 and 0.5. Incompressible materials have a Poisson's ratio of $\nu = 0.5$, as the volume of the material stays constant independent of the kind of deformation. Here, the E can be approximated by

$$E = 3 \cdot G \quad (2.1.9)$$

Another mechanical quantity is the bulk modulus K . It describes the resistance to compressibility of a material. Regarding homogeneous isotropic linear elastic materials, their elastic properties can be uniquely determined by any two moduli (E, G, ν, K). Any other elastic moduli can be calculated accordingly.

As mentioned, the linear model for the one-dimensional axial loading case given by Eq. 2.1.6 is only a simplification and may be extended to the generalized Hooke' law for linear isotropic elastic solids. Thus, under the condition of material homogeneity and isotropy, the general three-dimensional form of the linear elastic constitutive model as in Eq. 2.1.5 may also be expressed as

$$\sigma_{ij} = \lambda e_{kk} \delta_{ij} + 2\mu e_{ij}. \quad (2.1.10)$$

The elastic constant λ is called Lamé's constant and μ is referred to as the shear modulus. This yields two independent elastic constants describing the behavior of isotropic materials in three dimensions.

Time dependent elasticity

The viscosity of a material is a time dependent reaction and is a measure of its resistance to gradual deformation by shear stress.

For a fluid, the following experiment is considered to determine its shear viscosity η . Two parallel plates with an area A are separated by a distance L . This distance, i.e. gap, is filled with a fluid. The top plate is moved with a velocity \vec{v} relative to the bottom plate and the force required to move the top plate is determined in steady state. The force required is proportional to the area of the plates as well as the velocity gradient \vec{v}/L of the moving plate with respect to the gap size and is termed strain rate.

Thus, the relation of the shear viscosity to the force per unit area defined as stress σ is described by

$$\sigma = \eta \frac{\vec{v}}{L}. \quad (2.1.11)$$

The relation between stress and deformation of a material near equilibrium, i.e. when the deformation is small, is termed linear visco-elasticity. It implies that the material has both elastic and viscous properties. Thus, one part of the stress is due to the strain field as described in Eq. 2.1.2 and the other is due to the strain rate, the derivative of the strain field:

$$\gamma' = \frac{d\gamma}{dt}. \quad (2.1.12)$$

Mechanical models

Mechanical models are often used to describe the visco-elastic behavior of materials. Hookean elastic solids can be represented by a linear spring model with a spring constant μ , purely viscous fluids by a dash pot model with a coefficient of viscosity η . However, beyond certain limits, these models cannot longer be applied for true materials. In general, few biological tissues obey Hooke's law [10]. A combination of springs and dash pot in series or parallel results in a more complex mechanical model. The most common ones are the Maxwell model, the Kelvin-Voigt model and the Zener model (Fig. 2.2). The latter one is also known as the standard linear solid model.

2.2 Characteristics of Soft Tissue Elasticity

After introducing the fundamental concept of elasticity with regard to material science, this section focuses on elasticity characteristics of human soft tissues. Following a general overview on the structure and differences among various tissues types, an introduction to soft tissue modeling is provided. A more detailed description about two organs, namely liver and prostate, is given subsequently, as this work focuses on those two particular organs.

The anatomical definitions of soft tissue includes connective and non-connective tissues, with tendons, ligaments, fascia, skin, fibrous tissues, fat being the first and muscles, nerves and blood vessels being the latter category.

Soft tissues mostly investigated in MRE studies mainly include healthy tissues of abdominal organs, muscles, brain, female breast as well as benign or malignant changes within these organs [37, 38, 39, 40, 41, 42].

General soft tissue characteristics

Zooming from a macroscopic level of a healthy entire organ into its cellular structure, it is possible to divide the tissue into several pure biological materials and ground substances. For example, collagen is a basic structural element for biological soft tissues. It is the main load-carrying element giving mechanical integrity to blood vessels, skin, tendons, and other tissues. Depending on the tissue and organ type, collagen can be of different structural forms. Its molecules form fibrils, which then are organized into fibers and finally into different tissues. Each stage of structural organization is accompanied by the acquisition of new mechanical properties [10].

From a bio-mechanical point of view, the properties of a tissue are known if its constitutive equation is known, which can only be determined by experiments. A commonly conducted experiment to determine the constitutive equation of a bio-solid is the uni-axial tension test. From the recorded data, it is possible to deduce the stress-strain-relationship of the material under uni-axial loading [10].

Thus, the mechanical properties of biological tissues can be scaled from the cellular structures to a global mechanical response of entire organs [11, 12, 13]. For example, the biomechanic characteristics of the entire liver parenchyma depends on mechanical properties of hepatocytes, vascular structures and extracellular matrix [43].

Overall, soft tissues are considered to be incompressible. Their bulk compressional modulus K is, in general, several orders of magnitude larger than the shear modulus E . The major contribution to K of tissues comes from hydration, as water is the most abundant constituent of soft tissues. Therefore, K of all the soft tissues is close to that of water and varies within about 10% [44].

Assuming the incompressibility of soft tissues, mainly the shape of the stressed tissue changes, while the volume remains constant when a short external stress is applied to the soft tissue. Hence, the relationship between the stress and strain patterns is completely defined by the Young's modulus E only. The bulk modulus, whether it is infinitely large or only a few orders of magnitude higher than E , is not taken into account [15].

The E -modulus of soft tissues can span over a wide range of orders of magnitude. The variability of structural features of tissues, such as geometrical parameters of cells in different tissues and the degrees of heterogeneity and anisotropy, has a major effect on this range [15]. In literature, shear elasticity of various soft tissues varies over many orders of magnitude [45, 46]. It depends on the organs themselves, the tissue types within the organs and may differ among healthy, benign or malignant tissues. Even within one tissue type, shear elasticity may change by hundreds of percent during processes such as muscle contraction [45]. A change in mechanical properties of tissues may also be an indicator of underlying pathologic conditions [47].

First observations of medical staff revealed differences in mechanical stiffness between healthy and injured muscle in early stages of deep tissue injury development using palpation [48, 49]. Palpable mechanical differences in healthy tissue and suspicious lesions in the female breast yield the basis for breast self-examination as a way to early detect breast cancer.

Research suggests that changes in the mechanical properties of tissues may reflect disorders in the extracellular matrix, which can be an indication of developing pathology [1, 2]. Those pathologies may cover a wide range of diseases. Developing fibrotic tissue in the liver increases the tissue stiffness, which is proportional to the severity of the fibrotic changes, and is used as a diagnostic marker [4, 5, 50].

Malignant tumors are often characterized by an increase in stiffness, leaving the tumor more rigid than normal tissue [6]. Studies have investigated the stiffness of healthy and cancerous breast tissue and reported a stiffness contrast in the range of five to one for carcinomas [25, 51, 52, 23, 53, 54]. Another example are hepatocellular carcinoma that exhibit a denser cellularity, an increased amount of extracellular matrix and hyper vascularization in comparison with healthy parenchyma [55]. Studies in the field of mechanobiology have shown an influence of the mechanical environments to the function of cells [56]. Cancer cells that were grown on a stiff substrate were more likely to migrate, i.e. metastasize than those on a softer template [57].

Modeling of soft tissue in MRE

In order to describe the mechanical behavior of soft tissues within a model, simplifications need to be conducted to a certain degree. In MRE, the main parameter to describe biological soft tissues is the complex shear modulus G^* . As described above, the dynamics of G^* of soft tissues depend on several factors such as rigidity and topology of the multi-scale mechanical networks [58]. In the following, the most common model assumptions used in MRE are described.

The linear elastic isotropic media assumption: The simplest model for MRE inversion algorithms assumes a linear elastic isotropic tissue behavior [14, 17, 59]. It is based on Hooke's law of linear elasticity. In isotropic MRE, it is typical to only estimate the shear modulus, rather than the full elasticity tensor [60]. This approach facilitates the reconstruction of the shear modulus parameter. As the elements of the tensor vary over a similar range, studies have shown that it is very difficult to accurately recover the full elasticity tensor [61].

The visco-elastic isotropic media assumption: Other studies employed a visco-elastic rather than a linear elastic reconstruction as biological soft tissues does not only have elastic but also viscous properties [19, 26, 62]. The local visco-elastic parameters may be estimated through the displacement field resulting from the shear wave propagation. The sensitivity of visco-elastic constants to pathological tissue changes results from the hierarchical organization of mechanical structures in biological tissue [63]. In concrete terms, the effective shear modulus of biologic soft tissue is determined by architectural properties over a continuum of scales from cellular to macroscopic dimensions [64, 65]. If the viscous components are not taken into account, the shear modulus may be overestimated as effects originating from viscosity are associated to stem from the elasticity [19].

The linear visco-elastic transversely isotropic media assumption: As biological tissue is often fibrous, it results in material properties that depend on direction. Those tissues are called anisotropic and it requires several material parameters to describe these fibrous tissues [61]. As it is the case for muscle tissues, the epi-, peri- and edomysium structure causes the tissue to be anisotropic [59]. Studies proposed that the transversely isotropic model is appropriate in characterizing mechanical properties in biological tissues such as the skeletal muscle [66, 67]. It results in a simplified transversely isotropic linear visco-elastic model with isotropic viscosity that has five unknown elasticity coefficients. These coefficients include the two shear moduli μ_{\parallel} and μ_{\perp} as well as three compressional moduli λ_{\parallel} , λ_{\perp} , and λ_{mixed} . The compressional moduli describe the propagation of the compressional wave in different directions [68]. In this model isotropic viscosity is assumed, as anisotropic viscosity would require very high signal to noise

ratio (SNR) values. Tweten et al. describes another three models to characterize nearly incompressible transversely isotropic (ITI) materials: a closed-form expression for traveling waves, finite-element (FE) simulations of waves in homogenous ITI material and FE simulations of waves in heterogeneous material [61].

The visco-elastic anisotropic media assumption: The most generalized model to describe biological soft tissues is based on a visco-elastic anisotropic assumption [7]. For one, soft biological tissues exhibit both solid-like and fluid-like characteristics and are thus described as visco-elastic. For another, some tissues show anisotropic mechanical properties at the macroscopic scale. For example tissues such as skeletal muscle, cardiac muscle, kidney or brain exhibit directionally dependent mechanical properties [10]. Here, the speed of a shear wave depends both on the direction of propagation and the direction of material motion [69]. A more complex material model is required to interpret the MRE image of anisotropic tissues instead of a single elastic modulus [61]. Past research include studies on skeletal muscle [70, 71], breast tissue [72] and white matter in the brain [60]. Other factors might be considered in the model as well and include heterogeneity and boundary effects in living tissue, e.g. observed in the brain [73, 74, 75].

2.3 A Brief Overview of Organs of Interest

The following gives an overview of the anatomy, physiology and pathologies of the human liver and prostate. Those two organs were the focus of the MRE studies during this work. Additionally, literature values of the organ's elasticity are provided at the end of both sections.

Anatomy of the Liver

The liver lies just beneath the diaphragm in the upper part of the abdominal cavity. After the skin, it is the largest organ in the human body and weighs about 1.5 kg in an adult. It is a multi-lobed, wedge-shaped organ [76] and consists of soft and pliable tissue. The main part of the liver is shielded under the right costal margin. Its upper border is at the level of the fifth to sixth intercostal spaces, with its convex upper surface molded to the undersurface of the domes of the diaphragm. Inferiorly, the liver has an irregular visceral surface, which is set obliquely, facing downwards, backwards and to the left. The visceral surface is further divided into a right and smaller left lobe. The right lobe contains the small quadrate lobes anteriorly between the interlobar fissure and the gallbladder, and the caudate lobe behind the interlobar fissure and the inferior vena cava, separated by the porta hepatic, hepatic artery, common hepatic duct, and lymph vessels. The liver is mostly covered by peritoneum. It is attached to

the anterior abdominal wall and the diaphragm by four peritoneal folds. In thin subjects its inferior border may be palpated just below the right costal margin on deep inspiration. The diaphragm separates the liver from the heart and pericardium, lungs, pleura and chest wall. The left lobe is in contact with the abdominal esophagus, the fundus and the body of the stomach and the gastrohepatic omentum, which separates it from the pancreas. [77]

Physiology of the Liver

The liver is closely associated with the gastrointestinal system. Most absorbed nutrient are processed by the liver. The three main function of the liver are (1) contributions to the whole-body metabolism, (2) detoxification, and (3) excretion of protein-bound/lipid-soluble waste products. [76]

Hepatocytes are the major cell type in the liver. They contribute to the metabolism of the major nutrients, namely carbohydrates, lipids, and proteins and in conversion of one sugar to another. Hepatocytes are arranged in cords that form plates. Large quantities of blood can circulate around them. The plates of hepatocytes, which constitute the liver parenchyma, are nourished by a series of sinusoids. Those sinusoids are low-resistance cavities through which blood, coming from the portal vein and the hepatic artery, is supplied. The liver receives a high blood flow that is disproportionate to its mass in order to supply the hepatocytes with high quantities of both O₂ and nutrients. [76]

Pathologies of the Liver

As the liver serves as an agent between the digestive tract and rest of the body, its main task is to maintain the body's metabolic homeostasis. It detoxifies the body and is thus vulnerable to a wide variety of metabolic, toxic, microbial and circulatory insults. The disease process may be primary to the liver and the major pathologies are described in the following. In other instances, the hepatic involvement may be secondary and may relate to common diseases in humans, such as cardiac decompensation, diabetes, and extra-hepatic infections. The regenerative capacity of the liver tends to mask the clinical impact of early liver damage. [78]

Hepatic disorders tend to follow morphologic and clinical patterns, regardless of cause. The morphological changes in pattern occurring during liver injury include degeneration and intracellular accumulation, regeneration, necrosis and apoptosis, inflammation, fibrosis and cirrhosis. Most types of hepatic injury cause a variable mixture of inflammation and hepatocyte destruction. [78]

Cirrhosis Cirrhosis is among the top ten leading causes of death in the Western world [78]. It is defined as a diffuse process characterized by progressive parenchymal injury, fibrosis and the conversion of healthy hepatic cellular structures into structurally abnormal nodules. The major morphological changes that, in combination, create cirrhosis are hepatocellular death, regeneration, progressive fibrosis, and vascular changes. Overall, cirrhosis is mainly caused by alcoholism, chronic infections such as hepatitis B and C, autoimmune hepatitis, biliary diseases, iron overload, and nonalcoholic fatty liver disease (NAFLD). The morphological characteristics of advanced cirrhosis are similar, regardless of the cause of the disease. It is an end-stage liver disease. The main complications of cirrhosis may include a decreased liver function, portal hypertension, and increase risk of hepatocellular carcinoma. [78]

Hepatocellular carcinoma Hepatocellular carcinoma (HCC) is the sixth most common malignancy and the third leading cause of cancer mortality worldwide [79]. The liver is the most common site of secondary spread of cancer cells. The metastases are usually seen as nodular deposits that are located under the capsule [77].

Fibrosis Fibrous tissue is formed as a wound-healing reaction to inflammation or direct toxic insult to the liver. It progresses to scar formation when the injury does not only involve the parenchyma but also the supporting connective tissue. The subsequent deposition of collagen may alter the hepatic patterns of blood flow and perfusion of hepatocytes. [78]

Studies with wideband MRE on liver samples have shown that the fibrogenesis is associated with the replacement of soft and densely linked visco-elastic networks of healthy liver by sparsely cross-linked rigid fibers [80]. Liver fibrosis is seen in hundreds of millions of patients worldwide. The main causes are chronic viral hepatitis B and C and alcohol abuse [81]. To stage the extent of fibrosis in the liver, the determination of liver stiffness is regarded as a reliable biomarker [82]. Studies have non-invasively determined the elasticity of the liver with either transient ultrasound elastography (USE) [83, 84, 85, 86] or MRE [9, 87].

Hepatitis An injury to hepatocytes associated with an influx of acute or chronic inflammatory cells into the liver is termed hepatitis [78]. The chronic viral hepatitis (Type C) is one of the most common chronic liver diseases. With a prevalence of 2.8% worldwide, it globally affects over 185 million people [88]. Approximately 20% to 30% of patients with type C viral hepatitis develop cirrhosis [89]. The subsequent complications such as variceal bleeding, spontaneous bacterial peritonitis, hepatic encephalopathy and HCC account for the morbidity of this disease [90].

Table 2.1 – Elasticity of the healthy human liver reported in literature. Only articles reporting absolute values of G are included in this table. Values are given either as a range or as mean \pm standard deviation.

Elastographic technique	Frequency (Hz)	Shear stiffness G (kPa)	Literature
MRE	51	[1.99 3.07]	[91]
MRE	60	2.20 ± 0.31	[21]
MRE	60	1.95 ± 0.06	[92]
MRE	65	2.06 ± 0.26	[19]
MRE	80	2.0 ± 0.3	[22]
TE*	50	1.79 ± 0.30	[92]
TE	50	[1 2.7]	[83, 84, 93, 94]
ARFI**	n.a.	[0.9 3.0]	[95]

* Transient Elastography ** Acoustic Radiation Force Impulse

Alcohol and drug-induced liver disease Alcohol and drug-induced liver disease consists of three main components: hepatic steatosis, alcoholic hepatitis, and cirrhosis. These pathologies do not necessarily evolve as a continuum. The development of cirrhosis may take over 10 to 15 years of alcohol abuse and occurs only in a small proportion of chronic alcoholics. Alcoholic cirrhosis has the same morphologic and clinical features as cirrhosis caused by viral hepatitis. [78]

Non-alcoholic fatty liver disease The most common metabolic liver disease is NAFLD [78]. Due to inherent errors in the metabolism, including hemochromatosis, Wilson disease and α_1 antitrypsin deficiency and other, this pathology may present as steatosis (fatty liver) or nonalcoholic steatohepatitis (NASH). The latter one is similar to alcoholic hepatitis and involves hepatocyte destruction, parenchymal inflammation with neutrophils and mononuclear cells, and progressive pericellular fibrosis. [78]

Elasticity of the Liver

Reported values of the shear stiffness of the liver in literature are summarized in Table 2.1. The mean hepatic shear stiffness is suggested as a parameter for staging of liver fibrosis, as the shear stiffness increases with increasing staging of fibrosis. A statistically significant difference was observed for patients without substantial fibrosis ($G = 2.24 \text{ kPa} \pm 0.23 \text{ kPa}$, staging F0) compared to patients with intermediate fibrosis grade ($G = 2.56 \text{ kPa} \pm 0.24 \text{ kPa}$, staging F2-F3) and compared to patients with cirrhosis ($G = 4.68 \text{ kPa} \pm 1.61 \text{ kPa}$, staging F4) [19].

Anatomy of the Prostate

The prostate lies below the bladder on the urogenital diaphragm. It is a fibromuscular organ that contains glandular tissue. Its outer shape resembles a truncated cone with a diameter of approximately 3 cm. The prostate is divided into a base above, an apex below and two lateral surfaces. It is transversed by the urethra and the two ejaculatory ducts. These and fibrous septae divide the prostate into a median and two lateral lobes. Pelvic fascia invests the organ and its surrounding venous plexus. The fascia separates the prostate from the rectum. Superiorly to the prostate lies the bladder neck, inferiorly the urethral sphincter. Anterolateral lies the elevator ani and posteriorly lie the rectum and seminal vesicles. [77]

Pathologies of the Prostate

Prostatic diseases mostly fall into one of the categories: carcinoma, nodular hyperplasia, and inflammatory lesions (prostatitis) [78]. Digital rectal examinations (DRE) are performed in order to detect suspicious nodule by palpation. However, the deeper location of the prostate within the body is a fundamental challenge. The palpation of the prostate is mainly restricted to mass lesions in the posterior part of the gland. Furthermore, it depends on the experience and subjective estimation of the examiner and has only a poor spatial resolution. [96]

Prostate carcinoma Prostate carcinoma (PCa) is the most common visceral cancer in males. It is one of the most common causes of cancer-related deaths, after carcinoma of the lung [78, 97]. It is predominately a disease of older males, with a peak incidence between the ages of 65 and 75 years. Not all PCa are clinically apparent. Late cancers of the prostate are even more common with an overall frequency of more than 50 percent in men older than 80 years of age [78].

PCa mostly locates at the lateral lobes [77]. Seventy to eighty percent arise in the peripheral regions of the prostate [78]. It develops in the prostate glandular tissue, which is normally soft [98]. Most PCa are adenocarcinomas and exhibit variable degrees of differentiation and anaplasia [78]. In general, PCa is stiffer than normal tissue. When palpated during DRE, tumors appear as irregular hard nodules compared to the surrounding glandular tissue [78, 98]. Thus, stiffness in the posterior area could be an indication for PCa. [98]

Often, PCa are clinically silent during their early stages. Around 10 % are discovered by chance, for example during histological examinations of prostate tissue removed for nodal hyperplasia. If detect early, PCa can appear as firm, gray-white to yellow lesions that infiltrate the adjacent gland with ill-defined margins. If PCa are already locally advanced, they often infiltrate the seminal vesicles and periurethral zones of the prostate and may invade the adjacent soft tissues and the wall of the urinary bladder [78].

Table 2.2 – Elasticity of the human prostate as reported in literature. Only articles reporting absolute values of E are included in this table. Values are given either as a range or as mean \pm standard deviation.

Elastographic technique	Tissue type	Frequency (Hz)	Elasticity E (kPa)	Literature
MRE	in vivo healthy tissue	65.	[6.6 9.9]	[107]
MRE	in vivo prostatitis	n.a.	1.99 ± 0.66	[39]
MRE	in vivo lesions	n.a.	6.55 ± 0.47	[39]
Sonoelasticity (US)	in vivo healthy tissue	[0.1 250]	[3.8 25]	[24]
Sonoelasticity (US)	in vivo cancerous tissue	[0.1 250]	[7.8 40.6]	[24]
Mechanical testing	ex vivo healthy tissue	[0.1 4]	[55 71]	[25]
Mechanical testing	ex vivo healthy tissue	n.a.	17.0 ± 9.0	[108]
Mechanical testing	ex vivo benign prostatic hyperplasia	[0.1 4]	[36 41]	[25]
Mechanical testing	ex vivo cancerous tissue	[0.1 4]	[96 241]	[25]
Mechanical testing	ex vivo cancerous tissue	n.a.	24.1 ± 14.5	[108]
Mechanical testing	ex vivo cancerous tissue, untreated	[5 50]	110	[109]
Mechanical testing	ex vivo cancerous tissue, treated	[5 50]	118	[109]
Mechanical testing	ex vivo healthy tissue	150	40.4 ± 15.7	[110]

Secondary spread of the cancer is frequently to the vertebral column, with the cells being carried there in vertebral venous plexu [77]. More aggressive PCa may only show clinically through the presence of metastases [78].

In general, diagnostic methods include DRE, determination of PSA level and gray scale transrectal ultrasound (TRUS), and TRUS guided biopsies [99, 98]. However, not all tumors are detectable by TRUS [100]. Biopsies are therefore taken using a sampling scheme, but still tumors might easily be missed [98]. Due to sampling errors, 10 % to 30 % are not detected by this method [101].

Currently, multi-parametric MRI (mpMRI) is seen as the most sensitive imaging technique to detect and localize suspicious lesions within the prostate gland [102, 103, 104, 105, 106].

PCa is graded by the Gleason system that correlates parameters such as location, staging according to the TNM *Classification of Malignant Tumours*, and aggressiveness [78, 99].

Elasticity of the Prostate

Reported elasticity values of the human prostate in literature are summarized in Table 2.2. The values vary over two orders of magnitude. The mechanical properties of the prostate vary widely among different physiological and pathological states and depend, among other factors, on the tissue condition (ex vivo or in vivo), the frequency of excitation, type of pathology (healthy, benign, or malignant), and measurement methods (MRE, US, mechanical testing) [97]. However, studies show, that malignant human prostate tissue increases the stiffness as compared with normal tissue up to four-fold [24, 98].

2.4 Fundamentals of Magnetic Resonance Imaging

MRI is a medical imaging technique used to investigate the anatomy and physiology of the body. It is based on the magnetic properties of nuclei with a nuclear spin that differs from zero. In clinical routine, most images reflect the distribution of the ^1H hydrogen nuclei in the tissue. A total number of approximately 10^{27} hydrogen nuclei are found in the body, most of them in the water molecules. As it is the most abundant nucleus in the human body, it produces the strongest signal. There are also few other nuclei used for MRI, however these are beyond the scope of this thesis.

The following sections give a short overview of the physical effect of the nuclear spin that is used to form and record a signal from the nuclei. They are based on Haacke et al. [111], Levitt et al. [112], and Hanson et al. [113] unless cited otherwise and summarize the physical basics that are most important to understand the forthcoming of this thesis.

Nuclear Magnetic Resonance

Elementary particles, such as protons and neutrons, possess a nuclear spin \vec{I} . The nuclei rotate around their own axis and the rotation, i.e. spin, makes the nuclei magnetic along the axis of rotation. It is a quantum-mechanical phenomenon and an intrinsic property of the particle. The nuclear spin can be regarded as a vector quantity in some degree, since it has a definite magnitude and a direction, although it is quantized and thus differs from classical vector direction.

All elementary particles of a given kind have the same magnitude of nuclear spin. The magnitude is indicated by a spin quantum number, which may only take half-integer values. For example, protons and neutrons have a spin quantum number of $\frac{1}{2}$. Only nuclei with an odd number of protons or neutrons or both have a non-zero spin ($\vec{I} \neq 0$). Nuclides with an even number of protons and neutrons have a total spin of zero, because two identical particles cannot have the same spin orientation and will compensate to zero. This phenomenon is known as the Pauli exclusion principle.

Considering the ground state, the total angular momentum \vec{J} is determined only by the nuclear spin \vec{I} as the orbital angular momentum \vec{L} equals zero. Therefore, the magnetic moment $\vec{\mu}$ can be regarded as the product of the nuclear spin and a specific gyromagnetic ratio γ

$$\vec{\mu} = \gamma \vec{I}. \quad (2.4.1)$$

The gyromagnetic ratio is an element- dependent specific constant. For ^1H hydrogen nuclei, the gyromagnetic factor is $\frac{\gamma_{\text{proton}}}{2\pi} = 42.6 \text{ MHz/T}$.

The human body, or any living tissue, is largely composed of water molecules and the highest number of atoms that can be found in the body are those of hydrogen. Two protons are part of each water molecule and each ^1H has a spin of $\vec{I} = \frac{1}{2}$.

If no external magnetic field is present ($B \neq 0$), the spins of ^1H in the body are randomly orientated. The directions are uniformly distributed such that an equal number of spins pointing in every direction may be assumed. A net magnetization of all spins is near zero.

If the body is placed into a static and homogeneous external magnetic field $\vec{B} = B_0$, a degree of alignment of the spins is established. Now, there is a weak tendency for the spins to point along the magnetic field B_0 . The many hydrogen nuclei (approximately 10^{27}) form a total magnetization called the net magnetization.

The net magnetization is equivalent to around six per million nuclear spins per Tesla oriented along the direction of the field and can be calculated via the Boltzmann distribution

$$\frac{N_{+\frac{1}{2}}}{N_{-\frac{1}{2}}} = \exp\left(\frac{\Delta E}{kT}\right) \quad (2.4.2)$$

with the Boltzmann constant $k = 1.42 \times 10^{23} \text{ J K}^{-1}$, $N_{\pm\frac{1}{2}}$ being the number of spins in one of the two spin $\frac{1}{2}$ states ($m = \pm\frac{1}{2}$).

For $B_0 = 1.0 \text{ T}$ and $T = 310 \text{ K}$ the ratio is

$$\frac{N_{+\frac{1}{2}}}{N_{-\frac{1}{2}}} = 6.6 \text{ ppm.} \quad (2.4.3)$$

This excess of spins pointed along the magnetic field B_0 results in a macroscopic net magnetization \vec{M}_0 in the direction of \vec{B}_0 and can be calculated via Curies law.

The net magnetization can be brought away from the equilibrium so that it is no longer directed along the magnetic field $\vec{B} = B_0$. It subsequently rotates around the B_0 field with a frequency of $\frac{\gamma_{\text{proton}}}{2\pi} = 42.6 \text{ MHz/T}$ as described above. This rotation around the direction of the magnetic field is called precession. Based on the Ehrenfest theorem [114], the precession frequency is known as the Larmor frequency and connects the resonance frequency ω with the magnet field B_0 :

$$\omega = \gamma B_0 \quad (2.4.4)$$

The resonance frequency is thus proportional to the magnetic field. The Larmor equation expresses the ability of designing techniques based on the frequency differences observed in in-homogeneous fields. Relevant for this work is the possibility to design motion encoding imaging techniques.

Relaxation

Interactions between nuclei in a spin system induce that the magnetization constantly approaches its state of equilibrium. This process is called relaxation. The major contribution of contrast in MR images is due to the difference in consistency and the presence of large molecules that restrict free water movement.

There are two principal relaxation effects taking place when the spin system approaches a state of equilibrium. The first one is termed longitudinal or spin-lattice relaxation, and the second one transverse or spin-spin relaxation.

Longitudinal relaxation

The physical model of the longitudinal relaxation process is based on an energy transfer from the spin ensemble to the lattice. The rate of relaxation depends on the interaction of the protons with its environment, which in turn depends on the consistency of the substance. In a real spin system, such as human body tissue, every nuclei is surrounded by intra- and intermolecular magnetic moments. Thermal motion such as rotation and translation leads to an additional local fluctuating magnetic field $B_{loc}(t)$, which has a typical spectral distribution J_ω . The longitudinal components of J_ω at ω_0 (Larmor frequency) allow an energy transfer $\hbar\omega_0$ from the spin system to the lattice.

After an excitation of the spin system with an radio frequency (RF) pulse, the longitudinal magnetization M_z relaxes exponentially to the equilibrium state $M_z = M_0$ with a time constant T_1 . The phenomenological description of this relaxation process is the solution of the Bloch equation

$$\frac{dM_z}{dt} = (\gamma \times B)_z + \frac{M_0 - M_z}{T_1} \quad (2.4.5)$$

$$M_z(t) = M_0 \left[1 - \exp\left(\frac{-t}{T_1}\right) \right] \quad (2.4.6)$$

with $M_z = 0$ at $t = 0$.

In general, T_1 depends on size of molecules, mobility and kind of surrounding and is a measure of how fast a spin ensemble can transfer excess magnetic energy to lattice. Fat has a shorter T_1 compared to most liquids, as the surrounding of the protons are larger macro- molecules, such as lipids and amino acids, resulting in relatively little motion of the molecules. In contrast, cerebral spinal fluid is a liquid with many similarities to water. It has a faster molecular motion compared to changes in the local magnetic field. This results in fewer and less resonance. An equilibrium M_0 may be reached after approximately one second regarding brain tissue, whereas it takes several seconds for pure water.

Transverse relaxation

The second relaxation effect, the transverse relaxation process, is based on decreasing phase coherence after a 90° RF excitation pulse. The phases of the spins dephase due to an influence of the transverse components J_ω of the fluctuating magnetic field $B_{loc}(t)$. As there is no energy transfer in the spin system related to this process, there is also no influence of the T_2 relaxation on T_1 ; they are independent.

The relaxation in a real setting is even faster, as further influences of technical inhomogeneities of B_0 cause a faster decay of the phase coherence. This is known as the effective relaxation T_2^* . The phenomenological description of the spin-spin relaxation process is the solution of the Bloch equation

$$\frac{dM_{xy}}{dt} = (\gamma \times B)_{xy} + \frac{M_{xy}}{T_2} \quad (2.4.7)$$

$$M_{xy}(t) = M_0 \exp\left(\frac{-t}{T_2}\right) \quad (2.4.8)$$

with $M_{xy} = M_0$ at $t = 0$. Similar to spin-lattice relaxation, spin-spin relaxation and therefore T_2 also depends on the tissue type, however is mostly independent of the magnetic field strength B_0 . The transverse magnetization M_{xy} thus decreases exponentially on a time scale of approximately 100 ms for brain tissue and several seconds for pure water.

Magnetic Resonance Image Acquisition

To form a detectable MR signal, the magnetization needs to be rotated from its starting point ($M_z = M_0, M_{xy} = 0$) into the transverse plane and the phases of the precessing spins have to be synchronized. The tissue is exposed to an additional time-dependent (RF) field \vec{B}_1 . Those RF fields, also known as pulses, are magnetic fields that change direction in time. The frequency of the RF field must be in resonance with the frequency of the precessing spins (Eq. 2.4.4) in order to rotate the magnetization away from its equilibrium state. In the end, the obtained signal strength is proportional to the component of the magnetization that is perpendicular to the main magnetic field B_0 . The component of the magnetization that is in parallel to B_0 does not contribute to the signal. Furthermore, the RF field \vec{B}_1 brings the individual nuclei in phase, meaning they synchronously precess, i.e. oscillate, perpendicularly to B_0 .

A so-called sequence is an MRI measurement method consisting of serial events during measurements of MRI signals. Sequences include elements such as *excitation*, *dephasing*, *refocusing pulse*, *readout*, and *waiting times*.

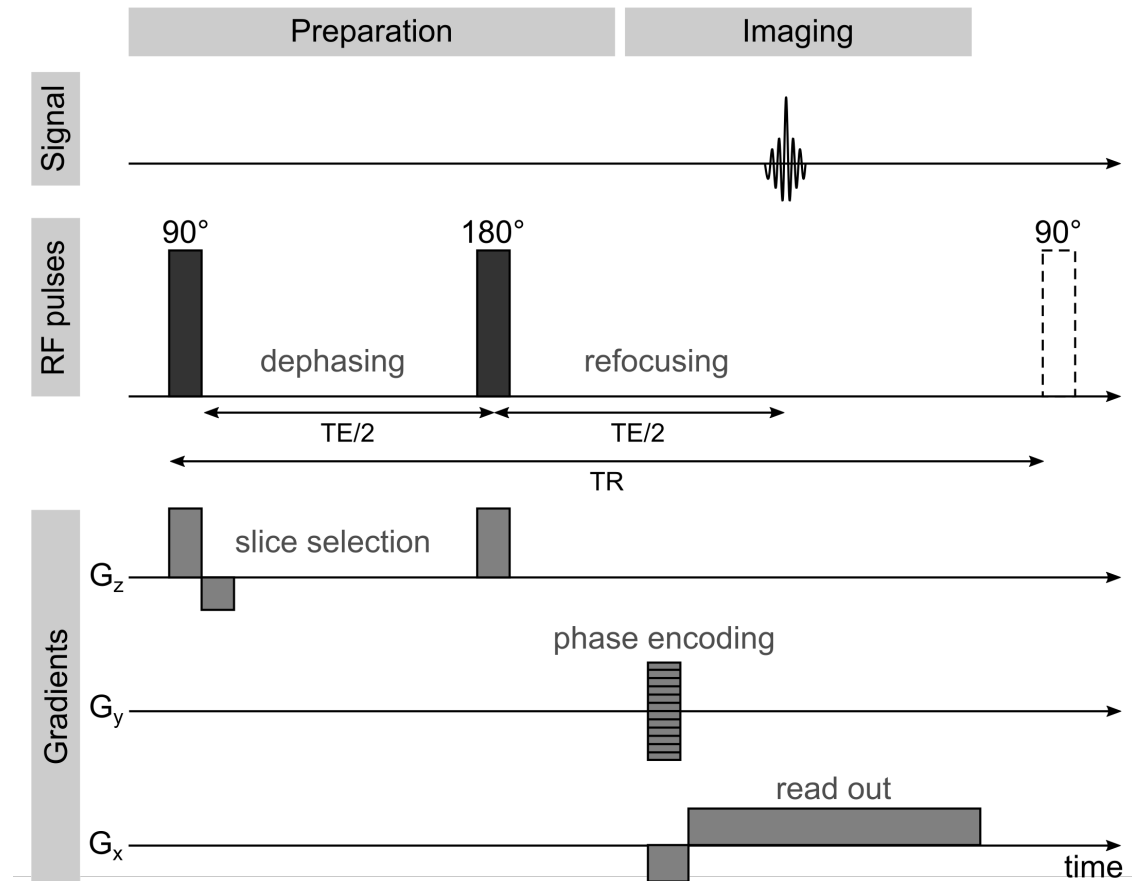


Figure 2.3 – Sequence diagram of a spin-echo sequence with essential building blocks of the sequence.

During a common *spin-echo sequence* (Fig. 2.3), a 90° pulse is applied in order to rotate the magnetization 90° away from equilibrium. After a short waiting period, spins dephased to certain degree due to magnetic field inhomogeneities. An 180° pulse, also termed refocusing pulse, is applied at a time of $\frac{T_E}{2}$, with T_E being called the echo time, after the first 90° pulse. The 180° pulse eliminates the dephasing effects of inhomogeneities. After another time $\frac{T_E}{2}$, the signal is rephased in the transverse plane and the signal is read out. The sequence is repeated after a repetition time T_R . Further sequence elements may include imaging gradients, bipolar gradients and more. Imaging gradients are used for the spatial localization of the signal. The latter one, bipolar gradients, are important for motion encoding during MRE and are described in detail in Sec. 2.5. There, a more complex sequence diagram of a motion encoding sequence, its readout, as well as reconstruction will be elaborated further.

In order to obtain images from the MR signal, the scanner is equipped with additional electromagnets called *gradient coils*. These gradient coils cause linear variations of the magnetic field. The resonance frequency ω then varies in the direction of the field gradient \vec{G}

$$\omega(\vec{x}) = \gamma (\vec{B}_0 + \vec{G}). \quad (2.4.9)$$

The resonance condition is only fulfilled in a perpendicular plane to the gradient. This principle is used for the following types of encoding in MRI: slice selection, phase encoding and read out. The difference is the timing of those three types.

For example, a gradient G_z increases the magnetic field from the feet to the head of a patient (Fig. 2.3). If G_z is applied simultaneously to an RF pulse with a certain frequency to excite protons, a single transverse slice is selected, i.e. a perpendicular plane to the direction of G_z .

To create a spatial localization within the slice, different patterns of the magnetization throughout the slice are generated with the remaining two other sets of gradients. They encode phase and frequency in a slice. The phase encoding gradient, G_y in Fig. 2.3, is set between excitation and read out and differentiates signals with respect to their spatial location along an specific axis within the slice. The read out gradient G_x is the last gradient. It sets a frequency dependent phase shift along the axis as a function of their spatial position within the gradient.

The returned radio wave signal of the tissue is then registered as a function of a \vec{k} -vector (k_x, k_y) and stored in a so-called *k-space*. It represents the spatial frequencies and phase information in the x - and y - directions. Each application of the phase encoding gradient fills another row of k -space. Using the inverse Fourier transform (FT), the k -space is transformed to a complex MR image. The representation of the complex MR image can be split in a magnitude and phase image, whereas the phase image contains the most relevant information for MRE.

2.5 Fundamentals of Magnetic Resonance Elastography

MRE was first described in 1995 [9] as a diagnostic tool that, like palpation, is able to detect abnormal stiffness differences in soft tissue. Before that publication, a theoretical approach has been proposed by Lewa [115] and other image-based palpation techniques using medical ultrasound [47] has been described before.

As already mentioned, the micromechanical properties of the hierarchically structured soft tissues are linked to the macroscopic global visco-elastic properties of the tissues [116]. The major objective of elastography, including MRE, remains to identify the relationship between tissue structures [63] and to produce a quantitative map of the tissue elastic modulus using the available measurements of displacement components [7]. Compared to other elastography techniques such as transient USE, dynamic MRE is able to evaluate larger volumes and providing 3D information on the visco-elastic parameters of in vivo soft tissues [9, 23, 62, 72, 117].

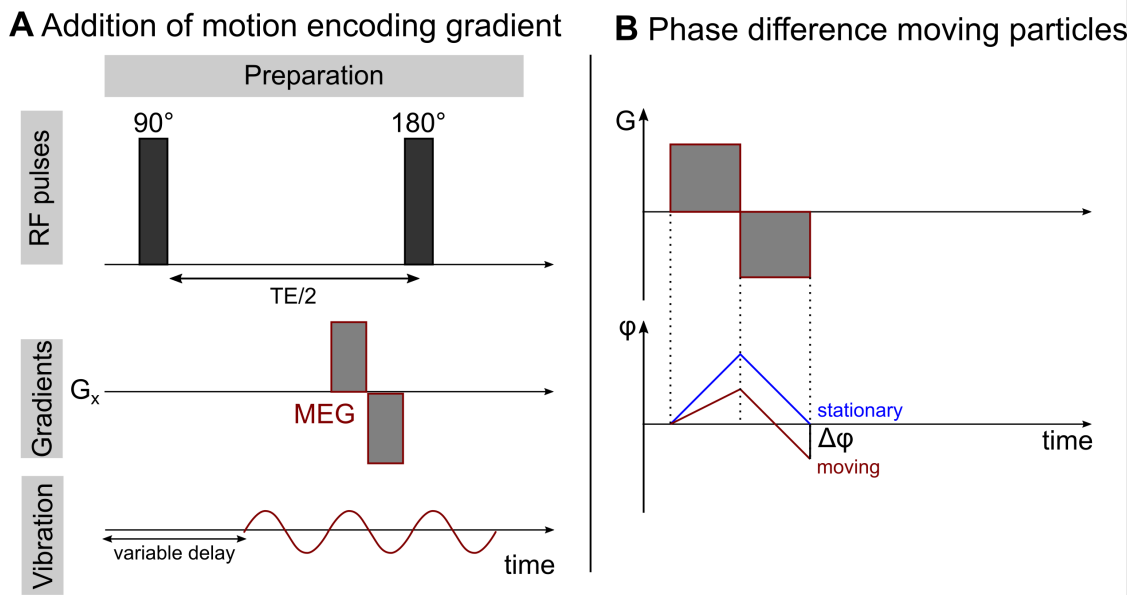


Figure 2.4 – Motion encoding of the vibration. **A:** An additional motion encoding gradient (MEG, red) is set prior to the 180° pulse. A variable delay, i.e. phase offset, is set between the vibrational wave and the MEG. **B:** Phase differences accumulate for moving particles in comparison to stationary particles, if a bipolar gradient is applied.

MRE is termed a dynamic phase-contrast MRI technique [32, 118], which is elaborated in the following section. A representative implementation of the MRE methodology is a three-step procedure. First, mechanical waves are generated in the tissue of interest. Second, the waves are imaged using a modified phase contrast MRI technique. Third, the wave images are processed using an inversion algorithm to produce quantitative images representing mechanical properties such as shear stiffness [9, 119].

The inducing of mechanical waves into tissue during an MR scan generates movement of the tissue, which causes artifacts called ghosting. Usually, this is seen as a detrimental effect that affects the image quality and should be avoided. However, motion artifacts are exploited in MRE: the displacement of a propagating mechanical becomes measurable with a phase encoding sequence [96, 118, 120]. The MR technique quantifies this spin motion captured in the phase of the detected MR signal with sensitivities down to tens of micrometers [121].

MRE image acquisition

Dynamic harmonic wave actuation

The aim of MRE is to quantify the tissue elasticity modulus based on available measurements of displacements components [7]. The displacement of the tissue is measured under an applied mechanical stress. This stress may be either dynamic or static. In the case of MRE, a dynamic,

repetitive time-harmonic shear motion is applied to the tissue near a ROI [7]. An actuator can generate this cyclic motion and contact friction between a contact plate and human skin is sufficient to transfer the shear motion across the interface [117]. The generated shear waves usually have a vibrational frequency in the range of 10 Hz to 1000 Hz and propagate with a wave velocity of $1 \frac{m}{s}$ to $5 \frac{m}{s}$ through the body, depending on the tissue type [24, 25]. The resulting cyclic displacements of the tissue are mapped into the phase of the MR signal using motion sensitive imaging gradients [32]. Several sequence types have been proposed for MRE signal acquisition.

Sequence types

Gradient echo (GRE) based sequences have been developed, e.g. for preliminary MRE validation studies for liver fibrosis staging [21, 122, 123, 124]. More recently, SE-EPI have been introduced for MRE, as they yielded a faster and more efficient sampling of hepatic tissue compared to conventional GRE-MRE [3, 19, 41, 125, 126]. Nevertheless, the measured stiffness values at any given frequency of external vibration should remain the same, independently of the employed sequence [125].

Motion encoding gradients

Motion sensitive imaging gradients, also called motion encoding gradients (MEGs), are implemented in the underlying sequences, e.g. a GRE or SE-EPI sequence. In the presence of a gradient field, a spin with a trajectory $\vec{x}(t)$ accumulates a phase [127]

$$\phi(t) = \phi(t_0) + \gamma \int_{t_0}^t \vec{G}(t') \cdot \vec{x}(t') dt' \quad (2.5.1)$$

Assuming a sinusoidal motion in MRE, the displacement is given by

$$\vec{x}(t) = \vec{x}_0 + A_m \cdot \sin \omega_m \cdot t + \phi_m \quad (2.5.2)$$

with \vec{x}_0 being the voxel position, A_m being the amplitude of the mechanical wave, ω_m being the frequency of the mechanical oscillation, and ϕ_m being the phase of the mechanical wave [127]. The MEGs are bipolar gradients and synchronized with the applied external vibration. The motion is thus encoded in the axis the MEGs are superimposed on (Fig. 2.4). Very high sensitivity to small shear wave amplitudes can be achieved by accumulating phase shifts over multiple cycle of mechanical excitation [117]. Mechanical waves in the ROI with amplitudes in the tens of micrometers can be imaged [119, 121].

The accumulated phase shift is proportional to the dot product of the gradient vector and the displacement vector, number of gradient cycles and periods of the gradient wave form:

$$\phi(\vec{x}, \theta) = \frac{2\gamma NT \left(\vec{G} \xi_0 \right)}{\pi} \sin\left(\vec{k} \vec{x} + \theta\right) \quad (2.5.3)$$

with θ the initial phase offset, N the number of gradient cycles, T the period of mechanical excitation, the initial phase offset, ξ_0 the displacement amplitude, and \vec{k} the wave vector [9]. Usually, two images are acquired for each repetition with a reversed polarity of the MEGs to reduce systematic phase errors and increase the sensitivity to small displacements [117].

Also, acquiring multiple images with varying phase offset between the externally applied mechanical wave and the MEG allows the calculation of the harmonic component at the frequency of interest and yields the amplitude and phase of the harmonic displacement at each spatial location [117]. A single MRE image acquires only one component of the displacement data, as the MEG encoded the motion in a single direction. By repeating image acquisition with varying MEG directions, all three orthogonal components of the displacements can be recorded [117].

Encoding efficiency

In order to achieve a sufficient SNR to reconstruct elasticity values from the phase images in post-processing, a spin displacement in the order of several micrometers within the ROI is usually required [121].

At a lower excitation frequency, attenuation and dispersion are typically lower [128], resulting in better wave penetration [129]. However, with the same field of view and the same matrix size, the resolution of the elasticity map is reduced at a lower mechanical frequency [130]. The overall acquisition time of the imaging sequence depends on T_E . A lower excitation frequency increases the duration of the MEG and thus T_E , which in turn leads to a lower SNR [97].

It is possible to use a second-harmonic approach. Here, the frequency of the MEG, e.g. 120 Hz is twice that of the mechanical excitation 60 Hz. A past study compared the sensitivity loss of the second-harmonic approach to the conventional MRE sequence and found that the sensitivity loss was offset by the SNR gain due to a shorter T_E [97].

Further, higher applicable gradient strengths can improve signal quality of the accumulated phase signal. Research groups have been using a MEG strength of $40 \frac{\text{mT}}{\text{m}}$ or higher [131].

Synchronization of the scanning sequence and the actuator is also important. Any phase shift between MEG of the imaging sequence and mechanical vibrations leads to a cumulative error in the measurement of wavelength in tissue and wavelength estimation [120].

Image reconstruction and elastograms

A set of phase images sampled at several time points within one mechanical wave cycle is recorded. From these images, wave images and an elastogram, which reflects the stiffness of the tissue, is reconstructed using a mathematical inversion algorithm [132]. A requirement for a reliable evaluation is a stable phase relationship of the of the mechanical wave to the MEG gradient [118]. More precisely, the quality depends on the spatial derivatives of the encoded phase [7].

Two classes of algorithms are commonly employed to reconstruct tissue stiffness from displacement data: direct inversion (DI) and nonlinear inversion (NLI) [133]. For this work, the focus is set on DI algorithms, which directly estimate mechanical properties by differentiation of the motion data [132, 134]. These algorithms are based on the wave equation and assume locally homogeneous, isotropic, nearly incompressible and mechanical properties [97].

The most common approach is the local frequency estimation LFE model [9].

The propagation of an acoustic wave in a locally homogeneous isotropic visco-elastic medium is described by the following partial differential equation for the total displacement \vec{u} [19]

$$\rho \partial_t^2 \vec{u} = \mu \nabla^2 \vec{u} + (\lambda + \mu) \nabla (\nabla \cdot \vec{u}) + \zeta \partial_t \nabla^2 \vec{u} + (\xi + \zeta) \partial_t \nabla (\nabla \cdot \vec{u}) \quad (2.5.4)$$

with ρ being the density of the material, μ the shear modulus, λ the second Lamé coefficient, ζ the shear viscosity accounting for attenuation within the medium and ξ the viscosity of the compressional wave. Other approaches include the algebraic inversion of the differential equation [135], curl based direct inversion [23, 132] and variational method [136, 137]. Before performing the direct inversion, the curl operator is applied to the displacement fields to remove the longitudinal (compressional) component of wave motion [97]. This leads in steady-state to the following equation of motion [19]

$$-\rho \omega^2 \vec{q} = (\mu + i\omega\zeta) \nabla^2 \vec{q} \quad (2.5.5)$$

with $\vec{q} = \nabla \times \vec{u}$. All other quantities are measured or assumed to be known in Eq. (2.5.5) and the method allows the estimation of the shear visco-elastic parameters μ and ζ (27, 28).

It has to be noted that the LFE algorithm assumes a purely elastic medium. Thus, if only shear waves are present in a purely elastic medium, local elastic modulus variations are determined via the relation

$$\mu = v^2 \lambda^2 \rho \quad (2.5.6)$$

with μ being the local shear modulus, v the frequency of the applied deformation, λ the measured local strain-wave wavelength and ρ the density of the medium [7].

Additionally, a bandpass directional filter can be applied to remove reflected waves [138].

The DI can be performed with either a 2D or 3D technique. A past study reported the 3D processing method to be more precise than the 2D method, especially regarding propagating waves in complex organs [139]. However, it requires the encoding and acquisition of the three orthogonal wave components and increases overall scan time. The 2D method can still accurately reconstruct the elasticities under the assumption that the shear waves in the tissue propagate within each image slice and not obliquely to them [122].

Applications

Within the last twenty years, MRE has shown to have a potential value in diverse applications. The largest benefit is seen in the additional diagnostic information regarding tumor detection and classification as well as in the assessment of hepatic fibrosis [27].

Several types of malignancy are known to be harder than healthy tissue [121]. For example, breast cancer is often stiffer than benign lesions and normal surrounding tissue. Breast cancer often shows a desmoplastic stromal reaction with reactive proliferation of connective tissue and fibroblasts around malignant epithelial cells [140]. The tissue reaction is the base on which breast lesions can be detected by palpation [121, 29]. However, a clinical breast examination using palpation is subjective, whereas MRE of the breast has shown to quantitatively evaluate the stiffness of suspicious lesions [134, 141, 142]. Various studies have shown the application of MRE for detection of tumors in other organs as well [6, 28, 37, 143, 144, 145].

Furthermore, hepatic MRE was performed in patients, including liver transplant recipients, where a good correlation was found between histologic grade of fibrosis and tissue stiffness measured with MRE [19, 21, 28, 146, 147].

MRE is unique in that it can also be used in regions such as the brain where conventional manual palpation is not applicable [118, 148, 149]. Similarly, it has been shown that despite the low SNR of proton MRE in the lungs, this technique can be used to differentiate stiffness distributions in the lung parenchyma under clinically feasible conditions [40, 131, 150, 151]. Other areas include research regarding the biomechanical properties of the skeletal muscle [27, 152, 153, 154, 155].

2.6 MRE Hardware

The periodic mechanical excitation generates motion in the tissues of interest and is the first step in the acquisition of MRE data. The movement in the tissue is a sinusoidal mechanical displacement with a certain amplitude and frequency. Besides adjusting the MR acquisition parameters to achieve a maximum SNR, optimizing the frequency and amplitude of the mechanical transducer is an important task [121]. To ensure the noninvasiveness of this methodology, it is desirable to place the vibration device outside the human body on the skin surface above the area of interest [27, 121]. A major problem with MRE is the design of an actuation system that allows the desired mechanical excitation in the magnetic field of the MRI without comprising the safety of the patient and the MRI [121].

Typically, MRE images are acquired with excitation amplitudes below 2 mm at the surface and frequencies below 500 Hz [121], with the majority of experiments using a lower frequency range of 40 Hz to 150 Hz [27]. In order to increase the penetration depth, generally lower frequencies are indicated, whereas the requirements for acquiring several wave periods within the FoV and increasing the spatial resolution of the elastogram indicates higher frequencies. Thus, a compromise must be reached [121].

Up to now, the parameters used in elastography have generally been determined by experimental tests on each new tissue type. There is no gold standard or commonly agreed rules for optimization of acquisition parameters [120]. It is important to find an optimal shear wave amplitude at each specific frequency at the body surface. The actuator should induce mechanical waves that fully penetrate the ROI and provide sufficient spin displacement. So far, this has been determined physically by performing trial runs for each MRE set-up. The determination of the optimal values of these parameters therefore depends strongly on the exact method and the place of excitation as well as on the tissue types. At least, the parameters do not usually have to be optimized in the individual subjects [121].

Literature review of actuation hardware

Several methods currently exist for dynamic harmonic mechanical excitation. These techniques are further elaborated in the following.

Acoustic driving systems

The most commonly used systems in earlier MRE studies are acoustic driving systems, also called remote pneumatic actuators [29, 30]. Here, shear waves are generated using pneumatic cushions powered by varying acoustic pressure levels.

These sinusoidal sound waves are generated by an active audio device (loud speaker) located outside the scanner room [21, 22, 28]. This loud speaker is connected via a flexible hose to the passive actuator that is placed near the organ of interest [153, 154, 156]. Frequencies in the range of 25 Hz to 100 Hz are commonly achieved with this approach while some studies applying frequencies of up to 200 Hz [134, 152].

Studies demonstrated that pneumatic solutions with large areas of surface contact can sufficiently induce mechanical waves to penetrate the deep lying region of the body, e.g. in organs such as the liver or the kidney [157]. Alternatively, pressure waves generated by a loud speaker can be transmitted to the surface near the heart or the head via a long carbon-fiber rod [121]. Another groups generated sine wave signals by a frequency synthesizer outside the MR room and transferred the signal to a commercial subwoofer placed against the wall of the MR room in line with the table. A carbon-fiber rod was placed at the cone of the subwoofer speaker to transmit the vibration. The rod was connected to a balloon inside a modified endorectal coil. The motion of the rod resulted in a contraction and dilation of the balloon and subsequent induction of shear waves in the adjacent surface [96]. The maximum vibration amplitudes of the subwoofer have been estimated to be in the range of 0.3 mm to 0.5 mm [158]. The resulting lateral vibration amplitudes were smaller, approximately 0.1 mm to 0.2 mm, due to the effective translation of longitudinal motion of the reversing mechanism to the lateral motion of the balloon [96].

In general, these pneumatic systems are simplistic, low-cost devices with a good MR compatibility, which is why this system is often chosen. An important limitation to be considered before using such an actuator type, however, is its limitation to low-frequency excitation [159]. The pneumatic drum drivers operate well in the lower frequency regime (≈ 60 Hz). At higher frequencies, however, it becomes problematic to sustain sufficiently large wave amplitudes and additional power amplification is necessary to maintain an adequately large displacement range. Furthermore, controlling the vibrational frequency and amplitude is difficult, therefore their application is limited to low-frequency excitation below 100 Hz [121, 159].

Electromechanical driving systems

Another method of inducing mechanical shear waves is the use of an electromagnetic actuator [87, 118, 129, 134]. The actuator generally consists of a coil with several wire windings. The coil is aligned orthogonally to the static magnetic field of the MR scanner [121]. If a sinusoidal current is applied to the coil, the actuator oscillates due to the magnetic induction (Lorentz force) about a fixed axis of rotation within the scanner [118, 160]. The periodic mechanical rotation of the coil can then be used to excite the tissue [121].

Another variant is the application of a commercially available electromagnetic shaker, which is located outside the scanner room. The vibrations can be transmitted via a semi-flexible

carbon-fiber rod and converted into vertical vibrations through a cantilever [43].

Several research groups have implemented electromechanically based actuators [87, 161, 162] and applied it for liver [3, 50], brain [160], and external actuation during prostate MRE without the need for endorectal actuation [163].

Despite a simple and cost-effective design of electromagnetic actuators, several issues arise during the implementation of electromechanical actuators for MRE signal acquisition [159]. The induction works well as long as the magnetic field is constant. The interaction is however influenced by switching gradient fields [164]. This effect can distort the desired sinusoidal oscillation. The interaction of electromechanical devices with magnetic field gradients can cause a wide spectrum of excitation away from the intended frequency [164], requiring these devices to be designed so that the inherent magnetic field of the device is dominant [121]. The effect can be minimized by optimizing the coil design in terms of diameter and number of turns but is never completely eliminated. In addition, the magnetic induction generates a fixed torque to move the coil, and therefore, the vibration amplitude is a function of the interface between the actuator and the subject [118, 121]. Furthermore, the magnetic field occurring in the electromechanical device itself disturbs the highly homogeneous field of the MR tomograph and must therefore be positioned sufficiently distant from the imaging area such that the image acquisition is not disturbed [121].

Although neither the pneumatic nor the electro-mechanical driver can achieve precise control of a piezoelectric actuator in terms of frequency and amplitude, both approaches presented so far have found niches for assessing the potential of MRE applications.

Piezoelectric driving systems

Other application-specific drivers have been proposed that use piezoelectric drivers [118, 165, 166]. A piezoelectric actuator is composed of a stack of piezoelectric crystals, often a material such as lead zirconate titanate is used, which expands when a voltage is applied. If this voltage is alternated and the stack is placed between a spring and rigid housing wall, a precise longitudinal vibration is generated [118]. This technology creates sinusoidal mechanical waves with a highly stable and precise control for a frequency range up to 500 Hz with amplitudes up to 1 mm [37, 121].

One study presented a piezoelectric based actuator including a lever that was used to transfer the oscillation generated by the piezoelectric ceramic to the surface of interest. The housing for the piezoelectric ceramic was made of aluminum. Smaller parts of the housing were manufactured from brass and titanium to meet certain mechanical requirements, as large forces can be generated with a piezoelectric actuator. The generation of large forces also allowed the use of a lever mechanism. The lever amplified the piezoelectric motion and reached an amplitude of up to 1 mm in a frequency range from 0 Hz to 300 Hz [118]. Depending on characteristics of the piezoelectric bending element and number of elements in the stack, other research groups achieved displacements of 24 μm to 200 μm [141, 167, 168].

Another variation of the actuator is divided into two parts, one for performing an oscillation using a driving element and the other for detecting the vibration using a pick-up element. The detected vibration is fed to an electronic feedback loop [98].

Another study published a custom piezoelectric actuator that was coupled to an endorectal coil. The actuator consisted of a 111 mm long stack of piezoelectric crystal enclosed in a polycarbonate housing. The design made it possible to produce cylindrical shear waves throughout the region of interest [37].

Compared to the pneumatic and electromechanical drivers presented above, the development of a piezoelectric system is cost-intensive. Its design is highly complex and requires a much greater design effort. Furthermore, problems regarding image distortions due to susceptibility and eddy currents as well as heat buildup during operation need to be addressed [121]. Materials for the actuator have to be selected in such a way that they do not impair the MR compatibility and safety of the imaging process [121].

Gravitational driving systems

A further transducer concept was presented by [169]. The so-called gravitational transducer is driven by a rotational eccentric mass. This is a similar approach as the driver presented in this thesis. However, the gravitational transducer is powered by a stepper motor that is attached to the gravitational transducer via a rotating rod making the set-up in the scanner room cumbersome and limiting the accessible surfaces.

Multiple drivers

An extension of the presented drivers is their application into a dual or multi-location actuation concept. Typically, only a single transducer is applied on the surface of interest. In some applications the penetration of shear wave can be limited through attenuation and shadowing of the waves. The physical damping of the propagating shear waves due to viscous losses of wave energy and geometric dispersion of wave fronts can lead to a very low amplitude of waves in the tissues remote from the wave source. This reduces the accuracy of the inversion results due to the increased influence of noise in the data [32]. Additionally, waves propagating through stiff tissue regions can be significantly attenuated. Shadowing occurs behind stiffer areas, where the wave's motion is attenuated and amplitude is decreased. As a result, the stiffness estimation might be less reliable.

In order to increase the actuator performance, dual or multiple driver approaches were presented by several groups to compensate for shear wave attenuation and to achieve better coverage over the entire region of interest [31, 32]. For one study, a pair of standard active subwoofers with airtight acrylic lids mounted over the speaker membrane were modified as air pressure sources. In the middle of the lids, a hose connector was mounted to a flexible tubing which

guided acoustic waves into the passive drivers at the surface of interest [159]. The usable frequency range for experiments with phantoms was up to 150 Hz during the study. Another study implemented a phased-array acoustic driver system capable of applying independently controlled waveforms to each of the eight channels [32]. Although it has been demonstrated that the use of two coupled drivers can improve MRE stiffness estimation, the benefits and advantages offered by the use of multiple, independent drivers have not been thoroughly investigated [170].

2.7 Technical Compliance

Patient safety in MRE examinations

Patients undergoing an MRE examination are exposed to mechanical vibrations during image acquisition. Depending on the study, the exposure to vibrations during the entire MRI examination is estimated to be less than 15 minutes. An analysis concluded that the typical vibrational displacements used in MRE studies are far below the values permitted by the EU whole body vibration standard (EU 2002/44/EC) [27]. For example, the average maximum tissue vibration amplitude during a sampling of hepatic MRE examinations was approximately 200 μm , with most areas of the liver tissue experiencing significantly less vibration [27].

Other in vivo MRE studies also evaluated patient comfort and did not report discontinuation of an examination because of patient complaints due to excessive vibrations. Another analogy is given regarding trans-perineal excitation methods. Since men experience considerable vibrations when cycling over moderately rough roads, a study concluded that no complaints were to be expected during prostate MRE with trans-perineal excitation [97].

MRE hardware restrictions due to the MRI environment

A major difficulty in the development and application of mechanical hardware is the MRI environment itself, as it imposes rigorous restrictions on MRE mechatronics to be MR-compatible [120]. These devices must be designed to avoid artifacts or electromagnetic noise and be suitable for use in the high magnetic field of an MRI scanner [27].

Electronic components are generally avoided, if they are not properly shielded. At best, they are at least 1 m to 2 m from the scanner and have filtered all input or output cables through low pass filters [171].

Components containing metallic material can induce eddy currents under the rapidly varying gradient and the interference of the RF pulses, which can lead to overheating and functional damage. In addition, since the actuator is positioned near the FoV and is in contact with the

scanned tissue, its MRI compatibility may significantly affect image quality [120]. If metallic components are considered as non-replaceable, the selection of brass, aluminum and titanium components is considered MRI safe and MRI compatible [121].

Standards and Norms

Various norms publish procedures for material evaluation in an MRI environment. For the measurements during material testing, this work consulted the standard of the the American Society for Testing Materials (ASTM) F2119 [172]. This standard provides a test method for the evaluation of MR image artifacts from passive implants. Also, the European Norm (EN) for MR systems for medical diagnostics EN60601-2-33 was taken into account [173]. It states requirements for the basic safety and essential performance of MR equipment for medical diagnosis. Other ASTM standards state methods for measurements of radio frequency induced heating on or near passive implants during MRI (ASTM F2182 [174]) and for measurements of magnetically induced torque on medical devices in the magnetic resonance environment (ASTM F2213 [175]). However, the developed hardware was only placed externally on the human body. Thus, only the extent of artifacts, but not heating and torque, was evaluated during this work.

Materials and Methods 3

The aims of this work divide into three main parts and the materials and methods are described accordingly:

- 3.1 Actuator development and evaluation
- 3.2 Linking the actuator to the MRI system
- 3.3 MRE image acquisition

The first part describes the design and implementation of the actuator divided into the passive pneumatic turbine located in the scanner room and the active driver controlling the pressure of the compressed air located in the control room. The methodology of evaluating the technical parameters of the turbine is presented.

The second part delineates the linking of the actuator to the MRI system. Here, the development of a sequence and a trigger synchronization as well as the application of a reconstruction toolbox is introduced.

The third part reports the implementation of the developed work-flow for MRE studies on tissue-mimicking phantoms developed in-house as well as in vivo studies.

The generation of shear waves with a frequency of 60 Hz is the most widely used actuation frequency in clinical applications at present [147, 176]. It is the reason why many experiments of this work focus on this particular actuation frequency of 60 Hz.

3.1 Actuator Development and Evaluation

3.1.1 The Passive Driver

Dynamic harmonic vibrations through the generation of centrifugal force

This study set out to investigate the feasibility of a novel method for sinusoidal mechanical wave generation based on the principle of centrifugal force. The design approach was similar to that of the industrially used compressed air vibrators, which are common in the bulk material handling sector. There, an eccentric weight, also called unbalance, within these pneumatic turbines generates a dynamic harmonic vibration. This results in a centrifugal force during rotation. The force depends on the driving frequency of the turbine as well as on the weight and dimensions of the unbalance. The frequency itself can be freely selected according to the applied air pressure level. However, due to the turbine material and centrifugal force range, commercial compressed air vibrators cannot be operated safely within high magnetic fields (> 1 T) and are not in the required range of mechanical wave actuation force for MRE.

The goal was to develop a new 3D printed pneumatic vibrator that was MR-compatible and corresponded to the range of wave amplitudes needed to generate suitable shear waves in human tissue for MRE.

In general, the generated force F depends on the weight of the unbalance m_{ecc} , the distance r_{ecc} between the mass center of gravity of the unbalance and the rotation center of the turbine, as well as the angular velocity ω of the turbine and can be calculated via $F = m_{ecc}r_{ecc}\omega^2$ (Fig. 3.1). Consequently, a greater force can be generated by:

- a) Using materials with higher densities for the unbalance,
- b) Increasing the volume of the unbalance,
- c) Changing the geometry so that the distance of the center of gravity of the unbalances increases to the center of rotation,
- d) Increasing the frequency of the turbine.

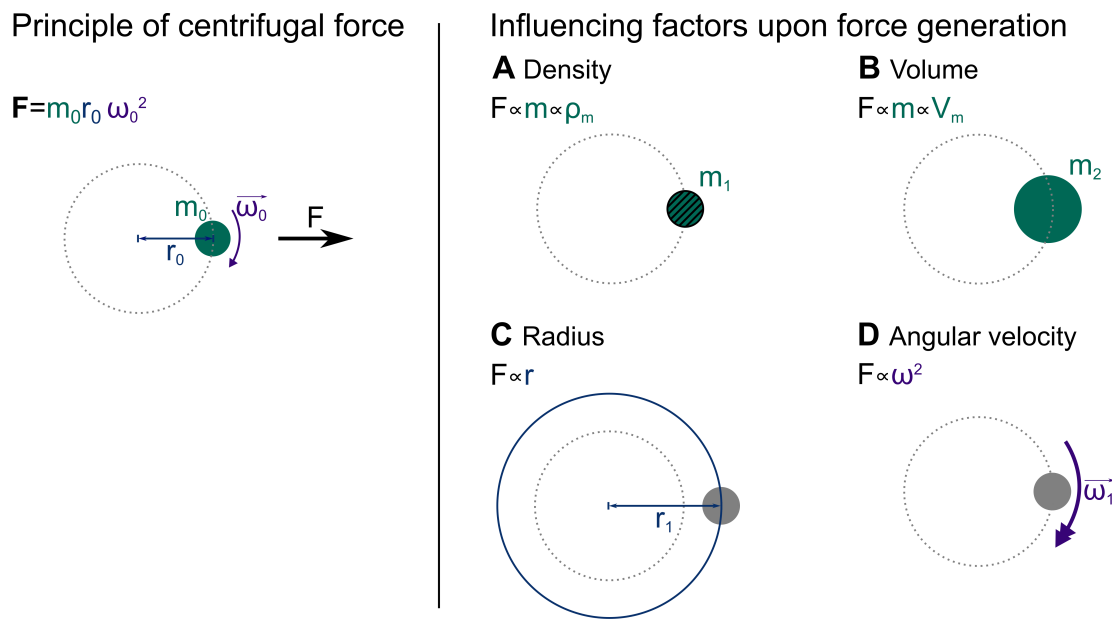


Figure 3.1 – Illustration of the influencing factors on the generation of centrifugal force. The generated force F is directed outward and can be manipulated by changes in **A**: the density of the unbalance m_0 (green), **B**: the volume of the unbalance, **C**: the distance between the mass center of gravity of the unbalance and the center of rotation r_0 (blue), and **D**: the squared angular velocity of the rotating unbalance ω_0 (purple).

Design requirements for the pneumatic turbine vibrator

Necessary requirements for the design of the pneumatic turbine were identified. They are divided into specifications regarding the generation of the centrifugal force and requirements enabling the transmission of information from the passive to the active driver. Furthermore, safety criteria and specifications for the application of the turbine for liver and prostate MRE were identified.

The **frequency range** of the generated dynamic harmonic vibration should span around a vibrational frequency of 60 Hz, while permitting variations of the frequency and its amplitude. A lower vibrational frequency yields better shear wave penetration due to less attenuation of the shear waves in the tissue. However, the spatial resolution decreases simultaneously. A frequency of 30 Hz was set as the lower boundary of the desirable frequency range of the pneumatic turbine. A higher vibrational frequency yields better a spatial resolution, but has the disadvantage of a higher attenuation of shear waves in the tissue, which leads to a lower detectable penetration depth of the shear wave. Thus, a frequency of at least 120 Hz was set as the upper boundary of the desirable frequency range of the pneumatic turbine.

The **frequency amplitude** of the generated dynamic harmonic vibration must be large enough to induce detectable shear waves in the region of interest (ROI) in the tissue. However, an amplitude that is too large may cause discomfort or pain to the patient and needs to be avoided. A common consensus on the amplitude at the surface of wave induction for MRE imaging is approximately 2 mm, which was deemed as a suitable range for this work. Additionally, it was aimed to cohere to the vibration safety limits based on the European Union directive EU 2002/44/EC adapted for MRE was aimed at [27].

The **frequency stability**, measurable by a narrow frequency spectrum is an important factor for an adequate synchronization of the mechanical wave to the MEG of the MRE imaging sequence.

The **sampling rate** of the rotational frequency of the turbine needed to be determined in real time such that the control unit could adequately adjust the input air pressure. A higher number of sampling points during a given rotation of the turbine served two purposes. Firstly, more sampling points used for the calculation of the rotational frequency yielded a higher accuracy of the calculated frequency. Secondly, faster updates on the actual rotation frequency, e.g. every half or quarter rotation of the turbine, could be provided and yielded a better control and faster adjustment of the vibrational frequency.

The **angular offset** from a defined position φ_0 of the turbine and its unbalance needed to be detected as the generated waves must be synchronized to the MRE sequence. During image acquisition, the MEG encoded the mechanical shear waves with varying phase offsets with respect to the vibrational frequency. For each encoding step, the onset of the bipolar gradient needed to shift by an increasing phase offset $\Delta\varphi$ with respect to the sinusoidal shear wave induced by the pneumatic actuator.

The **MR compatibility** of all materials for the pneumatic turbine was a mandatory condition as they were exposed to high magnetic fields ($> 1\text{ T}$) within the scanner room. Whenever possible, metal-free components should be selected. Additionally, the materials should not induce any artifacts that might affect the ROI.

The materials needed to exhibit an adequate **mechanical stability**. The axis of the turbine undergoes forces depending on the weight of the unbalance m_{ecc} , the distance r_{ecc} between the mass center of gravity of the unbalance and the rotation center of the turbine, as well as the angular velocity ω of the turbine. Thus, the geometry of the turbine and mechanical properties of the selected materials needed to be considered. The same held true for the roller bearings. Here, roller bearings with a life cycle greater than 24 hours at the maximum operating frequency of 150 Hz, equivalent to two weekly applications lasting 10 minutes for one year was defined adequate. Usually, a lower operating frequency of 60 Hz is expected to be employed, which significantly lengthens the life cycle of the bearings.

A secure handling and operation of the device is mandatory. A **risk management** was set up. It analyzed and evaluated the possibility and severity of possible risks and is elaborated in Sec. 3.1.4.

The **transmission of vibration** from the driver to the body surface depended on the specific MRE application. For liver MRE, a base plate with a curved surface on the right side of the patient's abdomen at the height of the ribs with an area large enough to cover the liver was desirable. For prostate MRE, a curved base plate that could be placed on the pubic symphysis of a patient lying supine was preferable.

A **fixation of the passive driver** and its base plate needed to be developed to securely fasten the passive turbine to the patient's body ensuring an optimal transmission of the generated vibration.

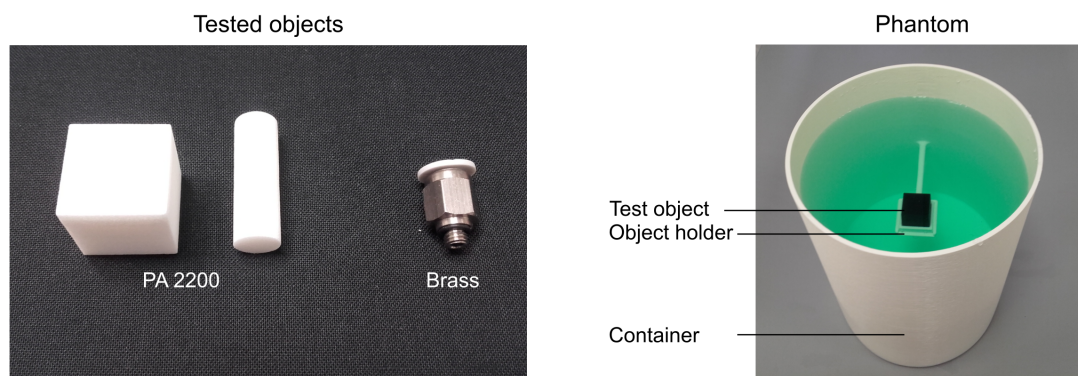
Based on these requirements, a pneumatic turbine generating dynamic harmonic vibrations through the centrifugal force was designed and manufactured. The turbine underwent a technical characterization prior to its application for MRE imaging. The next section describes the methodology applied for this technical evaluation.

Quantification of artifacts induced by selected materials

Any material introduced into the FoV during MRI imaging may affect the image quality, thus a study was conducted to determine the extend of the artifacts caused by the materials of the passive driver in a clinical 3 T scanner in accordance to the ASTM standard F2119 [172]. In a study by author of this thesis (Neumann et al. [177]), nine materials available for additive manufacturing were evaluated. The following methodology is based on this study but the results focus on the material polyamide (PA), as the other materials were not part of the actuator.

The main construction material PA 2200 was evaluated in MRI to quantify the amount of induced artifacts. For example, the base plate was 3D printed from PA 2200 and was in contact with the surface of the human body. PA 2200 is certified as a bio-compatible polymer. The material was printed in a cubical and cylindrical geometry to assess the extent of image artifacts generated by sharp edges as well as round surfaces. The cube had side lengths of 20 mm × 20 mm × 20 mm. The cylinder had a diameter of 10 mm and a height of 30 mm. The material was printed with selective laser sintering (SLS). Printing density was 100 % for the samples. The samples were stored in a dark room at room temperature to avoid changes in material properties due to post-production photo polymerization.

A Artifact evaluation: Test set up



B Artifact evaluation: MR image processing

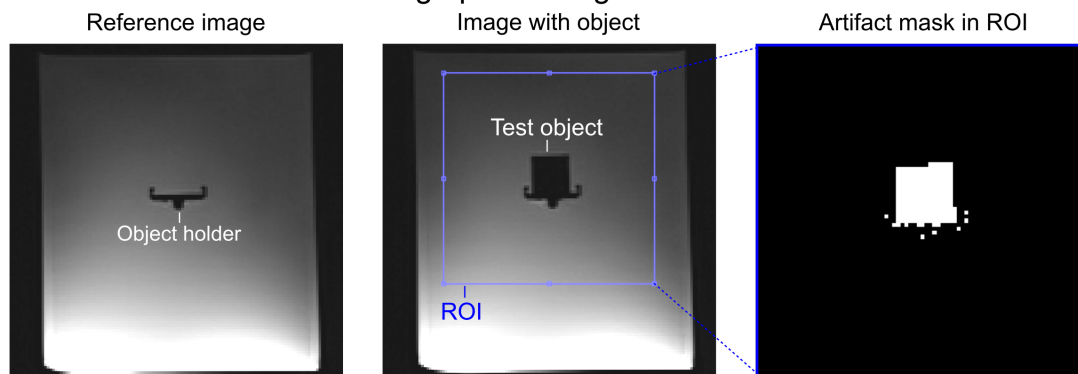


Figure 3.2 – Quantification of artifacts caused by the selected materials for the manufacturing of the pneumatic turbine. **A**: The test phantom filled with a solution of water with added NiSO_4 and NaCl to decrease the relaxivity of the water and mimicking the electrical conductivity of soft tissue. A cube and cylinder made of PA 2200 and the brass valve were tested. **B**: Reference images without an object placed on the holder were firstly acquired. Then, the object was placed into the phantom and images were obtained with the same imaging parameters. A mask with pixel intensity deviating more than 30 % was calculated.

Furthermore, the brass valve was evaluated. It served as the air inlet for compressed air at the turbine. Despite being 50 mm away from the human body surface, it was the only metal-containing material and prone to cause signal attenuation further afield.

A customized cylindrical sample holder with a diameter of 150 mm and a height of 200 mm made from white PLA was fabricated using a desktop 3D printer (Ultimaker 3 Extended, Ultimaker B.V., Geldermalsen, Netherlands). The wall thickness of the sample holder was 2 mm for bottom, lid and the sides. The sample holder included a mounting device, allowing reproducible placement and fixation of the material samples during the experimental evaluation (Fig. 3.2). The sample holder was filled with distilled water containing 0.375 % NiSO_4 , and 0.5 % NaCl (all chemicals obtained through Carl Roth, Karlsruhe, Germany). NiSO_4 reduced the relaxivity of water in MRI and provided tissue-mimicking susceptibility values, whereas NaCl increased the electrical conductivity of the liquid in order to simulate electrical conductivity close to human soft tissue. During measurements, the samples were submerged in the aqueous solution. This time was kept to a minimum to avoid water absorption and were less than 30 minutes for each individual sample.

MR images were acquired with a 3 T MRI Magnetom Skyra (Siemens Healthineers, Erlangen, Germany) with an integrated spine 32-channel coil. The PA 2200 cube and cylinder as well as the valve were consecutively placed in the phantom. The cube's axis was aligned in parallel with the main magnetic field B_0 . The cylinder's main axis was aligned orthogonally to B_0 . The following sequences were employed: (1) true fast imaging with steady-state free precession (TRUFI) and (2) turbo spin echo (TSE). The TRUFI is a real-time sequence used during MR-guided interventions and rather sensitive to artifacts. The TSE is employed as a verification sequence after interventional procedures as it has less artifacts than the TRUFI but at the cost of a longer acquisition time. All imaging parameters were kept constant for all samples. Images were acquired in the three standard imaging orientations (coronal, sagittal, transverse). For each imaging orientation, two acquisitions with the phase encoding and frequency encoding directions swapped were employed. An isotropic field of view of $140 \text{ mm} \times 140 \text{ mm}$, isotropic resolution of (128×128) pixels and a slice thickness of 1.5 mm were used. Echo time T_E and repetition time T_R were $2.74/4.94 \text{ ms}$ and $13/2200 \text{ ms}$, flip angle (FA) was 70° and 171° for the TRUFI and TSE, respectively. A reference scan without a sample placed in the phantom was performed between each object's scan using the same sequence parameters as described above.

Each image slice was then compared pixel-wise to the corresponding reference slice with MATLAB (Version 2017b (9.3.0.713579), The Mathworks, Inc., Natick, MA, USA). In adherence to the ASTM standard F2119 [172], a pixel in the background region was identified as an artifact, if the signal intensity changed by at least 30 % following the equation

$$\frac{P_{\text{Im}} - P_{\text{Ref}}}{P_{\text{Ref}}} \geq 30 \%. \quad (3.1.1)$$

The size of the artifact was determined as the percentage error δ of the area identified as artifacts A_A in mm^2 with respect to the cross sectional area of the sample taken from the computer aided design (CAD) construction data ($A_{\text{Cube}} = 400 \text{ mm}^2$; $A_{\text{Cyl1}} = 300 \text{ mm}^2$ or $A_{\text{Cyl2}} = 78.5 \text{ mm}^2$ depending on the slice orientation) and was calculated as

$$\delta = \frac{A_A - A_{\text{CAD}}}{A_{\text{CAD}}}. \quad (3.1.2)$$

Test set up for acceleration measurements

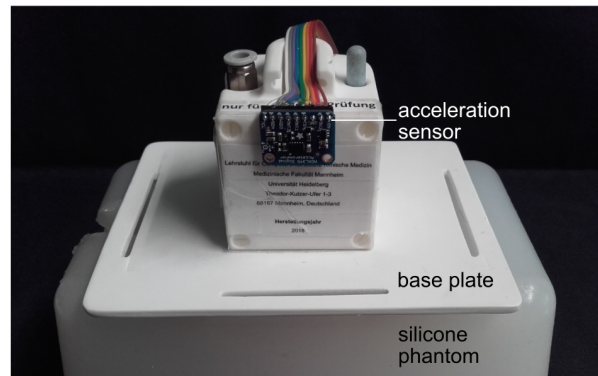


Figure 3.3 – Photograph of test set-up during acceleration measurements. The turbine was placed onto a silicone phantom. The acceleration sensor was attached to the housing of the turbine.

Exerted acceleration and force generated by passive driver

Two turbines with different weights of the unbalance were investigated with regard to the generated acceleration. The acceleration at frequencies ranging from 30 Hz to 80 Hz with a step width of 10 Hz were measured using a digital accelerometer (ADXL345, Analog Devices, Norwood, MA, USA) with a 13-bit measurement in a range of $\pm 14.95 \text{ ms}^{-2}$. The acceleration sensor was attached to the side housing of the turbine and the peak linear acceleration of the housing was recorded. The pneumatic turbine itself was placed on a silicone phantom during measurements (Fig. 3.3). The vibration frequency response spectrum was determined by a Fourier transformation of the recorded signal performed with MATLAB.

Furthermore, the generated axial force at frequencies ranging from 30 Hz to 80 Hz with a step width of 10 Hz was measured. For the first measurement, the turbine was placed onto a precision miniature load cell (9206-V0001, Burster Präzisionstechnik GmbH & Co. KG, Germany) and the exerted force was recorded at each frequency for each of the three unbalances. For the second measurement, silicone with a thickness of 20 mm was placed between the bottom of the turbine and the load cell and the exerted force was recorded at each frequency using the large unbalance (Fig. 3.4).

Operating life of the rolling-element bearings

The operating life of a rolling-element bearing depended on the cases of loading and was calculated according to DIN ISO 281 [178]. The nominal life L_{10} is the life expectancy with a 10% probability of failure of the bearing. It was calculated as

$$L_{10} = \left(\frac{C}{P} \right)^p \quad (3.1.3)$$

Test set up for axial force measurement

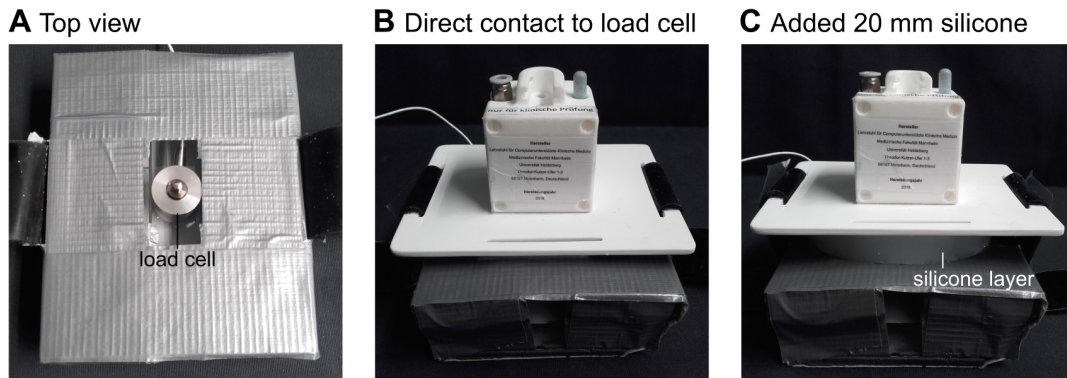


Figure 3.4 – Photographs of test set-up for axial force measurements. **A**: Top view of the load cell. **B**: Side view of the set-up. The turbine was placed in direct contact on top of the load cell and fixated with velcro fastener. **C**: For a second measurement series, silicone with a thickness of 20 mm was placed between the turbine and load cell.

with C being the dynamic load capacity obtained from the bearing's data sheet [179] measured in Newtons and p being the unit-less life time exponent defined as $p = 3$ for rolling-element bearings. The denominator P is the dynamic equivalent bearing load (in Newtons) and was calculated as

$$P = X_0 \cdot F_{\text{rad}} + Y_0 \cdot F_{\text{ax}} \quad (3.1.4)$$

while assuming a pure radial loading caused by the centrifugal forces of the rotating unbalance and neglecting any axial loading ($F_{\text{ax}} = 0$) as no lateral shifting occurred. The unit-less radial factor X_0 for single row rolling-element bearing is defined as $X_0 = 0.6$. The radial force F_{rad} increased proportionally to the weight of the unbalance m_{ecc} , the distance r_{ecc} between the mass center of gravity of the unbalance and the rotation center of the turbine as well as the rotational frequency f and was calculated via

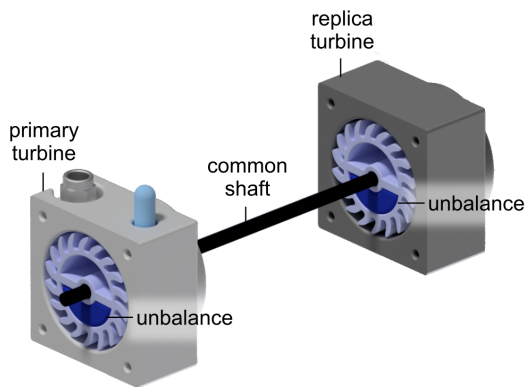
$$F_{\text{rad}} = m_{\text{ecc}} \cdot r_{\text{ecc}} \cdot (2\pi f)^2. \quad (3.1.5)$$

The distance r_{ecc} between the mass center of gravity of the unbalance and the rotation center of the turbine was round up to $r_{\text{ecc}} = 13$ mm. The weight of the unbalances m_{ecc} were $m_1 = 1.9$ g, $m_2 = 4.6$ g, and $m_3 = 9.9$ g. The nominal life L_{10} of the bearings was finally converted to the nominal life expressed in operating hours:

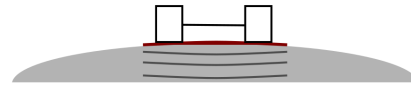
$$L_{10\text{h}} = \frac{10^6}{60n} \quad (3.1.6)$$

with n being the revolutions per minute, i.e. the rotational frequency, of the turbine.

CAD concept for coupled turbines



A Large surface actuation



B Dual source actuation

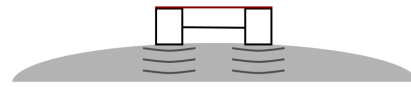


Figure 3.5 – CAD drawing of dual turbine design. The primary turbine is powered by compressed air. The unbalances of the primary and replica turbine (blue) are connected via a common shaft. The angular position of the unbalances relative to their pivot points are in-phase for this set-up. **A**: Principle for large surface actuation with coupled turbines. A common base plate (red) is between the two turbines and the body surface **B**: Dual source actuation with coupled turbines. Here, the turbines are in direct contact with the body surface without a common base plate.

3.1.2 A Dual Turbine Design for Coupled Actuation

The design of the pneumatic turbines enabled a series connection of multiple actuators with specific phase offsets of the sinusoidal vibrations. The set-up allowed the generation of shear waves at several surface locations and potentially a more uniform penetration of a larger volume of interest. Theoretically, two or more turbines could be coupled via a common shaft. A specific phase offset between the turbines could be set prior to the examination. In a feasibility study, two turbines were connected in-phase, with each unbalance having the same angular position of the unbalances relative to its pivot point (Fig. 3.5).

Large surface actuation with coupled turbines

The design of the single turbine was extended in-house [180] and its realization is described briefly in the results. The project also included optimization approaches of components of the previous turbine design, as well as application specific adaptations for the coupled turbines.

Dual source actuation with coupled turbines

A design variation for the large surface actuation with coupled turbines was additionally performed. The goal was to obtain two sources of wave actuation at the surface of interest. Prior studies, introduced in Sec. 2.6, showed that dual actuation may increase the spatial resolution of the elastogram due to constructive and destructive interference of the wave patterns.

3.1.3 The Active Driver

The active driver regulated the pressure level of compressed air fed to the turbine and provided an interface to the user. The active driver consisted of a proportional pressure regulator and two light sensors as well as a specifically developed control unit. In the following, the pressure regulator, light sensor and the software and hardware used for the development of the control unit are presented.

External hardware

The **proportional pressure regulator** VPPM-6L-L-G18-0L6H-V1N-S1 (Festo Vertrieb GmbH & Co. Kg, Esslingen, Germany) regulated the pressure of compressed air in a range from 0 bar to 6 bar proportionally to a set control voltage in the range of 0V to 10V (Fig. 3.6). The integrated pressure sensor detected the actual pressure at the input valve and compared it to the value set by the control voltage. If the actual value deviated from the set value, an adjustable valve of the pressure regulator opened or closed until the desired output pressure was reached [181].

Two identical **fiber-optic photoelectric sensors** (WLL1280T, Sick AG, Waldkirch, Germany) were employed to detect the frequency and phase offset of the rotating turbine. The fiber-optic fiber (LL3-DT01-05) uses a proximity system for detection. The fiber material is polymethylmethacrylat (PMMA) and the jacket material is polyethylen (PE) with a total fiber length of 5 m. The fiber head was made of non-magnetic stainless steel and has an M3 thread [182]. The model was particularly suitable for detecting very small and moving objects (Fig. 3.6) as it had a fast response time of 16 μ s. The analog-to-digital (ADC) unit has two fiber optic inputs for the transmitter LED and receiver [183]. The *2-point teach-in* mode was used, in which the light sensor determined the detected light intensity. Firstly with an object in proximity and secondly when the object is removed and only background signal is detected. The switching threshold was set between the first and second point.

The control unit: employed software

LTSpice XVII (Analog Devices, MA, USA) is a *Simulation Program with Integrated Circuit Emphasis* software used for the simulation of analog and digital circuits. It included a database with numerous electrical component of various companies. Based on these components, it was possible to create arbitrary circuit designs and to simulate their time dependent response. For this work, it was used to design electrical circuits for the supply voltage of the light sensor and the pressure regulator.

Active driver components

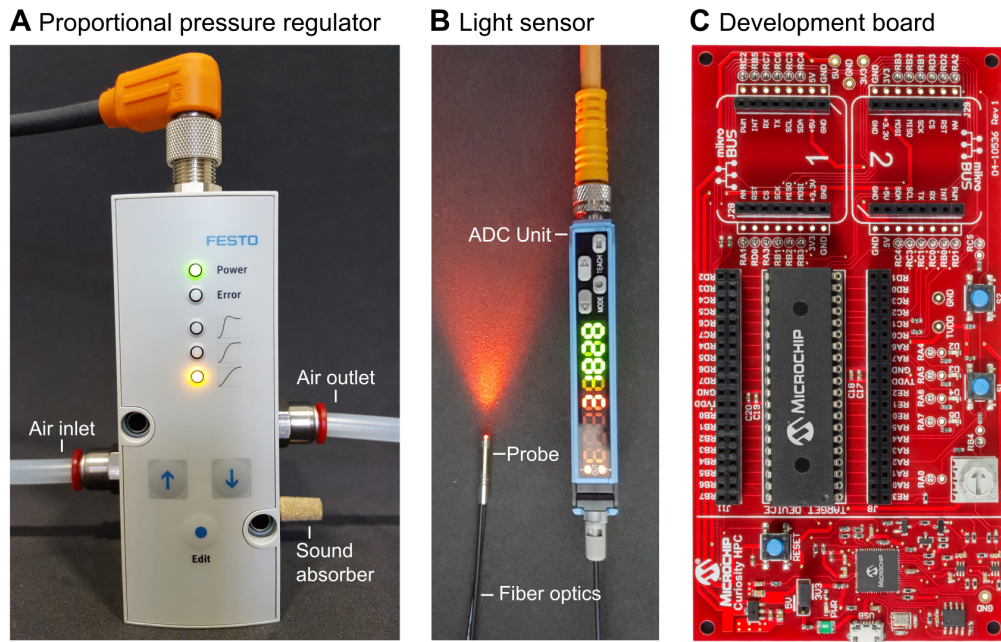


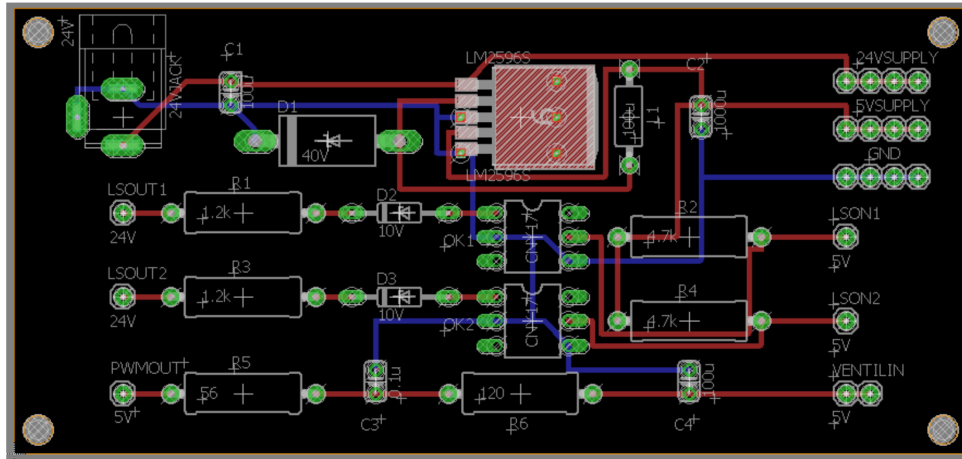
Figure 3.6 – Photographs of the active driver components. **A:** The proportional pressure regulator. The pressure inlet is located to the left, the pressure outlet to the top right, and a vent with a sound absorber to the bottom right. **B:** Photograph of fiber-optic photoelectric sensor with its probe and ADC unit. The LED status display and a dual 2 x 4-digit display are visible. The set threshold (green 4-digit display) and the actual detected intensity (red 4-digit display) are displayed simultaneously. **C:** Microchip Curiosity HPC Development Board (Microchip Technology, AZ, USA), adapted from [184].

To realize the simulated electrical circuit, the design software for printed circuit board (PCB) **Autodesk EAGLE** (Autodesk, Inc., San Rafael, CA, USA) was employed during this work. Via a graphical interface, a PCB design with multiple layers was created. The software included a large database of components, as well as the possibility to lay the tracks automatically and manually on the basis of the circuit. *Design rule checking* was used to check the electrical consistency and feasibility of the PCB. The final PCB layout included the circuits for the supply voltages and the signal processing unit (Fig. 3.7). The layout was then sent to the company Multi Circuit Boards Ltd. (Poole, Great-Britain) for manufacturing.

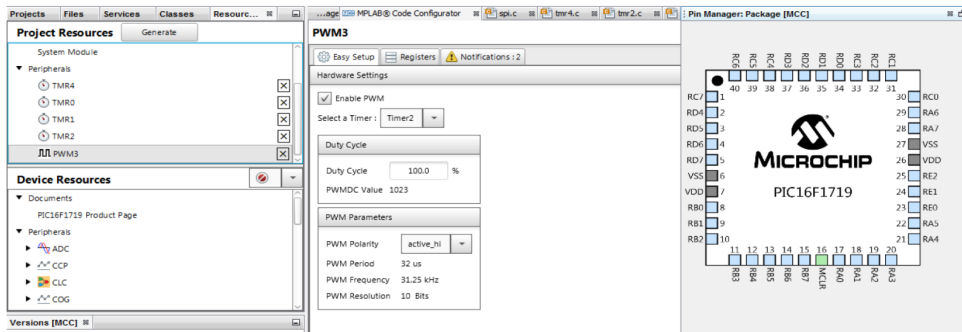
MPLAB X IDE (Microchip Technology, AZ, USA) is a software that offers a freely available development environment for programming the micro-controller. It consisted of a simulator, C compiler and code configurator. The simulator included a database of numerous micro-controller and enabled to test the written code without actually programming a micro-controller. The C compiler provided the possibility to write the code in C language avoiding an interaction with the assembler of the micro-controller. The code configurator included a graphical interface used to implement the periphery of the micro-controller. By selecting peripherals and their settings, the code configurator automatically generated a header and a C file for each peripheral with general functions that were relevant for each application. This

Circuit board design

A Circuit board layout for the supply voltage and signal processing unit



B MPLAB code configurator



C Circuit design of voltage regulator

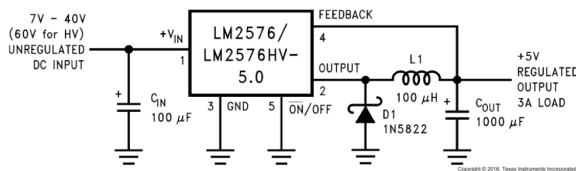


Figure 3.7 – The circuit board design of the active driver. **A:** Circuit board layout for the supply voltages and the signal processing unit designed with Autodesk EAGLE. The components of the power supply were located in the upper part of the board and those of the signal processing were located in the lower part. All inputs were located on the left and all outputs on the right. **B:** Screenshot of the code configurator (MPLAB X IDE) showing the graphical interface used for coding the micro-controller PIC16F1719. **C:** Circuit design of voltage regulator LM2576 (Texas Instruments), taken from [185].

way, a template code was created that was individually adaptable to the main program. The final version of the code was debugged in the development environment and then transferred to the micro-controller (Fig. 3.7).

All components of the control unit were placed in a custom-designed housing. The CAD software **Autodesk Inventor 2017** (Autodesk, Inc., San Rafael, CA, USA) was used to design 3D models of the housing components. The final designs were converted to *standard triangulation language* (STL) files and manufactured by rapid prototyping. The material was polylactide (PLA), a synthetic polymer.

The control unit: employed electronics

The **Microchip PIC16F1719** (Microchip Technology, AZ, USA) is a programmable micro-controller and was the central part of the active driver. It consisted of a central processing unit for all computations, a main memory and a number of different peripheral modules as well as an oscillator controlling the clock frequency. The requirements for the micro-controller were (1) multiple timers for various periodic tasks, (2) a high clock frequency, (3) a pulse-width modulation (PWM) module, and (4) a large number of I/O pins. The Microchip PIC16F1719 contained up to four timers and had a clock frequency of up to 32 MHz. The PWM module had a resolution of 10 bit, a serial peripheral interface (SPI) module for serial communication to operate other devices and the possibilities for external interrupts, which was crucial for the functionality of the program. In total, 35 Input/Output (I/O) pins were capable of intercepting external interrupts and allowed to connect the micro-controller with its environment in a simple way and to expand its range of tasks if deemed necessary [186]. The micro-controller was compatible with the Microchip Curiosity HPC development board.

The development board **Microchip Curiosity HPC** (Microchip Technology, AZ, USA) served as a basis for the practical execution of the developed code programmed on the micro-controller (Fig. 3.6). It consisted of a built-in programming device that allowed the micro-controller to be programmed on any computer without additional hardware [184]. Furthermore, it contained two push-buttons as an online interface, a reset button as an emergency stop and numerous ports for the connection to an LCD panel and other hardware.

Two levels of **supply voltages** were needed to power the various components, namely 24 V direct current (DC) and 5 V DC. A conventional, commercially available power supply unit was used to convert the power socket's 230 V alternating current to 24 V DC. This voltage was used as a supply voltage for the proportional pressure regulator and the ADC unit of the light sensor. An **LM2576 voltage regulator** (Texas Instruments, Sherman, TX, USA) was integrated in the in-house developed PCB and converted the 24 V DC to 5 V DC (Fig. 3.7). The digital output signal of the light sensor's ADC is based on 24 V DC [183]. It needed to be converted to 5 V DC with an **optocoupler CNY17-2** (Lite-on, Taiwan) in order to be compatible as an input signal for the micro-controller. Furthermore, the control voltage of the proportional pressure regulator is supplied by a **PWM module** integrated in the micro-controller. The PWM signal is a high frequency voltage signal that needed to be smoothed to ensure proper control of the pressure regulator. A simple second-order low-pass filter was applied here.

The accelerometer **ADXL 345** (Adafruit, New York City, NY, USA) was used during the technical evaluation of the pneumatic turbine. It measured the acceleration of the housing of the turbine for varying frequencies. The sensor was capable of detecting triple-axis acceleration.

Its sensitivity ranged between ± 16 g with a 13 bit resolution and output data rates of up to 3200 Hz [187], which was important for an accurate detection of the fluctuating acceleration of the housing. The sensor was connected to the micro-controller via an **SPI interface**.

3.1.4 In-house Certification of the Actuator

The actuator underwent the process of an internal evaluation prior to its application in an in vivo setting. This internal evaluation was conducted according to §7 (9) MPV and needed to include sections regarding product specifications, risk assessment and management, as well as product verification and validation.

3.2 Linking the Actuator to the MRI System

Two MRI scanner systems were employed during image acquisition, which are introduced in the following. A commercially available MRE sequence and reconstruction algorithm was implemented at the first scanner (Skyra). For the second scanner (Trio), a motion encoding sequence was developed in-house [188]. Furthermore, the sequence synchronization to the actuator was implemented with an in-house developed trigger system [189]. The sequence, its synchronization and the use of an open source reconstruction tool is described in the latter.

3.2.1 The Scanner Systems

The MRI scanners (Fig. 3.8) had a field strength of 3 T and were part of the Magnetom whole body scanner series (Siemens healthineers, Erlangen, Germany). They were located at the Department of Clinical Radiology at the University Medical Center Mannheim. Each scanner's static magnetic field was generated by superconducting coils cooled with liquid helium. The ring comprising the bore included the gradient system and transmitting coils. The patient table was located within the bore and included a spine coil for signal receiving. Additional coils such as 18-channel body coils or flex coils could also be connected to the scanner system. The examination rooms were adjacent to the control rooms. The examination rooms were shielded from external RF signals. Besides the door of each the examination and control room, there were two small pass-throughs, each with a diameter of 10 cm. They enabled the feed-through of various cables for the actuator, e.g. for the light sensor and trigger, as well as the compressed air tubes.

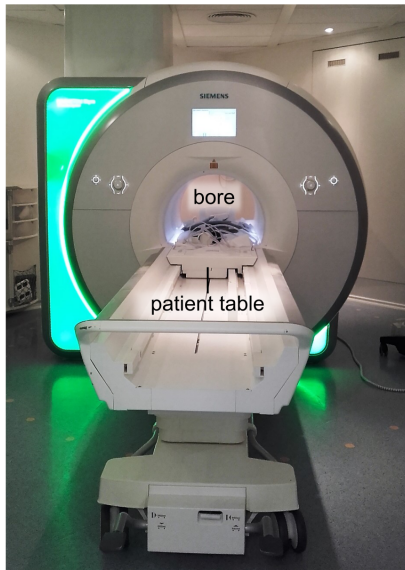
The host computer was located in the control room and formed the interface between the user and entire scanner system. The host computer had a serial interface, namely an RS-232 COM with a 9-pole D-Sub connector, which was considered to serve as the trigger signal input.

The first scanner (Magnetom Skyra) had a system length of 173 cm and a bore diameter of 70 cm. The maximum possible FoV is 500 mm × 500 mm × 450 mm. The maximum allowed gradient amplitude was $45 \frac{\text{mT}}{\text{m}}$ with a maximum allowed slew rate of the gradient system of $200 \frac{\text{T}}{\text{m}\cdot\text{s}}$ [191]. At this scanner, a commercially available work-in-progress (WiP) MRE sequence was employed and is described in Sec. 3.2.2.

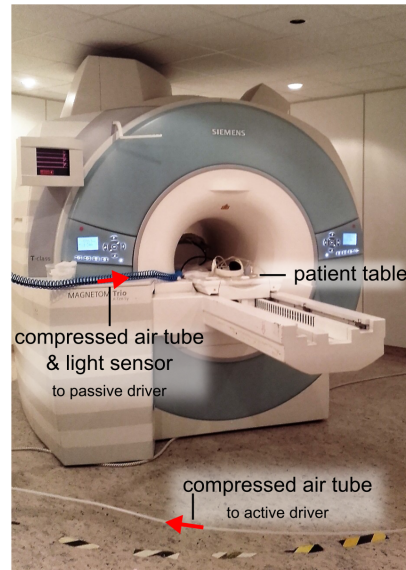
The second scanner (Magnetom Trio) had a system length of 213 cm and a bore diameter of 60 cm. The maximum possible FoV was 500 mm × 500 mm × 450 mm. The maximum allowed gradient amplitude was $40 \frac{\text{T}}{\text{m}\cdot\text{s}}$ with a maximum allowed slew rate of the gradient system of $200 \frac{\text{T}}{\text{m}\cdot\text{s}}$ [190]. Furthermore, an external trigger input/output was located at the side of the

The 3 T Magnetom scanner systems

A Skyra



B Trio



C External trigger

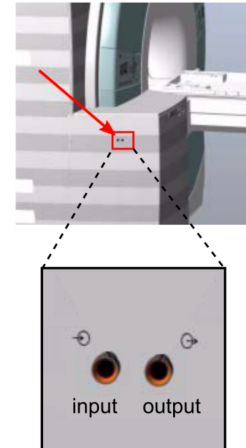


Figure 3.8 – Photographs of the two 3 T Magnetom whole body scanners employed during this work. **A:** The Skyra scanner with the commercially available WiP MRE sequence and reconstruction. **B:** The Trio scanner where an in-house developed sequence was implemented and connected to the actuator. **C:** The external trigger input/output located at the side of the scanner; adapted from [190].

scanner. The connections were cinch connectors, which are compatible with standard audio cables. For MRE image acquisition at this scanner system, a customized motion encoding sequence (Sec. 3.2.3) and a sequence trigger system (Sec. 3.2.4) was developed.

3.2.2 The MRE Sequence by Siemens

As part of a commercially available *MR Elastography* suite, a Siemens WiP package including an MRE imaging sequence was implemented at the Skyra MRI scanner. The following description of the WiP package is based on [192]. The WiP package included two imaging protocols: *greMRE-tra-bh* and *greMRE-tra-p2-bh*, which are both GRE based sequences. The first sequence acquires a single slice within 28 seconds. The latter one employs a parallel acquisition technique (PAT) with a factor of 2 and accelerates the acquisition time to 22 seconds for a single slice. The sequence employs a single, fixed MEG for an actuation frequency of 60 Hz.

The WiP package also included post-processing software that created the following data sets: MR magnitude images, MR phase difference images, wave images, a relative stiffness map, and a 95 % confidence interval for the relative stiffness map.

The MR magnitude images are the standard MR magnitude images. The MR phase difference images were obtained by subtracting the phases of two imaging acquired with opposing

(positive and negative) motion encoding. The images were scaled such that a phase accumulation of $-\pi$ ($+\pi$) was depicted as 0 (4095). Phase wraps were unwrapped using a least-square-fit. Four phase difference images were acquired to obtain displacement fields at four different phase offsets of the mechanical wave actuation. The displacement field is converted to relative stiffness by solving the Helmholtz equation for a linear elastic model. The algorithm employed assumptions of local homogeneity, incompressibility, and a material density equivalent to water. The relative stiffness map, i.e. elastogram, displayed the absolute value of the complex shear modulus G^* . The elasticity was calculated as being directly proportional to local wave lengths from the wave images. Stiffness data was color-coded and displayed with a linear scale ranging from 0 kPa to 8 kPa. The confidence interval of the relative stiffness map was calculated based on the ratio of wave amplitude relative to the noise in the phase images.

3.2.3 Developing a Motion Encoding Sequence

The aforementioned GRE-based MRE sequence had several shortcomings, e.g. an MEG of the sequence fixed to a single actuation frequency of 60 Hz and no synchronization options to third-party actuators, which are discussed in detail in Sec. 5.2. To overcome these issues, a motion encoding sequence was developed in-house [188] to enable customized MRE data acquisition with the presented actuator.

The IDEA framework was used for sequence development and was provided by Siemens healthineers. It was based on the programming language C++ and allowed to create, modify and manipulate new and existing sequence source files for MRI scanners. A SE-EPI sequence was chosen as the underlying sequence; the rationale is discussed in Sec. 5.2. A variable bipolar MEG needed to be implemented to encode the mechanical wave of the actuator to the phase signal during MRE imaging. The files then were compiled on a stand-alone computer and could be implemented on the host computer of the MRI scanner to create an MRE image acquisition protocol.

Elasticity reconstruction software

The freely available software MRE/Wave (Version 10.01.07, Rochester, MN, USA) was used to obtain elastograms based on the acquired motion encoded MR images. The magnitude and phase images were imported into the program and the parameters *mechanical frequency* and *number of phase offsets* were adjusted according to the acquisition parameters. The software included a phase unwrapping algorithm as well as Gaussian or Butterworth filters (low pass, high pass or broad pass with an adjustable number of order). It employed the LFE algorithm for the reconstruction of elastograms.

Table 3.1 – Technical specifications of the trigger input signal, adapted from [190].

Parameter	Value
U_L	[0 0.8] V
U_H	[2 15] V
t_L (min)	10 ms
t_H (min)	10 ms
Input current	min 2 mA
Input voltage	max ± 20 V
Internal contact	+
External contact	-

3.2.4 Triggering the MRE Sequence with the Actuator

In order to synchronize the MEG of the SE-EPI sequence with the mechanical waves induced by the actuator, a trigger system was developed in-house [189] and is described in the following. Three options were considered to synchronize the actuator to the sequence.

The first option was the use of the COM port at the host computer of the scanner. The developed motion encoding SE-EPI sequence (Sec. 3.2.3) was extended using the available sequence library of the MRI scanner. The trigger signal transmitted only information when the signal changed, e. g. from high to low. A function was implemented that detected signal changes at certain pins, namely pin 6 and pin 8, of the COM port.

The second option was to employ COM port at the system control unit. Besides the examination and control room, there is an utility room containing further electronics regarding computational hardware for gradient fields, RF power amplification, and system control. The system control hardware is the central computing unit of the system. It contains components for RF pulse generation, measurement sequence control, calibration of the shim coils and computation of the image. Like the host computer, the system control unit has an RS-232 COM port for the serial interface, usually used for software maintenance only [190]. The RS-232 COM port is a standardized serial interface and is designed to implement communication between the computer and external hardware components developed by the user. The pin assignment enabled the transmission of complete serial data without further software implementations.

The third option was to connect the actuator signal via the external trigger input/output at the scanner (Sec. 3.2.1). The external trigger signal needed to meet certain requirements to be detected by the scanner system (Table 3.1). The trigger signal was a digital signal containing only high and low level changes and no encrypted information. Thus, the implementation using the external trigger at the scanner was deemed a suitable interface for the integration of the trigger signal into the host computer.

3.3 MRE Image Acquisition

Anthropomorphic, i.e. human-like, phantoms are designed to mimic geometries, certain properties, or functions of body tissues. The materials for such a phantom are designed to behave like a particular body tissue with respect to a set of physical characteristics [193]. Depending on the application, a set of criteria for the minimum functionality of a phantom needs to be defined [194]. The requirements for this work were, firstly, the representation of a suitable anatomical site. The abdominal liver region or the male pelvic region were chosen for this work as it included relevant human anatomy such as a liver or prostate and tissue equivalent material. Moreover, the mechanical parameters, i.e. elastic properties, of the tissue mimicking material needed to cover the range of human soft tissue elasticities. Furthermore, MRI visibility and compliance were indispensable. So far, gelatin, hydrogels, agarose, and silicon gels have been widely used as benchmarking tools for MRE calibration [9, 74, 195, 196].

The goal was to find materials fulfilling these requirements in order to design and manufacture anthropomorphic MRE phantoms for the validation of the developed actuation device and sequence. The objectives of this chapter are the following:

3.3.1 **Material studies** split into

- a) Material selection
- b) Material evaluation with rheometric measurements

3.3.2 **Design of anthropomorphic tissue-mimicking phantoms** describing

- a) CAD modeling of molds in geometric and anthropomorphic shapes
- b) Manufacturing of the phantom
- c) Evaluation of imaging parameters

3.3.3 **MRE phantom studies** using

- a) The complex prostate phantom with the GRE sequence
- b) The complex prostate phantom with the SE-EPI sequence
- c) The anthropomorphic abdominal phantom with the SE-EPI sequence
- d) The anthropomorphic abdominal phantom with the SE-EPI sequence - dual actuation

3.3.4 **MRE in vivo studies** of the

- a) Liver
- b) Prostate

3.3.1 Material Studies

Material Selection

Based on experiences in design and manufacturing of anthropomorphic phantoms [197], the following criteria were deemed necessary to be fulfilled by tissue mimicking materials. Foremost, the material needed a specific, adaptable shear modulus that was adjustable within the range of human soft tissue shear moduli. Also, a simple handling of the material during the manufacturing process should improve reproducibility. Furthermore, the materials and phantoms should be easily storable and exhibit a long term mechanical stability.

Therefore, silicone was chosen as the main tissue-mimicking material over other classical gel-like phantom materials such as agar or gelatin. The latter materials require heating procedures during manufacturing, where the agar or gelatin water mixture is heated within a specific temperature range until all particles are dissolved. The cooling down period also needs to be controlled to ensure that a defined concentration of agar or gelatin dissolved in water. These steps in the manufacturing process would limit the criterion of reproducibility.

The characteristic properties of the silicones used for the tissue-mimicking phantoms are a high thermal stability, resistance to micro-organisms and fungi, and a homogeneous composition. Silicones are so-called polyorganosiloxanes, also known as silicone elastomer, which are chemically and thermally very resistant materials [198, 199].

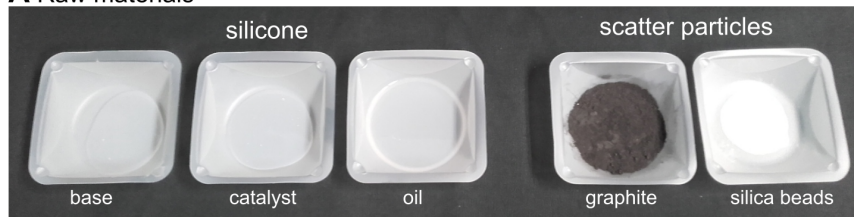
Silanols of the general molecular formula $R_3Si(OH)$, silanediols of the form $R_2Si(OH)_2$ and silane triols according to $RSi(OH)_3$ with an alkyl radical R are used for the preparation of these polymers. The condensation reactions of these silanol compounds produce higher molecular weight polysiloxanes, whose thermal stability and chemical resistance is due to the resulting siloxane bridges of the Si–O–Si form and the Si–CH₃ bond. It only decomposes at temperatures above 650 °C [199].

Compounds with different degrees of polymerization and thus different physical and chemical properties are formed. This process depends on the original composition of *silanols*, which act as the end group of a polymer chain and lead to chain termination, as well as the *silanediols*, which act as chain links, and the *silane triols*, which serve as branching points. In this way, compounds with oily, rubbery or low-viscosity properties can be synthesized. The condensation of silane triols results in a sheet structure that is characteristic of silicone rubber. With a predominant concentration of silanediols, e.g. dimethylsilanediols, the product is silicone oil, e.g. dimethylsiloxane, which forms long chains without further branching. [199]

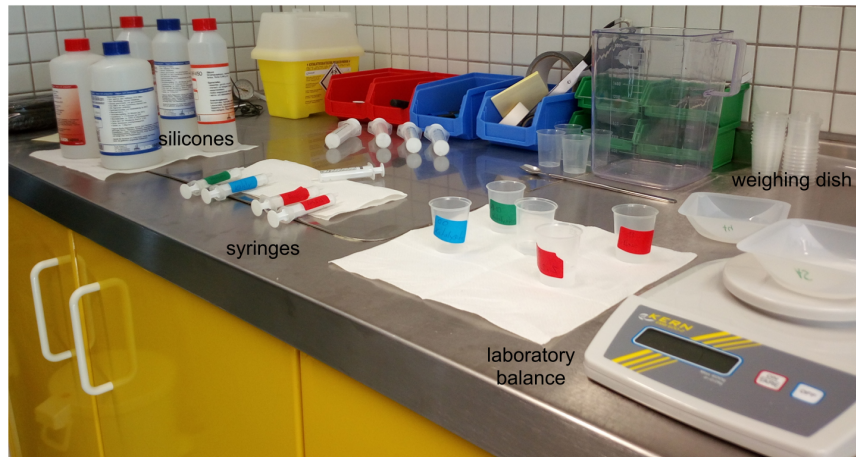
During this study, conventional two-components (base plus curative) silicones were chosen based on elastic parameters, long term stability, ease of handling, and molding properties with much of the same dimensional stability and non-flowing characteristics of a solid silicone

Silicone sample preparation

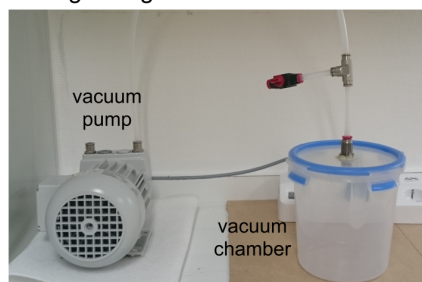
A Raw materials



B Work bench



C Degassing



D Cured and cut sample

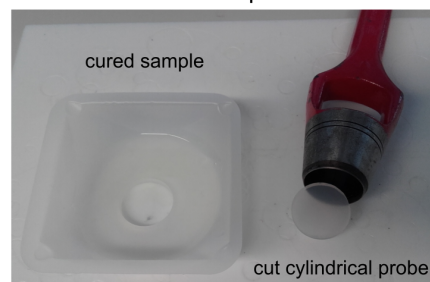


Figure 3.9 – Photographs of the manufacturing process of tissue-mimicking materials. **A**: The raw materials silicone base, silicone catalyst, and silicone oil as well as the scatter particles graphite and silica beads. **B**: Weighing and mixing of the components. **C**: Removal of air bubbles after mixing the component using a vacuum pump and vacuum chamber. **D**: The cured sample in a weighing dish. A stamp is used to cut each sample into a cylindrical shape.

elastomers. The silicones are room temperature vulcanizing (RTV) silicone, meaning they cure at temperatures of 20 °C to 25 °C [200] at a curing time of approximately 90 min. They can be stored long term, which enables significant reuse of the phantom without degradation [201]. Silicone oil can be added in order to decrease Young's modulus E and, consequently, the shear stiffness G of the material as the two parameters are linked by the approximation $E = 3G$. Furthermore, scatter particles may be added to extend the functionality of the material to multi-modal, namely MR and US, imaging. These scatter particles need to be solid, as water-based agents do not blend homogeneously with the hydrophobic silicone.

Material Evaluation

20 samples were prepared and rheometrically tested to determine the range of elasticity values of the silicone. An RTV2 silicone rubber with a Shore hardness of 00 ShA, further referred to as SF00, an RTV2 silicone rubber with a Shore hardness of 13 ShA, further referred to as SF13 and a low-viscosity silicone oil with a viscosity of 50 cSt, further referred to as SF-V50, were used during this study. All materials were obtained from Silikonfabrik (Ahrensburg, Germany). The silicones SF00 and SF13 are miscible with each other and can be diluted with SF-V50 (Fig. 3.9).

A precision laboratory balance (KERN/EMB 600-2, KERN & SOHN GmbH, Balingen, Germany) was used for weighing. The laboratory balance had a weighing capacity of up to 600 g, decimal places in steps of $d = 0.01$ g and a linearity deviation of $\Delta m = 0.03$ g (Fig. 3.9).

A total mass of 15 g for each sample was used to obtain a uniform sample thickness across all samples. The base and catalyst of each silicone were mixed in disposable weighing dishes (Carl Roth GmbH + Co. KG, Karlsruhe, Germany) at a 1:1 mixing ratio, as specified by the manufacturer. If silicone oil was added to the silicone, the base of the silicone was mixed with the silicone oil until blended homogeneously. Then the catalyst was added. According to the manufacturer, the maximum processing time was 20 min, the total curing time at room temperature was 90 min.

For example, a sample was mixed with a ratio of 50 % SF00 and 50 % SF13. Hence, 3.75 g of the two silicone bases were weighed on the weighing dish using disposable syringes and blended with a metal spatula. Then, 3.75 g of both silicone catalysts were added and blended with the base until a homogeneous distribution was achieved. The total mass of the sample was thus $2 \times (3.75 \text{ g} + 3.75 \text{ g}) = 15 \text{ g}$. During the mixing process, air bubbles formed. The sample was placed in a vacuum chamber for approximately one minute until all visible air bubble were removed (Fig. 3.9).

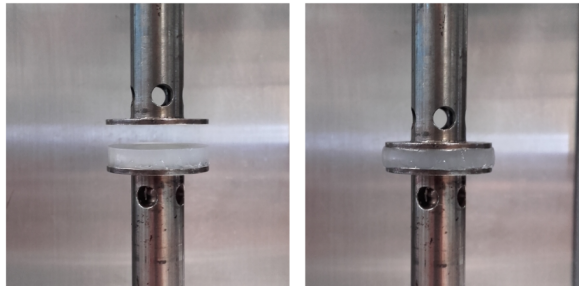
For the determination of the complex shear modulus of the silicone mixtures, the samples were analyzed with a strain-controlled rotational rheometer ARES-G2 (TA Instruments, Pittsburgh, PA, USA). The device was provided by the Institute of Technical Chemistry and Polymer Chemistry of the Karlsruhe Institute of Technology (Karlsruhe, Germany). The ARES-G2 rheometer was equipped with a temperature control system that could regulate and maintain the temperature of the sample from -150 °C to 600 °C or iterate them in a time-controlled manner. It was composed of a high-precision micro-stepping motor for independent measurements of shear strain and normal strain. At constant temperature and strain, iterations could be performed over frequencies ranging from 0.01 Hz to 100 Hz to obtain visco-elastic parameters. It had an integrated screen for parameter monitoring and was controlled via a user interface on the computer [202].

Strain-controlled rheometric measurements

A Rheometer ARES-G2



B Sample placement



C Measurement chamber

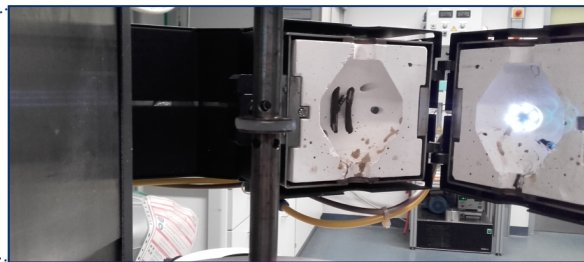


Figure 3.10 – Photograph of strain-controlled rheometric measurement device. **A**: The rheometer ARES-G2. **B**: Placement of one sample onto the stamp of the rheometer. **C**: The sample and the stamp were enclosed by the measurement chamber for temperature-controlled measurements.

Prior to shear modulus measurements, the linear domain of the material was determined with a strain sweep experiment to confirm the linear visco-elastic region and to ensure testing the silicon samples in the linear domain.

The frequency sweep as part of the rheometric measurements yielded frequency-dependent elasticity data of the sample and allowed for a comparison to MRE data. Thus, a frequency sweep covering a range of 5 Hz to 100 Hz with a step width of 2 Hz was conducted for all samples. The samples were measured at room temperature.

For measurements, a cylindrical disk (height 4 mm, diameter 25 mm) was cut out of each sample prepared in the weighing dishes (Fig. 3.9) and placed on the lower stamp of the rheometer (Fig. 3.10). The upper stamp was manually lowered until it exerted a force of $F = 1$ N on the sample. Both stamps were parallel plates (diameter 25 mm) made of *Invar*, a nickel-iron alloy with a low coefficient of thermal expansion. Hence, the geometry of the plates did not change even at higher temperatures. The pre-strain was set to $\epsilon = 0.1\%$ in order to stay within the linear regime of the samples. The obtained data included the shear storage modulus G' , shear loss modulus G'' and the loss factor $\tan\phi$ at each frequency. The data was exported to Excel 2016 (Microsoft Corporation, Redmond, WA, USA) and further data analyses was conducted with MATLAB.

The following tests were conducted to evaluate the mechanical characteristics of the silicone samples:

0 **Pretest: shear moduli at a frequency sweep:** 12 silicone mixtures with a Shore hardness ranging from 00 ShA to 45 ShA were evaluated in a pre-test. Results of the frequency sweep ranging from 30 Hz to 100 Hz showed that the shear moduli were one to two orders larger than the range of shear moduli of human soft tissue. Hence, the following tests were restricted to silicones with a Shore hardness of 13 ShA to 00 ShA and the latter being further diluted with silicone oil SF-V50.

1 **Shear moduli at a frequency sweep:** The concentration range covered mixtures of SF00 blended with SF13 and SF00 blended with up to 69% SF-V50. Overall, 20 samples were evaluated. One sample (SF00 diluted with 50% SF-V50) was produced five times to determine deviations due to variations in the production process. Another sample (SF00 diluted with 47% SF-V50) was measured multiple times to determine measurement uncertainties during rheometric measurements. The probe was inserted in the rheometer, measured and removed therefrom. The process was repeated five times. The frequency sweep was a linear sweep ranging from 30 Hz to 100 Hz with a step width of 1 Hz.

2 **Long term stability:** A subgroup consisting of 11 samples of the second test (listed in Table 4.2) were retested after four months to evaluate durability and long term effects on the shear modulus. The samples were stored at room temperature during this time without further measures. A linear frequency sweep from 30 Hz to 100 Hz with a step width of 2 Hz was conducted using the same geometry as described above.

3 **Batch effects:** The samples of the second test were manufactured once more using a different batch of silicones to evaluate effects caused by production variations of the raw materials (silicone base, curative and oil) on the shear modulus. A linear frequency sweep from 30 Hz to 100 Hz with a step width of 2 Hz using the same geometry as described above was conducted. The relative error was subsequently calculated as

$$\delta G = \frac{G_1 - G_0}{G_0} \quad (3.3.1)$$

with G_0 being the shear modulus at $t = 0$ and G_1 the corresponding shear modulus after a storage of four months. The absolute error was calculated as

$$\Delta G = G_1 - G_0. \quad (3.3.2)$$

4 **Resonance effects due to diameter of test plates:** From the same probes of the third test (batch effects), two cylindrical disks with different diameters were cut and tested. The first sample had a diameter of 25 mm, the second one had a diameter of 13 mm. A linear frequency sweep from 30 Hz to 100 Hz with a step width of 2 Hz was conducted.

5 **Sample heights effects:** One sample (SF00 diluted with 69 % SF-V50) was produced with three varying heights (3 mm, 5 mm, and 9 mm). A linear frequency sweep from 30 Hz to 100 Hz with a step width of 3 Hz was conducted. Also, two sample diameters were evaluated, namely 13 mm and 25 mm.

6 **Influence of scatter particle for multi-modal imaging:** Two types of scatter particles consisting of either graphite or silica beads (both Carl Roth GmbH + Co. KG, Karlsruhe, Germany) were added to a silicone sample of SF00 with 47 % SF-V50. The scatter particles enable additional US imaging. The influence on elasticity due to the added particles was evaluated during this test with a linear frequency sweep from 30 Hz to 100 Hz with a step width of 3 Hz. 0.15 g scatter particles were added to the sample. This was an amount of 1 % of the total sample weight (15 g). Two sample diameters were evaluated (13 mm and 25 mm).

3.3.2 Design of Anthropomorphic Tissue-Mimicking Phantoms

Based on the results of the evaluation of silicones as tissue-mimicking materials, tissue-mimicking phantoms with increasing complexity were developed for MRE measurements. They served as test objects for prostate MRE and liver MRE. The development of the phantoms followed a similar design and manufacturing process. CAD was employed for modeling molds and rigid anatomic structures. After the silicone base and catalyst were blended homogeneously, the mixture cured, i.e. hardened, within 90 minutes. It was thus possible to pour the silicone mixture into molds of almost arbitrary shape and obtain a self-supporting volume after curing and removal of the mold.

Customized geometric molds resembling a human prostate (volume of 95 ml), bladder (volume of 190 ml), and urethra (diameter of 5 mm) were developed in-house [203]. They were designed using the CAD software Autodesk Inventor Professional 2017 (Autodesk, Inc., San Rafael, CA, USA) and manufactured by rapid prototyping (Ultimaker 2, Ultimaker B. V., Geldermalsen, Netherlands) using PLA.

For the anthropomorphic liver phantom, a mold provided by the Fraunhofer Institute for Manufacturing Engineering and Automation (Mannheim, Germany) was used to mold a liver geometry. The mold was based on a morphological CT scan. The liver was contoured on each slice of the scan and a 3D volume based on the contours was created and converted to an STL file. This STL file was used to create a CAD model of molding parts surrounding the model. The parts were manufactured by rapid prototyping. Based on the same CT scan, the rib cage was also contoured and converted into an STL file. It was subsequently 3D printed from PA and used for the anthropomorphic liver phantom.

Manufacturing process of the complex prostate phantom

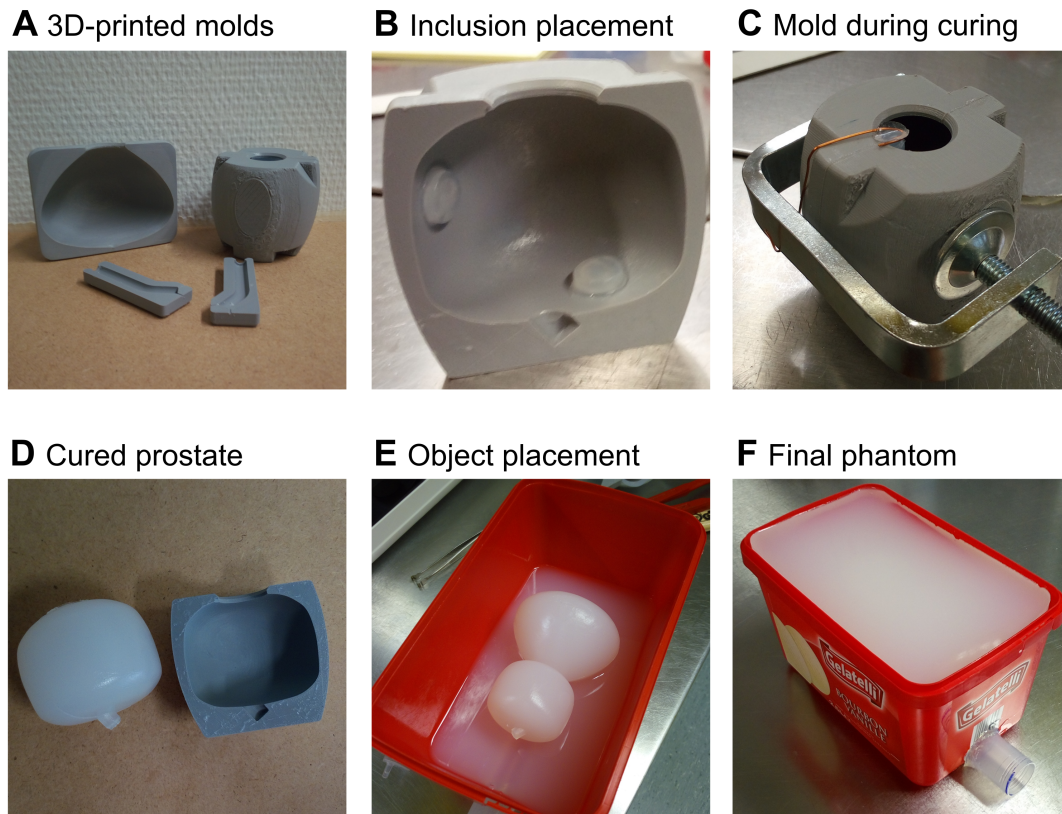


Figure 3.11 – Photographs of manufacturing process of the prostate phantom **A**: The 3D printed molds for bladder (left), prostate (right), and urethra (front). **B**: Placement of stiff inclusions at the walls of the prostate mold. **C**: The silicone urethra was placed into the prostate mold first, then the silicone for the prostate was poured into it. **D**: The cured prostate was released from the mold after curing. **E**: After a first layer of filling material cured in the container, the bladder and prostate were placed onto the layer. **F**: The final form of the phantom. A tube was placed at the bottom representing the rectum.

In the following, the general manufacturing process of the phantoms is described. Considering the human soft tissue elasticities, silicones with varying concentrations of silicone oil were selected for different parts of each phantom.

Manufacturing the prostate phantom

The simplified prostate phantom consisted of two geometric inclusions resembling the prostate and bladder and filling material surrounding the objects. For the prostate and bladder, silicone SF00 diluted with 47% and 41% silicone oil SF-V50 were chosen, respectively. The filling material had a silicone oil concentration of 57%. For prostate and bladder, the silicone base was mixed with the silicone oil until a homogeneous distribution was achieved. Then, the catalyst was added and blended until homogeneously. The material was degassed in the vacuum chamber to remove air bubbles and poured into the molds. The process was repeated

for the bladder. After curing, the molds were removed and two geometric objects resembling a prostate and bladder were obtained. A first layer of filling material was poured into a cylindrical container (diameter 120 mm, height 150 mm) and left to cure. Then, the prostate was placed onto the first layer and surrounded by a second layer of background material.

The design of the complex prostate phantom was based on the simplified version with the same silicon oil concentrations for the prostate and bladder. However, an urethra (52 % SF-V50) was manufactured and placed into the prostate. Additionally, three small cylindrical inclusions (diameter 10 mm, height 3 mm) were included into the prostate. They resembled malignant regions with increasing stiffness obtained through concentrations of 41 %, 20 % , and 13 % SF-V50. The bladder and prostate were placed into a cubical container (length 150 mm, width 200 mm, height 170 mm) and manufactured as described above with multiple layers of filling material (Fig. 3.11).

Manufacturing the abdominal phantom

The anthropomorphic abdominal phantom was the most complex phantom consisting of a liver and a rib cage (Fig. 3.12). The mold resembling the shape of a human liver was filled with silicone SF00 diluted with 60 % SF-V50, corresponding to a shear modulus of 2.72 kPa (Sec. 4.3.1). A total mass of 2 L was produced to fill the liver mold. The filling material was produced with a concentration of 41 % SF-V50, corresponding to 7.29 kPa. A total of 14 L were used. To achieve an elliptical human-like cross section, the silicone was poured into a paint bucket placed on the side. As the bucket was not completely filled, a flat and stable support surface was achieved. In addition to the silicone, which represented the liver and the surrounding soft tissue, a 3D printed PA rib cage model was inserted. This approach closely mimicked the human anatomy and allowed future evaluations of influences due to rigid structures.

MR and CT imaging of the phantoms

Prior to MRE imaging, the complex prostate and anthropomorphic abdominal phantom were evaluated in MR and CT imaging.

Firstly, the phantoms were scanned in the MRI scanner with a conventional T_1 -weighted and a T_2 -weighted sequence. The 18-channel body coil was placed onto the phantom during imaging. The T_1 -weighted sequence was a fast low angle shot (FLASH) sequence with the following imaging parameters $T_E = 2.78$ ms, $T_R = 265$ ms, $FA = 70^\circ$, and slice thickness = 5 mm. The T_2 -weighted sequence was a TSE sequence with the following imaging parameters $T_E = 102$ ms, $T_R = 2500$ ms, $FA = 160^\circ$, and slice thickness = 5 mm.

Manufacturing process of the anthropomorphic abdominal phantom

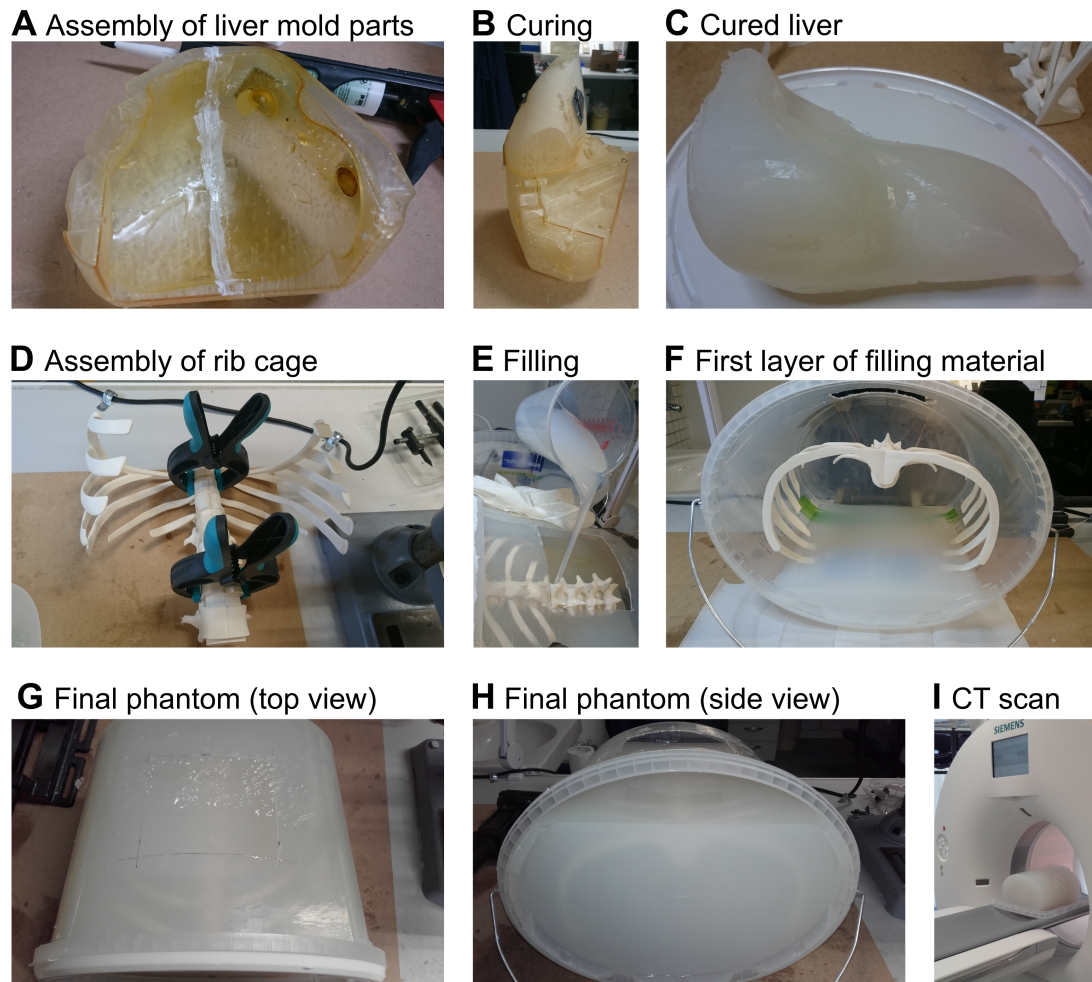


Figure 3.12 – Photographs of manufacturing process of the prostate phantom **A**: Assembly and sealing of parts of the 3D-printed mold for the liver. **B**: Whole liver mold during curing. **C**: After removal of the liver mold. **D**: Assembly of the two halves of the 3D-printed rib cage. **E**: Filling of liquid silicone into the container. **F**: Placement of rib cage in the outer container and curing of first layer of filling material. **G**: Top view and **H**: side view of the final form of the phantom. **I**: Placement of the phantom corresponding to a "head first supine" position in a CT scanner.

The FoV and acquisition matrix differed for the two phantoms and were FoV = 182 mm × 225 mm, acquisition matrix = 312 pixel × 384 pixel, and isometric pixel spacing = 0.58 mm, regarding the prostate phantom and FoV = 274 mm × 399 mm, acquisition matrix = 264 pixel × 384 pixel, and isometric pixel spacing = 1.04 mm, regarding the abdominal phantom.

Also, the phantoms were scanned with the GRE-based MRE sequence (Sec. 3.2.2) and with the SE-EPI based sequence (Sec. 3.2.3) and phase and magnitude images were obtained. Imaging parameters were $T_E = 23.72$ ms, $T_R = 50$ ms, FA = 25°, FoV = 298 mm × 375 mm, acquisition matrix = 204 pixel × 256 pixel, isometric pixel spacing = 1.46 mm, and slice thickness = 5 mm for the GRE-based MRE sequence. Imaging parameters were $T_E = 70$ ms, $T_R = 3500$ ms, FA = 90°, FoV = 222 mm × 375 mm, acquisition matrix = 76 pixel × 128 pixel, isometric pixel spacing = 2.93 mm, and slice thickness = 5 mm for the SE-EPI-based MRE sequence.

The signal to noise ratio (SNR) in a ROI of the included organs and filling material was determined according to [204] as

$$\text{SNR} = \frac{\mu_{\text{ROI}}}{\sigma_{\text{BG}}} \quad (3.3.3)$$

with μ_{ROI} being the measured mean signal in a ROI in the organs or filling material, and σ_{BG} being the standard deviation of the mean signal determined in a ROI placed in the background.

The contrast to noise ratio (CNR) of the included organ (O) with regard to the filling material (F) was determined via

$$\text{CNR} = \frac{\mu_{\text{O}} - \mu_{\text{F}}}{\sigma_{\text{BG}}}. \quad (3.3.4)$$

Furthermore, the phantoms were scanned in a 3rd generation dual source multi slice CT scanner (Somatom Force, Siemens Healthineers, Erlangen, Germany). Imaging parameters were: peak voltage = 100 kVp, X-ray tube current = 980 mA, slice thickness = 1 mm, FoV = 512 mm × 512 mm, isometric pixel spacing = 0.86 mm, pitch factor = 1, and a smoothing reconstruction kernel (Br36). The mean Hounsfield units (HU) were determined in a ROI of the prostate and bladder and filling material regarding the prostate phantom, and liver, rib cage, and filling material regarding the abdominal phantom.

3.3.3 MR Elastography - Phantom Studies

After the development of the actuator and the implementation of the motion encoding sequences at the scanner systems, MRE images were acquired using the manufactured prostate and abdominal phantom. A schematic test set-up in the MRI scanner and a post-processing work-flow are presented in Fig. 3.13).

The prostate phantom

MRE was performed on the complex prostate phantom as a proof-of-principle. The phantom was placed in the Magnetom Skyra MRI scanner (Sec. 3.2.1). A mechanical actuation frequency of 60 Hz of the actuator was employed. Imaging was conducted with the GRE based sequence (Sec. 3.2.2) and its parameters were $T_E/T_R = 23.75 \text{ ms}/50 \text{ ms}$, FoV = 239 mm × 400 mm, and slice thickness = 5 mm. Other actuation frequencies were restricted by fixed parameters of the GRE based sequence. Motion encoding was in a single direction. The WiP sequence incorporated a reconstruction algorithm and automatically created wave images and an elasticity map with a 95 % confidence interval for the fitted elasticities based on the obtained magnitude and phase images.

MRE image acquisition

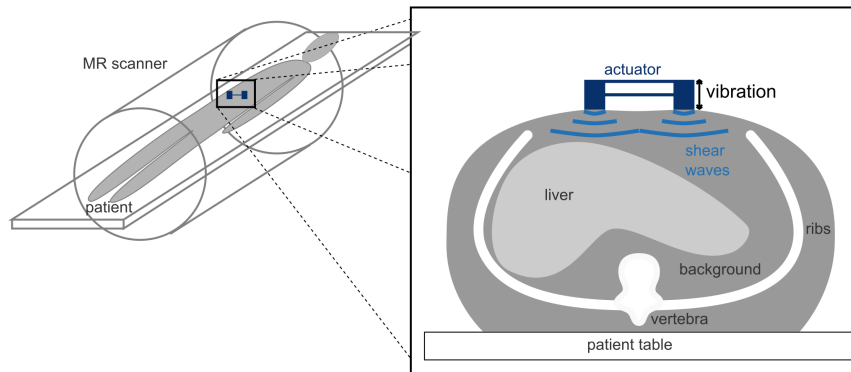
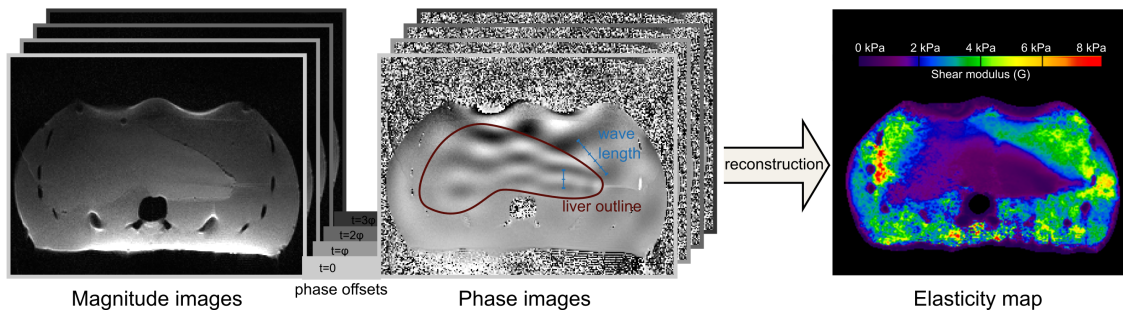
A Schematic test setup**B** Post-processing workflow

Figure 3.13 – Schematics of MRE image acquisition and post-processing work-flow. **A**: The phantom was placed in the scanner and the active driver was set on top of the phantom (here exemplary shown with the dual driver). Shear waves were generated and propagated through the phantom. **B**: Complex MR images (magnitude and phase) were acquired at multiple phase offsets. Based on these images, an elasticity map was reconstructed with the software MRE/Wave.

The complex prostate phantom was also imaged with the SE-EPI based sequence (Sec. 3.2.3) with an MEG of $5 \frac{\text{mT}}{\text{m}}$ in a single direction. The phantom was placed in the Magnetom Trio MRI scanner (Sec. 3.2.1). Magnitude and phase images were acquired at four actuation frequencies (50 Hz, 60 Hz, 70 Hz, 80 Hz) in a transverse and coronal slice. T_E shortened with increasing actuation frequencies and were 88 ms, 81 ms, 76 ms, and 73 ms, respectively. Other parameters were kept constant during image acquisition and were: $T_R = 3000$ ms, FoV = 200 mm \times 200 mm, acquisition matrix = 96 pixel \times 96 pixel, and slice thickness = 5 mm. An elasticity map was obtained at 60 Hz using the software MRE/Wave, which applied a local frequency estimation inversion algorithm (Sec. 3.2.3). No trigger was employed during acquisition of these images.

The abdominal phantom

The anthropomorphic abdominal phantom was also imaged with the SE-EPI based sequence (Sec. 3.2.3). The following parameters were kept constant for all measurements with the abdominal phantom: Images were acquired at the Magnetom Trio MRI scanner. Magnitude and phase images were acquired at four actuation frequencies of 50 Hz, 60 Hz, 70 Hz, and 80 Hz. Four images were acquired, each with an additional time offset of 4 ms, after the trigger signal was received. T_E varied with the actuation frequencies and was 194 ms, 188 ms, 183 ms, and 179 ms, respectively. Other imaging parameters were: $T_R = 2500$ ms, FoV = 281 mm \times 375 mm, acquisition matrix = 192 pixel \times 256 pixel, and slice thickness = 5 mm.

Varying the strength of the motion encoding gradient: The influence of the amplitude of the MEG was evaluated on the phase signal intensity. In general, the waves need to be sufficiently encoded in the phase signal yielding enough signal for adequate reconstruction. However, if the amplitude of the MEG is too large, it will cause phase wraps of the phase signal, which need to be unwrapped prior to reconstruction. Thus, using the sequence parameters described above, the strength of the MEG was varied. It ranged from $5 \frac{T}{ms}$ to $20 \frac{mT}{m}$ with step width of $5 \frac{mT}{m}$. Four actuation frequencies (50 Hz, 60 Hz, 70 Hz, and 80 Hz) were iterated.

Dual actuation with coupled turbines: The same set-up and parameters were also employed during imaging with the coupled turbines actuation set-up (Sec. 3.1.2). Both set-ups for large-surface actuation and dual source actuation were evaluated with the same acquisition scheme mentioned above. Again, the MEG was varied from $5 \frac{T}{ms}$ to $20 \frac{mT}{m}$ with step width of $5 \frac{mT}{m}$ at the actuation frequencies of 50 Hz, 60 Hz, 70 Hz, and 80 Hz.

An elasticity map was obtained for all frequencies and all actuation set-ups (single, large surface, and dual source) with the software MRE/Wave, which applied a local frequency estimation inversion algorithm (Fig. 3.13). The phase images with highest MEG strength, but without phase-wraps, were employed.

3.3.4 MR Elastography - In Vivo Studies

A prospective single-center study was approved by the Institutional Review Board (Medical Faculty Mannheim, Heidelberg University, Germany, decision number 2018-404M-MA §3 MPG - Eigenherstellung). For this work, one volunteers was scanned as a proof-of-principle of the successful implementation of the developed MRE work-flow.

For liver MRE, the volunteer was placed head first supine in the Magnetom Trio MRI scanner. The liver base plate was placed between the driver and the body surface. The passive driver was fixated on the right anterior-lateral side of the lower ribs of the patient. During ramp-up of the driver, constant visual and audio communication was maintained with the volunteer. Once the final actuation frequency was reached, the volunteer was asked if the induced vibration was deemed tolerable for the duration of the measurement. As it was affirmative, the motion encoding SE-EPI sequence was started. Images were obtained at a frequency of 80 Hz). T_E varied was 73 ms. Other parameters were : $T_R = 3000$ ms, FoV = 200 mm×200 mm, acquisition matrix = 96 pixel × 96 pixel, and slice thickness = 5 mm.

For prostate MRE, the base plate of the actuator was placed between the driver and the body surface and the passive driver was attached on the anterior side of the pubic symphysis. Then, the same imaging protocol as described above was applied.

As shear wave propagation was not visible during liver and prostate MRE, the set-up was repeated at the thigh with the same imaging parameters. The volunteer was in a feet first supine position and the actuator was fixed anterior on the thigh. An elasticity map was obtained using the software MRE/Wave (Sec. 3.2.3).

4.1 Actuator Development and Evaluation

4.1.1 The Passive Driver

Evolution of turbine design

The turbine design evolved during the construction process. CAD sketches of the developed versions are shown in Fig. 4.1. The first version V_1 was developed as a proof-of-principle. The model demonstrated that sinusoidal mechanical waves could be generated by means of compressed air using a rotational turbine with an included unbalance during MRE image acquisition. For the next version V_2 , the overall size of the turbine was increased with the objective of a larger force generation. Additionally, removable base plates were introduced for initial experiments regarding the transmission of mechanical waves to varying surface shapes. The third version V_3 mainly differed to version V_2 by a smaller overall geometry and higher

Evolution of turbine designs

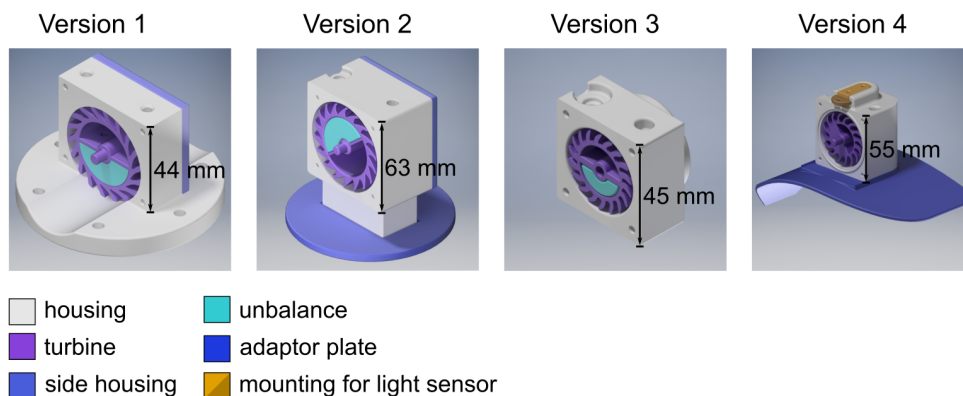


Figure 4.1 – Overview of the evolution of the turbine designs V_1 to V_4 . The CAD drawings display all 3D printed parts of the turbines except for the frontal side housing, which has been removed for a better visualization.

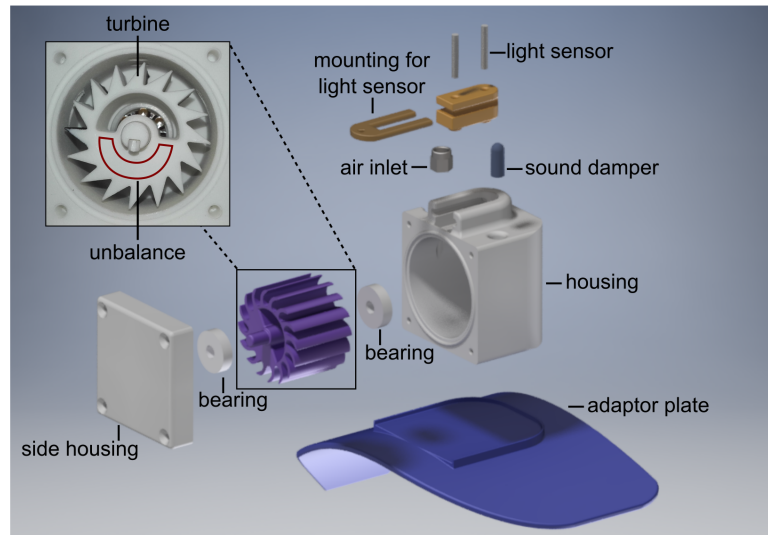


Figure 4.2 – CAD explosive view of turbine model V_4 . All components are shown, except for four screws, which attach the side housing to the main housing. **Top left:** Photograph of the turbine with the unbalance delineated in red.

maximum vibrational frequency. The latest version V_4 was developed incorporating results of an initial risk assessment for Version V_3 . Safety features were improved and a more stable operation of the turbine and an increased user-friendliness during set-up at the MRI scanner was achieved.

A description of the fundamental design of the pneumatic turbine has been published before [205, 206]. It particularly focused on V_2 and V_3 . In the following, the focus is set on the last versions V_4 and $V_{4\text{dual}}$. The technical evaluation of version V_4 is based on the determined requirements of Sec. 3.1.1.

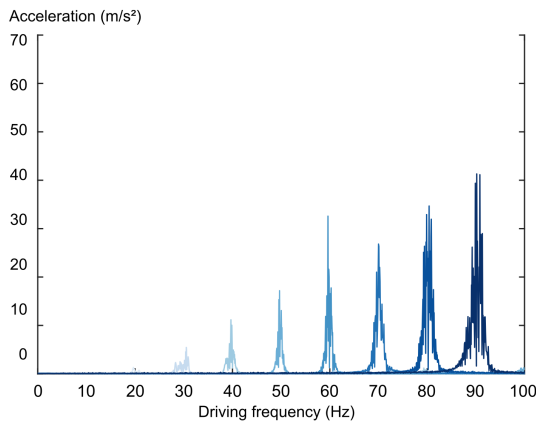
Turbine design - version V_4

The passive part of the actuator consisted of a compressed air turbine that could be placed on the volume of interest (Fig. 4.2). The components of V_4 were primarily 3D printed and included a turbine with an unbalance, a main housing, one side wall housing, a mounting adaptor for two light sensors (L_f and L_t) and a base plate. Those components were designed with CAD software and produced by SLS using PA 12 (Materialise GmbH, Gilching, Germany). Technical drawings of the components manufactured by rapid prototyping are in Appendix D. Other components were a sound damper and a valve, which served as the inlet for compressed air into the turbine, as well as rolling-element bearing and screws made of PA.

The **actuation frequency** was infinitely variable between 20 Hz to 120 Hz and thus fulfilled a prerequisite for multi-frequency MRE data acquisition. A lower controllable minimum actuation frequency was not possible, as a certain minimum air pressure was needed to overcome the turbine's inertia. However, lower frequencies only yield a reduced spatial resolution and is not

Vibration frequency response spectrum

A Small unbalance



B Large unbalance

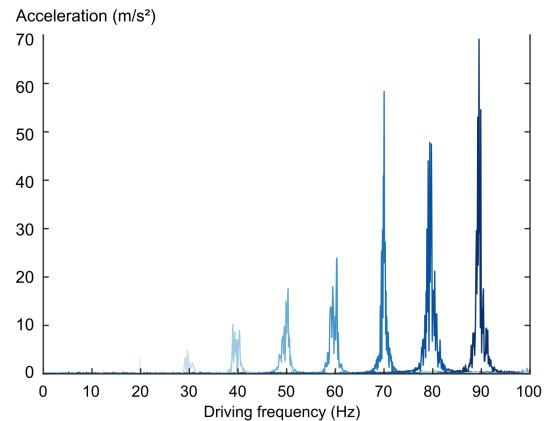


Figure 4.3 – Graphs of vibration frequency response spectrum for two unbalances with different weights. **A**: Small unbalance. **B**: Large unbalance. The vibration frequency response spectrum increased with the frequency as predicted for such systems. An outlier can be observed at 60 Hz (A) and 70 Hz (B). Here, the maximum acceleration was larger than at the subsequently larger frequency.

feasible for clinical MRE, The frequency range depended on the size of the unbalance. The maximum applicable frequency was 90 Hz for the larger unbalance and 120 Hz for the smaller unbalance and limited by the available in-house air pressure of $p_{\max} = 5$ bar.

The generated force (Fig. A.1) and acceleration (Fig. A.2) increased with increasing vibrational frequencies as predicted for such systems. Regarding the vibration frequency response spectrum (Fig. 4.3), an outlier was observed at 60 Hz for the small unbalance ($m_s = 2.5$ g) and at 70 Hz for the larger unbalance ($m_l = 5.0$ g). Here, the maximum acceleration value was larger than the value at the subsequently higher frequency. To determine the **frequency stability** over an interval of 20 seconds, the full width half maximum (FWHM) of the vibration frequency response spectrum was calculated and resulted in $\text{FWHM} = 0.71$ Hz for the small unbalance and $\text{FWHM} = 1.50$ Hz for the large unbalance at 60 Hz. A small FWHM enabled an adequate synchronization of the mechanical wave to the MEG of the motion encoding sequence. Additional data are provided in Table A.1.

The turbine V_4 consisted of 16 blades that were primarily used to drive the turbine by compressed air. However, they also served for the **sampling of the rotational frequency** of the turbine. The number of blades determined the sampling rate of the rotational frequency. A light sensor L_f was placed at the top of the housing between the air inlet and outlet. The top of every other blade was painted black with the other blades remaining white. This set-up yielded eight high and eight low signals per rotation transmitted to the control unit (Fig. 4.4).

Detected signals of light sensors

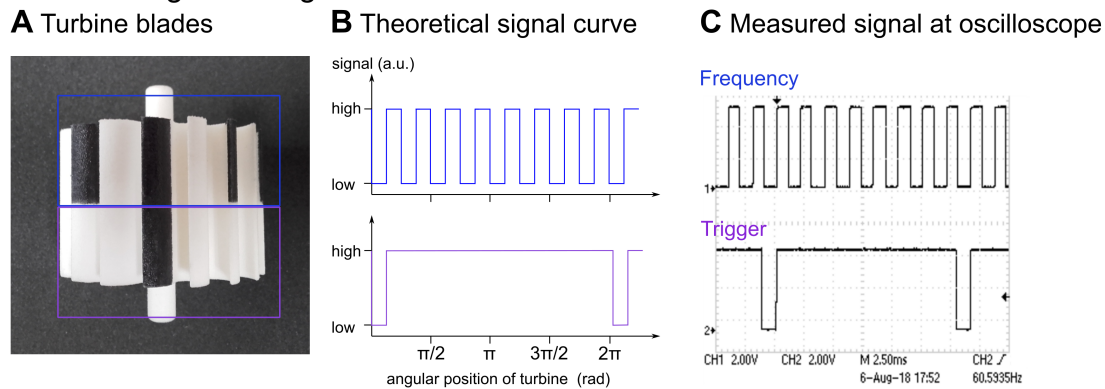


Figure 4.4 – Photograph of the turbine blades, a sampling schematics and measured signal. **A:** Photograph of the turbine blades of version V_4 . At the top half, every other blade was painted black. Here, the light sensor L_f detected 16 signals per rotation (eight high and eight low signals). At the bottom half, only one blade was painted black, thus the light sensor L_t detected only one signal at a determined position of the turbine during one rotation. This was used to synchronize the mechanical wave to the MEG of the MRE sequence. **B:** Theoretical signal curve of detected signals for the frequency (top) and trigger (bottom). **C:** The signal of frequency and trigger was measured with an oscilloscope and was in accordance with the expected sampling scheme.

The second light sensor L_t determined the **angular offset** of the turbine during rotation. Here, the bottom of only one blade was painted black with all other bottoms of the blades remaining white (Fig. 4.4). Thus a signal defining a zero position φ_0 of the turbine was obtained.

The turbine was located within the scanner room and was exposed to high magnetic fields of up to 3 T. Whenever possible, metal-free components of the turbine were selected to ensure its **MR compatibility** and minimize risks associated with heating, projectile forces and torques. Firstly, PA 12 was chosen for all 3D printed parts. The rolling-element bearings were made of polyoxymethylene (a thermoplastic) and glass (according to DIN 625-626). The sound damper was composed of plastic (M/1545, Norgren GmbH, Germany). The valve, which served as the inlet for compressed air into the turbine, was the only metal component (M022A0605, Norgren GmbH, Germany). However, it was made of non-magnetic brass and was not subject to any forces during MRI measurements.

Regarding the **mechanical stability** of the employed components, PA had a tensile strength of $\sigma_B = 48 \text{ MPa} \pm 3 \text{ MPa}$ (according to DIN EN ISO527) and a heat deflection temperature of 86°C (according to ASTM D648 (1.82 MPa)) [207]. The sound damper and valve were designed for a maximum operating pressure of 10 bar [208, 209] and thus suitable for the operation in the clinical examination rooms. There, the maximum available pressure output at the compressed air hose was 5 bar.

The nominal life in operating hours L_{10h} according to Eq. 3.1.6 with a 10% probability of failure of the bearings for three unbalances with varying weights of turbine V_4 is shown in Fig. 4.5. At a frequency of 60 Hz, the nominal life in operating hours was more than 10.000 h,

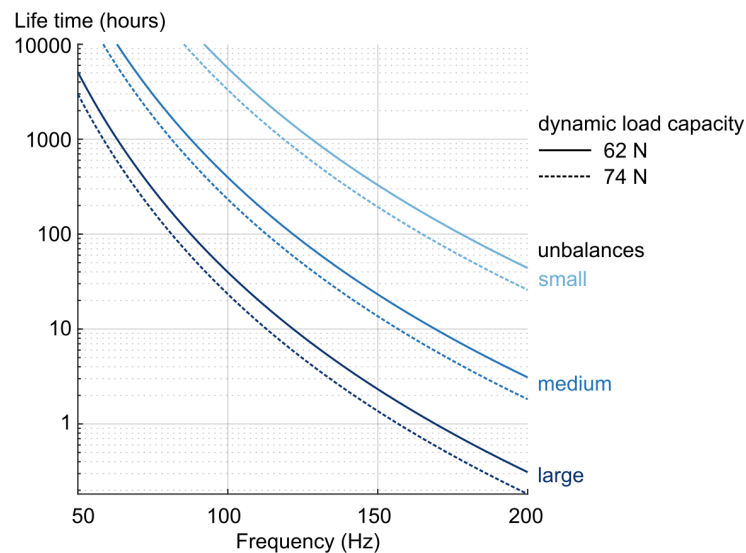


Figure 4.5 – Semi logarithmic plot of the nominal life expectancy L_{10h} of the rolling-element bearing in hours with respect to the operational rotational frequency for the small, medium and large unbalance of turbine V_4 .

1600 h, and 700 h for the small, medium and large unbalance, respectively. The nominal life decreased to 200 h, 15 h, and 1.5 h at a frequency for 150 Hz for the small, medium and large unbalance, respectively.

For the **transmission of vibration from the driver to the body surface**, two different base plates were designed. The vibration system was glued on the base plate, which in turn was attached to the patient.

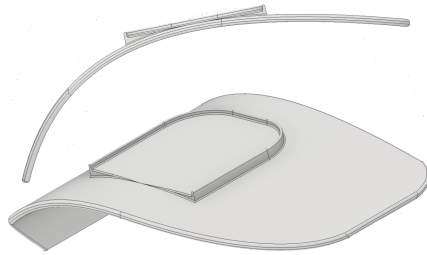
For liver MRE, a curved plate with a thickness of 3 mm was designed with CAD and manufactured by SLS using PA 12 (Fig. 4.6). The plate could be placed on the right anterior-lateral side of the lower ribs of the patient.

For prostate MRE, another curved plate was similarly designed. Here, the main focus was on the examination of the prostate gland such that the plate fitted anteriorly between the two hip bones. The trapezoidal base plate had a maximum width of 196 mm, a maximum length of 100 mm and a plate thickness of 3 mm. The base plate had a slight curvature, which allowed an ergonomic attachment to the patient. The 3 mm thick plate had a flat surface in the middle with frame-like indents of 2 mm. These were the counterpart to the elevations on the bottom of the housing and served for easy alignment and mounting of the turbine onto the base plate.

The **fixation of the passive driver** was realized with velcro fasteners. There were four longitudinal slots on the sides of the base plate. Two fixing straps were guided through these slots and the fixing straps then attached the base plate to the patient.

CAD drawings of base plates

A Liver



B Prostate

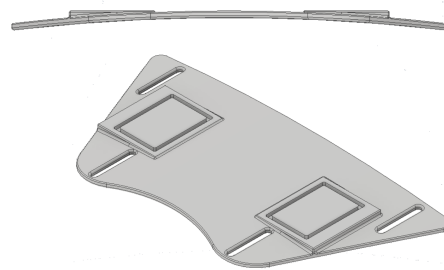


Figure 4.6 – CAD drawings of adaptor plates for **A**: liver and **B**: prostate MRE. A side view (top) demonstrates the different curvatures of the plates.

Quantification of artifacts induced by selected materials

Artifacts caused by the materials of the passive driver (PA and brass) were evaluated in a clinical 3T scanner in accordance to the ASTM standard F2119 [172] to determine their influence on image quality during MRE.

The size of the artifact during MRI was strongly limited to the vicinity of the PA cube and cylinder (Fig. 4.7). The largest relative error was observed in the transverse slice orientation. During a TRUFI (TSE) sequence, it was 57 % (24 %) and 105 % (43 %) for the cubical and cylindrical PA sample, respectively. No noticeable differences were detected with respect to the two phase encoding directions.

The largest relative error for the brass valve was 1136 % and 835 % during a TRUFI and TSE sequence, respectively. The valve caused a noteworthy elliptical signal attenuation with a maximum diameter of 60 mm surrounding the object. The artifact depended on the phase encoding direction (Fig. 4.7).

A dual turbine design for coupled actuation

Two turbines were connected in-phase. Both unbalances had the same angular position of the unbalances relative to their pivot points. After a feasibility study with version V_3 as a prototype for dual actuation experiments, two different actuation methods were developed with version V_4 : large surface actuation and two source surface actuation (Fig. 4.8). The turbine design underwent application specific adaptations for the coupled turbines. The results are described in the following.

Large surface actuation with coupled turbines: The vibration system consisted of two turbines, two housings with cover, one drive shaft and a base plate, as well as two attachments for light guides, a compressed air connection, a compressed air silencer, four ball bearings and

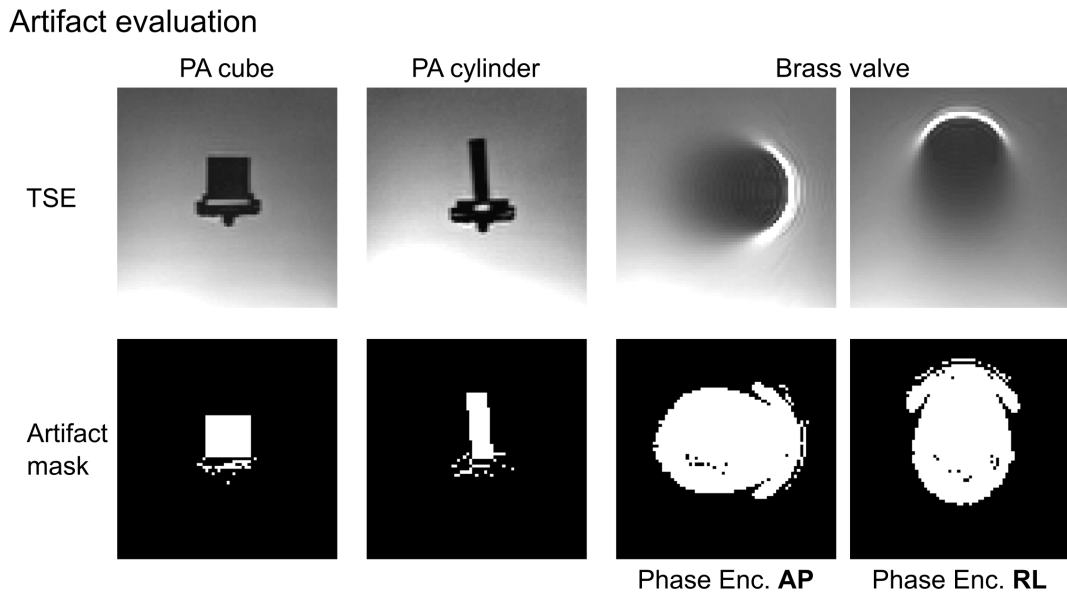


Figure 4.7 – Transverse MR magnitude images acquired with a TSE sequence and corresponding artifact masks for the PA cube (left) and PA cylinder (middle). The brass valve (right) is shown with both phase encoding directions. Signal attenuation were elliptical around the valve with a maximum diameter of 60 mm at its major axis.

eight plastic screws. Most parts were 3D printed by SLS and consisted of PA. The ball bearings were made of a polyoxymethylene (POM) cage and glass beads. The compressed air silencer (M/1545, Norgren GmbH, United Kingdom) was made entirely of plastic. The former compressed air connection, which was realized with the brass valve, was not used for this design. Rather, the tube was directly glued to the air inlet at the housing as described later in this section.

The drive shaft was optimized to allow coupled rotation of both turbines with equal phase. For the same phase rotation, the two turbines should not shift in their positions. The vibration system was designed modular and allowed changing the turbines and their unbalances. Thus, it was avoided to directly glue the turbines to the drive shaft. Instead, a tongue-and-groove connection was used (Fig. 4.9). The new drive shaft had a 3.0 mm deep, 3.2 mm wide and 47.0 mm long groove at both ends. Pushing the turbines and their tongues on both ends of the drift shaft ensured the fixation of the turbines and they rotated at the same frequency and phase. The drive shaft passed through the two housing. Its ends were in the ball bearings of the housing cover.

Two source surface actuation with coupled turbines: A design variation of the previously described coupled turbines was additionally developed. The goal was to obtain two sources of wave actuation at a surface of interest. Therefore, the base plate was removed. Instead, the two turbines were coupled with another fixation plate at the top. This design allowed an actuation at two source origins with coupled phases. A precise and controllable phase relationship of the shear waves was achieved as the positions of the unbalances were fixed with respect to each other through the common shaft.

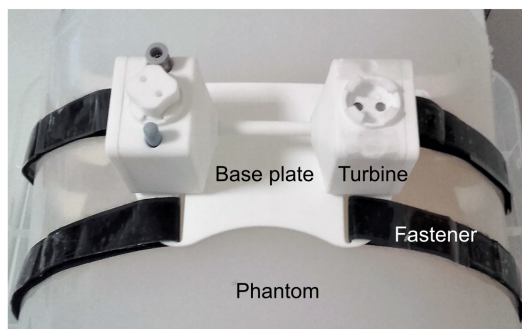
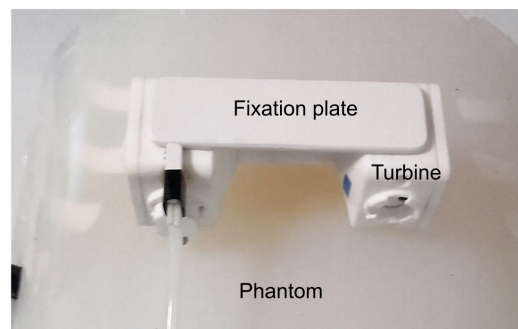
A Large surface actuation**B** Coupled actuation at two surface origins

Figure 4.8 – Photographs of dual turbines placed on the abdominal phantom. **A**: The first design enabled a large surface actuation with two coupled turbines. **B**: The second design generated shear waves at two origins.

Optimization of the passive driver

During construction of the dual actuation turbines, several components of the previous turbine design V_4 were optimized and the results are presented in the following (Fig. 4.10).

The quantification of artifacts demonstrated that severe signal attenuation surrounded the brass valve during image acquisition with a TSE sequence (Sec. 4.1.1). Compared to a relatively stable TSE sequence, an SE-EPI sequence is highly sensitive to such distortions. As the in-house developed motion encoding sequence is SE-EPI based, the air inlet was optimized to exclude the brass valve as a possible source of artifacts. The valve was removed and a compressed air tube with a length of 70 cm was directly glued to the housing with epoxy resin. A straight adaptor attached to the loose end of the tube further away from the FoV was employed to connect the tube from the turbine to the tube of the pressure regulator.

The former brass valve decreased the diameter of the inlet from 6.0 mm at the tube to 4.0 mm at the inside of the turbine housing, i.e. the aperture diameter decreased by 2.0 mm. As the valve was removed, the aperture diameter was further decreased at the inside of the turbine housing: The air inlet was firstly filled with epoxy resin and left to cure. Then, a hole with a diameter of 1.5 mm was drilled and a compressed air tube was glued to the air inlet. As the flow velocity is inversely proportional to the cross-sectional area, an increased flow velocity has been achieved. Thus, at the same air pressure, the rotational frequency of the turbine increased. Overall, the maximum achievable rotational frequency increased to over 150 Hz.

The dimensions of the roller bearings were additionally altered. The first versions had bearings with a dynamic load capacity of 62 N, resulting in a life expectancy of 6000 h (15 h) for the medium unbalance at 60 Hz (150 Hz). Another set of bearings had a larger dynamic load capacity of 74 N, resulting in a life expectancy of over 10.000 h (25 h). Thus, an increase in life time of over 66 % was achieved.

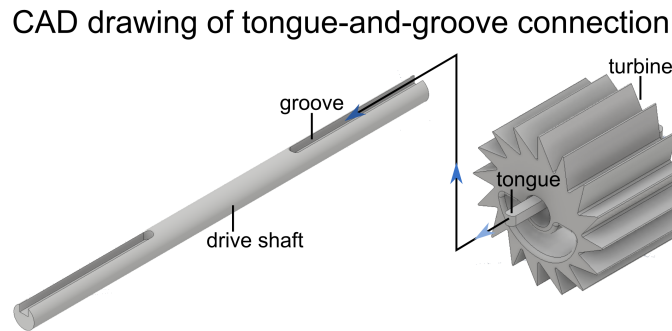


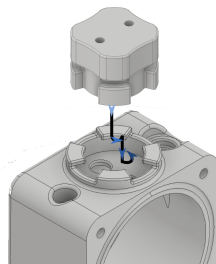
Figure 4.9 – CAD drawing of tongue-and-groove connection. It enabled a secure fixation of two turbines of the common drive shaft with a known phase relationship of the unbalances of the turbines.

Furthermore, the light sensor attachment was optimized. The new design was based on a bayonet lock design. The four bulges at the bottom of the attachment were responsible for the fixation. The attachment was inserted between the recesses on the housing and rotated by 45° . The light sensors (L_f and L_t) were screwed into the attachment and fixed in such a way that the light sensors could light up inside the housing and onto the turbine. Since air could also escape at the light sensor, a rubber seal was fitted into an annular groove at the bottom of the attachment. The seal had a diameter of 1.0 mm and was made of nitrile rubber.

Moreover, an elliptical groove was provided on the inside of the side housing to reduce air loss. The groove was mirrored on the housing at the same position and a rubber seal could be inserted. In addition to the refined closure, the positioning of the side wall onto the housing was also improved. Without the groove, the side housing would slightly shift, which was then avoided with the new design.

Optimization of turbine design

A Bayonet lock light sensor



B Groove for rubber seal

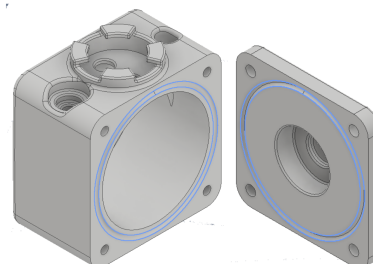


Figure 4.10 – CAD drawings of the turbine design optimization. **A**: The light sensors were included in a bayonet lock connecting to the housing to facilitate set-up at the MRI scanner. **B**: An elliptical groove with a rubber seal refined the closure of the side wall onto the main housing to reduce air loss.

4.1.2 The Active Driver

Most parts of the active driver were electrical and metallic components and have been introduced in Sec. 3.1.3. They were not MRI safe and were thus placed in the control room of the MRI scanner (Fig. 4.11).

Hardware of the active driver

The core of the active driver was the control unit with incorporated user interface. The developed electrical circuit processed all electrical signals and connected the external components such as the light sensor and the proportional pressure regulator with the micro-controller on the development board (Fig. 4.12). The electrical circuit consisted of three circuit components:

The first circuit component provided the different supply voltages to the light sensors, micro-controller (5 V) as well as the proportional pressure regulator (24 V). The main power supply was made available by an external 24 V source and needed to be converted to the aforementioned voltages. This was achieved with a voltage regulator.

The second circuit component converted the incoming digital 24 V light sensor signal to 5 V in order to be processed by the micro-controller. The micro-controller was only compatible to voltages smaller than 5 V. To convert the digital signal from the light sensor, an opto coupler was used. The opto coupler consisted of an LED and a photo diode. Whenever a 24 V signal of the light sensor was received, the opto coupler emitted a light signal and put the photo diode in a conductive state. In the process, the 5 V at the output was short-circuited via the photo diode and the micro-controller received a voltage potential of 0 V. Thus, the micro-controller detected an inverted digital signal of the light sensor. Since the signal processing of

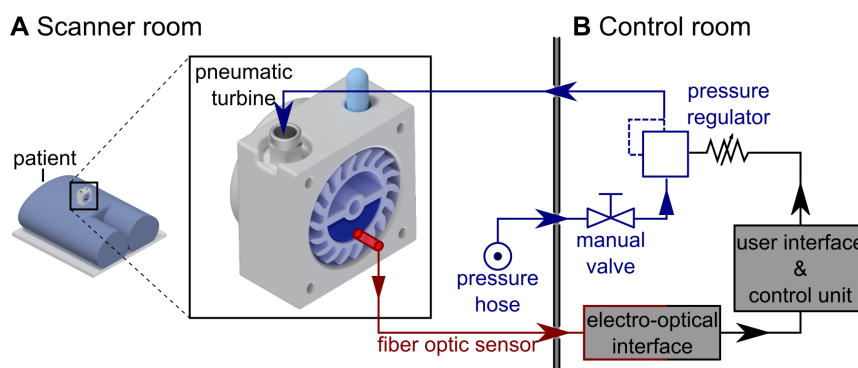


Figure 4.11 – Schematic hardware set-up. **A**: In the scanner room, the passive driver, i.e. pneumatic turbine, was located on the surface of interest on the patient. Compressed air was connected to the turbine via plastic tubes. **B**: All components of the active driver were located in the control room and included the ADC units of the fiber optic sensors, the active driver user interface and control unit, the pressure regulator and a manual valve.

Control unit of the active driver - the printed circuit board

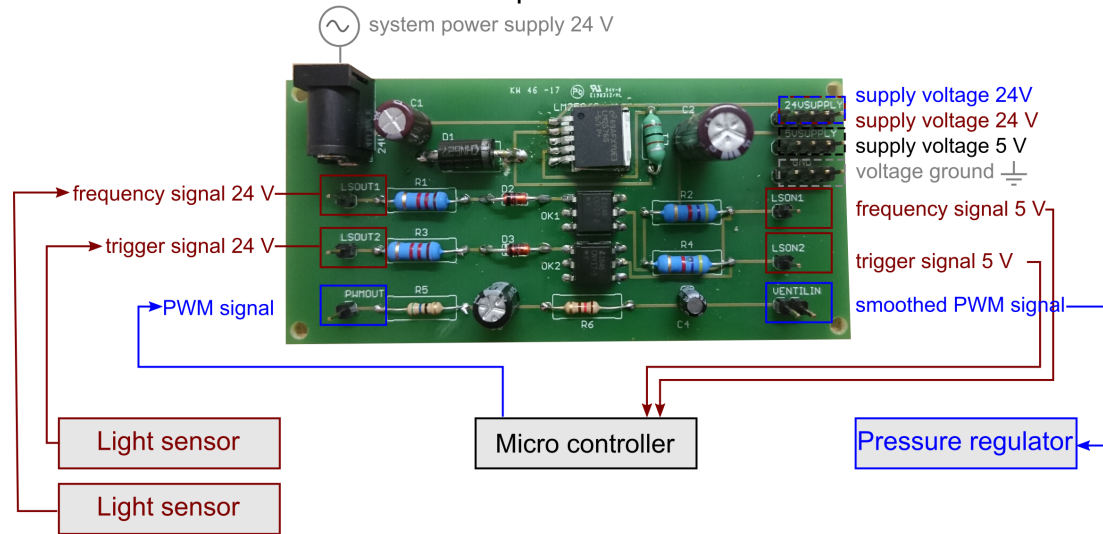


Figure 4.12 – Photographs of the PCB of the active driver control unit. Voltage supplies and signal path ways are delineated in red regarding the light sensor and blue regarding the pressure regulator. The supply voltage of the micro-controller is depicted in black.

the micro-controller only affected the edges of the signal, the inversion of the signal had no substantial influence. The reaction time of the opto coupler was approximately $5 \mu\text{s}$. This did not delay signal frequencies below 100 kHz [210].

The third circuit component used a passive second-order low-pass filter to smooth the outgoing PWM signal before it was transmitted as the voltage signal to the pressure regulator. The filtering ensured a proper control of the pressure regulator.

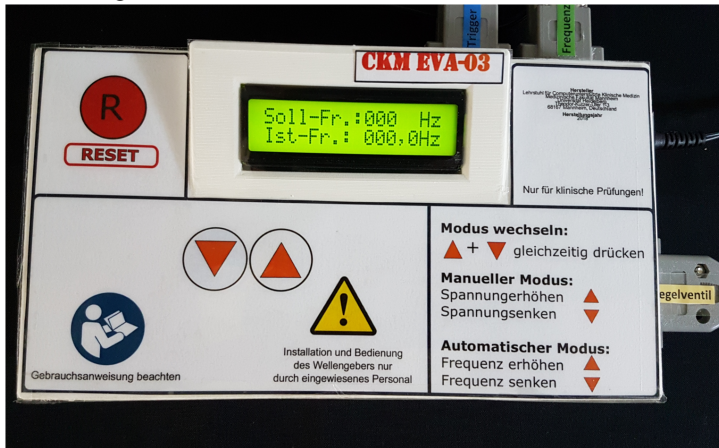
The control unit also contained the micro-controller with in-house developed application-specific programs, which are described in the following section. The central task of the micro-controller was to monitor and control the rotational frequency of the turbine.

The PCB and development board with the micro-controller were embedded in a housing with a graphical user interface, buttons and all connections required for the control of the passive driver (Fig. 4.13). The included connections were (1) a 24 V supply voltage, (2) two 9-pin D-sub connectors - identical to the standard COM port connectors - for the frequency and trigger light sensor (L_f and L_t), (3) a 9-pin D-sub connector for the connection of the trigger signal to a host computer, and (4) a cinch connector for the connection of the trigger signal to the MRI scanner.

The two light sensors (L_f and L_t) probes were connected to the housing such that light of the emitting probes was reflected by the turbine blades. The receiving probes of the light sensor then detected the reflected light. Via the user interface at the ADC unit of the light sensor, a threshold was either manually or automatically adjusted. It was set between 0 % and 100 % reflection and depended on the surrounding brightness. Different thresholds for laboratory and scanner conditions were determined automatically with the *2 point teach-in* mode of the ADC

Control unit of the active driver

A Housing with user interface



B Side housing and interior

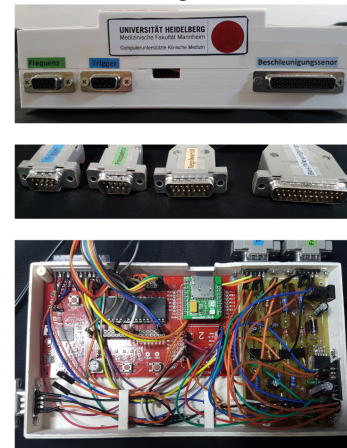


Figure 4.13 – Photographs of the active driver control unit. **A**: Top view of the housing with the user interface consisting of three buttons (reset, up, down) and an LED screen. **B**: Side view of the housing displacing the D-sub connectors and the corresponding cables. At the bottom, the interior of the housing is shown with the development board (red) and PCB (green).

unit of the light sensor as the brightness level differed at these locations. The response time t_s of the light sensor was $16 \mu\text{s}$. This determined the maximum sampling frequency f_a to be 31 250 Hz, according to the Nyquist-Shannon-sampling theorem ($f_a < \frac{1}{2t_s}$).

Frequencies used in MRE experiments were in the range of 20 Hz to 150 Hz yielding a maximum input signal frequency of the light sensor of $f_i = 8 \times 150 \text{ Hz} = 1200 \text{ Hz}$. This was well below the maximum sampling frequency f_a .

The turbine blade design was not only limited by the response time but also by a minimum length of each segment that could be detected by the light sensor. According to the manufacturer's data sheet, the minimum detectable length, i.e. arc length of each blade, was 0.0015 mm [183]. The arc length of each blade was $l_{\text{arc}} = 7.8 \text{ mm}$ and thus well above the required minimum length.

Software of the active driver

The micro-controller was equipped with three modi: an automatic mode, a manual mode, and an evaluation mode for acceleration measurements. The following gives a short distinction between each mode. More details are provided in Appendix D. The active driver always employed one of the three modi. Functions such as frequency calculations, inquires about pushed buttons and potentially the calculation of acceleration values worked in the background.

The user could set and adjust a nominal frequency of the turbine during **automatic mode** using the *Up* and *Down* button at the user interface of the active driver. The program then automatically adjusted the air pressure supplied to the turbine until the nominal rotational frequency was reached.

LT Spice: Simulation of passive circuit

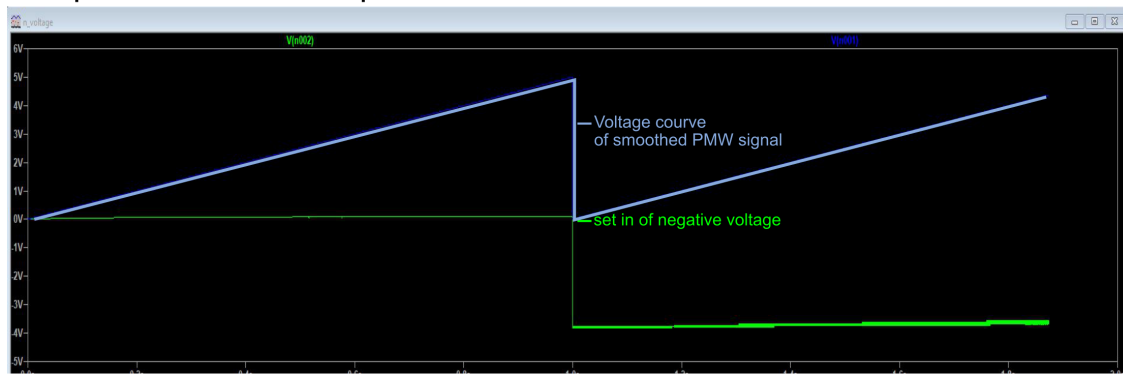


Figure 4.14 – Screenshot of the added passive circuit. The signal increases the range of the control voltage at the proportional pressure regulator. The simulated voltage curve (blue) with the set in of the negative PWM signal (green).

During **manual mode**, the user directly set values corresponding to a defined control voltage at the proportional pressure regulator. The step width was 5 mV, which corresponded approximately to a pressure increase of 2.5 mBar. The frequency of the turbine was then set proportionally to the control voltage.

The **evaluation mode for acceleration measurements** included an additional function that displayed the maximum acceleration per second recorded by an external acceleration sensor (Sec. 3.1.3).

Optimization of the active driver

The proportional pressure regulator was designed to be operated with a control voltage in a range of 10 V. The application of the maximum control voltage resulted in a maximum transmittable output pressure of the compressed air $p_{\text{outmax}} = 0.9 \cdot p_{\text{in}}$. The pressure hose in the scanner room supplied compressed air with a pressure of $p_{\text{outmax}} = 5.0$ bar and thus the maximum transmittable output pressure of the pressure regulator during clinical applications in the scanner rooms was 4.5 bar. However, the PWM signal of the micro-controller that set the control voltage at the proportional pressure regulator only had a range of 5 V. This resulted in half of the maximum transmittable output pressure (2.25 bar) and a maximum rotational frequency of the turbine of 70 Hz. To increase the rotational frequency of the turbine, a higher pressure needed to be applied and, in turn, the control voltage range fed from the micro-controller had to be extended.

One possibility was the application of an active voltage amplifier. However, this would have decreased the accuracy of the control voltage and thus also would have decreased the accuracy of the set rotational frequency. Another possibility was the development of a passive circuit. It consisted of a PWM signal that generated a negative voltage. By connecting it to the main circuit a larger voltage difference was obtained. The additional passive circuit was built and simulated in LTspice and included in the design of the PCB (Fig. 4.14). As a result, a maximum rotational frequency of the turbine of 150 Hz could be achieved.

4.1.3 In-house Certification of the Actuator

The internal evaluation resulted in an extensive technical documentation. Parts of this technical documentation were the results of a supervised bachelor's thesis [211], namely II a), II b) II c), III, V a), V b). The documents printed in bold below are appended in Appendix D. All others are included in the electronic version of this thesis. The technical documentation splits into the following chapters:

I Declaration of the manufacturer according to §7 (9) MPV

II Description of the product

- a) General description of the product
- b) Intended use of the product
- c) Classification according to Annex IX, RL 93/42/EWG
- d) User manual
- e) Labels
- f) List of applied standards

III Risk management of the product

- a) Risk analysis and risk acceptance
 - i. Structure chart
 - ii. Failure mode and effects analysis - Passive Driver
 - iii. Failure mode and effects analysis - Active Driver
- b) Risk management plan

IV Product specifications

- a) **Design documentation - Passive Driver**
- b) **Design documentation - Active Driver**
- c) Technical data sheet

V Product verification and validation

- a) Test records
- b) Results of calculations and tests
- c) Clinical evaluation according to Annex X, Directive 93/42/EWG
- d) Bio-compatibility

The declaration of the manufacturer according to §7 (9) MPV stated that the clinical evaluation according to Annex X, Directive 93/42/EWG was fulfilled. The following description of the product specified the intended use of the product. For example, it excludes the use of the actuator at sensitive body parts such as head and neck. A user's manual was established to ensure the correct handling of the actuator system. Based on the failure mode and effects analysis for the passive and active driver, an optimization of the passive driver design and in the programming code of the active driver were realized. The design documentation includes CAD drawings of the passive driver and pseudo-code software developed for the active driver. At last, further records of test results and technical parameters were included.

Other norms provided guidelines for the evaluation and certification of a medical device. The following standards were taken into account during the planning, development, completion and testing phases of the actuator system:

- 1 **Medizinprodukte-Richtlinie (93/42/EWG):** Definition of essential requirements that medical devices must meet
- 2 **DIN EN ISO 14971:** Application of risk management to medical devices
- 3 **ISO 13485:** Requirements for a comprehensive management system for the design and manufacture of medical devices
- 4 **DIN EN ISO 7010:** Definition of prohibition signs, mandatory signs and warning signs
- 5 **DIN EN ISO 14155:** Clinical testing of medical devices
- 6 **DIN EN 82079-1:** Drafting and creation of instructions, structuring, content and presentation.

4.2 Linking the Actuator to the MRI System

4.2.1 A Motion Encoding Sequence for MRE

The in-house developed sequence [188] was based on the approach published by Herzka et al. [212]. A conventional single-shot 2D SE-EPI-based sequence was modified. MEGs and a trigger system was developed. The following sequence elements were implemented in the special card of the imaging user interface (Fig. 4.15). The elements could be activated and deactivated and their parameters could be adjusted during image acquisition. The most important elements were as follows:

- 1 **Trigger active:** Activating the trigger check box allowed to activate the trigger and start each measurement of the sequence only after the trigger signal was received. If it is deactivated, any incoming trigger signal is ignored.
- 2 **Sinusoidal MEG:** Deactivated as a default, a trapezoidal MEG is employed. If activated, the shape of the MEG changed to a sinusoidal one - however, this feature was only implements for an actuation frequency of 60 Hz.
- 3 **MEG only before refocusing pulse:** The sequence used two bipolar MEGs by default; the first one being before, the second one being after the refocusing pulse. Activating this check box removed the second MEG, resulting in a shorter acquisition time at the cost of less signal encoded in the phase.
- 4 **MEG amplitude:** The gradient strength of the MEG could be adjusted between $0 \frac{\text{mT}}{\text{m}}$ and $25 \frac{\text{mT}}{\text{m}}$.
- 5 **Actuator frequency:** The frequency of the trapezoidal bipolar MEG could be adjusted to the vibrational frequency of the actuator in a range of 40 Hz to 120 Hz.
- 6 **Phase offset between consecutive measurements:** Consecutive measurements could be acquired and an offset in time, i.e. a phase offset of the induced mechanical wave, could be set between these measurements.
- 7 **Encoding direction:** The encoding direction of the MEG could be set to be in slice, phase or read-out direction.

A change in actuator frequency or activating the sinusoidal MEG could result in a change of T_E or T_R . Any timing collision was checked with a solve handler and T_E or T_R were increased if necessary. A sequence diagram is shown in Fig. 4.16.

Screenshot of sequence special card and implemented external trigger

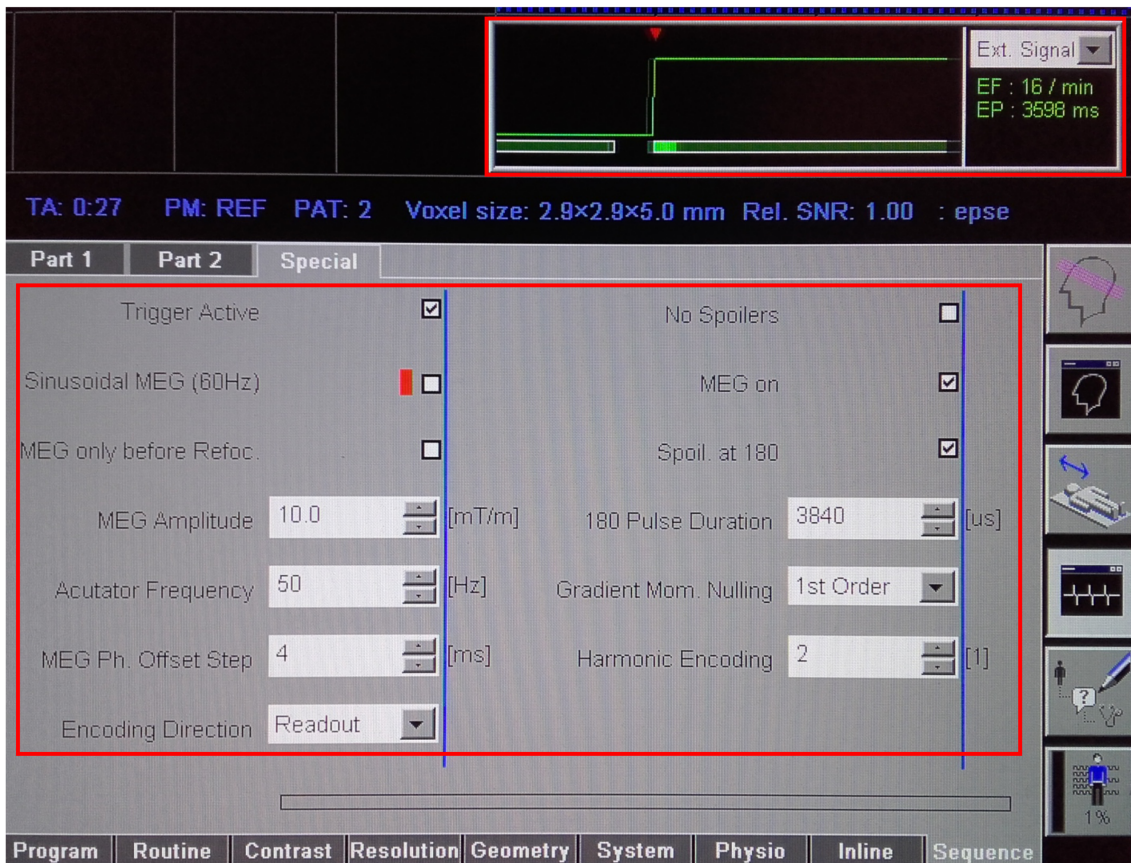


Figure 4.15 – Screenshot of implemented special card of the developed SE-EPI-based MRE sequence and the implemented external trigger (both delineated in red). The card included option to activate or deactivate check boxes and change various parameters to adapt the sequence to the vibrational frequency of the actuator. The inline display of the external trigger (top right) displays a signal change due to the signal sent from the active driver.

4.2.2 Triggering the MRE Sequence with the Actuator

In order to synchronize the MEG of the SE-EPI sequence with the phase of the actuator, a in-house trigger system was developed [189] and the results are described briefly in the following.

The turbine was divided into a section for a frequency and an angular zero position detection, both measured by an independent light sensor probe (L_f and L_t).

The signal was processed in two steps. Firstly, it was adapted to the micro-controller. Similarly to the frequency signal, the high level of the light sensor was at 24 V and had to be converted to 5 V to be processed by the micro-controller. Secondly, the external trigger connection of the Magnetom Trio MRI scanner only accepted signals with a frequency smaller than 50 Hz. As the employed actuation frequencies of the actuator could be as large as 150 Hz, the signal was further adjusted by creating an artificial time gap. This time gap did not affect the real time of the signal flanks as only the software of the micro-controller was extended. The additional

Sequence diagram of motion-encoding sequence with bipolar MEGs

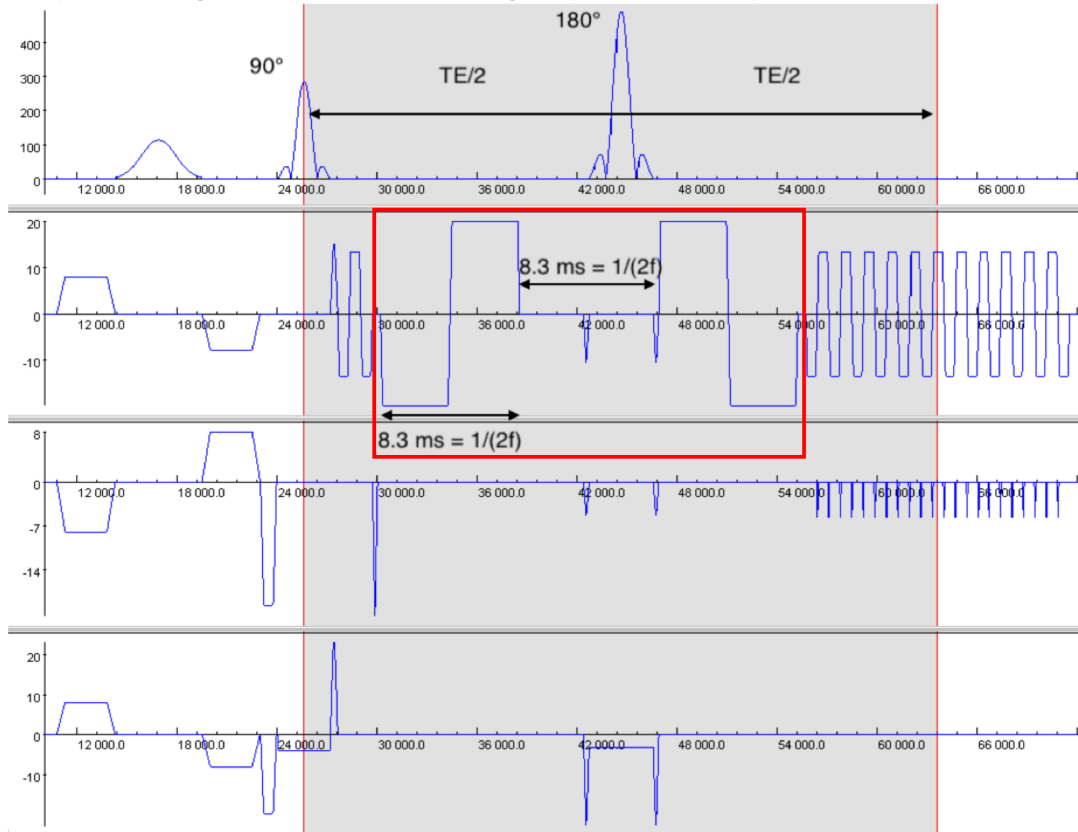


Figure 4.16 – Sequence diagram of developed SE-EPI-based MRE sequence for a mechanical actuation of 60 Hz. The second line shows the two implemented bipolar MEGs (delineated in red) placed symmetrically around the 180° pulse. The length of each MEG and the spacing in between was 8.3 ms, which was equal to $1/(2f)$. The core of the sequence encoding from onset of the 90° until half of the read out with a length of T_E is highlighted in grey. Figure adapted from [188].

code used an input and output pin as well as a peripheral timer. By using the timer, the length of the input signal from the light sensor was extended to meet the minimum length required for the input signal at the scanner (Table 3.1). The additional signals of the light sensors received in between were ignored. After the minimum signal length at the scanner elapsed, the next flank from the light sensor was used for the next trigger input.

The actuator and active driver were connected to a computer that simulated the triggered SE-EPI sequence. The micro-controller recognized the trigger signal and sent it via the COM port to the computer. This started the simulation of the sequence. Furthermore, a simulation of a sequential triggering for the acquisition multiple images with variable delay was successfully conducted. After the simulation, the actuator and active driver were connected to the host computer of the scanner system.

There, however, the signal sent to the COM port of the scanner's host computer was not recognized. The active driver was subsequently connected to the COM port of the system control hardware in the utility room of the scanner system, but similarly, no signal was detected. According to the manufacturer, the available COM port connection was only intended for system maintenance and was deactivated during normal operation.

Lastly, the trigger was connected to the external trigger input directly located at the scanner. Here, the signal sent from the micro-controller to the external trigger input was recognized and displayed in the physio-sequence card of the host computer. Thus, the start of the sequence could be triggered by the light sensor signal I_t with a variable delay in the phase offset between consecutive measurements as described above.

4.3 MRE Image Acquisition

4.3.1 Material Studies - Rheometric Evaluation of Silicones

In a pre-test, twelve silicones with a Shore hardness ranging from 00 ShA to 13 ShA were evaluated (Table 4.1). The complex shear modulus ranged from 26 kPa to 108 kPa and 210 kPa for pure SF00, 50 % SF00 mixed with 50 % SF13, and pure SF13, respectively, at a frequency of 60 Hz. The shear moduli were one to two orders larger than the shear modulus range of human soft tissue (Table 2.1). Hence, the following tests focused on silicones with a Shore hardness of 00 ShA being further diluted with silicone oil SF-V50.

The minimum shear modulus at a frequency of 60 Hz was achieved with SF00 diluted with 69 % SF-V50, namely 1.21 kPa. The shear modulus of pure SF00 at 60 Hz was 25.91 kPa. The resulting complex shear moduli obtained by the frequency sweep from 30 Hz to 100 Hz is shown in Fig. 4.17 and Fig. 4.18. The shear moduli obtained at 60 Hz are listed in Table 4.2.

One sample (SF00 diluted with 50 % SF-V50) was produced five times to determine the standard deviation due to variations in the production process. The standard deviation was always smaller than $\sigma = 0.21$ kPa for all measured frequencies and was $\sigma_{60\text{ Hz}} = 0.07$ kPa at a frequency of 60 Hz.

Another sample (SF00 diluted with 47 % SF-V50) was measured five times in the rheometer to determine the standard deviation of measurement uncertainties. The standard deviation was always smaller than $\sigma = 0.11$ kPa for all measured frequencies and was $\sigma_{60\text{ Hz}} = 0.05$ kPa at a frequency of 60 Hz.

Table 4.1 – Complex shear modulus of tested silicone samples ranging from SF00 to SF13.

Sample number	Concentration		Shear modulus at 60 Hz (kPa)		
	SF 13	SF 00	G*	G'	G''
Pre-test 1	1.00	0.00	209.50	207.64	27.84
Pre-test 2	0.83	0.17	139.51	136.52	28.72
Pre-test 3	0.67	0.33	145.94	144.53	20.22
Pre-test 4	0.50	0.50	108.11	107.06	16.00
Pre-test 5	0.47	0.53	90.48	89.00	16.25
Pre-test 6	0.40	0.60	87.67	86.67	13.21
Pre-test 7	0.33	0.67	64.05	62.43	14.31
Pre-test 8	0.27	0.73	56.38	55.14	11.78
Pre-test 9	0.20	0.80	57.68	56.76	10.30
Pre-test 10	0.13	0.87	47.76	46.94	8.81
Pre-test 11	0.07	0.93	40.21	39.61	6.95
Pre-test 12	0.00	1.00	25.91	25.02	6.89

A subgroup consisting of eleven samples of the second test was retested after four months to evaluate durability and long term effects on the shear modulus (Fig. C.1). The relative error (Eq. 3.3.1) depended on the sample and was largest for pure SF00 with $\delta G = 1.66$ and smallest for pure SF13 with $\delta G = 0.05$ at 60 Hz. The absolute error (Eq. 3.3.2) was largest for pure SF13 with $\Delta G = 11.341$ kPa and smallest for SF00 diluted with 50 % SF-V50 with $\Delta G = 0.170$ kPa at 60 Hz.

The samples of the second test, listed in Table 4.2, were manufactured using a different batch of silicones to evaluate effects caused by production variations of the raw material on the shear modulus. The relative error (Eq. 3.3.1) was negative for samples made of SF13, but always positive for samples made of SF00 and SF-V50. At 60 Hz, the relative error was largest for SF00 diluted with 69 % SF-V50 with $\delta G = 1.85$ and smallest for SF00 diluted with 38 % SF-V50 with $\delta G = 0.39$. The absolute error (Eq. 3.3.2) was, at 60 Hz, largest for pure SF13 with $\Delta G = 85.300$ kPa and smallest for SF00 diluted with 56 % SF-V50 with $\Delta G = 2.224$ kPa.

From the same probes of the fourth test (batch effects), two cylindrical disks with different diameters were cut and tested for resonance effects due to diameter of test plates. The first sample had a diameter of 25 mm, the second one a diameter of 13 mm. In general, the shear modulus continuously increased with increasing frequency. However, the samples with a diameter of 25 mm showed a steep increase of G^* followed by a decrease at frequencies of 60 Hz, 72 Hz, and 90 Hz. An even more pronounced increase followed by a decrease in G^* was observed for the samples with a diameter of 13 mm in a similar frequency regime (Fig. C.4).

One sample (SF00 diluted with 69 % SF-V50) was produced with three varying heights: 3 mm, 5 mm, and 9 mm. Two diameters of the sample were tested (13 mm and 25 mm). In the

Table 4.2 – Complex shear modulus of tested silicone samples.

Sample number	Concentration			Shear modulus at 60 Hz (kPa)		
	SF 13	SF 00	Silicone oil	G^*	G'	G''
1	1.00	0.00	0.00	209.50	207.64	27.84
2	0.50	0.50	0.00	108.25	107.05	16.09
3	0.00	1.00	0.00	25.95	25.02	6.89
4	0.00	0.63	0.38	8.64	8.34	2.26
5^{a)}	0.00	0.59	0.41	7.29	7.02	1.97
6	0.00	0.56	0.44	6.20	5.91	1.87
7^{b)}	0.00	0.53	0.47	5.17	4.93	1.56
8	0.00	0.48	0.52	3.95	3.75	1.24
9^{c)}	0.00	0.43	0.57	3.21	3.06	0.98
10	0.00	0.40	0.60	2.72	2.65	0.60
11	0.00	0.31	0.69	1.47	1.47	0.11

^{a)} chosen as inclusion A (Bladder) ^{b)} chosen as inclusion B (Prostate) ^{c)} chosen as filling material of the phantom

The silicone's shear modulus depends on (1) its Shore hardness and (2) the amount of added silicone oil

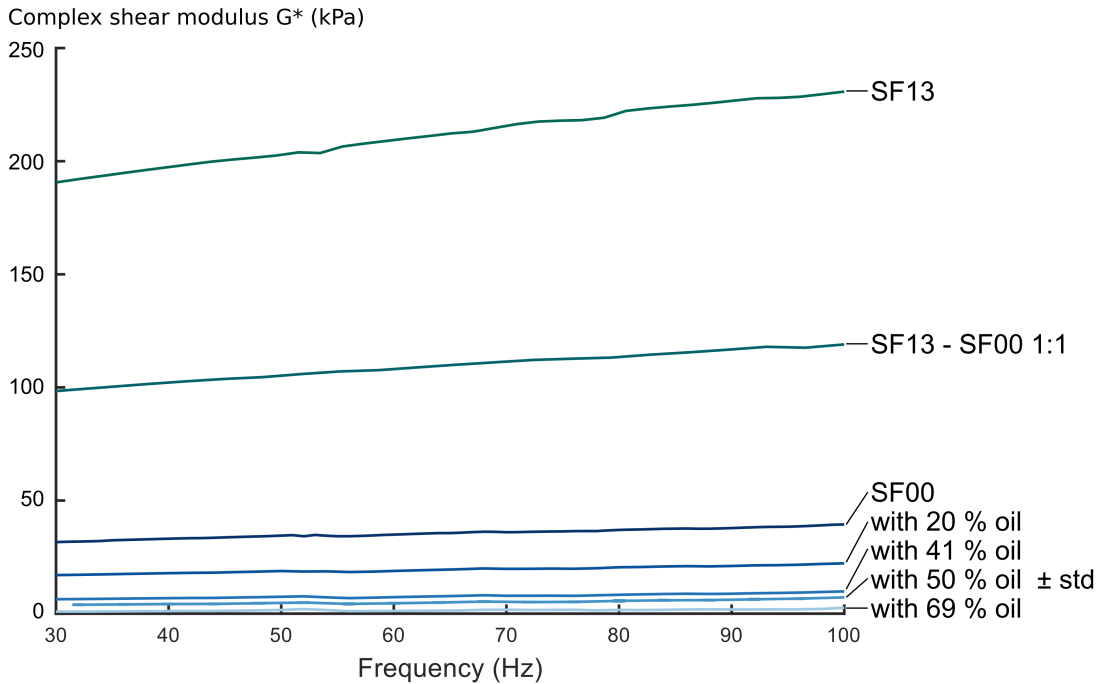


Figure 4.17 – Diagram showing the shear moduli measured by a frequency sweep of the strain-controlled rheometer. Selected samples covering the minimum and maximum range of shear moduli of the evaluated silicon samples are shown.

The silicone's shear modulus decreases with increasing amounts of added silicone oil

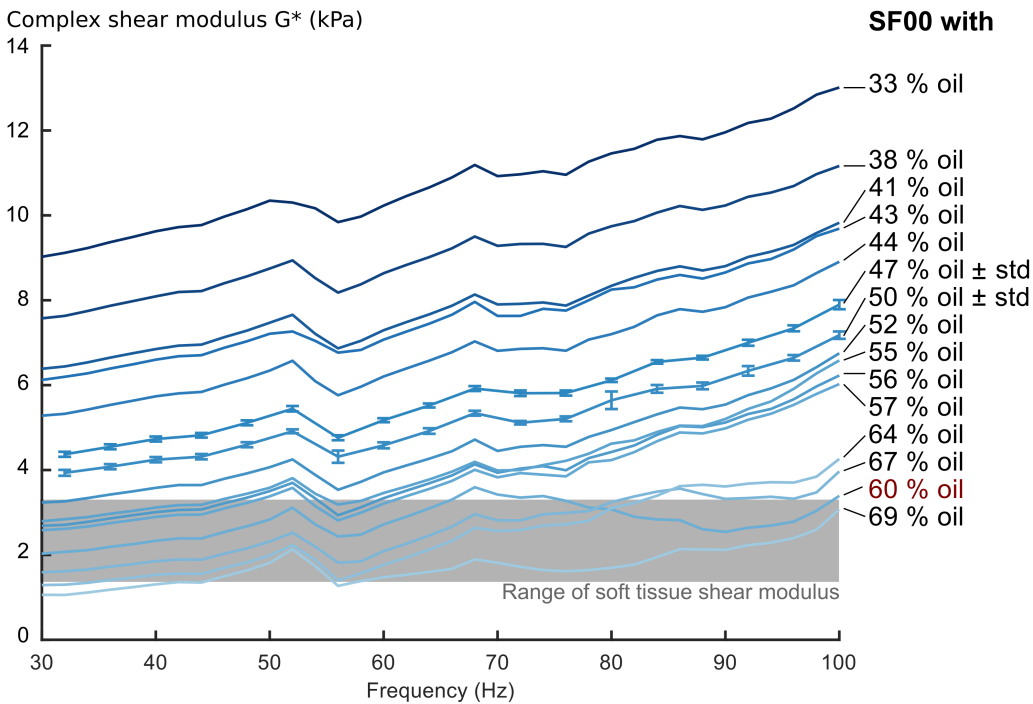


Figure 4.18 – Diagram showing the shear moduli measured by a frequency sweep of the strain-controlled rheometer. Samples of SF00 diluted with 33% up to 69% SF-V50 are shown. An approximate range of the shear modulus of human soft tissue is displayed in grey.

frequency range of 30 Hz to 54 Hz, all samples followed a similar pattern and increased linearly. At a frequency of 60 Hz and 72 Hz, the samples with a diameter of 13 mm exhibited a steep increase followed by sharp decrease. The behavior was more pronounced for the sample with the largest height (Fig. C.5).

Samples with scatter particles made of silica beads and graphite were compared to a sample without added particles. At a sample diameter of 25 mm and a frequency of 60 Hz, the complex shear modulus of the reference sample was $G_{\text{Ref}}^* = 12.12$ kPa. The corresponding complex shear modulus of the samples with added silica beads and graphite were $G_{\text{Sil}}^* = 13.64$ kPa and $G_{\text{Gra}}^* = 13.97$ kPa, which was an increase of 12.5% and 15.3%, respectively (Fig. C.6). The elasticity curve recorded for a sample diameter of 13 mm exhibited a similar trend with an increased shear modulus due to scatter particles. Furthermore, the curve displayed the same fluctuating behavior as observed in Fig. C.5.

4.3.2 Design of Anthropomorphic Tissue-Mimicking Phantoms

The complex prostate phantom and abdominal phantom were later used for MRE imaging. Prior, the phantoms were evaluated with morphological MR and CT imaging (Fig. 4.19). Furthermore, the phantoms were imaged with the MRE sequences (GRE and SE-EPI) without mechanical actuation (Fig. 4.20).

Regarding the complex prostate phantom in MRI, the SNR and CNR of a ROI of the bladder, prostate and filling material were evaluated and the results are listed in Table 4.3. In CT, the mean HU were $HU_P = 126 \pm 4$, $HU_B = 130 \pm 4$, and $HU_F = 123 \pm 5$ of the prostate, bladder, and filling material, respectively.

Table 4.3 – SNR and CNR of the prostate and abdominal liver phantom during MR imaging.

	T_1 -weighted	T_2 -weighted	MRE	
	FLASH	TSE	GRE	SE-EPI
SNR Bladder	287.9	240.8	124.2	54.0
SNR Prostate	287.1	248.0	130.0	53.9
SNR Filling	279.3	239.5	149.5	58.5
CNR Bladder - Filling	3.7	0.3	5.3	1.1
CNR Prostate - Filling	4.0	1.9	4.1	1.2
CNR Bladder - Prostate	0.4	3.5	2.2	0.6
SNR Liver	701.3	1011.6	63.6	71.5
SNR Filling	671.0	883.3	42.3	55.0
CNR Liver - Filling	32.0	130.0	17.3	16.5

Regarding the abdominal phantom in MRI, the SNR and CNR of a ROI of the liver and filling material were evaluated and the results are listed in Table 4.3. The included anthropomorphic features such as the liver and rib cage were clearly visible in MR images.

In CT, the mean HU were $HU_L = 106 \pm 6$, $HU_R = 166 \pm 6$, and $HU_F = 120 \pm 7$ of the liver, rib cage and filling material, respectively.

MRI and CT: morphological imaging of the phantoms

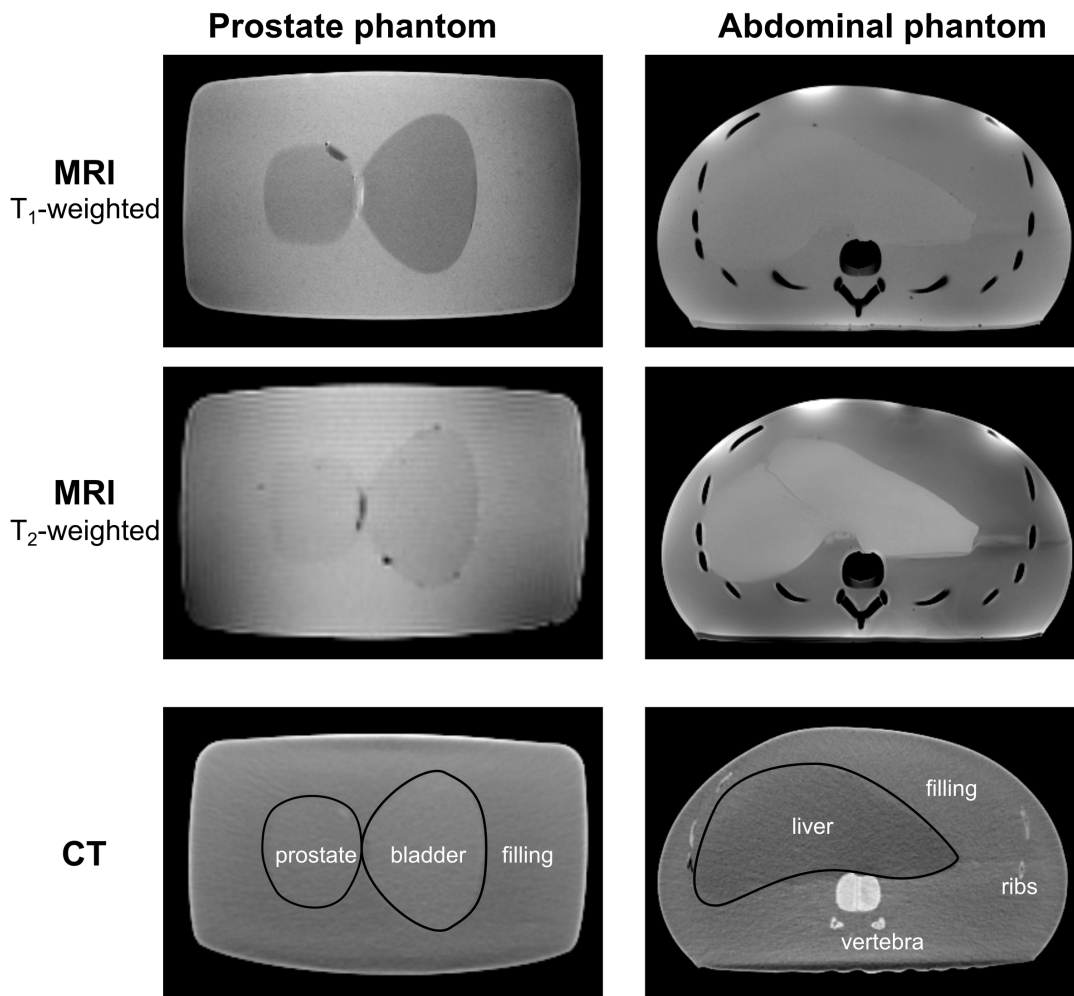


Figure 4.19 – Morphological MR and CT images of an exemplary coronal slice of the prostate phantom (left) and a transverse slice of the abdominal phantom (right). **Top:** T₁-weighted MR image. **Middle:** T₂-weighted MR image. **Bottom:** CT image. The included organs (bladder and prostate/liver) are delineated in black in the CT images. Images have been cropped for better visualization.

MRE imaging of the phantoms without actuation

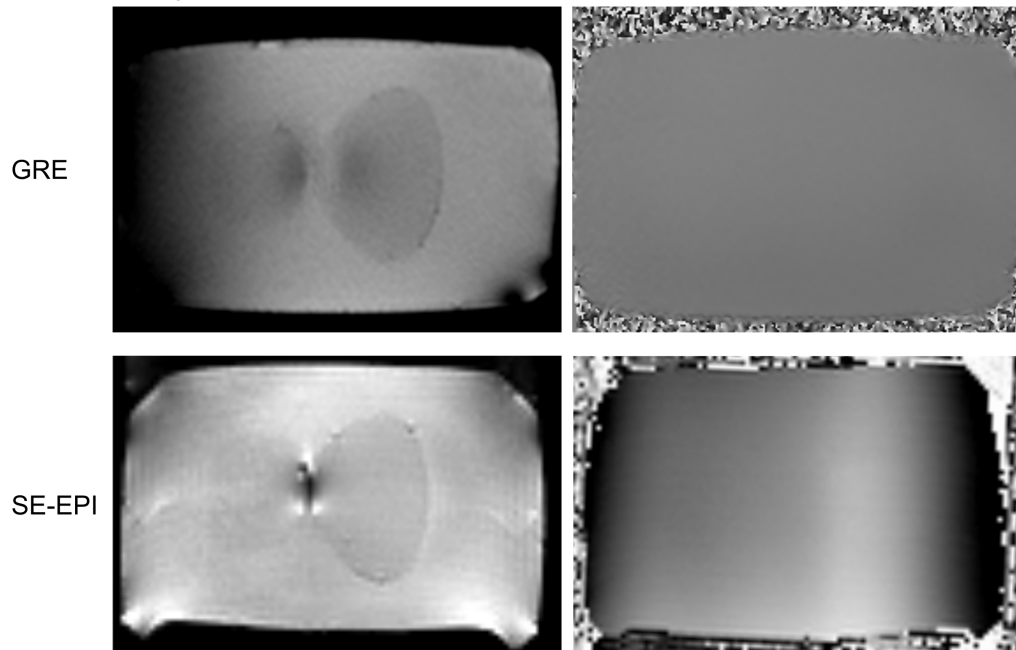
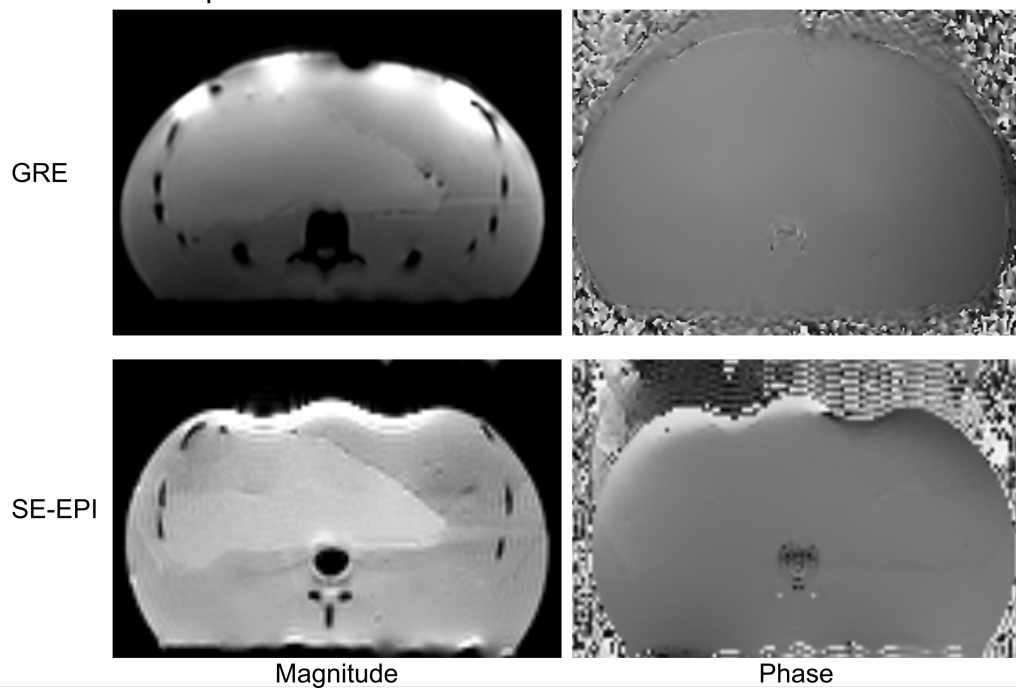
A Prostate phantom**B** Abdominal phantom

Figure 4.20 – Magnitude and phase images of the GRE and SE-EPI based MRE sequences without actuation. **A:** The prostate phantom. **B:** The abdominal phantom. Images have been cropped for better visualization.

4.3.3 MR Elastography - Phantom Studies

The prostate phantom

MRE was firstly performed on the complex prostate phantom with two sequences and the results are presented in the following.

The GRE based sequence (Sec. 3.2.2) was employed with an actuation frequency of 60 Hz. The passive driver did not generate any relevant artifacts in the ROI of the acquired MR images. The incorporated reconstruction algorithm automatically created wave images and an elasticity map with 95 % confidence interval for the fitted elasticities based on the obtained magnitude and phase images (Fig. 4.21). In the obtained elastogram, the elasticity in the bladder was stiffer than in the filling material. However, the color-coded values exceeded the range of the depicted shear modulus and were thus greater than 8 kPa. Signal attenuation was visible, most likely due to air inclusions, at the interface of the bladder and prostate. Here, a small circular checker-board pattern was also displayed in the elasticity map. It indicated an insufficient fit with values outside of the 95 % confidence interval. The spherical inclusions, simulating stiffer tissue, were also visible in the magnitude image. However, they were not visible in the elasticity map.

Secondly, the complex prostate phantom was imaged with the SE-EPI based sequence, which was introduced in Sec. 3.2.3. Geometric distortions were visible at the interface between the actuator and phantom images, but not within the ROI.

Magnitude and phase images were acquired at four actuation frequencies (50 Hz, 60 Hz, 70 Hz, 80 Hz) in a transverse and coronal slice (Fig. 4.22). Shear waves propagating through the phantom was visible in the phase images of both slice orientations. The measured wave lengths in the transverse slice was 1.5 times longer in the bladder compared to the wave lengths in the filling material. A 25-pixel-long line profile was obtained in the bladder at the four actuation frequencies. As expected, the wave length shortened with increasing actuation frequencies, e.g. from 36 mm at 50 Hz to 26 mm at 80 Hz (Fig. 4.23).

Elastograms were reconstructed for two frequencies (70 Hz and 80 Hz) in both slice orientations as a proof-of-principle (Fig. 4.24). In the transverse slice, the shear modulus in the bladder had an increased shear modulus compared to the filling material. The shear modulus was increased at the higher frequency (80 Hz) compared to 70 Hz. The elastogram of the coronal slice also displayed an increased shear modulus in the bladder and prostate compared to a lower shear modulus in the filling material. As no trigger was implemented during MRE image acquisition, the absolute values of the reconstructed shear modulus was deemed unreliable and is thus not provided for the above mentioned MRE imaging studies.

MRE with the complex prostate phantom and GRE sequence

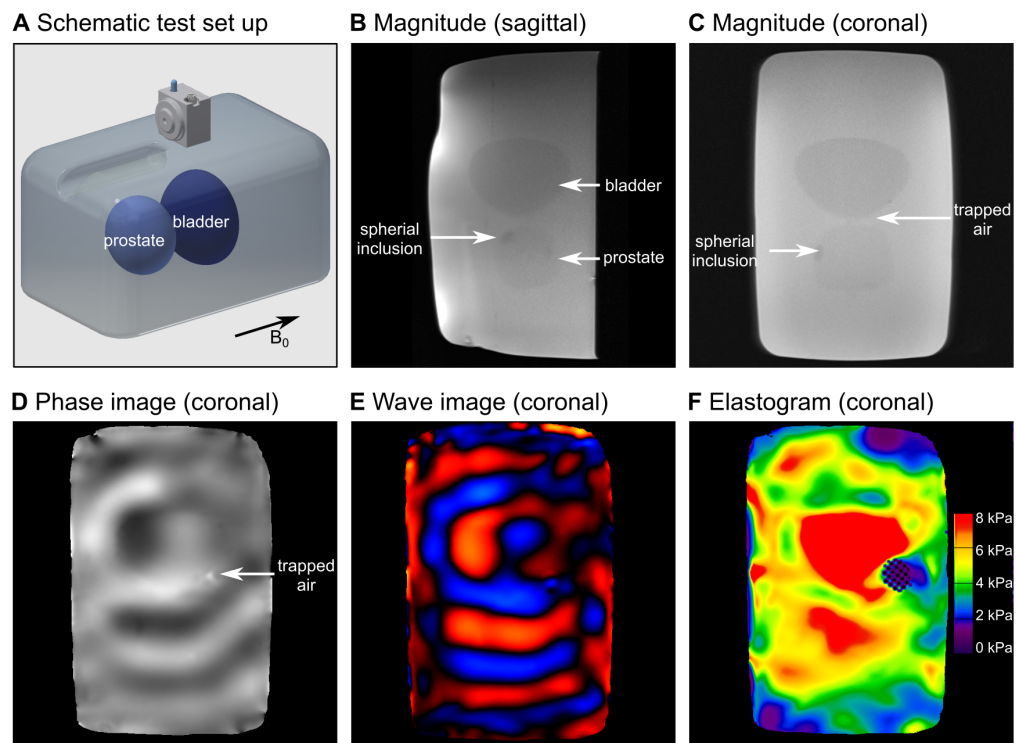


Figure 4.21 – MRE: results of the prostate phantom with GRE sequence. **A**: Schematic test set up of the phantom with the actuator placed on top. The included bladder and prostate are depicted in dark and light blue, respectively. **B**: Sagittal and **C**: coronal magnitude image. The bladder and prostate with spherical inclusions simulating small tumors were visible. Furthermore, air bubbles were trapped at the interface of the bladder and prostate. **D**: Coronal phase image. **E**: Reconstructed wave image. **F**: Elasticity map displaying the shear modulus in a range of 0 kPa to 8 kPa. Checkerboard pattern indicate areas with insufficient fit quality.

MRE with the complex prostate phantom and SE-EPI sequence

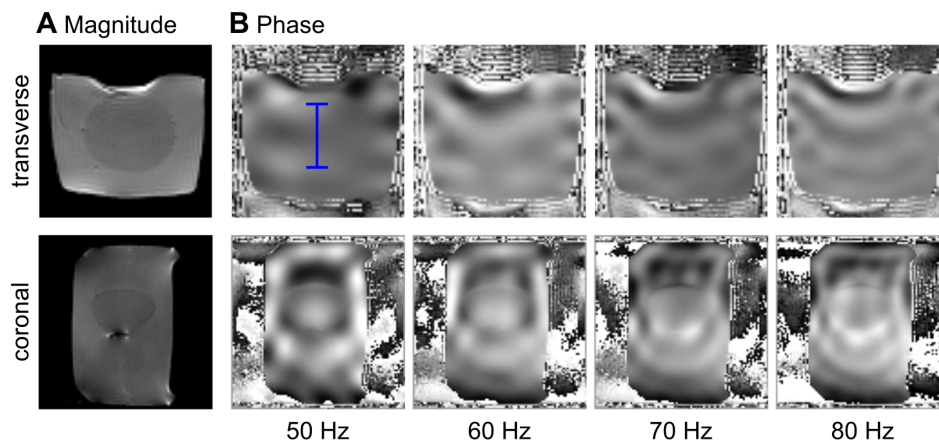


Figure 4.22 – MRE: results of the prostate phantom with SE-EPI sequence. The actuator was placed on top of the phantom similarly to imaging with the GRE sequence. Top row displays a transverse slice showing the included bladder, bottom row displays a coronal slice with both organs (bladder and prostate). **A**: Magnitude images. Trapped air was visible between the inclusions and the filling material which yielded to artifacts. **B**: Phase image were obtained for frequencies ranging between 50 Hz and 80 Hz. The phase ranges from $-\pi$ (black) to π (white). A blue line in the transverse phase image at 50 Hz shows the location of the obtained line profile.

Phase line profile in the inclusion at varying actuation frequencies

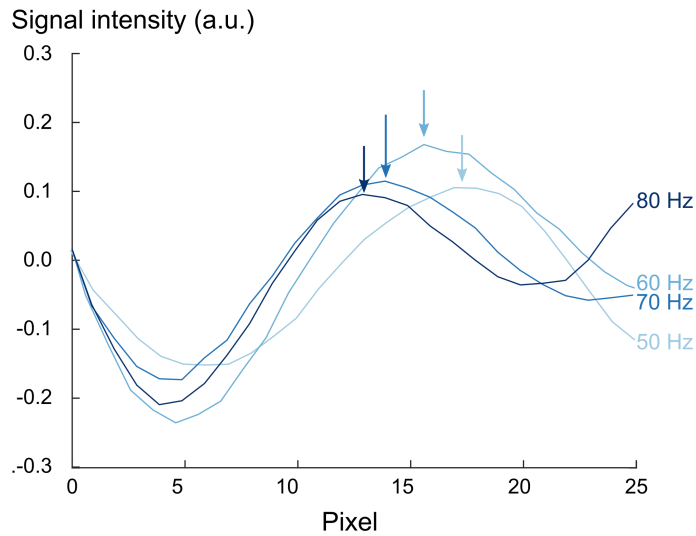


Figure 4.23 – MRE: line profiles of phase signal at 50 Hz, 60 Hz, 70 Hz, and 80 Hz in the bladder of the complex prostate phantom. A 25-pixel-line was placed in the inclusion and compared at four actuation frequencies. The wave length shortened with increasing frequencies as indicated by arrows at the first maximum of each line profile.

MRE elastograms of complex prostate phantom

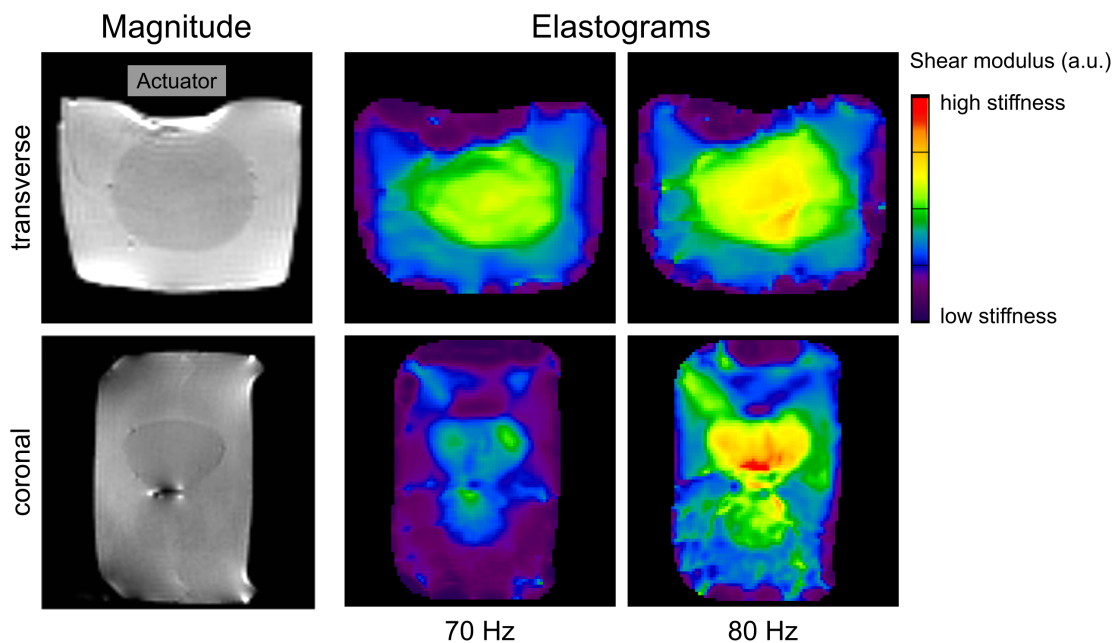


Figure 4.24 – MRE: elastograms of the prostate phantom in a coronal and transverse slice at 70 Hz and 80 Hz. The shear modulus in the region of the prostate and bladder was higher compared to the filling material. Elasticity values are qualitative as no synchronization of the mechanical actuation to the MEG of the sequence was performed.

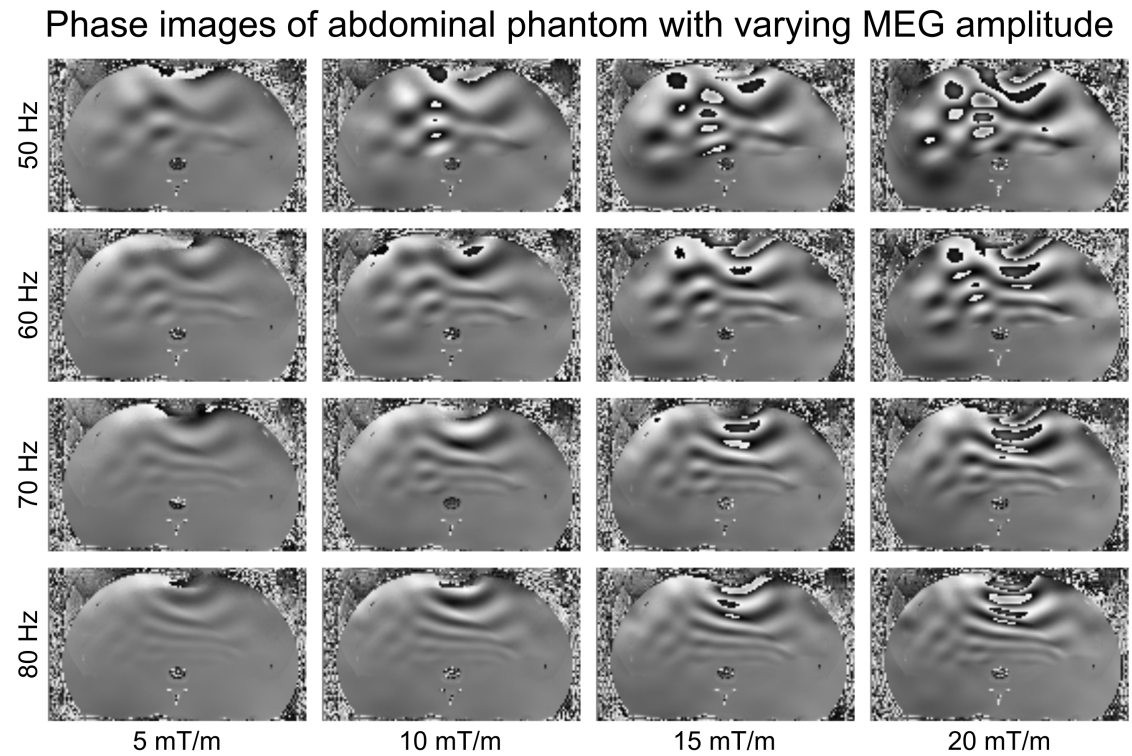


Figure 4.25 – MRE - results of the abdominal phantom with SE-EPI sequence, single actuation and varying MEG strength increasing from $5 \frac{\text{mT}}{\text{m}}$ to $20 \frac{\text{mT}}{\text{m}}$ (left to right). Phase images with an actuation frequency of 50 Hz, 60 Hz, 70 Hz, and 80 Hz (top to bottom) are shown. The phase ranges from $-\pi$ (black) to π (white). Phase wraps depended on the actuation frequency and motion encoding gradient strength.

The abdominal phantom

The anthropomorphic abdominal phantom was also imaged with the SE-EPI based sequence. Magnitude and phase images were acquired at four actuation frequencies of 50 Hz, 60 Hz, 70 Hz, and 80 Hz. Similarly to the prostate phantom, geometric distortions were visible at the interface between the actuator and phantom images but not within the ROI.

Varying the strength of the motion encoding gradient

The amplitude of the MEG was increased from $5 \frac{\text{mT}}{\text{m}}$ to $20 \frac{\text{mT}}{\text{m}}$ with a step width of $5 \frac{\text{mT}}{\text{m}}$ at the four actuation frequencies (50 Hz, 60 Hz, 70 Hz, 80 Hz). At 50 Hz, phase wraps were observed at an MEG of $10 \frac{\text{mT}}{\text{m}}$ and were increasingly pronounced with increasing MEG amplitude. At 80 Hz, phase wraps were observed at an MEG of $20 \frac{\text{mT}}{\text{m}}$, the highest MEG amplitude. Here, those phase wraps were only present in the proximity of the actuation source (Fig. 4.25).

Consecutive triggered phase images were obtained with the MEG being synchronized to the mechanical waves at increasing offsets. A propagation of the wave through the phantom could be observed (Fig. 4.26).

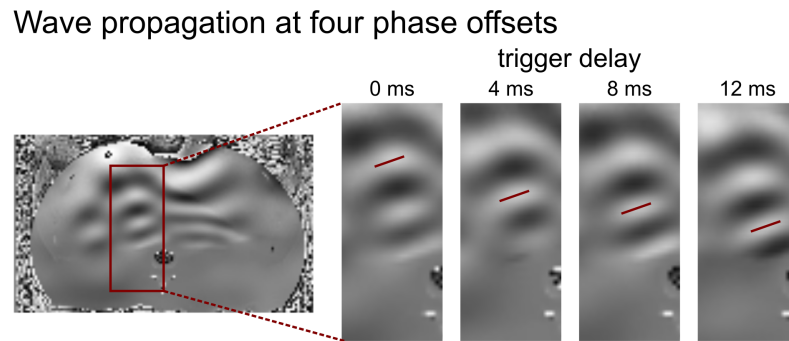


Figure 4.26 – MRE: results of the abdominal phantom with SE-EPI sequence, single actuation and four consecutive phase offsets between the mechanical wave and the MEG of the sequence. A red line indicates one wave peak that propagates towards the bottom during the four consecutive measurements. The phase ranges from $-\pi$ (black) to π (white).

Phase images of the actuation differed (Fig. 4.27). The intensity of the motion encoded phase images was evaluated by setting a threshold of 25% deviation from the mean phase signal to serve as an indicator of the sufficiently encoded tissue motion. The phase signal was less encoded for the single actuation in the lateral regions compared to the dual source actuation. At 50 Hz, the relative area of white pixels to the total area of the phantom was 12.7%, 15.6%, and 18.1% for the single, large surface, and dual source actuation, respectively. At 80 Hz, it was 22.2%, 21.1%, and 18.8% for the three actuation types, respectively. For the single actuation, the phase intensity was less attenuated in the center region compared to the lateral regions. In contrast, wave propagation was clearly visible in the center region during dual actuation. In comparison, phase images of the single actuation and large surface actuation differed less. For the single actuation, the phase intensity was attenuated more in the central region compared to the a lateral regions (Fig. 4.28).

The wave lengths were measured in the abdominal phantom (Fig. D.1). Regarding the single source actuation, the measured wave lengths were 25 mm, 23 mm, 21 mm, and 19 mm in the liver and 62 mm, 54 mm, 50 mm, and 41 mm in the filling material at the four actuation frequencies (50 Hz, 60 Hz, 70 Hz, 80 Hz). As expected, the wavelength shortened with increasing actuation frequencies. The three actuation set-ups showed no noteworthy differences in the wave lengths. The wave lengths increased for increasing elasticities, e.g. when comparing the softer liver to the stiffer filling material. This is in accordance to the obtained results by a single actuator.

Wave images (Fig. 4.29) and elastograms (Fig. 4.30) were also obtained. Similarly to the prostate phantom, an increased stiffness in the liver compared to the filling material could be observed. The elasticity map obtained at 60 Hz yielded a shear modulus of 1.12 ± 0.16 kPa in a ROI in the liver and a shear modulus of 4.37 ± 0.52 kPa in the filling material. This is lower than the shear modulus measured by rheometric testing (liver: 2.72 kPa, filling material: 7.3 kPa) but still in the range of soft tissue elasticity.

MRE phase images of abdominal phantom

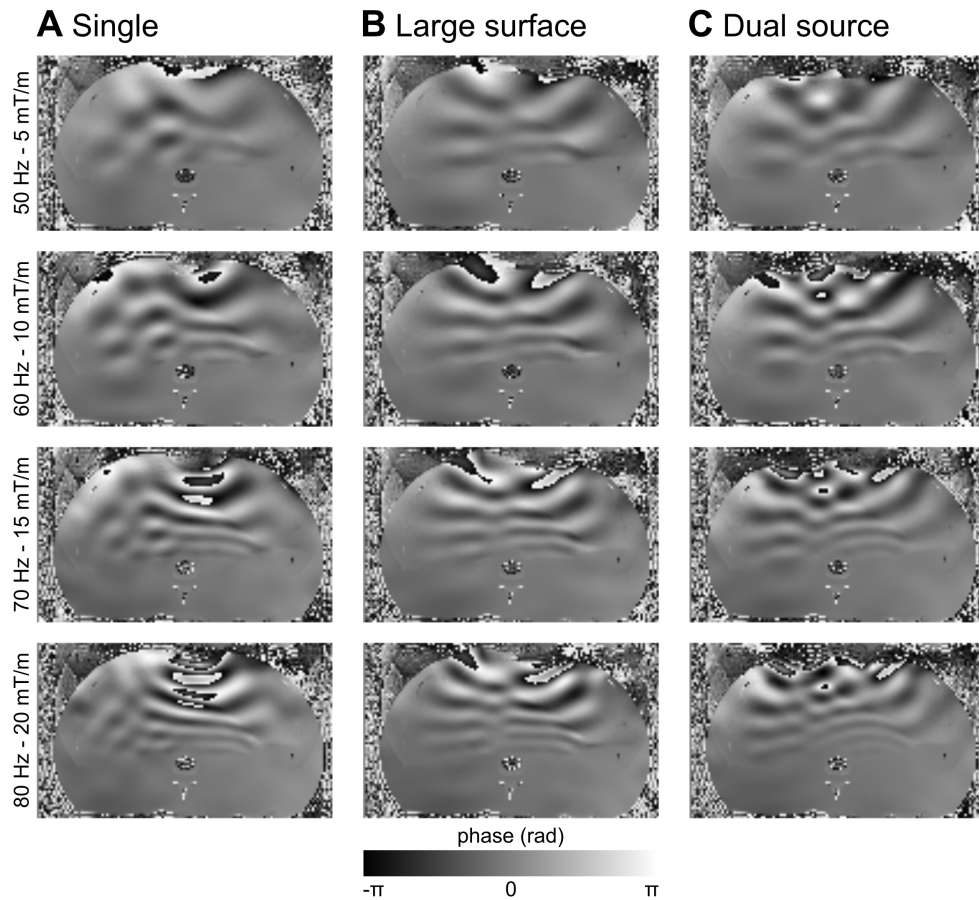


Figure 4.27 – MRE: phase images of the abdominal phantom in a transverse slice at 50 Hz, 60 Hz, 70 Hz, and 80 Hz for the three actuation types single, large surface, and dual source. The phase ranges from $-\pi$ (black) to π (white). The strength of the MEG was adapted for each image for best phase encoding without phase wraps.

Dual actuation with coupled turbines

Both set-ups for large surface actuation (Fig. D.2) and dual source actuation (Fig. D.3) showed shear wave propagation in the phase images. Geometric distortions were visible at the interface between the actuator and phantom but the passive driver did not generate any relevant artifacts in the ROI of the acquired MR images.

The amplitude of the MEG was increased from $5 \frac{\text{mT}}{\text{m}}$ to $20 \frac{\text{mT}}{\text{m}}$ with a step width of $5 \frac{\text{mT}}{\text{m}}$ at two actuation frequencies. At 50 Hz, phase wraps were observed at an MEG of $10 \frac{\text{mT}}{\text{m}}$ and were increasingly pronounced with increasing MEG amplitude. At 80 Hz, phase wraps were observed at an MEG of $20 \frac{\text{mT}}{\text{m}}$, the highest MEG amplitude. Furthermore, those phase wraps were only present in the proximity of the actuation source.

MRE thresholded phase intensity of abdominal phantom

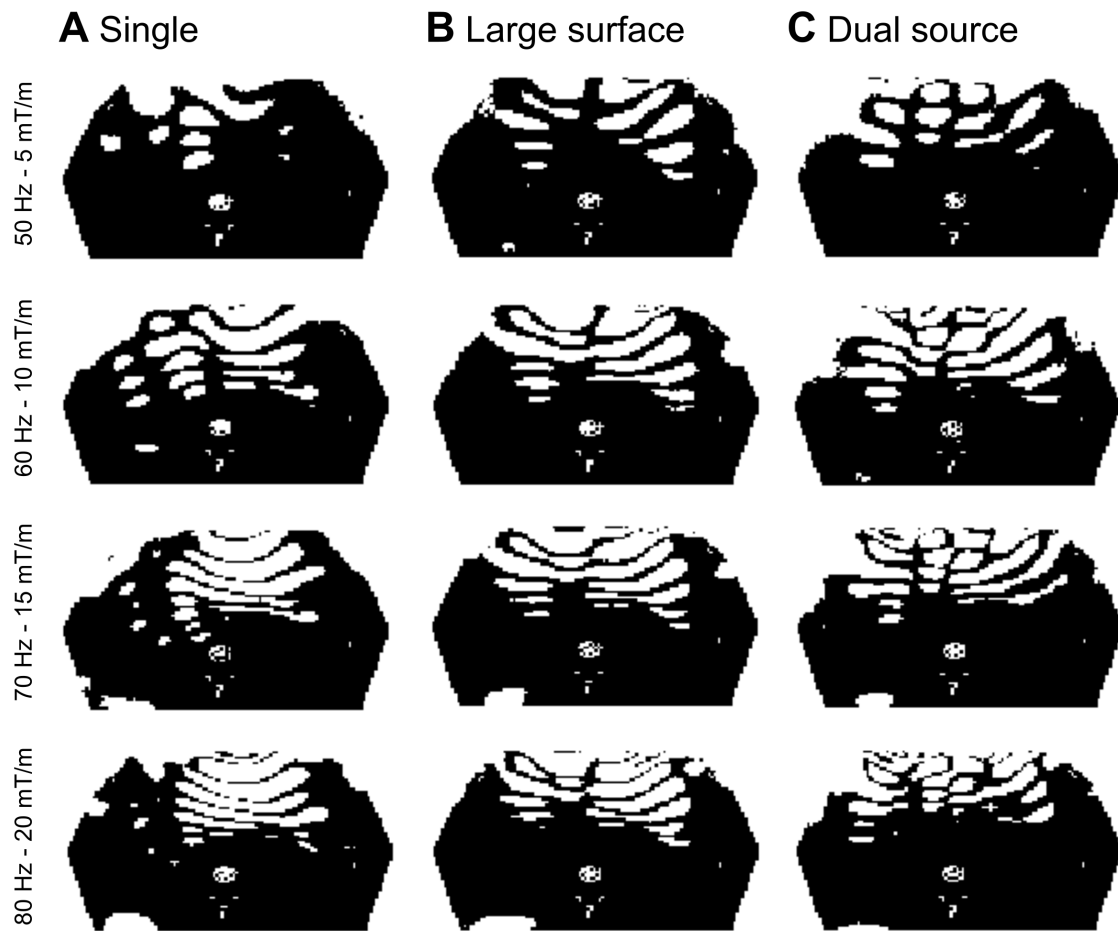


Figure 4.28 – Thresholded phase images of abdominal phantom. White pixels represent a phase intensity deviating by more than 25% from the mean phase signal and served as an indicator of the encoding intensity of the tissue motion. **A**: Single actuation. **B**: Large surface actuation. **C**: Dual source actuation. The pattern differed depending on the actuation set-up.

MRE wave images of abdominal phantom

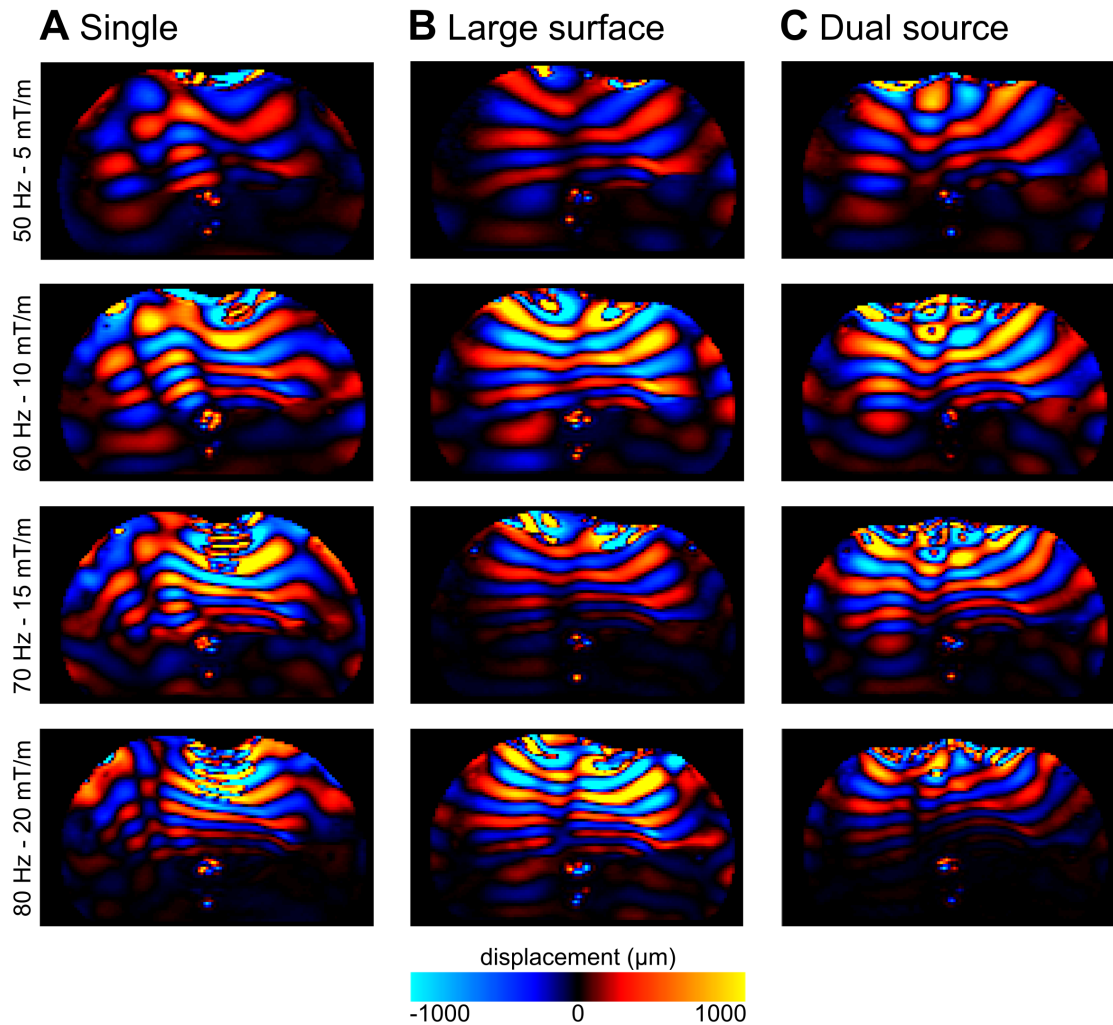


Figure 4.29 – MRE: wave images of the abdominal phantom in a transverse slice at 50 Hz, 60 Hz, 70 Hz, and 80 Hz for the three actuation types. **A**: Single actuation. **B**: Large surface actuation. **C**: Dual source actuation. The displacement amplitude of the encoded waves decreases with increasing distance to the wave source. Especially in the lower half of the phantom, this leads to insufficient data for accurate reconstruction of the elasticity parameters.

MRE elastograms of abdominal phantom

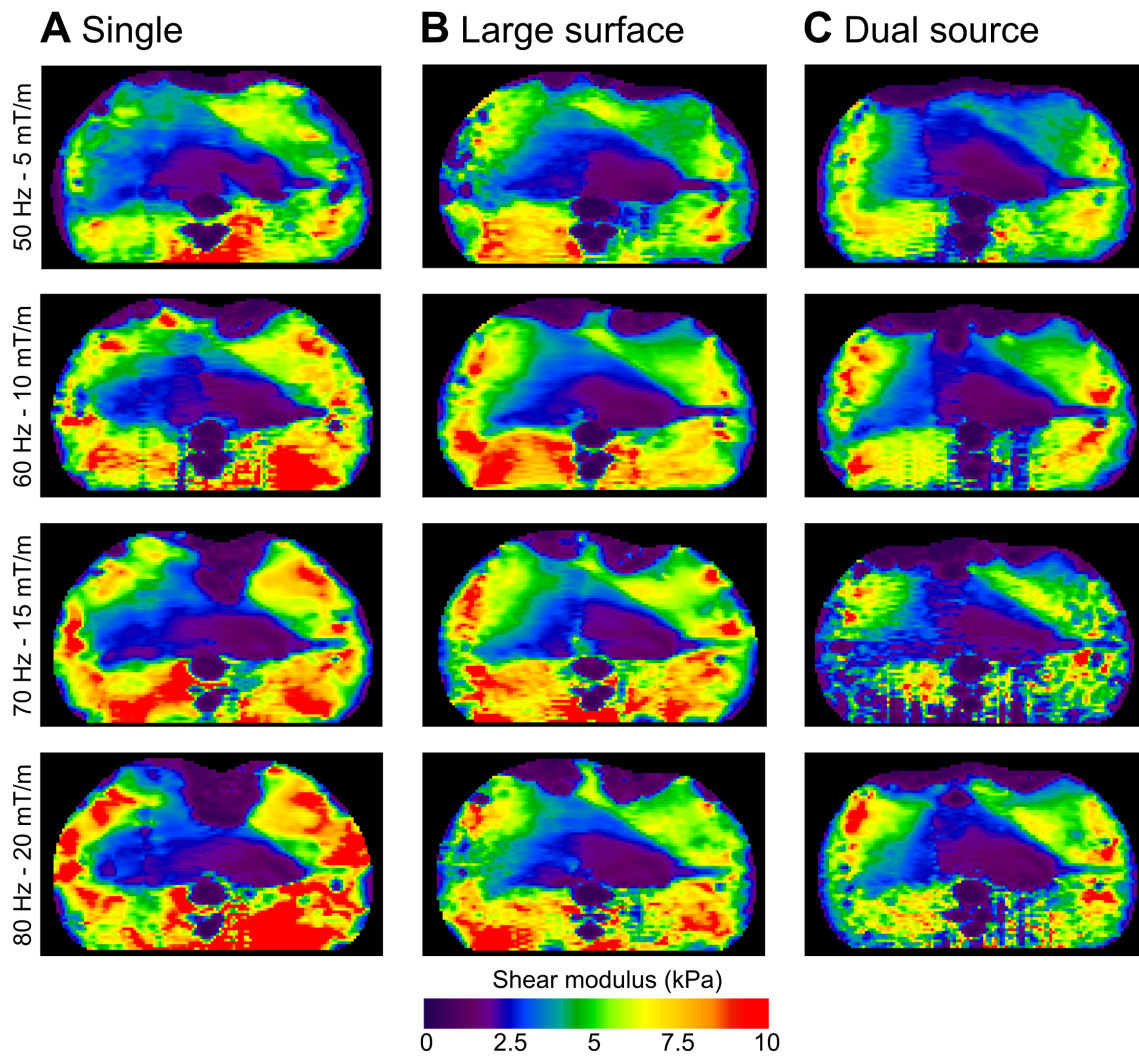


Figure 4.30 – MRE: elastograms of the abdominal phantom in a transverse slice at 50 Hz, 60 Hz, 70 Hz, and 80 Hz for the three actuation types. **A** Single actuation. **B** Large surface actuation. **C** Dual source actuation. The shear modulus was increased in the liver compared to the filling material and also increased for increasing actuation frequencies.

4.3.4 MR Elastography - In Vivo

The developed MRE system was also tested on a volunteer for liver and prostate in vivo imaging. The MRE set-up of the actuation hardware took additional five minutes. Magnitude and phase images were obtained with the SE-EPI based sequence without mechanical actuation. Then, MRE imaging was begun. The start-up routine of the actuator with a progressive ramping of the vibration from 0 Hz to the actual vibration frequency was well tolerated by the volunteer. Motion encoded phase images were obtained at 80 Hz for liver and prostate MRE (Fig. 4.31). The actuator did not cause any significant artifacts, however, insufficient signal in the motion encoded phase images prohibited the reconstruction of valid elastograms. Based on these results, the thigh was also imaged as an alternative region, where artifacts due to breathing or peristalsis can be avoided. Here, shear wave propagation was visible in the region close to the actuator. An elastogram of this region was obtained (Fig. 4.31).

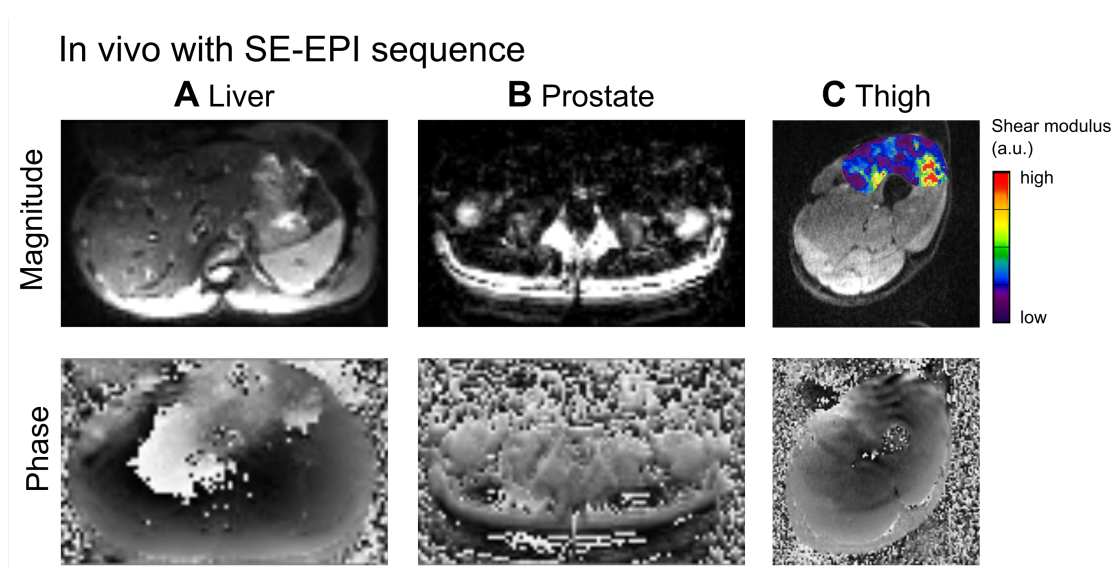


Figure 4.31 – MRE - results of in vivo study with the SE-EPI sequence. Magnitude (top) and phase images (bottom) of a transverse slice were obtained. **A:** Liver. **B:** Prostate. **C:** Thigh. The actuator did not cause any artifacts. However, only during imaging of the thigh muscle, wave fronts were visible close to the actuator placed anterior. An elastogram of this region was obtained and is displayed in the magnitude image.

Discussion 5

This thesis pursued three aims: The first aim was to develop an actuator based on centrifugal force for MRE. After its development and technical evaluation, the second aim was to implement the actuation system on a clinical MRI whole body scanner. The third aim was to acquire MRE images of phantoms and in vivo. These aims are discussed in the following subsections.

5.1 Actuator Development and Evaluation

For the quantification of soft tissue stiffness with MRI, mechanical shear waves need to be generated and transmitted to a ROI. Thus, some form of actuation method is always involved. According to Uffmann et al. [118], the actuator must meet various criteria. These include a variable actuation frequency and an adaptable amplitude and type of excitation depending on the area of application. The actuator should not create artifacts nor disturb the image phase to avoid interference with the MRE acquisition. So, the design and material of the actuator have to be chosen carefully.

A major restriction of MRE for a broader clinical impact is the additionally required software and hardware. We developed a simple stand-alone actuator, where the source of the wave generation and wave transmissions is at the same location. The MRE actuator, a pneumatic turbine, generated a centrifugal force, which was transmitted to the tissue for the required motion during MRE. Thus, no transmission technique, e.g. through a rigid rod, is required and the need for an extra driver is eliminated. This simplified configuration allowed an easy implementation in the scanner. Moreover, it was demonstrated how the pneumatic vibrator can readily be installed using the in-house compressed air system, 3D printing and a programmable micro-controller unit.

Contrary to the gravitational design by Runge et al., the design presented here eliminated the stepper motor connected by a rotating rod [169]. The electric stepper motor needs to be at a certain distance to the scanner due to MR safety restrictions. The distance between the

stepper motor and transducer is overcome by a lengthy rod. As the rod transmits the rotation, it needs to be mechanically stable and its rigidity limits the accessible surfaces. Thus, more surfaces are deemed accessible with the actuator presented here.

Technical parameters: Acceleration

The maximum acceleration values were experimentally determined. As expected, the evaluated frequencies (ranging from 30 Hz to 100 Hz) showed that the acceleration increased with the square of frequency and with larger weights of the inserted unbalances. The frequency spectrum is broader at lower frequencies, e.g. 40 Hz, and should be improved in future designs. For example, the pressure stability of the compressed air used to power the turbine has an impact on the frequency stability. Less air pressure loss in the housing, a more efficient turbine blade design and improved pressure adjustments based on the feedback loop in the active driver could improve the vibrational frequency stability. Overall, the passive driver generated vibration amplitudes sufficiently large to entirely penetrate the phantom during the feasibility studies for frequencies ranging from 50 Hz to 80 Hz at 3 T.

Vibration safety limits

Several safety standards regarding static magnetic fields, time-variable gradients, and RF used in conventional MRI are well established. These are also relevant for MRE imaging. The safety of the applied mechanical vibrations for the living human being is an additional concern. It was important to estimate the risks due to additionally induced vibrations to obtain approval for human studies on MRE [213, 214]. This is also relevant as MRE is in the process of becoming a clinical diagnostic imaging instrument [27].

The availability of an accepted standard for chronic occupational vibration exposure was adapted by Ehman et al. for the evaluation of vibration safety limits [27]. Under consideration of ISO 5349-1 [215] and the vibrational acceleration limits of the EU directive EU 2002/44/EC on the limitation of occupational exposure to whole-body and extremity vibrations [216], the vibrational acceleration for time and frequency of exposure were converted to displacement values during MRE imaging.

The average maximum tissue vibration amplitude that has been observed in hepatic MRE exams was approximately 200 μm with most areas of the hepatic tissue experiencing substantially less vibration [27]. This is in accordance to the observation made during phantom MRE imaging. The MRE images demonstrated that the highest vibration amplitudes typically lie in the adjacent areas next to the driver. Vibrational amplitudes in the deeper tissues and organs, which are the focus of clinical imaging, are greatly attenuated. Furthermore, during

in vivo measurements, the healthy volunteer tolerated the applied vibrations well during the entire image acquisition time. Thus, the generated vibrations were deemed safe as they were in the same range as published by past studies and well below the vibration safety limits.

Quantification of artifacts

A vast number of 3D printing materials are available for manufacturing. An in-house study quantified the artifacts induced by three rigid materials for MRI, namely PA, PLA and VeroWhite [177]. In that study, the mechanical properties of PA were shown to be superior to PLA and it was more cost-efficient than VeroWhite.

MR images were acquired with two sequences and evaluated for artifacts caused by the materials. The TRUFI sequence belongs to the class of GRE sequences with a T_1/T_2 contrast, which is sensitive to susceptibility [217]. Differences in magnetic susceptibilities of fluids or materials such as the tested objects create local magnetic field inhomogeneities. These inhomogeneities can change the phase and frequency of local spins and result in geometric distortion artifacts, which are particularly pronounced in the direction of frequency encoding [218, 219]. The TSE sequence is more stable with regard to artifacts, however its acquisition time is longer compared to the TRUFI sequence.

Neither the PA cube nor the cylinder showed pronounced artifacts except in their close proximity, which is not expected to impair image or diagnostic quality inside the body where the ROI is located. As the artifacts caused by the PA were in general quite small, an encoding direction dependency could not be observed. Overall, the artifacts were restricted to millimeters surrounding the samples. This is in accordance to previous work that found the apparent diameter of a PLA cylinder increase from 2.9 mm to 4.0 mm, resulting in a relative error of 90 % [220].

In contrast, the valve made of brass showed highly pronounced signal attenuation with a relative error as large as 1136 %. It also showed a more pronounced encoding direction dependency. As a consequence, it was removed and replaced by a compressed air tube directly glued to the air inlet of the housing. Overall, as the 3D printed material is intended to be used for the actuator placed on the body surface, the signal alterations will be restricted to the very proximity of the device. As only minor variations were found regarding the extent of artifacts, the potential artifacts caused by the tested materials will most likely not be of clinical relevance during imaging. Thus, PA was chosen for the 3D printed parts of the driver.

The samples were tested at a field strength of 3 T as MRE imaging was conducted at 3 T MRI scanners during this work instead of the more commonly used 1.5 T during MRE [221]. However, artifacts are predicted to be smaller at 1.5 T as the artifact-to-noise ratio is lower compared to 3 T and the artifacts are masked by the statistical image noise at 1.5 T [222]. Furthermore, although the SNR is twice as large at 3 T, susceptibility artifacts also increase [223, 224, 225]. In either case, the actuator is expected to perform at both field strengths without causing significant artifacts.

Another study found only minor differences between varying manufacturers and batches for the same material [226]. Nevertheless, the range of induced artifacts is expected to remain stable across platforms.

The ASTM standard F2119 defines the size of an artifact as a rectangle with the maximum horizontal and vertical distance in millimeters between the edges of the artifact [172]. Using this approach, a single outlier pixel can exorbitantly increase the size of the rectangle without a significant influence on image quality. Instead, the area of all pixels identified as an artifact was calculated. Then, the relative error of the artifact was evaluated with respect to the cross sectional area of the CAD sample data. Thus, the uncertainties by various causes were taken into account as their individual proportion of error was difficult to obtain. The artifact included manufacturing uncertainties such as the geometric deviations of the digital CAD model to the real printed object and MRI specific uncertainties such as geometric material distortions, image resolution and partial volume effects.

Optimization of the actuator

Several improvements of the actuator design have already been implemented during this work (Sec. 4.1.1) including:

- 1 Artifacts were reduced by removing the brass valve and glueing a compressed air tube directly to the housing,
- 2 Compressed air was used more efficiently by decreasing the diameter of the air inlet to increase flow velocity of the compressed air,
- 3 The light sensors were included in a bayonet lock connecting to the housing to facilitate set-up at the MRI scanner, and
- 4 An elliptical groove with a rubber seal refined the closure of the side wall onto the main housing to reduce air loss.

Further improvements are proposed, which will be detailed in the following paragraphs.

The transmission of shear waves from the actuator to the body surface: Two base plates were developed to facilitate the transmission of the generated vibration from the passive driver to the body surface. As the plates were manufactured from PA, they were relatively stiff. It had the advantages of a virtually loss-free transmission of the mechanical waves. However, the plates were not form-fitting for every surface given by the variety of existing body types. An alternative would be the use of a slightly more elastic material, which provides a better interface between the actuator and different body surfaces. The disadvantage is that a more elastic material damps the mechanical shaft more than a stiffer material. An optimal ratio between

surface connection and damping of the material of a new base plate should be evaluated. Ito et al. investigated the use of an elastic belt that tightens the upper abdomen during liver MRE. An acoustic driver was placed over the brace. Since the belt located organs closer and more tightly together, mechanical waves were assumed to be guided from the driver at the anterior body surface to the abdominal organs. Their study concluded that the areas of theoretical miscalculation for the stiffness values with the elastic belt became significantly smaller [227]. The incorporation of such an elastic belt in combination with an improved base plate of the actuator is deemed feasible and could be realized in future work.

Design adaptations to fit the receive coils: Until now, the actuator only fits a limited number of coils, for example a Siemens 4-channel flex coil, while the Siemens 18-channel body surface coil is too small for its size. The geometry of the turbine housing might be altered to fit in the holes of surfaces coil. Another option is the use of intervention coils as the coil's biopsy windows should offer sufficient space for the placement of the actuator.

The feedback loop between the passive actuator and active driver: A dependency on frequency was found during the FWHM analysis of the generated vibrations. The delay between the adjustment and the delivered actuation frequencies remains an issue. An inherent challenge is the pressure delay between the set pressure of the compressed air at the proportional pressure regulator and the turbine through the long (> 5 m) pressure supply tubes. As the design of the actuator evolved, the sampling rate of the light sensor was already increased from 2 sampling points to 16 sampling points per rotation. An increased measurement accuracy could either be achieved with longer measurement times or an altered turbine design yielding more sampling points per rotation. The latter option is favored as more sampling points allow faster frequency measurements and thus a faster adaptation.

An improved sampling scheme is also beneficial for a faster start-up routine. For example during volunteer studies, it took approximately 20 seconds until an actuation frequency of 60 Hz was reached and a further 10 seconds until the actuation vibration was sufficiently stable to start measurements. Adaptations to a new frequency took approximately 10 seconds. Nevertheless, a certain length of the start-up routine is also feasible to increase volunteer acceptance. A gradual start-up ensures that the volunteer can get accustomed to the vibrations.

Dual actuation

This work also demonstrated the technical feasibility of coupling two pneumatic turbines via a common shaft to receive a dual-actuation system for MRE. The frequency of the obtained vibrations was in a feasible range for mechanical shear waves applied during MRE. Through the coupling approach, the phase relationship of both turbines could be controlled. A past study implemented a phased-array acoustic driver system capable of applying independently controlled wave forms to each of the eight channels [32]. The invasiveness of this approach

might be a hindrance in its transfer to clinical studies. Another study employed membrane actuators for in vivo prostate MRE [163]. Two actuators were placed posterior to the patient's pelvic region, another was placed anterior to the pubic symphysis. As those drivers are vibrated with air pressure pulses generated outside the scanner room, the influence of phase lags due to tubing lengths remains unknown.

The large surface actuation distributed the generated mechanical waves over a large body surface. Naturally, the design would also be realizable with a larger single turbine. However, coupled turbines allow for a smaller geometry of each turbine and a possible placement in the loops of commercially available surface coils. Future studies should investigate the influence of bent base plates. Analogously to focused US imaging, the wave fronts could be focused through a curved transmission plate, which increases the wave amplitude in the ROI as geometric dispersion of the waves is decreased.

The results of this work demonstrated that the actuator is a suitable alternative to the conventionally used pneumatic cushions. By using centrifugal forces instead of sound pressure levels, the pneumatic vibrator offers an elegant solution for sufficiently large wave actuation at higher frequencies compared to air cushions where the amplitude of sound pressure waves decreases with increasing frequencies.

5.2 Linking the Actuator to the MRI System

After the development of an actuation system, the second aim was its implementation on a clinical MRI whole body scanner. Firstly, the GRE sequence of a WiP package provided by a vendor was employed. As discussed in the following, it had several shortcomings, which is why the development of motion encoding sequence based on the SE-EPI was pursued during this work. At last, considerations for the future post-processing of the acquired MRE data are discussed.

The GRE based MRE sequence

The provided WiP package had the major advantage of an implemented post-processing work-flow at the host computer of the scanner. However, several disadvantages limited the application of the WiP package during this study. The sequence was proprietary and its MEG was fixed to a single actuation frequency of 60 Hz with an unknown MEG strength. The sequence could not be synchronized to third party actuators. Furthermore, the sequence was only implemented on a single scanner and could not readily be installed on another scanner. This will restrict future comparative studies with multiple devices or at multiple centers and limit the type and size of patient cohorts.

The post-processing unit of the WiP package included a wave inversion algorithm that reconstructed an elastogram of the acquired data. According to the manufacturer, the local wave length at any given pixel is calculated based on the pixel surrounding. The resulting stiffness map is deemed the most meaningful if the tissue is homogeneous in an area with a radius of at least 1 cm. This is rather large for the detection of smaller lesions. However, the assumption of a homogeneous distribution is deemed necessary to avoid partial volume effects [192]. Furthermore, the reliability of the results depends on the amplitude of the induced mechanical waves. Other parameters influencing the quality of the results are motion of the patient, an incorrect placement of the driver for liver imaging, or image acquisition with breath-holding in the end expiration phase.

Past studies used GRE based MRE sequences, e.g. for measuring kidney stiffness [2, 228]. Notably, slices with a large thickness of 10 mm were employed during those studies. The standard acquisition time of the GRE sequence is rather long with 28 seconds (accelerated 22 seconds with PAT2) for a single slice and one motion encoding direction only. According to Huwart et al. this might pose a problem for the clinical application of 3D MRE.

Four dynamic acquisitions per direction multiplied by three spatial directions need to be acquired for a full 3D data set of the wave propagation, resulting in a long acquisition time [3]. For example, during this thesis it took more than 4.5 minutes to encode 10 consecutive slices with one spatial wave direction with the GRE sequence; yielding a total acquisition time of over 13 minutes for a full 3D data set.

Also, using a GRE based method requires the acquisition of two images with opposing MEGs (positive and negative) to calculate a phase difference image. This may further result in motion artifacts, if the image acquisition time is not significantly shortened [3]. Moreover, acquisition time increases if images are acquired under breath-holding, depending on the respiration rate of the patient and the gating efficiency as the images need to be synchronized to the expiration phase to avoid motion problems [3].

The GRE based sequence was also found to be sensitive to a higher magnetic field strength. A comparison of technical failure rate of MRE with a 2D GRE pulse sequence has demonstrated a substantially higher failure rate at 3 T (15.3 %) compared to the failure rates at 1.5 T (3.5 %) [221]. The stated reasons for failure included the use of 3 T, beside patient specific factors such as body mass index and liver iron deposition. A probable reason is the increase in susceptibility artifacts at 3 T [223, 224] because they increase signal loss and rephasing [225], which in turn might decrease the quality of the wave image.

Development of an SE-EPI based MRE sequence

Numerous approaches were proposed to accelerate MRE acquisition. Alternatives to the GRE based sequences are a fractional GRE, fast spoiled GRE, balanced steady-state free precession (BSSFP) or single shot EPI pulse sequence. Fast spoiled GRE and BSSFP have, for example, been employed for liver MRE before [21, 22, 91, 229]. Single shot EPI sequences have been used for brain MRE [139] or liver MRE for staging of liver fibrosis [20]. An SE-EPI based sequence approach was chosen for this work and an additional MEG was implemented in the sequence. The rationale is discussed in the following paragraphs of this section.

Huwart et al. demonstrated that MRE of the liver could be performed with a SE-EPI sequence [3]. The acquisition time was substantially decreased by using breath-hold EPI and was found to yield an equivalent diagnostic ability through better wave encoding with fewer artifacts and wider anatomical coverage compared to conventional SE or GRE imaging [3, 41, 122, 126]. Those are important factors for the integration into clinical practice and the implementation of an SE-EPI based sequence is recommended [221, 228].

Using comparable imaging parameters, acquisition time was significantly decreased from 28 seconds to 14 seconds for a slice transverse slice orientation with a single motion encoding direction. Thus, acquisition time was halved compared to the previously employed GRE sequences. This enables image acquisition also for patients that cannot tolerate longer breath-holds.

Using the developed SE-EPI sequence, an encoding of all three wave directions in a 3D volume covering the whole liver triples acquisition time resulting in 42 seconds. This is only a minimal extension of the examination time and will facilitate the incorporation of an MRE examination into a standard MRI imaging protocol and increase patient acceptance.

There are multiple possibilities to increase image quality. For one, a reduction of acquisition time is critical for the reduction of inherent EPI artifacts to obtain less blurred images due to T_2^* effects. Stronger and faster gradients would decrease sequence encoding time. The slew rate of the Trio scanner was limited to a maximum of $27 \frac{\text{mT}}{\text{m}}$ due to software restrictions. Other groups employed gradients with a slew rate as fast as $60 \frac{\text{mT}}{\text{m}}$ [163]. A higher slew rate further reduces T_E and thus overall acquisition time as well as artifacts. However, there are limits on the practically usable slew rate, as peripheral nerve stimulation may be induced above certain thresholds [230]. For another, k-space filling could be optimized, as suggested by [42], since the main information of the MRE phase image is located around the center of k-space. The developed SE-EPI based sequence already included the option of fractional encoding of the mechanical wave using the higher harmonic encoding scheme, which is important to further accelerate image acquisition time [229]. During fractional encoding, the frequency of the motion encoding gradient is higher than the actuation frequency of the mechanical wave. For example, a second or third harmonic of the mechanical wave is encoded. This approach further reduces T_E , as the length of the MEG is decreased. Using second harmonic encoding, the encoding time of the MEG is halved compared to a first harmonic MEG with the same frequency as the mechanical actuation. Fractional encoding also enables multi-frequency [231, 232] and multi-directional [233] sequences. Both strategies aim to reduce the number of acquisitions. The encoding over multiple frequencies allows to obtain data about the frequency depended elasticity parameters. For example, not only the shear modulus but also the loss modulus can then be reconstructed.

Trigger implementation to synchronize the actuator to the scanner

The sequential triggering for capturing multiple images with variable delay is particularly desirable as it allows the wave to be displayed realistically on a continuous basis. This plays an important role in obtaining diagnostically relevant data. Other hardware, such as the pneumatic cushions, usually employ a trigger that synchronizes the vibration of the cushion to the imaging sequence. As the ramp-up time of the developed turbine took up to 30 seconds, an inverse trigger pathway was designed for this work. Here, the trigger synchronized the imaging sequence of the scanner to the phase offset of the unbalance in the rotating pneumatic turbine. This trigger pathway is not expected to cause any delay compared to the conventional approach.

A simulation of the set-up in the laboratory demonstrated the feasibility of the driver to start a synchronized imaging sequence. The signal was processed without any loss of information and the delay between the ADC unit of the light sensor, micro-controller and COM port at the computer was in the range of $10 \mu\text{s}$ to $20 \mu\text{s}$. The delay is sufficiently short to not influence the triggering.

Three possibilities were considered for feeding the trigger signal to the host computer of the MRI scanner. The first one was the input/output port directly at the scanner designated for external triggering. It was the easiest technical implementation as it was the designated port for external trigger. However, the signal from the active driver in the control room needed to be led back to the scanner room with an approximately 5 m long cable, which slightly increased the set-up time. The second possibility was the COM port at the host computer in the control room. It significantly shortened the cable from the active driver to the host computer, as both devices were located in the control room. The last possibility was the COM port at the system hardware computer in the utility room. As the utility room was located even further away, this would have significantly complicated the driver set-up. At least, the software and port design active driver allowed the implementation of all three options. However, the trigger signal was not recognized at the host computer of the scanner using the COM port approaches, despite a working sequence simulation. As a consequence, the sequence did not start after the input of the trigger signal. In contrast, the input/output port at the scanner recognized the external trigger signal and this solution was implemented for the synchronization of the sequence to the actuator.

Elasticity reconstruction

The shear modulus is a physical quantity and it describes the response of incompressible material to shear strain [234]. An external dynamic vibration causes tissue displacements in the ROI, which are imaged by the motion encoding MRE sequence. Assuming incompressible materials, longitudinal waves practically do not exist as they propagate too fast to be imaged. Yet, shear waves propagate with finite speed and can be imaged [235].

To determine the elasticity distribution, an inverse problem must be solved. The wave equation for linear, isotropic, elastic materials is often used for this inverse problem as it is the equation that links the visco-elastic properties of the material with the displacement data [236, 237]. Based on the wave images, an elasticity map is created depicting the shear modulus at each point calculated by the wave equation [50].

Various algorithms have been developed to reconstruct the distribution of shear moduli within the ROI [23, 134, 137, 138, 238, 239]. During this work, two post-processing work-flows were employed, both based on the established LFE algorithm.

Reconstruction based on the LFE: The first reconstruction algorithm was incorporated in the WiP package. A limitation is the required assumption of tissue homogeneity. Studies showed that the spatial heterogeneity of in vivo tissue must be considered when estimating an isotropic shear modulus [60, 61, 240]. McGrath et al. showed that the errors occurred at tissue interfaces due to the violation of the local homogeneity assumption of the direct inversion algorithm [240]. This is especially true, when the wave lengths are longer than the

locally homogeneous regions [61]. Arani et al. noted that the LFE algorithm is not capable to give accurate stiffness values until half a wave length is included inside the boundary of the ROI [241]. A further limitation of the LFE algorithm is that it does not account for wave attenuation [241].

After image acquisition of the SE-EPI sequence, the software MRE/Wave was used for elasticity reconstruction. The software also employed the LFE inversion algorithm. A major issue were phase wraps in the acquired phase images. Although the software already employed phase unwrapping algorithms with reasonable outcome, phase wraps should in general be avoided. During measurements, the MEG had to be adjusted for every actuation frequency as the amplitude at the surface differed for various frequencies. In general, a large amplitude at the surface also increases the amplitude in the deep ROI and a sufficiently high amplitude is needed for an adequate reconstruction [167]. Either excessive actuation amplitude or MEG strength could cause phase wraps [132]. The displacement phase gradients were also found to be increased near soft/hard interfaces, higher in areas of relatively softer tissue and also affected by the object and deformation geometry. Those excessive phase wraps could lead to areas of significant signal loss analogous to flow dephasing in conventional MRI. The resulting reconstruction would suffer from this signal loss [7].

Extension to a three dimensional reconstruction: Image acquisition and reconstruction during this work was confined to 2D data. Both the GRE and SE-EPI sequence allowed the acquisition of multiple slices, but only a 2D shear modulus reconstruction within an individual slice in a single motion encoding direction. In the future, an extended sequence could include motion encoding in all three directions (slice, phase, and read out) - an important step to 3D wave inversion, where the shear wave propagation needs to be recorded in three orthogonal spatial directions to obtain the complete 3D displacement vector [50]. 3D data acquisition and elasticity reconstruction may improve the accuracy of the elasticity distribution compared to a 2D reconstruction.

A 2D algorithm assumes that the shear waves propagate in parallel to the imaging plane and ignores that shear wave propagation is typically more complex [242]. This may lead to an overestimation of the wave length of waves that obliquely intersect the imaging planes. More complex in vivo geometries increase the probability that out of plane components could be neglected [7]. Consequently, the shear modulus in the ROI could be overestimated [243, 244]. For example, Morisaka et al. observed that a measured lower stiffness in the liver was caused by the 3D processing procedure [122]. The differences were found to be in a range of approximately 5% to 10% in a soft phantom and 19% to 20% in a stiff phantom as well as in vivo liver with high stiffness value [122].

Thus, a 3D wave acquisition over a 3D volume and 3D inversion is an obvious solution. However, this increased accuracy comes at the expense of increased scan time [7, 242], questioning its practical feasibility for clinical routine. The use of EPI read out for SE sequences shortens total acquisition time [7]. This is another reason why an MEG SE-EPI sequence was

developed for this work. Further, Corbin et al. proposed to use only three phase offsets. This is the minimum number required to apply the discrete Fourier transformation motion according to the Nyquist Shannon sampling theorem. The acquisition of fewer phase offsets then naturally reduces the total acquisition time [245].

Extension to an anisotropic visco-elastic model: The elasticity reconstruction models during this study were rather simplistic in terms of anatomic and material assumptions. A large area around the reconstructed pixels was assumed to be homogeneous tissue and the tissue itself was expected to be purely elastic, which was a valid approximation for phantom MRE. These assumptions are also employed in MRE reconstruction, e.g. for brain MRE [246] or kidney [247]. However, it has been established that soft biological tissues not only exhibit purely elastic properties but also contain viscous elements [10]. The modeling of visco-elastic behavior is not trivial and the choice of an appropriate model may affect the results [248]. Commonly, the Voigt and Maxwell model are employed. The Voigt model has been found to be suitable for describing visco-elastic properties of tissue in the low frequency range, i.e. 50 Hz to 500 Hz [249, 250, 251, 252]. Furthermore, the attenuation of the shear waves are included in the Voigt model; the dissipative effects that limit the penetration depth of waves in MRE are taken into account [9, 72]. The Maxwell model is also used by research groups but more applicable to fluids than to solids [72].

The assessment of all unknown parameters for the most accurate depiction of the elasticity tensor is not feasible during MRE. In general, the tensor consists of 21 independent quantities and cannot be solved by the current number of equations provided by MRE experiments [72]. The accuracy of the reconstructed shear moduli may also be increased by including certain anisotropy assumption as the local value of elasticity of biologic tissue is different in different spatial directions [10, 161]. The model used during this work assumed complete isotropy, which was feasible considering the phantom material. In vivo however, tissue anisotropy may influence the directions the waves follow locally [235]. Gennisson et al. observed for USE that shear wave speed travelled approximately two times faster parallel to the fiber compared to the perpendicular direction, resulting in different reconstructed shear moduli for both directions ($\mu_{\parallel} = 5.86$ kPa, $\mu_{\perp} = 1.58$ kPa) [250]. Qin et al. found similar results in a muscle sample and concluded that an isotropic model might average the storage moduli for all directions [14]. Although the impact might be smaller for rather isotropic tissue such as liver, anisotropy might partly account for variations in future stiffness measurements in other organs such as brain or kidney [247] and should be considered in future reconstruction approaches.

Implementation of other inversion algorithms: The implementation of other inversion algorithms might also be considered. For example, Kwon et al. presented a method without the assumption of local homogeneity [253]. Further, it also required only a single differentiation of data. This is advantageous in contrast to the direct algebraic inversion method [254], which requires a double differentiation of the measured displacement data prone to increase noise [253]. Also, the complex shear modulus is a frequency dependent quantity. Thus, frequency dependent wave quantities could be adapted to the rheological models at multiple frequencies [75, 233].

5.3 MRE Image Acquisition

The third aim was MRE image acquisition of phantoms and in vivo. Silicone-based materials served as tissue-mimicking material for the design of anthropomorphic phantoms. The actuation system was firstly evaluated on these phantoms and proved its feasibility of generating shear waves for MRE image acquisition. Finally, an in vivo set-up was successfully tested on the liver and prostate as a proof-of-principle.

Material Studies - Rheometric Evaluation of Silicones

In this work, silicone-based materials were examined for their suitability as MR-compatible tissue-mimicking material for MRE image evaluation. Silicone samples were analyzed with a strain controlled rotational rheometer in the range of 30 Hz to 100 Hz. This frequency range covers the range that was later employed during MRE imaging. The rheometer yielded especially reliable results in the lower frequency regime. As an actuation frequency of 60 Hz is commonly used during MRE, the rheometer proved as a reliable validation technique.

The performance of the rheometer became increasingly unstable at frequencies above 80 Hz [243, 255]. This phenomenon has similarly been observed at other mechanical tests such as dynamic mechanical analysis (DMA). Frequencies above 100 Hz could not be evaluated due to hardware restrictions of the rheometer - an issue also faced by other research groups [256, 257, 258, 259, 260, 261]. A comparison of rheometric testing and MRE results at frequencies over 100 Hz would need to be performed by extrapolation rheometric results to higher frequencies, with a restricted validity of these results.

Prior to shear modulus measurements, the linear domain of the material was determined with a strain sweep experiment. It confirmed that the testing was conducted in the linear visco-elastic region of the materials. This is in accordance to other phantom studies [237, 248]. For example, the use of a linear visco-elastic model on gelatin phantoms [248] and soft tissue [262] has been suggested.

A minimum shear modulus of 1.21 kPa was measured for SF00 diluted with 71 % SF-V50 at a frequency of 60 Hz. The measured shear moduli of the silicone samples are in the range of human soft tissue values reported by literature MRE measurements (Table 2.1 and Table 2.2) and ex vivo bio-mechanical tests [14, 63, 263, 264, 265]. Increasing concentrations of silicone oil led to an decrease of the shear modulus. The stiffness of silicone could be manipulated to mimic the desired stiffness for phantom material fabrication.

The standard deviation due to manufacturing uncertainties and the standard deviation during measurements were smaller than 0.11 kPa and 0.21 kPa, respectively. This is a percentual deviation of $\pm 2\%$ and $\pm 4\%$. A commercial liver fibrosis phantom (CIRS shear wave liver fibrosis phantoms, model 039) was stated with a a precision of $\pm 4\%$ [266]. Thus, the deviations of

the samples manufactured during this work are in agreement with the data provided from the commercial CIRS phantom.

The influence of sample geometry was also evaluated. Two cylindrical samples with different diameters were cut and tested for diameter dependent resonance effects. The frequency dependent shear modulus curve exhibited a high degree of variability. As already observed for gelatin samples in a past study, this might be caused by hardware limitations and inherent variability of the material [237]. For example, it is possible that slipping took place at the interface of the sample and rheometric testing plates. Despite visual observation via a camera of the sample during testing, surface effects might have occurred that were visibly undetectable. Their influence could be decreased in future experiments with the use of roughened plates with a sandpaper or teeth plate geometry. Another alternative is either the use of a sandwich DMA device, which evaluates a sliding shear instead of the rotational shear, or the use of a DMA torsion test, which evaluates the E-modulus of samples. The E-modulus could then be converted to the shear modulus G with the simplification of $E = 3G$.

Silicone as an alternative to gelatin and PVC

Other studies have presented gelatin or PVC as tissue elasticity mimicking materials. Richards et al. presented a phantom made with 7.1% gelatin solution and inclusions with higher concentration of gelatin resulting in an elevated stiffness resembling tumors [237]. Gelatin requires heating the gelatin-water mixture within a specific temperature range during manufacturing and maintaining this temperature until all particles are dissolved. The cooling down period also needs to be controlled to ensure a known concentration of gelatin dissolved in water. Gelatin-based phantoms also need to be kept in air-tight containers to limit water loss, which would stiffen the phantom. Furthermore, the gelatin may exhibit a high variability of stiffness depending on the temperature at which it was tested [267].

The manufacturing process of PVC phantoms is rather complex. The material required heating between 150 °C and 175 °C during fabrication and a curing time for more than 90 days to ensure stabilization of the mechanical properties of the material [268]. Therefore, silicone was chosen as the main tissue-mimicking material over other classical phantom gel-like materials such as gelatin or PVC. These outlined steps in the manufacturing process would limit the criterion of reproducibility.

Extension to multi-modal imaging

The imaging characteristics of the phantom could be extended for multi-modal imaging, e.g. by introducing scatter particles in the material for US imaging. For example, silica particles can be suspended in gelatin. It was shown in a past study that the particles served as scatterers and a reproduction of a full speckle image has been possible [237]. During this work, two types

of scatter particles (graphite or silica beads) were included in material samples. Rheometric testing showed that the scatter particles increased the shear modulus by 12.5% to 15.3% but the shear modulus of the samples were still in the range of human soft tissue. Hence, it will be possible to extend the phantom design to a multi-modal phantom for MR and US elastography by suspending scatter particles in the silicone.

Design of anthropomorphic tissue-mimicking phantoms

During this work, tissue-elasticity mimicking anthropomorphic, MR-compatible phantoms for MRE evaluation were designed. After the fabrication of a preliminary prostate phantom as a proof-of-principle, a complex prostate phantom and an abdominal phantom were manufactured. The elasticity of the silicone depended on the amount of added silicone oil as determined by the rheometric testing. For example, the elasticity values obtained from the elastogram in a ROI in the liver of the abdominal phantom were in accordance to literature human liver elasticity values, e.g. (2.20 ± 0.31) kPa and (1.95 ± 0.06) kPa [147, 176], respectively. Less silicone oil results in a higher stiffness and a closer approximation to literature values. Using silicone as the main component, it was possible to manufacture customized shapes. The silicone provided sufficient signal for MRE imaging with the motion encoding SE-EPI sequence. Furthermore, the liver could be clearly distinguished from the filling material. The included rib cage allows the evaluation of influences due to rigid structures in the future. The silicone phantoms could easily be stored, especially compared to gelatin phantoms that need to be kept in air-tight containers to limit water loss.

Overall, this work demonstrated the fabrication of phantoms with known elasticities and arbitrary shapes. The manufacturing work-flow was designed to be simple and repeatable. Since commercial phantoms contain proprietary material and their design can only be customized at high costs, the silicone-based custom-made phantoms offer an excellent alternative.

MR Elastography - Phantom Studies

The prostate phantom

The technical feasibility of the dual actuation system for mechanical wave generation during MRE was demonstrated with the MRE image acquisition of phantoms. The actuator was easy to set up and did not interfere with the imaging procedure. The complex prostate phantom was firstly imaged with the GRE based sequence.

One elastogram was obtained in a transverse slice of the prostate phantom. It showed increased stiffness above 8 kPa in the area of the two inclusions. However, these values were not in accordance to the measured values of 5.17 kPa (prostate) and 7.29 kPa (bladder) during rheometric testing. Furthermore, the implementation of a trigger to synchronize an external actuator to the sequence was not provided. As a consequence, a quantitative elastogram could not be reliably reproduced.

Using the SE-EPI sequence, MRE images could be obtained at multiple frequencies. The applicable range was from 30 Hz to 120 Hz. Also, the strength of the MEG could be freely adjusted with a maximum strength of $25 \frac{\text{mT}}{\text{m}}$. To optimize MRE image acquisition, it is important to adjust the MEG to the mechanical waves induced by the actuator. A complete penetration of the wave in the ROI with sufficient spin displacement is desirable. As the amplitude of the mechanical wave depends on the rotational frequency, the MEG needs to be adjusted for each frequency.

The actuation system was evaluated at four driving frequencies. The line profile of the motion encoded phase image at four actuation frequencies showed decreasing wave lengths for increasing frequencies, as expected.

The influence of larger or smaller eccentric weights for the actuation amplitude as well as a bi-frequency excitation with two differently designed eccentric weights in a turbine could be explored in future studies. Differences between the phantom and in vivo application also need to be considered. At least, the parameters do not usually have to be optimized for the individual subject [121].

The outer geometry of the prostate phantom was relatively small compared to the abdominal phantom and in vivo applications. This led to shear wave reflections off the walls of the phantoms. These and mode conversion of shear waves to longitudinal waves between interfaces in the phantom might affect the accuracy of future reconstructions [241]. Dittmann et al. also suggest to mechanically decouple phantoms from the MRI scanner to avoid residues of vibrations in the reconstructed wave images due to scanner vibrations [269]. As a consequence, a second phantom, the abdominal phantom was manufactured. Wave reflections were minimized in the larger phantom, where the shear waves were attenuated in the phantom before reflecting on the outer boundaries.

The abdominal phantom

The SE-EPI sequence was also employed for MRE image acquisition with the abdominal phantom. Shear waves propagated in the phantom and wave length differences in the filling material and liver were consistent with the expected results. The strength of the MEG gradient was varied from $5 \frac{\text{mT}}{\text{m}}$ to $20 \frac{\text{mT}}{\text{m}}$ at four actuation frequencies. Phase wraps were already observable at $5 \frac{\text{mT}}{\text{m}}$ for 50 Hz and were increasing for higher gradient strengths. In

contrast, phase wraps were only visible at an MEG strength of $20 \frac{\text{mT}}{\text{m}}$ at an actuation frequency of 80 Hz. This demonstrates the importance of adjusting the strength of the MEG to the rotational frequency of the actuator.

Lower frequency mechanical waves are less attenuated than waves with a higher frequency [117] as the dissipative effects in visco-elastic soft tissues limit the penetration depth of waves in MRE [9]. These frequencies are deemed applicable for sensitive body parts such as the head, as MRE in a range below 25 Hz overcomes damping problems and uncomfortable stimulation for the patient [269]. However, a higher frequency yields a higher spatial resolution, especially important for the detection of smaller inclusions or MRE acquisition of smaller organs, e.g. prostate or kidney.

The actuation system demonstrated the possibility to induce waves at various frequencies in the range of 30 Hz to 150 Hz, making it suitable for a wide range of future applications. As the magnitude of the shear modulus is significantly larger at higher frequencies [270], multi-frequency data acquisition is important for accurate rheometric modeling in the future.

The dual source actuation demonstrated a different wave propagation pattern compared to a single actuator, especially in the peripheral regions of the phantom. The dual actuation set-up promises a more homogeneous shear wave propagation through larger volumes of interest as the effects of geometric dispersions are minimized. Further, the ROI is illuminated from different directions, which increases the phase signal. This should result in more accurate stiffness estimates, as high-amplitude shear waves tend to be less noisy and a more uniform illumination of the ROI improves the quality of the elastogram [32, 170].

More research is required to determine the effects of constructive or destructive wave patterns caused by two, or more, actuators. Zheng et al. demonstrated with invasive twin needle drivers that wave patterns were different compared to those of a single driver as the twin driver generated an interference pattern of waves [170]. Future work will thus include an evaluation of different phase offsets of the unbalances with respect to each other. Especially the potential effects on the wave amplitude within small regions due to unintentional destructive interference should be studied [32].

The centrifugal force increased quadratically with the actuation frequency. Thus, the pneumatic vibrator generated a sufficiently large amplitude at higher frequencies. This makes it an alternative to conventional pneumatic cushions. Those cushions can also be set in series, however varying length of long compressed air tubes to each cushion and other interfering factors might cause a phase delay of the shear waves with respect to the actuators.

MR Elastography - In Vivo Studies

After successful phantom MRE image acquisition, the same set-up was applied to in vivo measurements on volunteers. The set-up of the actuator was well tolerated by the volunteer, which was ensured with upheld communication during start-up of the vibration. A progressive ramping of the vibration from 0 Hz to the actual vibrational frequency was incorporated as suggested by [271, 97]. This avoided an abrupt transition from rest to full vibration that could startle patients and decrease overall acceptance.

Despite promising results during phantom measurements, the MRE in vivo data obtained during this study need major improvements. The GRE sequence is already known to be vulnerable, e.g. to the effects of iron deposition in the liver, and showed a higher failure rate of liver MRE compared to SE-EPI sequences [125, 244]. The iron deposition decreases the signal intensity of the liver due to a reduced T_2^* [122]. As an external trigger synchronization could not be achieved with the GRE, only two sets of images could be obtained: (1) without mechanical actuation, (2) with mechanical actuation but without triggering. The first set of images already displayed a high degree of artifacts in the magnitude and phase images. The resulting images of the second set were not usable due to excessive motion artifacts caused by the lack of synchronization.

Images acquired with the SE-EPI sequence yielded very little signal during in vivo measurements. Past research compared SE and EPI sequences and concluded that the EPI sequence maintained image quality and diagnostic performance of MRE for staging liver fibrosis all while decreasing data acquisition time [272]. This is in contrast to another study that states EPI readout to be associated with geometric artifacts and enhanced susceptibility due to residual motion from the patient, e.g. through breathing or peristalsis. This is in accordance to our results. Thus, future work must include an improved image acquisition scheme of the SE-EPI yielding more signal during in vivo measurements. As priorly mentioned, this might be achieved through an accelerated image acquisition time using higher harmonic encoding of the mechanical wave [229].

Location of actuation source

For liver MRE, the base plate was placed against the lowermost ribs of the volunteer who lied in a supine position. Past research has shown that locating the actuation source at the ribs (termed the trans-costal approach) yields better wave propagation through the liver than a sub-costal approach [50]. The actuator creates compressional waves that propagate through the liver and shear waves are obtained by mode conversion at tissue interfaces [50]. The trans-costal excitation yields waves that propagate almost completely through the whole liver. The subcostal actuation only covers the interior part of the liver. These different characteristics could be caused by the ribs as they might function as wave sources according to the Huygen principle [121].

The effect of these wave sources could also be studied using the abdominal phantom, which included a rib cage with a well-known geometry. The validation of these results in an *in vivo* setting remains an important goal. The accuracy of the stiffness measurements in phantoms will always be limited by the general phantom design. Wave interference patterns are more likely to be caused in a phantom as the waves are prone to be reflected off the walls of the phantom. These reflections are not expected to be a significant factor *in vivo* because of the high attenuation of shear waves in tissue and should remain an intrinsic limitation of phantom studies [37].

For prostate MRE, the base plate was placed ventral to the pubic bone, as suggested by Kemper et al. [107]. During their study, the volunteer was in prone position to use the body weight for sufficient contact pressure of the transducer to the pubic bone. This is in contrast of the set-up during our study. Here, the volunteer was in supine position and Velcro straps fixated the base plate above the pubic bone to ensure sufficient contact.

In general, the placement of the actuator during prostate MRE remains a challenge. Different techniques have been suggested in literature and include transurethral [241, 273], endorectal [96, 274], and transperineal [18, 275] actuation. The first two approaches are invasive. Although they allow the application of higher mechanical frequencies, the patient acceptance rate is lower and less suitable for screening examinations than for externally placed drivers [163]. Surface drivers have difficulties achieving sufficient shear wave propagation in the prostate gland due to the central location of the prostate in the pelvis leading to damping [273]. This limits the applicable upper mechanical actuation frequency. One study has stated an excitation frequency of 65 Hz to be a suitable compromise between resolution and attenuation [107], although this frequency might still be too low to resolve stiffness details of highly heterogeneous prostate tissue in small tissue volumes [163].

Thus, large amplitudes at the surface would help to achieve sufficient amplitude in the deep ROI [167] as attenuation is a continuous decrease of the amplitude as a function of distance to the source of excitation [107]. Using the developed transducer, higher amplitudes at lower frequencies could be achieved with an increased eccentric mass within the turbine. Amplitudes at higher frequencies are intrinsically increased, as the generated centrifugal force proportionally increases with the square of the frequency. This is an advantage to other actuation systems; for example Rouviere et al. stated that they could not employ frequencies higher than 76 Hz because their driving system did not induce sufficient displacements at higher frequencies [157].

Multi-frequency actuation during MRE

Actuation frequencies applied *in vivo* were adjusted in a range of 40 Hz to 100 Hz with the presented driver. However, the maximum pressure output and thus maximum rotational frequency was not reached as it was not the scope of the study to test the maximum vibrational frequency *in vivo*. A rise in the lower limit is most likely due to a more secure fixation of the

actuator on the abdomen to ensure a safe operation during volunteer measurements. The upper frequency limit of 100 Hz was deemed sufficient for this in vivo feasibility study.

In general, multi-frequency data acquisition will be necessary in the future. Measured tissue stiffness is frequency dependent due to the dispersive and visco-elastic properties of soft tissue [161, 247]. The viscous effects vary with the strain rate [10]. In literature, *shear stiffness* often describes the shear modulus from the measured velocities of waves ($\mu = \rho c^2$) and this assumption is only valid in purely elastic tissues [25, 110, 161]. To fit more complex rheologic models, multi-frequency MRE data need to be acquired.

Optimized image acquisition time

A volunteer was scanned with the developed SE-EPI sequence for liver MRE. The SE-EPI recorded the liver volume two times faster than the GRE sequence. This will facilitate incorporation of MRE image acquisition into clinical protocols as the additional imaging time is decreased. Furthermore, the longest breath-hold interval was decreased from 28 seconds to 14 seconds. This will improve patient cooperation during breath-holding and decrease motion artifacts. These residual motion artifacts appear as band-like structures [3] and may decrease the accuracy of the reconstruction elastogram. These are further pronounced with GRE sequence, as the application of imaging gradients has been observed to cause phase incoherences between imaging shots due to the mechanical vibration induced by the imaging gradients [232].

MRE in comparison to other approaches

MRE is not the only medical technique that can be used for the quantification of tissue stiffness and that can act as a surrogate for the diagnosis and staging of diseases. Other methods include the invasive biopsy [50], which is a reference procedure, and other elasticity imaging methods such as the noninvasive US based transient elastography [276, 277, 278], which employs the dispersive characteristics of soft tissue to quantify both tissue elasticity and viscosity [23, 161, 231, 279, 280].

Biopsy: A biopsy of the liver or the prostate are gold standard examinations for the detection and staging of liver fibrosis or prostate carcinomas [50]. Although biopsies have been a standard diagnostic tool, it is an imperfect histologic reference [281]. It is an invasive procedure with a potential risk of complications and it raises concerns about tumor spreading [282]. Its accuracy depends on the sample size and is influenced by the sampling variability due to the heterogeneity of the organ, e.g. considering liver or prostate [50, 283, 284, 285]. Morisaka et al. showed that the diagnostic accuracy of liver fibrosis staging using MRE was equivalent to that of liver biopsy [283]. A key limitation for the cross validation of the MRE data with

tissue elasticities obtained from histopathological samples is the time between MRE evaluation, sample harvesting and mechanical testing. The effects of anoxia, cell death and autolysis as well as an inevitable fixation process alter the cells and tissues and influence their mechanical parameters [161, 275].

Ultrasound based transient elastography: A major advantage of USE is that it is relatively fast, less claustrophobic for some patients and is available for patients where MRE is contraindicated [286]. However, USE usually only allows sufficient spatial resolution in the axial plane and is limited to two dimensions [107]. It is also restricted by the acoustic window required for US-based techniques [117]. In contrast, MRE is capable of measuring the displacement in all three dimensions and covering a larger overall volume [107]. Liver MRE can also be performed in obese patients and those with ascites [50]. As MRE is capable of measuring the full 3D displacement vector, the data allow for a more precise analysis of visco-elastic parameters [50, 107]. USE measures the shear wave velocities by pressing the US probe to the body. The applied pressure may differ by the operator. This could change the measured velocities as the stiffness of liver tissue might increase with increasing probe compression [287].

Some cross validation between MRE and USE has been made in tissue mimicking phantoms [195, 288] and for the evaluation of liver fibrosis [195, 289]. Yet, an entirely suitable gold standard method to validate the quantified tissue elasticity during MRE is lacking [161]. Differences in elasticities could result from the intrinsic differences of the medical devices, their different shear wave excitation methods and the differences in the inversion algorithms between USE and MRE [288].

MRE data acquisition of other organs

This work focused on two, organs liver and prostate. The liver is the most established organ for MRE and data acquisition is facilitated through the larger volume, mostly homogeneous tissue and closeness to the body surface. The prostate is a more challenging organ due to its small volume and location deep within the body. Research has also been extended to other organs such as brain [243, 290, 291, 292], heart [293, 294], kidney [247, 286, 295] and breast [296, 297] and will certainly be subject to future investigation. Further studies also examined organs such as the thyroid [160, 298] and the pancreas [227, 299].

Every organ poses unique challenges such as varying tissue structures, small overall volume, its location within the body, low intrinsic SNR as in the lung, or inherent motion as in the heart. The transfer of hardware design, sequence protocols, and reconstruction algorithm needs to be adapted to every organ and remains a vast research field.

Integration of MRE data acquisition during clinical MRI

MRE examination can be performed on most contemporary MRI systems, such as a 1.5 T (or higher) whole body MRI scanners [50, 247], which is available in many radiologic departments. Practical limitations are the same as for conventional MRI examinations, e.g. claustrophobic patients or certain active implants. The diameter for patient positioning within the bore is further slightly decreased by the presence of the actuator, but excludes only very obese patients [50]. Future research should include an investigation, if MRE parameters yield an equivalent diagnostic accuracy to currently used contrast-agent based protocols. Thus, the use of gadolinium contrast agents might be reduced or enable previously excluded patients with renal impairments [96, 300, 301, 302] to obtain better diagnostic results.

The clinical value of liver MRE: Many studies in MRE have focused on the characterization of liver tissue to provide an alternative to the invasive biopsy that serves as a reference standard. It has been shown that MRE is capable of non-invasively evaluating and staging liver fibrosis [3, 19, 20, 21, 22, 23, 50, 146, 303], as the shear elasticity of the liver increases according to the stage of liver fibrosis [304]. The assessment and continuous monitoring of patients with chronic liver disease is often needed. The technical success rate of MRE examinations in a study by Huwart et al. was 94 % overall and is higher than the success rate of USE (84 %) [305]. Failed examinations can also be repeated since MRE is non-invasive [283].

Studies are less clear, however, about the evaluation of cirrhosis. Here, tissue abnormalities were found to appear earlier in the left lobe, implicating that the mean shear velocity could be different in the left and right liver lobes [287]. This stresses the importance of acquiring MRE data of the whole liver volume. Moreover, elasticity maps have appeared more heterogeneous with increasing fibrosis [50, 122], emphasizing the need for accurate reconstruction algorithms. Only few studies have examined the role of MRE in the diagnosis of liver tumors [306]. So far, it has been shown that malignant tumors have a greater elasticity than benign ones [28]. In another study, mainly an increased viscosity in malignant tumors relative to benign tumors has been stated [307]. It is hypothesized to be due to disorganized vascular structures, which abnormally attenuate the shear waves [234]. Thus, more elaborate rheometric models might be necessary in future studies for an accurate reconstruction. In the future, MRE of liver tumors could assess the tumor response to treatment [128].

The clinical value of prostate MRE: Multi-parameteric MRI of the prostate is already clinically significant for the detection of PCa [99, 102]. However, accuracy in the detection and staging of PCa was reported to vary widely [308, 309]. Thus, it seems feasible to append an MRE examination to already existing imaging protocols to obtain another independent parameter [96, 107]. The information on mechanical properties might further increase the sensitivity and specificity of detecting and staging PCa [275].

For international, multi-center studies, differences in the European and US consensus on multi-parametric MRI needs to be considered. The main one is that endorectal coils are more frequently used in the US. They yield potentially better SNR than surface coils, but are less patient friendly [102]. The same holds true for the use of an external surface actuator. These might limit the obtained SNR of the motion encoded signal, as the reliable induction of shear waves with sufficient amplitude remains a challenge [275]. The accurate reconstruction is also difficult as the wavelength of the vibration is of the same order as the dimension of the organ, e.g. reported as 45 mm at 60 Hz [157, 310]. Here, the implementation of a direction inversion algorithm is suggested [157].

Regardless of each specific application, this work took the first steps towards a reliable and robust MRE imaging work-flow in our clinic based on the presented actuator and motion encoding SE-EPI sequence.

Summary and Outlook 6

MRE is a unique technique for the identification of various pathologies as visco-elastic characteristics may vary between healthy and diseased tissue. The quantification of the shear modulus is, therefore, a promising additional parameter for MR diagnostics within a variety of clinical applications.

In this work, a new method was developed for the generation of shear waves for MRE imaging: a 3D printed pneumatic turbine vibrator that is MR-safe and can generate shear waves in the range needed to induce suitable tissue motion during MRE. The design is adaptable and reproducible through low-cost 3D printing. It has also been aimed to meet clinical demands and can readily be used at a field strength of 3 T. Three aims were pursued for this thesis:

Firstly, the technical feasibility of a novel MRI-compatible set-up based on centrifugal force was demonstrated. A mechanical device was designed and manufactured that induced sinusoidal tissue movements. The technical assessment showed that the developed pneumatic turbine generated suitable vibrations in the range of 20 Hz to 150 Hz. The acceleration values increased for higher rotational frequencies, contrary to the conventionally applied air cushions. The vibrational frequency spectrum of the acceleration had a FWHM of 1.5 Hz. Artifacts were negligible for the 3D printed parts made of PA. The larger signal attenuation caused by the brass valve was removed during the optimization process. The design of the actuator was extended to a series connection of two pneumatic turbines with specific phase offsets of the sinusoidal vibrations. The set-up allowed the generation of shear waves at several surface locations and a more uniform penetration of a larger volume of interest. An in-house certification according to §7 (9) MPV was conducted and in-house in vivo clinical testing of the developed hardware was approved by the local ethics committee.

Secondly, the mechanical response of the induced vibrations was meaningfully resolved in the complex MR signal. A SE-EPI sequence was extended to include adjustable MEGs, a trigger was implemented that synchronized the sequence to the actuator, and the actuator was integrated into the MRI scanner system to enable MRE data acquisition.

Thirdly, the feasibility to quantify soft tissue stiffness was evaluated using the integrated actuator system and tissue mimicking phantoms. A prostate phantom with two inclusions mimicking a bladder (shear modulus 7.29 kPa) and a prostate (5.17 kPa) as well as an anthropomorphic abdominal phantom with a liver (2.72 kPa) were manufactured. The stiffness was verified with rheometric testing and closely matched elasticity values of human tissues. The phantoms yielded sufficient MR signals during imaging with the developed motion encoding SE-EPI sequences in terms of SNR (liver: 71.5) and CNR (liver: 16.5). The phantoms may also be used for future multi-modal imaging. In CT, the HUs were also in the range of soft tissue (liver: 106 ± 6 HU). Adding scatter particles enables US imaging of the silicones; then a cross validation of USE and MRE on these phantoms could be possible. The prostate and abdominal phantoms served as test objects with known elasticities for the evaluation of the actuators. The actuator was efficiently to set up, did not interfere with the imaging procedure and could be integrated into existing clinical equipment. MRE images were obtained at multiple actuation frequencies ranging from 50 Hz to 80 Hz. Wave images and elastograms were reconstructed. The elasticity map obtained at 60 Hz yielded a shear modulus of 1.12 ± 0.16 kPa in a ROI in the liver and a shear modulus of 4.37 ± 0.52 kPa in the filling material. The dual actuator was used to investigate if the attenuation of shear waves can be compensated by using an increased number of wave sources. Especially in the peripheral region of the abdominal phantom, larger displacements compared to the single actuation could be observed in the wave images. Furthermore, an in vivo study of a volunteer was conducted. The actuator was well tolerated by the volunteer, for both liver and prostate MRE. A non-invasive actuation technique and a short additional set-up time (less than five minutes) to incorporate MRE in a routine MRI examination will facilitate clinical and patient acceptance.

Elasticity imaging may provide additional quantitative data during clinical MRI examinations. It can provide physicians with a method of indirectly palpating deep-lying soft tissue to identify normal and diseased tissue [7, 15]. This work developed an MRE imaging set-up based on a novel actuation method and demonstrated its first implementation at the clinical scanner in our clinic.

For further improvements, three important areas within the field of MRE should be considered:

Sequence development: MRE acquisition time should be shortened to enable the implementation of advanced MRE data acquisition during clinical MRI examinations. 3D wave fields should be obtained as it is not advisable to measure only selected components of the wave fields. Covering the whole volume of an entire organ should be envisioned for in vivo studies on clinical MRI scanners.

Furthermore, the effects of organ motion, e.g. due to breathing or peristalsis, may diminish with shorter acquisition times. This will improve alignment of subsequently measured wave fields, when 3D wave data are obtained. Shortening the acquisition time will also, for example, allow cardiac MRE imaging. The myocardial stiffness changes during the cardiac cycle and can be an important parameter for the evaluation of myocardial infarction.

Rheometric modelling: Obtaining more detailed MRE wave data will improve rheometric modelling. So far, most methods consider a pure elastic medium and therefore only tissue elasticity is quantified. However, tissues exhibit visco-elastic, anisotropic behaviors to varying degrees. As the tissues are subjected to periodic oscillation, the complex modulus consisting of the storage and loss modulus could be reconstructed.

A gold standard for MRE: For a thorough cross validation of MRE data, a gold standard for clinical MRE data acquisition is yet missing. The lack of a gold standard limits the comparison of conventional MRE approaches and model improvements and it restricts the comparability of results obtained by different research groups as different parameter settings might influence the reconstructed elasticity data. A gold standard and thus comparable data for both phantoms and in vivo images may help to determine the most relevant clinical MRE technique.

MRE is emerging as a commercial application, demonstrating the progress and importance of the technique [15, 27]. Nevertheless, further studies are needed to justify the use of MRE in clinical routine. Multi-center studies performed with different MRI scanners as well as the standardization and automation of an MRE protocol is required. The work here presents the first steps towards a clinical application due to the simplicity of the set-up. With this, we envision the further use of the technique to find bio-markers to diagnose diseases, and characterize cancers without the need for invasive biopsy analysis.

List of Figures

2.1	Normal stress, normal strain and relative contraction	6
2.2	Graphical representation of visco-elastic models	8
2.3	Sequence diagram of a spin-echo sequence	23
2.4	Sequence diagram of a motion encoding sequence	25
3.1	Principle of centrifugal force generation	39
3.2	Quantification of artifacts caused by selected materials	42
3.3	Photograph of test set-up during acceleration measurements	44
3.4	Photographs of test set-up for axial force measurements	45
3.5	CAD drawing of dual turbine design	46
3.6	Photographs of active driver components	48
3.7	Circuit board design	49
3.8	Photographs of 3 T Magnetom whole body scanners	53
3.9	Photographs of manufacturing process of the tissue-mimicking material	58
3.10	Photographs of strain-controlled rheometric measurement device	60
3.11	Photographs of manufacturing process of the prostate phantom	63
3.12	Photographs of manufacturing process of the abdominal phantom	65
3.13	Schematics of MRE image acquisition and post-processing work-flow	67
4.1	Overview of the development of turbine designs	71
4.2	CAD explosive view of turbine model V_4	72
4.3	Graphs of vibration frequency response spectrum for two unbalances	73
4.4	Photograph of the turbine blades, a sampling scheme, and measured signal	74
4.5	Graph of nominal life expectancy L_{10h} of the rolling-element bearing	75
4.6	CAD drawings of base plates for liver and prostate MRE	76
4.7	MR images and artifact masks for the PA cube, PA cylinder, and brass valve	77
4.8	Photographs of dual turbine designs	78
4.9	CAD drawing of tongue-and-groove connection	79
4.10	CAD drawings of turbine design optimization	79
4.11	Schematic hardware set-up	80
4.12	Photographs of the PCB of the active driver control unit	81

4.13	Photographs of the active driver control unit	82
4.14	Screenshot of the simulated of the added passive circuit's signal	83
4.15	Screenshot of implemented special card of the SE-EPI-based MRE sequence	87
4.16	Sequence diagram of developed SE-EPI-based MRE sequence	88
4.17	Diagram of shear modulus vs frequency of SF13 and SF00 silicones	92
4.18	Diagram of shear modulus vs frequency of SF00 silicones diluted with SF-V50	92
4.19	Morphological MR and CT images of the prostate and abdominal phantoms	94
4.20	MRE - magnitude and phase images without actuation	95
4.21	MRE - results of prostate phantom with GRE sequence	97
4.22	MRE - results of prostate phantom with SE-EPI sequence	97
4.23	MRE - line profile of prostate phantom	98
4.24	MRE - elastograms of prostate phantom	98
4.25	MRE - results of abdominal phantom with single actuation and varying MEG strength	99
4.26	MRE - results of abdominal phantom with single actuation and varying phase offsets	100
4.27	MRE - results of abdominal phantom with all actuation types	101
4.28	MRE - thresholded phase images of abdominal phantom	102
4.29	MRE - wave images of abdominal phantom	103
4.30	MRE - elastograms of abdominal phantom	104
4.31	MRE - results of in vivo liver and prostate study	105
A.1	Diagrams of force measurements of the passive driver	169
A.2	Diagrams of acceleration measurements of the passive driver	170
C.1	Diagram of elasticity changes of silicone samples after four months	191
C.2	Diagram of elasticity variations due to long term storage and batch variations	192
C.3	Diagram of elasticity changes of silicone due to different batches of raw material	193
C.4	Diagram of elasticity curve of silicone with two different diameters	194
C.5	Diagram of elasticity curve of silicone with varying sample geometry	195
C.6	Diagram of elasticity curve of silicone with scatter particles	195
D.1	MRE - measured wave length in abdominal phantom	197
D.2	MRE - abdominal phantom, SE-EPI sequence, large surface actuation, varying MEG	198
D.3	MRE - abdominal phantom, SE-EPI sequence, dual source actuation, varying MEG	198

List of Tables

2.1	Elasticity of the healthy human liver reported in literature	16
2.2	Elasticity of the healthy human prostate reported in literature	18
3.1	Technical specifications of the trigger input signal, adapted from [190].	55
4.1	Complex shear modulus of tested silicone samples ranging from SF00 to SF13.	90
4.2	Complex shear modulus of tested silicone samples.	91
4.3	SNR and CNR of the prostate and abdominal liver phantom during MR imaging.	93
A.1	Additional parameters acquired during acceleration measurements.	169

Acronyms

ADC	Analog to digital converter
ASTM	American society for testing materials
BSSFP	Balanced steady-state free precession (sequence)
CAD	Computer aided design
CNR	Contrast to noise ratio
CT	Computed tomography
DC	Direct current
DI	Direct inversion (algorithm)
DMA	Dynamic mechanical analysis
DRE	Digital rectal examinations
EN	European norm
EPI	Echo planar imaging (sequence)
FA	Flip angle
FLASH	Fast low angle shot (sequence)
FoV	Field of view
FT	Fourier transformation
FWHM	Full width half maximum
GRE	Gradient echo based (sequence)
HCC	Hepatocellular carcinoma
HU	Hounsfield units
I/O	Input/Output (pins)
LED	Light emitting diode
LFE	Local frequency estimation (algorithm)
MEG	Motion encoding gradient
mpMRI	Multi-parametric magnetic resonance imaging
MR	Magnetic resonance
MRE	Magnetic resonance elastography
MRI	Magnetic resonance imaging
NAFLD	Nonalcoholic fatty liver disease
NLI	Nonlinear inversion (algorithm)

PA	Polyamide
PAT	Parallel acquisition technique
PCa	Prostate carcinoma
PCB	Printed circuit board
PLA	Poly lactide
PVC	Polyvinyl chloride
PWM	Pulse width modulation
RF	Radio frequency
ROI	Region of interest
RTV	Room temperature vulcanizing (silicone)
SE	Spin echo (sequence)
SE-EPI	Spin echo echo planar imaging (sequence)
SF-V50	Flow-viscosity silicone oil with a viscosity of 50 cSt
SF00	RTV2 silicone rubber with a Shore hardness of 00 ShA
SF13	RTV2 silicone rubber with a Shore hardness of 13 ShA
SLS	Selective laser sintering
SNR	Signal to noise ratio
STL	Standard triangulation language
TRUFI	True fast imaging with steady-state free precession (sequence)
TRUS	Transrectal ultrasound
TSE	Turbo spin echo (sequence)
US	Ultra sound
USE	Ultra sound elastography
WiP	Work in progress (sequence package)

Notation

B_0	Main magnetic field oriented along the main bore axis
E	Elasticity modulus
G^*	Complex shear modulus
G	Shear modulus
K	Bulk compressional modulus
T_E	Echo time
T_R	Repetition time
γ	Gyromagnetic ratio
γ	Shear strain
μ_{\parallel}	Elasticity coefficient (parallel shear modulus)
μ_{\perp}	Elasticity coefficient (perpendicular shear modulus)
σ	Normal stress
τ	Shear stress
ε	Normal strain

References

- [1] Z. J. Domire, M. B. McCullough, Q. Chen, and K.-N. An, "Wave attenuation as a measure of muscle quality as measured by magnetic resonance elastography: Initial results," *Journal of biomechanics*, vol. 42, no. 4, pp. 537–540, 2009.
- [2] S. F. Bensamoun, L. Robert, G. E. Leclerc, L. Debernard, and F. Charleux, "Stiffness imaging of the kidney and adjacent abdominal tissues measured simultaneously using magnetic resonance elastography," *Clin Imaging*, vol. 35, no. 4, pp. 284–7, 2011.
- [3] L. Huwart, N. Salameh, L. ter Beek, E. Vicaut, F. Peeters, R. Sinkus, and B. E. Van Beers, "MR elastography of liver fibrosis: preliminary results comparing spin-echo and echo-planar imaging," *Eur Radiol*, vol. 18, no. 11, pp. 2535–41, 2008.
- [4] J. Chen, J. A. Talwalkar, M. Yin, K. J. Glaser, S. O. Sanderson, and R. L. Ehman, "Early detection of nonalcoholic steatohepatitis in patients with nonalcoholic fatty liver disease by using MR elastography," *Radiology*, vol. 259, no. 3, pp. 749–56, 2011.
- [5] P. Asbach, D. Klatt, U. Hamhaber, J. Braun, R. Somasundaram, B. Hamm, and I. Sack, "Assessment of liver viscoelasticity using multifrequency MR elastography," *Magn Reson Med*, vol. 60, no. 2, pp. 373–9, 2008.
- [6] P. Garteiser, S. Doblas, J. L. Daire, M. Wagner, H. Leitao, V. Vilgrain, R. Sinkus, and B. E. Van Beers, "MR elastography of liver tumours: value of viscoelastic properties for tumour characterisation," *Eur Radiol*, vol. 22, no. 10, pp. 2169–77, 2012.
- [7] D. S. Derek, L. C. Thomas, R. S. Andrei, and Y. E. Stanislav, "Three-dimensional static displacement, stimulated echo NMR elasticity imaging," *Physics in Medicine and Biology*, vol. 45, no. 6, p. 1633, 2000.
- [8] S. McDonald, D. Saslow, and M. H. Alciati, "Performance and reporting of clinical breast examination: a review of the literature," *CA Cancer J Clin*, vol. 54, no. 6, pp. 345–61, 2004.
- [9] R. Muthupillai, D. J. Lomas, P. J. Rossman, J. F. Greenleaf, A. Manduca, and R. L. Ehman, "Magnetic resonance elastography by direct visualization of propagating acoustic strain waves," *Science*, vol. 269, no. 5232, pp. 1854–7, 1995.
- [10] Y. C. Fung, *Biomechanics: Mechanical Properties of Living Tissues*, 2nd ed. Heidelberg: Springer, 1993.
- [11] B. Suki, A. L. Barabasi, and K. R. Lutchen, "Lung tissue viscoelasticity: a mathematical framework and its molecular basis," *J Appl Physiol (1985)*, vol. 76, no. 6, pp. 2749–59, 1994.

- [12] M. A. Meyers, P.-Y. Chen, A. Y.-M. Lin, and Y. Seki, "Biological materials: Structure and mechanical properties," *Progress in Materials Science*, vol. 53, no. 1, pp. 1–206, 2008.
- [13] R. L. Magin, "Fractional calculus models of complex dynamics in biological tissues," *Computers and Mathematics with Applications*, vol. 59, no. 5, pp. 1586–1593, 2010.
- [14] E. C. Qin, R. Sinkus, G. Geng, S. Cheng, M. Green, C. D. Rae, and L. E. Bilston, "Combining MR elastography and diffusion tensor imaging for the assessment of anisotropic mechanical properties: a phantom study," *J Magn Reson Imaging*, vol. 37, no. 1, pp. 217–26, 2013.
- [15] A. Sarvazyan, T. J. Hall, M. W. Urban, M. Fatemi, S. R. Aglyamov, and B. S. Garra, "An overview of elastography - an emerging branch of medical imaging," *Curr Med Imaging Rev*, vol. 7, no. 4, pp. 255–282, 2011.
- [16] J. B. Fowlkes, S. Emelianov, J. G. Pipe, A. R. Skovoroda, P. L. Carson, R. S. Adler, and A. P. Sarvazyan, "Magnetic-resonance imaging techniques for detection of elasticity variation," *Med Phys*, vol. 11, no. 1, pp. 1771–8, Nov 1995.
- [17] A. R. Skovoroda, S. Y. Emelianov, and M. O'Donnell, "Tissue elasticity reconstruction based on ultrasonic displacement and strain images," *IEEE Trans Ultrason Ferroelectr Freq Control*, pp. 747–765, 1995.
- [18] R. S. Sahebjavaher, G. Nir, M. Honarvar, L. O. Gagnon, J. Ischia, E. Jones, S. D. Chang, L. Fazli, S. L. Goldenberg, R. Rohling, P. Kozlowski, R. Sinkus, and S. E. Salcudean, "MR elastography of prostate cancer: quantitative comparison with histopathology and repeatability of methods," *NMR Biomed*, vol. 28, no. 1, pp. 124–39, Jan 2015.
- [19] L. Huwart, F. Peeters, R. Sinkus, L. Annet, N. Salameh, L. C. ter Beek, Y. Horsmans, and B. E. Van Beers, "Liver fibrosis: non-invasive assessment with MR elastography," *NMR Biomed*, vol. 19, no. 2, pp. 173–9, 2006.
- [20] L. Huwart, C. Sempoux, N. Salameh, J. Jamart, L. Annet, R. Sinkus, F. Peeters, L. C. ter Beek, Y. Horsmans, and B. E. Van Beers, "Liver fibrosis: noninvasive assessment with mr elastography versus aspartate aminotransferase to platelet ratio index," *Radiology*, vol. 245, no. 2, pp. 458–66, 2007.
- [21] M. Yin, J. A. Talwalkar, K. J. Glaser, A. Manduca, R. C. Grimm, P. J. Rossman, J. L. Fidler, and R. L. Ehman, "Assessment of hepatic fibrosis with magnetic resonance elastography," *Clin Gastroenterol Hepatol*, vol. 5, no. 10, pp. 1207–1213.e2, 2007.
- [22] O. Rouviere, M. Yin, M. A. Dresner, P. J. Rossman, L. J. Burgart, J. L. Fidler, and R. L. Ehman, "MR elastography of the liver: preliminary results," *Radiology*, vol. 240, no. 2, pp. 440–8, 2006.
- [23] R. Sinkus, M. Tanter, T. Xydeas, S. Catheline, J. Bercoff, and M. Fink, "Viscoelastic shear properties of in vivo breast lesions measured by MR elastography," *Magn Reson Imaging*, vol. 23, no. 2, pp. 159–65, 2005.
- [24] K. Hoyt, B. Castaneda, M. Zhang, P. Nigwekar, P. A. di Sant'agnese, J. V. Joseph, J. Strang, D. J. Rubens, and K. J. Parker, "Tissue elasticity properties as biomarkers for prostate cancer," *Cancer Biomark*, vol. 4, no. 4-5, pp. 213–25, 2008.
- [25] T. A. Krouskop, T. M. Wheeler, F. Kallel, B. S. Garra, and T. Hall, "Elastic moduli of breast and prostate tissues under compression," *Ultrason Imaging*, vol. 20, no. 4, pp. 260–74, 1998.

- [26] S. Chatelin, I. Charpentier, N. Corbin, L. Meylheuc, and J. Vappou, "An automatic differentiation-based gradient method for inversion of the shear wave equation in magnetic resonance elastography: specific application in fibrous soft tissues," *Physics in Medicine and Biology*, vol. 61, no. 13, pp. 5000–5019, 2016.
- [27] E. C. Ehman, P. J. Rossman, S. A. Kruse, A. V. Sahakian, and K. J. Glaser, "Vibration safety limits for magnetic resonance elastography," *Phys Med Biol*, vol. 53, no. 4, pp. 925–35, 2008.
- [28] S. K. Venkatesh, M. Yin, J. F. Glockner, N. Takahashi, P. A. Araoz, J. A. Talwalkar, and R. L. Ehman, "MR elastography of liver tumors: preliminary results," *AJR Am J Roentgenol*, vol. 190, no. 6, pp. 1534–40, 2008.
- [29] J. R. Hawley, P. Kalra, X. Mo, B. Raterman, L. D. Yee, and A. Kolipaka, "Quantification of breast stiffness using mr elastography at 3 Tesla with a soft sternal driver: A reproducibility study," *J Magn Reson Imaging*, vol. 45, no. 5, pp. 1379–1384, 2017.
- [30] V. Khozikov, P. J. Rossman, and R. L. Ehman, "Passive array mechanical driver for magnetic resonance elastography of the breast." Proc. 14th Annu. Meeting of ISMRM, 2006, Conference Proceedings.
- [31] Y. Zheng, G. Li, M. Chen, Q. C. Chan, S. G. Hu, X. N. Zhao, R. L. Ehman, E. Y. Lam, and E. S. Yang, "Magnetic resonance elastography with twin pneumatic drivers for wave compensation," *Conf Proc IEEE Eng Med Biol Soc*, vol. 2007, pp. 2611–3, 2007.
- [32] Y. K. Mariappan, P. J. Rossman, K. J. Glaser, A. Manduca, and R. L. Ehman, "Magnetic resonance elastography with a phased-array acoustic driver system," *Magn Reson Med*, vol. 61, no. 3, pp. 678–85, 2009.
- [33] J. Rösler, H. Harders, and M. Bäker, *Mechanisches Verhalten der Werkstoffe*. Springer Vieweg, 2016.
- [34] G. Gottstein, *Materialwissenschaft und Werkstofftechnik*. Springer Vieweg, 2014.
- [35] M. H. Sadd, *Elasticity*. Elsevier Butterworth-Heinemann, 2005.
- [36] A. P. Deshpande, J. Krishnan, and S. Kumar, *Rheology of Complex Fluids*. Springer, 2010.
- [37] A. Arani, D. Plewes, A. Krieger, and R. Chopra, "The feasibility of endorectal MR elastography for prostate cancer localization," *Magn Reson Med*, vol. 66, no. 6, pp. 1649–57, 2011.
- [38] A. Kolipaka, K. P. McGee, A. Manduca, N. Anavekar, R. L. Ehman, and P. A. Araoz, "In vivo assessment of MR elastography-derived effective end-diastolic myocardial stiffness under different loading conditions," *J Magn Reson Imaging*, vol. 33, no. 5, pp. 1224–8, 2011.
- [39] S. Li, M. Chen, W. Wang, W. Zhao, J. Wang, X. Zhao, and C. Zhou, "A feasibility study of MR elastography in the diagnosis of prostate cancer at 3 t," *Acta Radiol*, vol. 52, no. 3, pp. 354–8, 2011.
- [40] Y. K. Mariappan, K. J. Glaser, R. D. Hubmayr, A. Manduca, R. L. Ehman, and K. P. McGee, "MR elastography of human lung parenchyma: technical development, theoretical modeling and in vivo validation," *J Magn Reson Imaging*, vol. 33, no. 6, pp. 1351–61, 2011.

- [41] G. I. Nedredal, M. Yin, T. McKenzie, J. Lillegard, J. Luebke-Wheeler, J. Talwalkar, R. Ehman, and S. L. Nyberg, "Portal hypertension correlates with splenic stiffness as measured with MR elastography," *J Magn Reson Imaging*, vol. 34, no. 1, pp. 79–87, 2011.
- [42] M. C. Murphy, K. J. Glaser, A. Manduca, J. P. Felmlee, r. Huston, J., and R. L. Ehman, "Analysis of time reduction methods for magnetic resonance elastography of the brain," *Magn Reson Imaging*, vol. 28, no. 10, pp. 1514–24, 2010.
- [43] L. Juge, A. Petiet, S. A. Lambert, P. Nicole, S. Chatelin, V. Vilgrain, B. E. Van Beers, L. E. Bilston, and R. Sinkus, "Microvasculature alters the dispersion properties of shear waves—a multi-frequency MR elastography study," *NMR Biomed*, vol. 28, no. 12, pp. 1763–71, 2015.
- [44] M. Levy, H. E. Bass, and R. R. Stern, *Handbook of elastic properties of Solids, Liquids, and Gases*, 1st ed., ser. 1. Academic Press, 2000.
- [45] T. A. Krouskop, D. R. Dougherty, and F. S. Vinson, "A pulsed doppler ultrasonic system for making noninvasive measurements of the mechanical properties of soft tissue," *J Rehabil Res Dev*, vol. 24, no. 2, pp. 1–8, 1987.
- [46] A. P. Sarvazyan, A. R. Skovoroda, S. Y. Emelianov, J. B. Fowlkes, J. G. Pipe, R. S. Adler, R. B. Buxton, and P. L. Carson, *Biophysical Bases of Elasticity Imaging, Acoustical Imaging*. Springer, 1995.
- [47] J. Ophir, I. Cespedes, H. Ponnekanti, Y. Yazdi, and X. Li, "Elastography: a quantitative method for imaging the elasticity of biological tissues," *Ultrason Imaging*, vol. 13, no. 2, pp. 111–34, 1991.
- [48] J. Black, M. Baharestani, S. Black, J. Cavazos, T. Conner-Kerr, L. Edsberg, B. Peirce, E. Rivera, and G. Schultz, "An overview of tissue types in pressure ulcers: a consensus panel recommendation," *Ostomy Wound Manage*, vol. 56, no. 4, pp. 28–44, 2010.
- [49] J. M. Black, C. T. Brindle, and J. S. Honaker, "Differential diagnosis of suspected deep tissue injury," *Int Wound J*, vol. 13, no. 4, pp. 531–9, 2016.
- [50] L. Huwart and B. E. van Beers, "MR elastography for the noninvasive staging of liver fibrosis," *Gastroenterol Clin Biol*, vol. 32, no. 6 Suppl 1, pp. 68–72, 2008.
- [51] A. Samani, J. Zubovits, and D. Plewes, "Elastic moduli of normal and pathological human breast tissues: an inversion-technique-based investigation of 169 samples," *Phys Med Biol*, vol. 52, no. 6, pp. 1565–76, 2007.
- [52] A. Samani and D. Plewes, "An inverse problem solution for measuring the elastic modulus of intact ex vivo breast tissue tumours," *Phys Med Biol*, vol. 52, no. 5, pp. 1247–60, 2007.
- [53] A. Srivastava, Y. Verma, K. D. Rao, and P. K. Gupta, "Determination of elastic properties of resected human breast tissue samples using optical coherence tomographic elastography," *Strain*, vol. 47, no. 1, pp. 75–87, 2011.
- [54] X. Liang, A. L. Oldenburg, V. Crecea, S. Kalyanam, M. F. Insana, and S. A. Boppart, "Modeling and measurement of tissue elastic moduli using optical coherence elastography," in *SPIE BiOS*, vol. 6858. SPIE, 2008, Conference Proceedings, p. 8.

- [55] P. Sanz-Cameno, M. Trapero-Marugan, M. Chaparro, E. A. Jones, and R. Moreno-Otero, "Angiogenesis: from chronic liver inflammation to hepatocellular carcinoma," *J Oncol*, vol. 2010, p. 272170, 2010, 1687-8469.
- [56] J. Guck, F. Lautenschlager, S. Paschke, and M. Beil, "Critical review: cellular mechanobiology and amoeboid migration," *Integr Biol (Camb)*, vol. 2, no. 11-12, pp. 575-83, 2010.
- [57] D. E. Discher, P. Janmey, and Y. L. Wang, "Tissue cells feel and respond to the stiffness of their substrate," *Science*, vol. 310, no. 5751, pp. 1139-43, 2005.
- [58] J. Guo, O. Posnansky, S. Hirsch, M. Scheel, M. Taupitz, J. Braun, and I. Sack, "Fractal network dimension and viscoelastic powerlaw behavior: An experimental study of structure-mimicking phantoms by magnetic resonance elastography," *Phys Med Biol*, vol. 57, no. 12, pp. 4041-53, 2012.
- [59] J. L. Nelissen, L. de Graaf, W. A. Traa, T. J. Schreurs, K. M. Moerman, A. J. Nederveen, R. Sinkus, C. W. Oomens, K. Nicolay, and G. J. Strijkers, "A MRI-compatible combined mechanical loading and MR elastography setup to study deformation-induced skeletal muscle damage in rats," *PLoS One*, vol. 12, no. 1, p. e0169864, 2017.
- [60] A. Romano, M. Scheel, S. Hirsch, J. Braun, and I. Sack, "In vivo waveguide elastography of white matter tracts in the human brain," *Magn Reson Med*, vol. 68, no. 5, pp. 1410-22, 2012.
- [61] D. J. Tweten, R. J. Okamoto, and P. V. Bayly, "Requirements for accurate estimation of anisotropic material parameters by magnetic resonance elastography: A computational study," *Magn Reson Med*, vol. 78, no. 6, pp. 2360-2372, 2017.
- [62] K. D. Paulsen, E. E. W. V. Houten, M. M. Doyley, and J. B. Weaver, "Magnetic resonance elastography in the breast: initial reconstructions of damping coefficient," in *Proceedings IEEE International Symposium on Biomedical Imaging*, 2002, Conference Proceedings, pp. 157-160.
- [63] S. Ipek-Ugay, T. Driessle, M. Ledwig, J. Guo, S. Hirsch, I. Sack, and J. Braun, "Tabletop magnetic resonance elastography for the measurement of viscoelastic parameters of small tissue samples," *J Magn Reson*, vol. 251, pp. 13-8, 2015.
- [64] I. Sack, K. Jöhrens, J. Würfel, and J. Braun, "Structure-sensitive elastography: on the viscoelastic powerlaw behavior of in vivo human tissue in health and disease," *Soft Matter*, vol. 9, no. 24, pp. 5672-5680, 2013.
- [65] O. Posnansky, J. Guo, S. Hirsch, S. Papazoglou, J. Braun, and I. Sack, "Fractal network dimension and viscoelastic powerlaw behavior: A modeling approach based on a coarse-graining procedure combined with shear oscillatory rheometry," *Phys Med Biol*, vol. 57, no. 12, pp. 4023-40, 2012.
- [66] D. A. Morrow, T. L. Haut Donahue, G. M. Odegard, and K. R. Kaufman, "Transversely isotropic tensile material properties of skeletal muscle tissue," *Journal of the Mechanical Behavior of Biomedical Materials*, vol. 3, no. 1, pp. 124-129, 2010.
- [67] S. S. Blemker and S. L. Delp, "Three-dimensional representation of complex muscle architectures and geometries," *Ann Biomed Eng*, vol. 33, no. 5, pp. 661-73, 2005.
- [68] D. Royer and E. Dieulesaint, *Elastic waves in solids*. Springer, 1996.

- [69] B. L. Schwartz, Z. Yin, T. K. Yasar, Y. Liu, A. A. Khan, A. Q. Ye, T. J. Royston, and R. L. Magin, "Scattering and diffraction of elastodynamic waves in a concentric cylindrical phantom for MR elastography," *IEEE Trans Biomed Eng*, vol. 63, no. 11, pp. 2308–2316, 2016.
- [70] S. Papazoglou, J. Rump, J. Braun, and I. Sack, "Shear wave group velocity inversion in MR elastography of human skeletal muscle," *Magn Reson Med*, vol. 56, no. 3, pp. 489–97, 2006.
- [71] D. Klatt, S. Papazoglou, J. Braun, and I. Sack, "Viscoelasticity-based MR elastography of skeletal muscle," *Phys Med Biol*, vol. 55, no. 21, pp. 6445–59, 2010.
- [72] R. Sinkus, M. Tanter, S. Catheline, J. Lorenzen, C. Kuhl, E. Sondermann, and M. Fink, "Imaging anisotropic and viscous properties of breast tissue by magnetic resonance-elastography," *Magn Reson Med*, vol. 53, no. 2, pp. 372–87, 2005.
- [73] I. Sack, B. Beierbach, J. Wuerfel, D. Klatt, U. Hamhaber, S. Papazoglou, P. Martus, and J. Braun, "The impact of aging and gender on brain viscoelasticity," *Neuroimage*, vol. 46, no. 3, pp. 652–7, 2009.
- [74] M. A. Green, L. E. Bilston, and R. Sinkus, "In vivo brain viscoelastic properties measured by magnetic resonance elastography," *NMR Biomed*, vol. 21, no. 7, pp. 755–64, 2008.
- [75] E. H. Clayton, J. R. Garbow, and P. V. Bayly, "Frequency-dependent viscoelastic parameters of mouse brain tissue estimated by mr elastography," *Phys Med Biol*, vol. 56, no. 8, pp. 2391–406, 2011.
- [76] B. M. Koeppen and B. A. Stanton, Eds., *Berne and Levy Physiology*, 6th ed. Philadelphia, PA, USA: Mosby Elsevier, 2010.
- [77] P. Abrahams, J. Craven, and J. Lumley, *Illustrated Clinical Anatomy*. New York, USA: Hodder Education, 2005.
- [78] V. Kumar, A. K. Abbas, N. Fausto, and R. N. Mitchell, Eds., *Robbins Basic Pathology*, 8th ed. Philadelphia, PA, USA: Saunders Elsevier, 2007.
- [79] C. Bosetti, F. Turati, and C. La Vecchia, "Hepatocellular carcinoma epidemiology," *Best Pract Res Clin Gastroenterol*, vol. 28, no. 5, pp. 753–70, 2014.
- [80] R. Reiter, C. Freise, K. Johrens, C. Kamphues, D. Seehofer, M. Stockmann, R. Somasundaram, P. Asbach, J. Braun, A. Samani, and I. Sack, "Wideband MRE and static mechanical indentation of human liver specimen: sensitivity of viscoelastic constants to the alteration of tissue structure in hepatic fibrosis," *J Biomech*, vol. 47, no. 7, pp. 1665–74, 2014.
- [81] T. Poynard, M.-F. Yuen, V. Ratzin, and C. L. Lai, "Viral hepatitis C," *The Lancet*, vol. 362, no. 9401, pp. 2095–2100, 2003.
- [82] M. J. OBrien, N. M. Keating, S. Elderiny, S. Cerda, A. P. Keaveny, N. H. Afdhal, and D. P. Nunes, "An assessment of digital image analysis to measure fibrosis in liver biopsy specimens of patients with chronic hepatitis c," *American Journal of Clinical Pathology*, vol. 114, no. 5, pp. 712–718, 2000.
- [83] L. Castera, J. Vergniol, J. Foucher, B. Le Bail, E. Chanteloup, M. Haaser, M. Darriet, P. Couzigou, and V. De Ledinghen, "Prospective comparison of transient elastography, fibrotest, APRI, and liver biopsy for the assessment of fibrosis in chronic hepatitis C," *Gastroenterology*, vol. 128, no. 2, pp. 343–50, 2005.

- [84] L. Sandrin, B. Fourquet, J. M. Hasquenoph, S. Yon, C. Fournier, F. Mal, C. Christidis, M. Ziol, B. Poulet, F. Kazemi, M. Beaugrand, and R. Palau, "Transient elastography: a new noninvasive method for assessment of hepatic fibrosis," *Ultrasound Med Biol*, vol. 29, no. 12, pp. 1705–13, 2003.
- [85] W. C. Yeh, P. C. Li, Y. M. Jeng, H. C. Hsu, P. L. Kuo, M. L. Li, P. M. Yang, and P. H. Lee, "Elastic modulus measurements of human liver and correlation with pathology," *Ultrasound Med Biol*, vol. 28, no. 4, pp. 467–74, 2002.
- [86] M. Ziol, A. Handra-Luca, A. Kettaneh, C. Christidis, F. Mal, F. Kazemi, V. de Ledinghen, P. Marcellin, D. Dhumeaux, J. C. Trinchet, and M. Beaugrand, "Noninvasive assessment of liver fibrosis by measurement of stiffness in patients with chronic hepatitis C," *Hepatology*, vol. 41, no. 1, pp. 48–54, 2005.
- [87] R. Muthupillai, P. J. Rossman, D. J. Lomas, J. F. Greenleaf, S. J. Riederer, and R. L. Ehman, "Magnetic resonance imaging of transverse acoustic strain waves," *Magnetic Resonance in Medicine*, vol. 36, no. 2, pp. 266–274, 1996.
- [88] K. Mohd Hanafiah, J. Groeger, A. D. Flaxman, and S. T. Wiersma, "Global epidemiology of hepatitis c virus infection: new estimates of age-specific antibody to hcv seroprevalence," *Hepatology*, vol. 57, no. 4, pp. 1333–42, 2013.
- [89] T. Takamura, U. Motosugi, S. Ichikawa, K. Sano, H. Morisaka, T. Ichikawa, N. Enomoto, and H. Onishi, "Usefulness of MR elastography for detecting clinical progression of cirrhosis from child-pugh class A to B in patients with type C viral hepatitis," *J Magn Reson Imaging*, vol. 44, no. 3, pp. 715–22, 2016.
- [90] A. Lawson, S. Hagan, K. Rye, N. Taguri, S. Ratib, A. M. Zaitoun, K. R. Neal, S. D. Ryder, and W. L. Irving, "The natural history of hepatitis C with severe hepatic fibrosis," *Journal of Hepatology*, vol. 47, no. 1, pp. 37–45, 2007.
- [91] D. Klatt, P. Asbach, J. Rump, S. Papazoglou, R. Somasundaram, J. Modrow, J. Braun, and I. Sack, "In vivo determination of hepatic stiffness using steady-state free precession magnetic resonance elastography," *Invest Radiol*, vol. 41, no. 12, pp. 841–8, 2006.
- [92] S. F. Bensamoun, L. Wang, L. Robert, F. Charleux, J.-P. Latrive, and M.-C. Ho Ba Tho, "Measurement of liver stiffness with two imaging techniques: Magnetic resonance elastography and ultrasound elastometry," *Journal of Magnetic Resonance Imaging*, vol. 28, no. 5, pp. 1287–1292, 2008.
- [93] M. Fraquelli, C. Rigamonti, G. Casazza, D. Conte, M. F. Donato, G. Ronchi, and M. Colombo, "Reproducibility of transient elastography in the evaluation of liver fibrosis in patients with chronic liver disease," *Gut*, vol. 56, no. 7, pp. 968–73, 2007.
- [94] J. Foucher, E. Chanteloup, J. Vergniol, L. Castera, B. Le Bail, X. Adhoute, J. Bertet, P. Couzigou, and V. de Ledinghen, "Diagnosis of cirrhosis by transient elastography (fibroscan): a prospective study," *Gut*, vol. 55, no. 3, pp. 403–8, 2006.
- [95] M. L. Palmeri, M. H. Wang, J. J. Dahl, K. D. Frinkley, and K. R. Nightingale, "Quantifying hepatic shear modulus in vivo using acoustic radiation force," *Ultrasound in medicine and biology*, vol. 34, no. 4, pp. 546–558, 2008.
- [96] G. Thormer, M. Reiss-Zimmermann, J. Otto, K. T. Hoffmann, M. Moche, N. Garnov, T. Kahn, and H. Busse, "Novel technique for MR elastography of the prostate using a modified standard endorectal coil as actuator," *J Magn Reson Imaging*, vol. 37, no. 6, pp. 1480–5, 2013.

- [97] R. S. Sahebjavaher, A. Baghani, M. Honarvar, R. Sinkus, and S. E. Salcudean, "Transperineal prostate MR elastography: initial in vivo results," *Magn Reson Med*, vol. 69, no. 2, pp. 411–20, 2013.
- [98] V. Jalkanen, B. M. Andersson, A. Bergh, B. Ljungberg, and O. A. Lindahl, "Resonance sensor measurements of stiffness variations in prostate tissue in vitro—a weighted tissue proportion model," *Physiol Meas*, vol. 27, no. 12, pp. 1373–86, 2006.
- [99] D. Yakar, O. A. Debats, J. G. Bomers, M. G. Schouten, P. C. Vos, E. van Lin, J. J. Futterer, and J. O. Barentsz, "Predictive value of mri in the localization, staging, volume estimation, assessment of aggressiveness, and guidance of radiotherapy and biopsies in prostate cancer," *J Magn Reson Imaging*, vol. 35, no. 1, pp. 20–31, 2012.
- [100] W. Tobocman, M. I. Resnick, and T. G. Pretlow, "Ultrasound reflections fail to reflect the histopathology of the prostate," *Prostate*, vol. 30, no. 1, pp. 33–40, 1997.
- [101] C. R. King and J. P. Long, "Prostate biopsy grading errors: a sampling problem?" *Int J Cancer*, vol. 90, no. 6, pp. 326–30, 2000.
- [102] L. Dickinson, H. U. Ahmed, C. Allen, J. O. Barentsz, B. Carey, J. J. Futterer, S. W. Heijmink, P. J. Hoskin, A. Kirkham, A. R. Padhani, R. Persad, P. Puech, S. Punwani, A. S. Sohaib, B. Tombal, A. Villers, J. van der Meulen, and M. Emberton, "Magnetic resonance imaging for the detection, localisation, and characterisation of prostate cancer: recommendations from a european consensus meeting," *Eur Urol*, vol. 59, no. 4, pp. 477–94, 2011.
- [103] H. U. Ahmed, A. Kirkham, M. Arya, R. Illing, A. Freeman, C. Allen, and M. Emberton, "Is it time to consider a role for MRI before prostate biopsy?" *Nat Rev Clin Oncol*, vol. 6, no. 4, pp. 197–206, 2009.
- [104] J. J. Futterer, M. R. Engelbrecht, H. J. Huisman, G. J. Jager, C. A. Hulsbergen-van De Kaa, J. A. Witjes, and J. O. Barentsz, "Staging prostate cancer with dynamic contrast-enhanced endorectal MR imaging prior to radical prostatectomy: experienced versus less experienced readers," *Radiology*, vol. 237, no. 2, pp. 541–9, 2005.
- [105] J. Kurhanewicz, D. Vigneron, P. Carroll, and F. Coakley, "Multiparametric magnetic resonance imaging in prostate cancer: present and future," *Curr Opin Urol*, vol. 18, no. 1, pp. 71–7, 2008.
- [106] F. Pinto, A. Totaro, A. Calarco, E. Sacco, A. Volpe, M. Racioppi, A. D'Addessi, G. Gulino, and P. Bassi, "Imaging in prostate cancer diagnosis: present role and future perspectives," *Urol Int*, vol. 86, no. 4, pp. 373–82, 2011.
- [107] J. Kemper, R. Sinkus, J. Lorenzen, C. Nolte-Ernsting, A. Stork, and G. Adam, "MR elastography of the prostate: initial in-vivo application," *Rofo*, vol. 176, no. 8, pp. 1094–9, 2004.
- [108] B. M. Ahn, J. Kim, L. Ian, K. H. Rha, and H. J. Kim, "Mechanical property characterization of prostate cancer using a minimally motorized indenter in an ex vivo indentation experiment," *Urology*, vol. 76, no. 4, pp. 1007–11, 2010.
- [109] S. Phipps, T. H. Yang, F. K. Habib, R. L. Reuben, and S. A. McNeill, "Measurement of tissue mechanical characteristics to distinguish between benign and malignant prostatic disease," *Urology*, vol. 66, no. 2, pp. 447–50, 2005.

- [110] M. Zhang, P. Nigwekar, B. Castaneda, K. Hoyt, J. V. Joseph, A. di Sant'Agnese, E. M. Messing, J. G. Strang, D. J. Rubens, and K. J. Parker, "Quantitative characterization of viscoelastic properties of human prostate correlated with histology," *Ultrasound Med Biol*, vol. 34, no. 7, pp. 1033–42, 2008.
- [111] E. M. Haacke, R. W. Brown, M. R. Thomsson, , and R. Venkatesan, *Magnetic Resonance Imaging: Physical Principles and Sequence Design*. J. Wiley and Sons, 1999.
- [112] M. H. Levitt, *Spin dynamics: Basics of Nuclear Magnetic Resonance*. J. Wiley and Sons, 2008.
- [113] L. G. Hanson, "Chapter 3 - the ups and downs of classical and quantum formulations of magnetic resonance," in *Anthropic Awareness*, C. Szántay, Ed. Boston: Elsevier, 2015, pp. 141 – 171.
- [114] P. Ehrenfest, "Bemerkung über die angenäherte Gültigkeit der klassischen Mechanik innerhalb der Quantenmechanik," *Zeitschrift für Physik*, vol. 45, pp. 455–57, 1927.
- [115] C. J. Lewa, "Magnetic resonance imaging in the presence of mechanical waves," *Spectroscopy Letters*, vol. 24, no. 1, pp. 55–67, 1991.
- [116] A. A. Gurtovenko and A. Blumen, *EPolymer Analysis, Polymer Theory*. Springer, 2005.
- [117] A. Manduca, T. E. Oliphant, M. A. Dresner, J. L. Mahowald, S. A. Kruse, E. Amromin, J. P. Felmlee, J. F. Greenleaf, and R. L. Ehman, "Magnetic resonance elastography: non-invasive mapping of tissue elasticity," *Med Image Anal*, vol. 5, no. 4, pp. 237–54, 2001.
- [118] K. Uffmann, C. Abicht, W. Grote, H. H. Quick, and M. E. Ladd, "Design of an MR-compatible piezoelectric actuator for MR elastography," *Concepts in Magnetic Resonance*, vol. 15, no. 4, pp. 239–254, 2002.
- [119] R. Muthupillai and R. L. Ehman, "Magnetic resonance elastography," *Nature Medicine*, vol. 2, p. 601, 1996.
- [120] Z. T. Tse, H. Janssen, A. Hamed, M. Ristic, I. Young, and M. Lamperth, "Magnetic resonance elastography hardware design: a survey," *Proc Inst Mech Eng H*, vol. 223, no. 4, pp. 497–514, 2009.
- [121] K. Uffmann and M. E. Ladd, "Actuation systems for MR elastography: design and applications," *IEEE Eng Med Biol Mag*, vol. 27, no. 3, pp. 28–34, 2008.
- [122] H. Morisaka, U. Motosugi, K. J. Glaser, S. Ichikawa, R. L. Ehman, K. Sano, T. Ichikawa, and H. Onishi, "Comparison of diagnostic accuracies of two- and three-dimensional MR elastography of the liver," *J Magn Reson Imaging*, vol. 45, no. 4, pp. 1163–1170, 2017.
- [123] S. K. Venkatesh, G. Wang, S. G. Lim, and A. Wee, "Magnetic resonance elastography for the detection and staging of liver fibrosis in chronic hepatitis B," *European Radiology*, vol. 24, no. 1, pp. 70–78, 2014.
- [124] B. H. Kim, J. M. Lee, Y. J. Lee, K. B. Lee, K. S. Suh, J. K. Han, and B. I. Choi, "MR elastography for noninvasive assessment of hepatic fibrosis: experience from a tertiary center in asia," *J Magn Reson Imaging*, vol. 34, no. 5, pp. 1110–6, 2011.

- [125] M. Wagner, C. Besa, J. Bou Ayache, T. K. Yasar, O. Bane, M. Fung, R. L. Ehman, and B. Taouli, "Magnetic resonance elastography of the liver: Qualitative and quantitative comparison of gradient echo and spin echo echoplanar imaging sequences," *Invest Radiol*, vol. 51, no. 9, pp. 575–81, 2016.
- [126] S. K. Venkatesh, M. Yin, and R. L. Ehman, "Magnetic resonance elastography of liver: technique, analysis, and clinical applications," *J Magn Reson Imaging*, vol. 37, no. 3, pp. 544–55, 2013.
- [127] S. Hirsch, J. Braun, and I. Sack, *Magnetic resonance elastography - Physical background and medical applications*. Wiley-VCH, 2017.
- [128] R. Sinkus, K. Siegmann, T. Xydeas, M. Tanter, C. Claussen, and M. Fink, "MR elastography of breast lesions: understanding the solid/liquid duality can improve the specificity of contrast-enhanced MR mammography," *Magn Reson Med*, vol. 58, no. 6, pp. 1135–44, 2007.
- [129] J. Bishop, G. Poole, M. Leitch, and D. B. Plewes, "Magnetic resonance imaging of shear wave propagation in excised tissue," *J Magn Reson Imaging*, vol. 8, no. 6, pp. 1257–65, 1998.
- [130] A. Manduca, V. Dutt, D. T. Borup, R. Muthupillai, R. L. Ehman, and J. F. Greenleaf, "Reconstruction of elasticity and attenuation maps in shear wave imaging: An inverse approach," ser. Medical Image Computing and Computer-Assisted Intervention MICCAI98. Springer Berlin Heidelberg, Conference Proceedings, pp. 606–613.
- [131] J. P. Marinelli, D. L. Levin, R. Vassallo, R. E. Carter, R. D. Hubmayr, R. L. Ehman, and K. P. McGee, "Quantitative assessment of lung stiffness in patients with interstitial lung disease using MR elastography," *J Magn Reson Imaging*, vol. 46, no. 2, pp. 365–374, 2017.
- [132] A. Manduca, T. E. Oliphant, M. A. Dresner, J. L. Mahowald, S. A. Kruse, E. Amromin, J. P. Felmlee, J. F. Greenleaf, and R. L. Ehman, "Magnetic resonance elastography: non-invasive mapping of tissue elasticity," *Med Image Anal*, vol. 5, no. 4, pp. 237–54, 2001.
- [133] L. Tan, M. D. McGarry, E. E. Van Houten, M. Ji, L. Solamen, J. B. Weaver, and K. D. Paulsen, "Gradient-based optimization for poroelastic and viscoelastic MR elastography," *IEEE Trans Med Imaging*, vol. 36, no. 1, pp. 236–250, 2017.
- [134] R. Sinkus, J. Lorenzen, D. Schrader, M. Lorenzen, M. Dargatz, and D. Holz, "High-resolution tensor MR elastography for breast tumour detection," *Physics in Medicine and Biology*, vol. 45, no. 6, p. 1649, 2000.
- [135] T. E. Oliphant, A. Manduca, R. L. Ehman, and J. F. Greenleaf, "Complex-valued stiffness reconstruction for magnetic resonance elastography by algebraic inversion of the differential equation," *Magn Reson Med*, vol. 45, no. 2, pp. 299–310, 2001.
- [136] A. J. Romano, J. J. Shirron, and J. A. Bucaro, "On the noninvasive determination of material parameters from a knowledge of elastic displacements theory and numerical simulation," *IEEE Transactions on Ultrasonics, Ferroelectrics, and Frequency Control*, vol. 45, no. 3, pp. 751–759, 1998.
- [137] A. J. Romano, J. A. Bucaro, R. L. Ehnman, and J. J. Shirron, "Evaluation of a material parameter extraction algorithm using MRI-based displacement measurements," *IEEE Trans Ultrason Ferroelectr Freq Control*, vol. 47, no. 6, pp. 1575–81, 2000.

- [138] A. Manduca, D. S. Lake, S. A. Kruse, and R. L. Ehman, "Spatio-temporal directional filtering for improved inversion of mr elastography images," *Med Image Anal*, vol. 7, no. 4, pp. 465–73, 2003.
- [139] U. Hamhaber, I. Sack, S. Papazoglou, J. Rump, D. Klatt, and J. Braun, "Three-dimensional analysis of shear wave propagation observed by in vivo magnetic resonance elastography of the brain," *Acta Biomater*, vol. 3, no. 1, pp. 127–37, 2007.
- [140] L. Meng, J. Zhou, H. Sasano, T. Suzuki, K. M. Zeitoun, and S. E. Bulun, "Tumor necrosis factor alpha and interleukin 11 secreted by malignant breast epithelial cells inhibit adipocyte differentiation by selectively down-regulating ccaat/enhancer binding protein alpha and peroxisome proliferator-activated receptor gamma: mechanism of desmoplastic reaction," *Cancer Res*, vol. 61, no. 5, pp. 2250–5, 2001.
- [141] E. E. Van Houten, M. M. Doyley, F. E. Kennedy, J. B. Weaver, and K. D. Paulsen, "Initial in vivo experience with steady-state subzone-based MR elastography of the human breast," *Journal of Magnetic Resonance Imaging*, vol. 17, no. 1, pp. 72–85, 2003.
- [142] A. L. McKnight, J. L. Kugel, P. J. Rossman, A. Manduca, L. C. Hartmann, and R. L. Ehman, "MR elastography of breast cancer: Preliminary results," *American Journal of Roentgenology*, vol. 178, no. 6, pp. 1411–1417, 2002.
- [143] M. C. Murphy, r. Huston, J., K. J. Glaser, A. Manduca, F. B. Meyer, G. Lanzino, J. M. Morris, J. P. Felmlee, and R. L. Ehman, "Preoperative assessment of meningioma stiffness using magnetic resonance elastography," *J Neurosurg*, vol. 118, no. 3, pp. 643–8, 2013.
- [144] T. Xydeas, K. Siegmann, R. Sinkus, U. Krainick-Strobel, S. Miller, and C. D. Claussen, "Magnetic resonance elastography of the breast: correlation of signal intensity data with viscoelastic properties," *Invest Radiol*, vol. 40, no. 7, pp. 412–20, 2005.
- [145] M. Simon, J. Guo, S. Papazoglou, H. Scholand-Engler, C. Erdmann, U. Melchert, M. Bonsanto, J. Braun, D. Petersen, I. Sack, and J. Wuerfel, "Non-invasive characterization of intracranial tumors by magnetic resonance elastography," *New Journal of Physics*, vol. 15, no. 8, p. 085024, 2013.
- [146] P. Asbach, D. Klatt, B. Schlosser, M. Biermer, M. Mueche, A. Rieger, C. Loddenkemper, R. Somasundaram, T. Berg, B. Hamm, J. Braun, and I. Sack, "Viscoelasticity-based staging of hepatic fibrosis with multifrequency MR elastography," *Radiology*, vol. 257, no. 1, pp. 80–6, 2010.
- [147] S. K. Venkatesh, M. Yin, and R. L. Ehman, "Magnetic resonance elastography of liver: clinical applications," *J Comput Assist Tomogr*, vol. 37, no. 6, pp. 887–96, 2013.
- [148] L. Xu, Y. Lin, Z. N. Xi, H. Shen, and P. Y. Gao, "Magnetic resonance elastography of the human brain: a preliminary study," *Acta Radiol*, vol. 48, no. 1, pp. 112–5, 2007.
- [149] G. R. Liu, P. Y. Gao, Y. Lin, J. Xue, X. C. Wang, B. B. Sui, L. Ma, Z. N. Xi, Q. Bai, and H. Shen, "Brain magnetic resonance elastography on healthy volunteers: a safety study," *Acta Radiol*, vol. 50, no. 4, pp. 423–9, 2009.
- [150] Y. K. Mariappan, A. Kolipaka, A. Manduca, R. D. Hubmayr, R. L. Ehman, P. Araoz, and K. P. McGee, "Magnetic resonance elastography of the lung parenchyma in an in situ porcine model with a noninvasive mechanical driver: correlation of shear stiffness with trans-respiratory system pressures," *Magn Reson Med*, vol. 67, no. 1, pp. 210–7, 2012.

- [151] Y. K. Mariappan, K. J. Glaser, D. L. Levin, R. Vassallo, R. D. Hubmayr, C. Mottram, R. L. Ehman, and K. P. McGee, "Estimation of the absolute shear stiffness of human lung parenchyma using 1H spin echo, echo planar elastography," *J Magn Reson Imaging*, vol. 40, no. 5, pp. 1230–7, 2014.
- [152] I. Sack, J. Bernarding, and J. Braun, "Analysis of wave patterns in mr elastography of skeletal muscle using coupled harmonic oscillator simulations," *Magnetic Resonance Imaging*, vol. 20, no. 1, pp. 95–104, 2002.
- [153] J. R. Basford, T. R. Jenkyn, K.-N. An, R. L. Ehman, G. Heers, and K. R. Kaufman, "Evaluation of healthy and diseased muscle with magnetic resonance elastography," *Archives of Physical Medicine and Rehabilitation*, vol. 83, no. 11, pp. 1530–1536, 2002.
- [154] S. F. Bensamoun, S. I. Ringleb, L. Littrell, Q. Chen, M. Brennan, R. L. Ehman, and K.-N. An, "Determination of thigh muscle stiffness using magnetic resonance elastography," *Journal of Magnetic Resonance Imaging*, vol. 23, no. 2, pp. 242–247, 2006.
- [155] M. A. Dresner, G. H. Rose, P. J. Rossman, R. Muthupillai, A. Manduca, and R. L. Ehman, "Magnetic resonance elastography of skeletal muscle," *J Magn Reson Imaging*, vol. 13, no. 2, pp. 269–76, 2001.
- [156] K. Uffmann, S. Maderwald, W. Ajaj, C. G. Galban, S. Mateiescu, H. H. Quick, and M. E. Ladd, "In vivo elasticity measurements of extremity skeletal muscle with MR elastography," *NMR in Biomedicine*, vol. 17, no. 4, pp. 181–190, 2004.
- [157] O. Rouviere, R. Souchon, G. Pagnoux, J. M. Menager, and J. Y. Chapelon, "Magnetic resonance elastography of the kidneys: feasibility and reproducibility in young healthy adults," *J Magn Reson Imaging*, vol. 34, no. 4, pp. 880–6, 2011.
- [158] I. Sack, B. Beierbach, U. Hamhaber, D. Klatt, and J. Braun, "Non-invasive measurement of brain viscoelasticity using magnetic resonance elastography," *NMR Biomed*, vol. 21, no. 3, pp. 265–71, 2008.
- [159] P. Latta, M. L. Gruwel, P. Debergue, B. Matwiy, U. N. Sbotto-Frankensteen, and B. Tomanek, "Convertible pneumatic actuator for magnetic resonance elastography of the brain," *Magn Reson Imaging*, vol. 29, no. 1, pp. 147–52, 2011.
- [160] D. K. Yeung, K. S. Bhatia, Y. Y. Lee, A. D. King, P. Garteiser, R. Sinkus, and A. T. Ahuja, "MR elastography of the head and neck: driver design and initial results," *Magn Reson Imaging*, vol. 31, no. 4, pp. 624–9, 2013.
- [161] S. A. Kruse, J. A. Smith, A. J. Lawrence, M. A. Dresner, A. Manduca, J. F. Greenleaf, and R. L. Ehman, "Tissue characterization using magnetic resonance elastography: preliminary results," *Phys Med Biol*, vol. 45, no. 6, pp. 1579–90, 2000.
- [162] J. Braun, K. Braun, and I. Sack, "Electromagnetic actuator for generating variably oriented shear waves in MR elastography," *Magn Reson Med*, vol. 50, no. 1, pp. 220–2, 2003.
- [163] F. Dittmann, R. Reiter, J. Guo, M. Haas, P. Asbach, T. Fischer, J. Braun, and I. Sack, "Tomoelastography of the prostate using multifrequency MR elastography and externally placed pressurized-air drivers," *Magn Reson Med*, vol. 79, no. 3, pp. 1325–1333, 2018.
- [164] K. Uffmann, C. Abicht, H. H. Quick, H. Ulbrich, and M. E. Ladd, "Characterization of an electromagnetic actuator for MR elastography." Proc. 9th Annu. Meeting of ISMRM, 2001, Conference Proceedings, p. 1635.

- [165] P. J. Rossmann, K. J. Glaser, J. P. Felmlee, and R. L. Ehman, "Piezoelectric bending elements for use as motion actuators in MR elastography." Proc. 11th Annu. Meeting of ISMRM, 2003, Conference Proceedings.
- [166] J. Bishop, A. Samani, J. Sciarretta, and D. B. Plewes, "Two-dimensional MR elastography with linear inversion reconstruction: methodology and noise analysis," *Phys Med Biol*, vol. 45, no. 8, pp. 2081–91, 2000.
- [167] Q. C. Chan, G. Li, R. L. Ehman, R. C. Grimm, R. Li, and E. S. Yang, "Needle shear wave driver for magnetic resonance elastography," *Magn Reson Med*, vol. 55, no. 5, pp. 1175–9, 2006.
- [168] J. B. Weaver, E. E. W. Van Houten, M. I. Miga, F. E. Kennedy, and K. D. Paulsen, "Magnetic resonance elastography using 3D gradient echo measurements of steady-state motion," *Medical Physics*, vol. 28, no. 8, pp. 1620–1628, 2001.
- [169] J. H. Runge, S. H. Hoegl, J. Sudakova, A. S. Dokumaci, J. L. Nelissen, J. Lee, J. Stoker, A. J. Nederveen, D. Nordsletten, and R. Sinkus, "A novel MR elastography transducer concept based on a rotational eccentric mass: the gravitational transducer." *Proc. Int. Soc. Magn. Reson. Med.*, vol. 25, 2017.
- [170] Y. Zheng, Q. C. Chan, and E. S. Yang, "Magnetic resonance elastography with twin drivers for high homogeneity and sensitivity," *Conf Proc IEEE Eng Med Biol Soc*, vol. 1, pp. 1916–9, 2006.
- [171] R. Gassert, E. Burdet, and K. Chinzei, "MRI-compatible robotics," *IEEE Engineering in Medicine and Biology Magazine*, vol. 27, no. 3, pp. 12–14, 2008.
- [172] *Standard test method for evaluation of MR image artifacts from passive implants*, ASTM F2119-07, 2007.
- [173] *Medical electrical equipment - Part 2-33: Particular requirements for the basic safety and essential performance of magnetic resonance equipment for medical diagnosis*, EN 60601:2-33, 2017.
- [174] *Standard test method measurements of radio frequency induced heating on or near passive implants during magnetic resonance imaging*, ASTM F2182-11a, 2011.
- [175] *Standard test method for measurement magnetically induced torque on medical devices in the magnetic resonance environment*, ASTM F2213-06, 2006.
- [176] S. D. Serai, M. Yin, H. Wang, R. L. Ehman, and D. J. Podberesky, "Cross-vendor validation of liver magnetic resonance elastography," *Abdom Imaging*, vol. 40, no. 4, pp. 789–94, 2015.
- [177] W. Neumann, T. P. Pusch, M. Siegfarth, L. R. Schad, and S. J., "CT and MRI compatibility of flexible 3D printed materials for soft actuators and robots used in image-guided interventions," *submitted to Journal of Soft Robotics on 24.08.2018*, 2018.
- [178] *Wälzlager - Dynamische Tragzahlen und nominelle Lebensdauer*, DIN ISO 281:2010-10, 2010.
- [179] *Datasheet Kunststoff-Radial-Rillenkugellager, einreihig, 626-POM/GLAS*, Reely, 2010.
- [180] V. Lehnart, "Realisierung zweier parallel betriebener Turbinenvibratoren für die Magnetresonanz-Elastographie," *Bachelor's Thesis*, 2018.

- [181] Festo. (2017) Proportional-druckregelventile VPPM. [Online]. Available: https://www.festo.com/cat/en-gb_gb/data/doc_DE/PDF/DE/VPPM-G_DE.PDF
- [182] Sick. (2018) Fiber-optic sensors and fibers LL3-DT01-05. [Online]. Available: <https://www.sick.com/de/en/photoelectric-sensors/fiber-optic-sensors-and-fibers/ll3/ll3-dt01-05/p/p261670>
- [183] ——. (2018) WLL180T: Fiber-optics sensors and fibers online data sheet. [Online]. Available: https://www.sick.com/media/pdf/7/67/167/dataSheet_WLL180T-P434_6039095_en.pdf
- [184] Microchip. (2016) Curiosity high pin count (HPC) development board user's guide. [Online]. Available: <http://ww1.microchip.com/downloads/en/DeviceDoc/40001856A.pdf>
- [185] Texas Instruments. (2016) LM2576xx series simple switcher(r) 3-a step-down voltage regulator. [Online]. Available: <http://www.ti.com/lit/ds/symlink/lm2576.pdf>
- [186] Microchip. (2015) PIC16(L)F1717/8/9: Cost-effective 8-bit intelligent analog flash microcontrollers. [Online]. Available: <http://ww1.microchip.com/downloads/en/DeviceDoc/40001740B.pdf>
- [187] Analog devices. (2015) ADXL345: Digital accelerometer data sheet. [Online]. Available: <http://www.analog.com/media/en/technical-documentation/data-sheets/ADXL345.pdf>
- [188] Y. Vetter, "Development of a motion-encoding sequence for magnetic resonance elastography," *Master's Thesis*, 2018.
- [189] A. Bichert, "Technische Entwicklung einer Schnittstelle zur Trigger-Signalübertragung zwischen Aktuator und Aufnahmesequenz für die Magnetresonanz-Elastographie," *Bachelor's Thesis*, 2018.
- [190] *Magnetom Trio Operating Instruction*, 2nd ed., Siemens AG, Wittelsbacher Platz 2, 80333 München, 2004.
- [191] *Magnetom Skyra Owner's Manual*, 2nd ed., Siemens AG, Wittelsbacher Platz 2, 80333 München, 2012.
- [192] *Gebrauchsanweisung - MR Elastography*, Drucknr. MR-06020.640.05.02.01 ed., Siemens AG, Wittelsbacher Platz 2, 80333 München, 2014.
- [193] D. White, J. Booz, R. Griffith, J. Spokas, and I. Wilson, "Tissue substitutes in radiation dosimetry and measurements," *International Commission on Radiation Units and Measurements*, 1989.
- [194] P. Steidl, D. Richter, C. Schuy, E. Schubert, T. Haberer, M. Durante, and C. Bert, "A breathing thorax phantom with independently programmable 6D tumour motion for dosimetric measurements in radiation therapy," *Phys Med Biol*, vol. 57, no. 8, pp. 2235–50, 2012.
- [195] J. Oudry, J. Chen, K. J. Glaser, V. Miette, L. Sandrin, and R. L. Ehman, "Cross-validation of magnetic resonance elastography and ultrasound-based transient elastography: a preliminary phantom study," *J Magn Reson Imaging*, vol. 30, no. 5, pp. 1145–50, 2009.

- [196] K. C. Chu and B. K. Rutt, "Polyvinyl alcohol cryogel: an ideal phantom material for mr studies of arterial flow and elasticity," *Magn Reson Med*, vol. 37, no. 2, pp. 314–9, 1997.
- [197] W. Neumann, F. Lietzmann, L. R. Schad, and F. G. Zollner, "Design of a multimodal (1H/23Na MR/CT) anthropomorphic thorax phantom," *Z Med Phys*, vol. 27, no. 2, pp. 124–131, 2017.
- [198] A. F. Holleman and E. Wiberg, Eds., *Lehrbuch der anorganischen Chemie (German Edition)*, 102nd ed. Walter de Gruyter and Co, 1964.
- [199] E. Riedel, Ed., *Allgemeine und Anorganische Chemie (German Edition)*, 10th ed. Walter de Gruyter and Co, 2010.
- [200] A. S. Kashif, T. F. Lotz, M. D. McGarry, A. J. Pattison, and J. G. Chase, "Silicone breast phantoms for elastographic imaging evaluation," *Med Phys*, vol. 40, no. 6, p. 063503, 2013.
- [201] H. Homma, C. L. Mirley, J. Ronzello, and S. A. Boggs, "Field and laboratory aging of rtv silicone insulator coatings," *IEEE Transactions on Power Delivery*, vol. 15, no. 4, pp. 1298–1303, 2000.
- [202] T. I. Inc., *ARES-G2 Rheometer*, 2018. [Online]. Available: <http://www.tainstruments.com/ares-g2/>
- [203] J. Fleischhauer, "Gewebeelastizitäts-imitierendes Adomen Phantom für MRE," *Bachelor's Thesis*, 2017.
- [204] O. Dietrich, J. G. Raya, S. B. Reeder, M. F. Reiser, and S. O. Schoenberg, "Measurement of signal-to-noise ratios in MR images: influence of multichannel coils, parallel imaging, and reconstruction filters," *J Magn Reson Imaging*, vol. 26, no. 2, pp. 375–85, 2007.
- [205] W. Neumann, L. R. Schad, and F. G. Zoellner, "A novel 3D-printed mechanical actuator using centrifugal force for magnetic resonance elastography," *39th Annual International Conference of the IEEE EMBC*, pp. 3541–3544, July 2017.
- [206] W. Neumann, A. Bichert, J. Fleischhauer, A. Stern, R. Figuli, M. Wilhelm, L. R. Schad, and F. G. Zöllner, "A novel 3D printed mechanical actuator using centrifugal force for magnetic resonance elastography: initial results in an anthropomorphic prostate phantom," *PlosOne*, 2018.
- [207] Materialise. Manufacturing - Materials - PA 12 (SLS). Accessed on 29.09.2017. [Online]. Available: <http://www.materialise.com/en/manufacturing/materials/pa-12-sls>
- [208] Technical data sheet. Druckluft-Schalldämpfer Norgren AuSSengewinde M5 10 bar. Accessed on 14.02.2018. [Online]. Available: <https://www.conrad.biz/de/gerade-verbinder-norgren-aussengewinde-m5-rohr-o-6-mm-582729>
- [209] ——. Gerade-Verbinder Norgren Aussengewinde: M5 Rohrdurchmesser: 6 mm. Accessed on 14.02.2018. [Online]. Available: <https://www.conrad.biz/de/gerade-verbinder-norgren-aussengewinde-m5-rohr-o-6-mm-582729>
- [210] *Photocoupler Product data sheet CNY 17-1 through CNY 17-4 series*, Lite-On Corp. Optoelectronics, Taiwan, R.O.C., 2001.
- [211] K. Knossalla, "Zertifizierung eines Wellengebers für die MR-Elastographie - Risikomanagement nach DIN EN ISO 14971:2013-04," *Bachelor's Thesis*, 2017.

- [212] D. A. Herzka, M. S. Kotys, R. Sinkus, R. I. Pettigrew, and A. M. Gharib, "Magnetic resonance elastography in the liver at 3 Tesla using a second harmonic approach," *Magn Reson Med*, vol. 62, no. 3, p. 284291, 2009.
- [213] E. Kanal, A. J. Barkovich, C. Bell, J. P. Borgstede, J. Bradley, W. G., J. W. Froelich, T. Gilk, J. R. Gimbel, J. Gosbee, E. Kuhni-Kaminski, J. Lester, J. W., J. Nyenhuis, Y. Parag, D. J. Schaefer, E. A. Sebek-Scoumis, J. Weinreb, L. A. Zaremba, P. Wilcox, L. Lucey, and N. Sass, "ACR guidance document for safe MR practices: 2007," *AJR Am J Roentgenol*, vol. 188, no. 6, pp. 1447–74, 2007.
- [214] J. Marshall, T. Martin, J. Downie, and K. Malisza, "A comprehensive analysis of MRI research risks: in support of full disclosure," *Can J Neurol Sci*, vol. 34, no. 1, pp. 11–7, 2007.
- [215] *Mechanische Schwingungen - Messung und Bewertung der Einwirkung von Schwingungen auf das Hand-Arm-System des Menschen - Teil 1: Allgemeine Anforderungen (ISO 5349-1:2001)*, DIN EN ISO 5349-1:2001-12, 2012.
- [216] *Directive 2002/44/EC - vibration*, EU directive, 2002.
- [217] K. Scheffler and J. Hennig, "Is TrueFISP a gradient-echo or a spin-echo sequence?" *Magn Reson Med*, vol. 49, no. 2, pp. 395–7, 2003.
- [218] Z. H. Cho and Y. M. Ro, "Reduction of susceptibility artifact in gradient-echo imaging," *Magn Reson Med*, vol. 23, no. 1, pp. 193–200, 1992.
- [219] L. M. White, J. K. Kim, M. Mehta, N. Merchant, M. E. Schweitzer, W. B. Morrison, C. R. Hutchison, and A. E. Gross, "Complications of total hip arthroplasty: MR imaging-initial experience," *Radiology*, vol. 215, no. 1, pp. 254–62, 2000.
- [220] K.-H. Herrmann, C. Gärtner, D. Güllmar, M. Krämer, and J. R. Reichenbach, "3D printing of MRI compatible components: Why every MRI research group should have a low-budget 3D printer," *Medical Engineering and Physics*, vol. 36, no. 10, pp. 1373–1380, 2014.
- [221] M. Wagner, I. Corcuera-Solano, G. Lo, S. Esses, J. Liao, C. Besa, N. Chen, G. Abraham, M. Fung, J. S. Babb, R. L. Ehman, and B. Taouli, "Technical failure of MR elastography examinations of the liver: Experience from a large single-center study," *Radiology*, vol. 284, no. 2, pp. 401–412, 2017.
- [222] O. Dietrich, M. F. Reiser, and S. O. Schoenberg, "Artifacts in 3 T MR: physical background and reduction strategies," *Eur J Radiol*, vol. 65, no. 1, pp. 29–35, 2008.
- [223] M. A. Bernstein, r. Huston, J., and H. A. Ward, "Imaging artifacts at 3.0 T," *J Magn Reson Imaging*, vol. 24, no. 4, pp. 735–46, 2006.
- [224] H. Graf, U. A. Lauer, A. Berger, and F. Schick, "RF artifacts caused by metallic implants or instruments which get more prominent at 3 T: an in vitro study," *Magn Reson Imaging*, vol. 23, no. 3, pp. 493–9, 2005.
- [225] E. M. Merkle, B. M. Dale, J. Thomas, and E. K. Paulson, "MR liver imaging and cholangiography in the presence of surgical metallic clips at 1.5 and 3 Tesla," *Eur Radiol*, vol. 16, no. 10, pp. 2309–16, 2006.
- [226] D. F. Craft, S. F. Kry, P. Balter, M. Salehpour, W. Woodward, and R. M. Howell, "Material matters: Analysis of density uncertainty in 3D printing and its consequences for radiation oncology," *Med Phys*, vol. 45, no. 4, pp. 1614–1621, 2018.

- [227] Y. Itoh, Y. Takehara, T. Kawase, K. Terashima, Y. Ohkawa, Y. Hirose, A. Koda, N. Hyodo, T. Ushio, Y. Hirai, N. Yoshizawa, S. Yamashita, H. Nasu, N. Ohishi, and H. Sakahara, "Feasibility of magnetic resonance elastography for the pancreas at 3 T," *J Magn Reson Imaging*, vol. 43, no. 2, pp. 384–90, 2016.
- [228] S. Maderwald, K. Uffmann, C. J. Galban, A. de Greiff, and M. E. Ladd, "Accelerating MR elastography: a multiecho phase-contrast gradient-echo sequence," *J Magn Reson Imaging*, vol. 23, no. 5, pp. 774–80, 2006.
- [229] J. Rump, D. Klatt, J. Braun, C. Warmuth, and I. Sack, "Fractional encoding of harmonic motions in MR elastography," *Magn Reson Med*, vol. 57, no. 2, pp. 388–95, 2007.
- [230] M. Davids, B. Guérin, M. Malzacher, L. R. Schad, and L. L. Wald, "Predicting magnetostimulation thresholds in the peripheral nervous system using realistic body models," *Scientific Reports*, vol. 7, no. 1, p. 5316, 2017.
- [231] D. Klatt, U. Hamhaber, P. Asbach, J. Braun, and I. Sack, "Noninvasive assessment of the rheological behavior of human organs using multifrequency MR elastography: a study of brain and liver viscoelasticity," *Phys Med Biol*, vol. 52, no. 24, pp. 7281–94, 2007.
- [232] P. Garteiser, R. S. Sahebjavaher, L. C. Ter Beek, S. Salcudean, V. Vilgrain, B. E. Van Beers, and R. Sinkus, "Rapid acquisition of multifrequency, multislice and multidirectional MR elastography data with a fractionally encoded gradient echo sequence," *NMR Biomed*, vol. 26, no. 10, pp. 1326–35, 2013.
- [233] D. Klatt, T. K. Yasar, T. J. Royston, and R. L. Magin, "Sample interval modulation for the simultaneous acquisition of displacement vector data in magnetic resonance elastography: theory and application," *Physics in medicine and biology*, vol. 58, no. 24, pp. 8663–8675, 2013.
- [234] S. Papazoglou, C. Xu, U. Hamhaber, E. Siebert, G. Bohner, R. Klingebiel, J. Braun, and I. Sack, "Scatter-based magnetic resonance elastography," *Phys Med Biol*, vol. 54, no. 7, pp. 2229–41, 2009.
- [235] R. Namani and P. V. Bayly, "Shear wave propagation in anisotropic soft tissues and gels," *Conf Proc IEEE Eng Med Biol Soc*, vol. 2009, pp. 1117–22, 2009.
- [236] M. Honarvar, R. Rohling, and S. E. Salcudean, "A comparison of direct and iterative finite element inversion techniques in dynamic elastography," *Phys Med Biol*, vol. 61, no. 8, pp. 3026–48, 2016.
- [237] M. S. Richards, P. E. Barbone, and A. A. Oberai, "Quantitative three-dimensional elasticity imaging from quasi-static deformation: a phantom study," *Phys Med Biol*, vol. 54, no. 3, pp. 757–79, 2009.
- [238] E. E. Van Houten, K. D. Paulsen, M. I. Miga, F. E. Kennedy, and J. B. Weaver, "An overlapping subzone technique for MR-based elastic property reconstruction," *Magn Reson Med*, vol. 42, no. 4, pp. 779–86, 1999.
- [239] E. E. Van Houten, M. I. Miga, J. B. Weaver, F. E. Kennedy, and K. D. Paulsen, "Three-dimensional subzone-based reconstruction algorithm for MR elastography," *Magn Reson Med*, vol. 45, no. 5, pp. 827–37, 2001.
- [240] D. M. McGrath, N. Ravikumar, I. D. Wilkinson, A. F. Frangi, and Z. A. Taylor, "Magnetic resonance elastography of the brain: An in silico study to determine the influence of cranial anatomy," *Magn Reson Med*, vol. 76, no. 2, pp. 645–62, 2016.

- [241] A. Arani, D. Plewes, and R. Chopra, "Transurethral prostate magnetic resonance elastography: prospective imaging requirements," *Magn Reson Med*, vol. 65, no. 2, pp. 340–9, 2011.
- [242] M. Yin, A. Manduca, A. J. Romano, K. J. Glaser, C. S. Drapaca, D. S. Lake, and R. L. Ehman, "3D local frequency estimation inversion for abdominal MR elastography." Proc. 15th Annu. Meeting of ISMRM, 2007, Conference Proceedings, p. 960.
- [243] K. J. Glaser, A. Manduca, and R. L. Ehman, "Review of mr elastography applications and recent developments," *J Magn Reson Imaging*, vol. 36, no. 4, pp. 757–74, 2012.
- [244] Y. Shi, K. J. Glaser, S. K. Venkatesh, E. I. Ben-Abraham, and R. L. Ehman, "Feasibility of using 3D MR elastography to determine pancreatic stiffness in healthy volunteers," *J Magn Reson Imaging*, vol. 41, no. 2, pp. 369–75, 2015.
- [245] N. Corbin, J. Vappou, E. Breton, Q. Boehler, L. Barbe, P. Renaud, and M. de Mathelin, "Interventional MR elastography for MRI-guided percutaneous procedures," *Magn Reson Med*, vol. 75, no. 3, pp. 1110–8, 2016.
- [246] D. M. McGrath, N. Ravikumar, L. Beltrachini, I. D. Wilkinson, A. F. Frangi, and Z. A. Taylor, "Evaluation of wave delivery methodology for brain MRE: Insights from computational simulations," *Magn Reson Med*, vol. 78, no. 1, pp. 341–356, 2017.
- [247] G. Low, N. E. Owen, I. Joubert, A. J. Patterson, M. J. Graves, K. J. Glaser, G. J. Alexander, and D. J. Lomas, "Reliability of magnetic resonance elastography using multislice two-dimensional spin-echo echo-planar imaging (SE-EPI) and three-dimensional inversion reconstruction for assessing renal stiffness," *J Magn Reson Imaging*, vol. 42, no. 3, pp. 844–50, 2015.
- [248] C. Amador, M. W. Urban, S. Chen, Q. Chen, K. N. An, and J. F. Greenleaf, "Shear elastic modulus estimation from indentation and SDUV on gelatin phantoms," *IEEE Trans Biomed Eng*, vol. 58, no. 6, pp. 1706–14, 2011.
- [249] S. Catheline, J.-L. Gennisson, G. Delon, M. Fink, R. Sinkus, S. Abouelkaram, and J. Culioli, "Measurement of viscoelastic properties of homogeneous soft solid using transient elastography: An inverse problem approach," *The Journal of the Acoustical Society of America*, vol. 116, no. 6, pp. 3734–3741, 2004.
- [250] J. L. Gennisson, T. Defieux, E. Mace, G. Montaldo, M. Fink, and M. Tanter, "Viscoelastic and anisotropic mechanical properties of in vivo muscle tissue assessed by supersonic shear imaging," *Ultrasound Med Biol*, vol. 36, no. 5, pp. 789–801, 2010.
- [251] A. H. Henni, C. Schmitt, and G. Cloutier, "Shear wave induced resonance elastography of soft heterogeneous media," *Journal of Biomechanics*, vol. 43, no. 8, pp. 1488–1493, 2010.
- [252] T. Defieux, G. Montaldo, M. Tanter, and M. Fink, "Shear wave spectroscopy for in vivo quantification of human soft tissues visco-elasticity," *IEEE Transactions on Medical Imaging*, vol. 28, no. 3, pp. 313–322, 2009.
- [253] O. I. Kwon, C. Park, H. S. Nam, E. J. Woo, J. K. Seo, K. J. Glaser, A. Manduca, and R. L. Ehman, "Shear modulus decomposition algorithm in magnetic resonance elastography," *IEEE Trans Med Imaging*, vol. 28, no. 10, pp. 1526–33, 2009.
- [254] D. Gilbar and T. N. S., Eds., *Sobolev Spaces. Elliptic partial differential equations of second order. Classics in Mathematics*. Springer, 2011.

- [255] U. Hamhaber, F. A. Grieshaber, J. H. Nagel, and U. Klose, "Comparison of quantitative shear wave MR-elastography with mechanical compression tests," *Magn Reson Med*, vol. 49, no. 1, pp. 71–7, 2003.
- [256] I. M. Perreard, A. J. Pattison, M. Dooley, M. D. McGarry, Z. Barani, E. E. Van Houten, J. B. Weaver, and K. D. Paulsen, "Effects of frequency- and direction-dependent elastic materials on linearly elastic MRE image reconstructions," *Phys Med Biol*, vol. 55, no. 22, pp. 6801–15, 2010.
- [257] M. M. Dooley, I. Perreard, A. J. Patterson, J. B. Weaver, and K. M. Paulsen, "The performance of steady-state harmonic magnetic resonance elastography when applied to viscoelastic materials," *Med Phys*, vol. 37, no. 8, pp. 3970–9, 2010.
- [258] R. J. Okamoto, E. H. Clayton, and P. V. Bayly, "Viscoelastic properties of soft gels: comparison of magnetic resonance elastography and dynamic shear testing in the shear wave regime," *Phys Med Biol*, vol. 56, no. 19, pp. 6379–400, 2011.
- [259] J. Vappou, E. Breton, P. Choquet, C. Goetz, R. Willinger, and A. Constantinesco, "Magnetic resonance elastography compared with rotational rheometry for in vitro brain tissue viscoelasticity measurement," *MAGMA*, vol. 20, no. 5-6, pp. 273–8, 2007.
- [260] S. I. Ringleb, Q. Chen, D. S. Lake, A. Manduca, R. L. Ehman, and K. N. An, "Quantitative shear wave magnetic resonance elastography: comparison to a dynamic shear material test," *Magn Reson Med*, vol. 53, no. 5, pp. 1197–201, 2005.
- [261] Q. Chen, S. I. Ringleb, T. Hulshizer, and K. N. An, "Identification of the testing parameters in high frequency dynamic shear measurement on agarose gels," *J Biomech*, vol. 38, no. 4, pp. 959–63, 2005.
- [262] S. Tomita, H. Suzuki, I. Kajiwarra, S. Tadano, G. Nakamura, and Y. Jiang, "MRE simulation based on finite element vibration analysis of viscoelastic model." IFNBE Proceedings 43 - Springer International Publishing, 2014, Conference Proceedings, p. 168.
- [263] E. M. Bosboom, C. V. Bouten, C. W. Oomens, F. P. Baaijens, and K. Nicolay, "Quantifying pressure sore-related muscle damage using high-resolution MRI," *J Appl Physiol (1985)*, vol. 95, no. 6, pp. 2235–40, 2003.
- [264] E. C. Qin, L. Juge, S. A. Lambert, V. Paradis, R. Sinkus, and L. E. Bilston, "In vivo anisotropic mechanical properties of dystrophic skeletal muscles measured by anisotropic mr elastographic imaging: the mdx mouse model of muscular dystrophy," *Radiology*, vol. 273, no. 3, pp. 726–35, 2014.
- [265] E. M. Bosboom, M. K. Hesselink, C. W. Oomens, C. V. Bouten, M. R. Drost, and F. P. Baaijens, "Passive transverse mechanical properties of skeletal muscle under in vivo compression," *J Biomech*, vol. 34, no. 10, pp. 1365–8, 2001.
- [266] L. Chami, Y. Jin Long, O. Lucidarme, M. Lefort, and C. Pellot-Barakat, "Feasibility of liver shear wave elastography with different transducers," *2016 IEEE International Ultrasonics Symposium (IUS)*, pp. 1–4.
- [267] T. J. Hall, M. Bilgen, M. F. Insana, and T. A. Krouskop, "Phantom materials for elastography," *IEEE Transactions on Ultrasonics, Ferroelectrics, and Frequency Control*, vol. 44, no. 6, pp. 1355–1365, 1997.

- [268] S. P. Arunachalam, P. J. Rossman, A. Arani, D. S. Lake, K. J. Glaser, J. D. Trzasko, A. Manduca, K. P. McGee, R. L. Ehman, and P. A. Araoz, "Quantitative 3D magnetic resonance elastography: Comparison with dynamic mechanical analysis," *Magn Reson Med*, vol. 77, no. 3, pp. 1184–1192, 2017.
- [269] F. Dittmann, S. Hirsch, H. Tzschatzsch, J. Guo, J. Braun, and I. Sack, "In vivo wideband multifrequency MR elastography of the human brain and liver," *Magn Reson Med*, vol. 76, no. 4, pp. 1116–26, 2016.
- [270] S. M. Atay, C. D. Kroenke, A. Sabet, and P. V. Bayly, "Measurement of the dynamic shear modulus of mouse brain tissue in vivo by magnetic resonance elastography," *J Biomech Eng*, vol. 130, no. 2, p. 021013, 2008.
- [271] M. C. Murphy, r. Huston, J., J. Jack, C. R., K. J. Glaser, A. Manduca, J. P. Felmlee, and R. L. Ehman, "Decreased brain stiffness in alzheimer's disease determined by magnetic resonance elastography," *J Magn Reson Imaging*, vol. 34, no. 3, pp. 494–8, 2011.
- [272] S. Ichikawa, U. Motosugi, H. Morisaka, K. Sano, T. Ichikawa, N. Enomoto, M. Matsuda, H. Fujii, and H. Onishi, "Validity and reliability of magnetic resonance elastography for staging hepatic fibrosis in patients with chronic hepatitis B," *Magn Reson Med Sci*, vol. 14, no. 3, pp. 211–21, 2015.
- [273] R. Chopra, A. Arani, Y. Huang, M. Musquera, J. Wachsmuth, M. Bronskill, and D. Plewes, "In vivo MR elastography of the prostate gland using a transurethral actuator," *Magn Reson Med*, vol. 62, no. 3, pp. 665–71, 2009.
- [274] A. Arani, M. Da Rosa, E. Ramsay, D. B. Plewes, M. A. Haider, and R. Chopra, "Incorporating endorectal MR elastography into multi-parametric MRI for prostate cancer imaging: Initial feasibility in volunteers," *J Magn Reson Imaging*, vol. 38, no. 5, pp. 1251–60, 2013.
- [275] R. S. Sahebjavaher, G. Nir, L. O. Gagnon, J. Ischia, E. C. Jones, S. D. Chang, A. Yung, M. Honarvar, L. Fazli, S. L. Goldenberg, R. Rohling, R. Sinkus, P. Kozlowski, and S. E. Salcudean, "MR elastography and diffusion-weighted imaging of ex vivo prostate cancer: quantitative comparison to histopathology," *NMR Biomed*, vol. 28, no. 1, pp. 89–100, 2015.
- [276] K. F. Stock, B. S. Klein, M. T. Vo Cong, O. Sarkar, M. Romisch, C. Regenbogen, M. Buttner, T. Schuster, E. Matevossian, K. Amann, D. A. Clevert, U. Heemann, and C. Kuchle, "ARFI-based tissue elasticity quantification in comparison to histology for the diagnosis of renal transplant fibrosis," *Clin Hemorheol Microcirc*, vol. 46, no. 2-3, pp. 139–48, 2010.
- [277] T. Syversveen, K. Brabrand, K. Midtvedt, E. H. Strom, A. Hartmann, J. A. Jakobsen, and A. E. Berstad, "Assessment of renal allograft fibrosis by acoustic radiation force impulse quantification—a pilot study," *Transpl Int*, vol. 24, no. 1, pp. 100–5, 2011.
- [278] R. Arndt, S. Schmidt, C. Loddenkemper, M. Grunbaum, W. Zidek, M. van der Giet, and T. H. Westhoff, "Noninvasive evaluation of renal allograft fibrosis by transient elastography—a pilot study," *Transpl Int*, vol. 23, no. 9, pp. 871–7, 2010.
- [279] S. Chen, M. Fatemi, and J. F. Greenleaf, "Quantifying elasticity and viscosity from measurement of shear wave speed dispersion," *J Acoust Soc Am*, vol. 115, no. 6, pp. 2781–5, 2004.

- [280] S. Chen, M. W. Urban, C. Pislaru, R. Kinnick, Y. Zheng, A. Yao, and J. F. Greenleaf, "Shearwave dispersion ultrasound vibrometry (SDUV) for measuring tissue elasticity and viscosity," *IEEE Trans Ultrason Ferroelectr Freq Control*, vol. 56, no. 1, pp. 55–62, 2009.
- [281] R. G. Barr, G. Ferraioli, M. L. Palmeri, Z. D. Goodman, G. Garcia-Tsao, J. Rubin, B. Garra, R. P. Myers, S. R. Wilson, D. Rubens, and D. Levine, "Elastography assessment of liver fibrosis: Society of radiologists in ultrasound consensus conference statement," *Radiology*, vol. 276, no. 3, pp. 845–61, 2015.
- [282] K. Shyamala, H. C. Girish, and S. Murgod, "Risk of tumor cell seeding through biopsy and aspiration cytology," *Journal of International Society of Preventive and Community Dentistry*, vol. 4, no. 1, pp. 5–11, 2014.
- [283] H. Morisaka, U. Motosugi, S. Ichikawa, T. Nakazawa, T. Kondo, S. Funayama, M. Matsuda, T. Ichikawa, and H. Onishi, "Magnetic resonance elastography is as accurate as liver biopsy for liver fibrosis staging," *J Magn Reson Imaging*, vol. 47, no. 5, pp. 1268–1275, 2018.
- [284] P. Bedossa, D. Dargere, and V. Paradis, "Sampling variability of liver fibrosis in chronic hepatitis c," *Hepatology*, vol. 38, no. 6, pp. 1449–57, 2003.
- [285] E. Cholongitas, M. Senzolo, R. Standish, L. Marelli, A. Quaglia, D. Patch, A. P. Dhillon, and A. K. Burroughs, "A systematic review of the quality of liver biopsy specimens," *Am J Clin Pathol*, vol. 125, no. 5, pp. 710–21, 2006.
- [286] C. U. Lee, J. F. Glockner, K. J. Glaser, M. Yin, J. Chen, A. Kawashima, B. Kim, W. K. Kremers, R. L. Ehman, and J. M. Gloor, "MR elastography in renal transplant patients and correlation with renal allograft biopsy: a feasibility study," *Acad Radiol*, vol. 19, no. 7, pp. 834–41, 2012.
- [287] C. Kaminuma, Y. Tsushima, N. Matsumoto, T. Kurabayashi, A. Taketomi-Takahashi, and K. Endo, "Reliable measurement procedure of virtual touch tissue quantification with acoustic radiation force impulse imaging," *J Ultrasound Med*, vol. 30, no. 6, pp. 745–51, 2011.
- [288] J. Oudry, J. Vappou, P. Choquet, R. Willinger, L. Sandrin, and A. Constantinesco, "Ultrasound-based transient elastography compared to magnetic resonance elastography in soft tissue-mimicking gels," *Phys Med Biol*, vol. 54, no. 22, pp. 6979–90, 2009.
- [289] U. Motosugi, T. Ichikawa, F. Amemiya, H. Sou, K. Sano, A. Muhi, N. Enomoto, and T. Araki, "Cross-validation of mr elastography and ultrasound transient elastography in liver stiffness measurement: discrepancy in the results of cirrhotic liver," *J Magn Reson Imaging*, vol. 35, no. 3, pp. 607–10, 2012.
- [290] A. Di Ieva, F. Grizzi, E. Rognone, Z. T. Tse, T. Parittotokkaporn, Y. B. F. Rodriguez, M. Tschabitscher, C. Matula, S. Trattinig, and Y. B. R. Rodriguez, "Magnetic resonance elastography: a general overview of its current and future applications in brain imaging," *Neurosurg Rev*, vol. 33, no. 2, pp. 137–45; discussion 145, 2010.
- [291] S. A. Kruse, G. H. Rose, K. J. Glaser, A. Manduca, J. P. Felmlee, J. Jack, C. R., and R. L. Ehman, "Magnetic resonance elastography of the brain," *Neuroimage*, vol. 39, no. 1, pp. 231–7, 2008.
- [292] S. Chatelin, A. Constantinesco, and R. Willinger, "Fifty years of brain tissue mechanical testing: from in vitro to in vivo investigations," *Biorheology*, vol. 47, no. 5-6, pp. 255–76, 2010.

- [293] R. Mazumder, S. Schroeder, X. Mo, A. S. Litsky, B. D. Clymer, R. D. White, and A. Kolipaka, "In vivo magnetic resonance elastography to estimate left ventricular stiffness in a myocardial infarction induced porcine model," *J Magn Reson Imaging*, vol. 45, no. 4, pp. 1024–1033, 2017.
- [294] H. Dong, R. Mazumder, V. S. P. Illapani, X. Mo, R. D. White, and A. Kolipaka, "In vivo quantification of aortic stiffness using MR elastography in hypertensive porcine model," *Magn Reson Med*, vol. 78, no. 6, pp. 2315–2321, 2017.
- [295] K. J. Streitberger, J. Guo, H. Tzschatzsch, S. Hirsch, T. Fischer, J. Braun, and I. Sack, "High-resolution mechanical imaging of the kidney," *J Biomech*, vol. 47, no. 3, pp. 639–44, 2014.
- [296] K. C. Siegmann, T. Xydeas, R. Sinkus, B. Kraemer, U. Vogel, and C. D. Claussen, "Diagnostic value of MR elastography in addition to contrast-enhanced MR imaging of the breast-initial clinical results," *Eur Radiol*, vol. 20, no. 2, pp. 318–25, 2010.
- [297] J. Lorenzen, R. Sinkus, M. Lorenzen, M. Dargatz, C. Leussler, P. Roschmann, and G. Adam, "MR elastography of the breast: preliminary clinical results," *Rofo*, vol. 174, no. 7, pp. 830–4, 2002.
- [298] M. M. Bahn, M. D. Brennan, R. S. Bahn, D. S. Dean, J. L. Kugel, and R. L. Ehman, "Development and application of magnetic resonance elastography of the normal and pathological thyroid gland in vivo," *Journal of Magnetic Resonance Imaging*, vol. 30, no. 5, pp. 1151–1154, 2009.
- [299] Y. Shi, Y. Liu, Y. Q. Liu, F. Gao, J. H. Li, Q. J. Li, and Q. Y. Guo, "Early diagnosis and severity assessment of acute pancreatitis (AP) using MR elastography (MRE) with spin-echo echo-planar imaging," *J Magn Reson Imaging*, vol. 46, no. 5, pp. 1311–1319, 2017.
- [300] F. Stacul, A. J. van der Molen, P. Reimer, J. A. Webb, H. S. Thomsen, S. K. Morcos, T. Almen, P. Aspelin, M. F. Bellin, O. Clement, and G. Heinz-Peer, "Contrast induced nephropathy: updated ESUR Contrast Media Safety Committee guidelines," *Eur Radiol*, vol. 21, no. 12, pp. 2527–41, 2011.
- [301] H. S. Thomsen, "How to avoid nephrogenic systemic fibrosis: current guidelines in europe and the united states," *Radiol Clin North Am*, vol. 47, no. 5, pp. 871–5, vii, 2009.
- [302] R. A. Vitti, "Gadolinium-based contrast agents and nephrogenic systemic fibrosis," *Radiology*, vol. 250, no. 3, pp. 959; author reply 959–60, 2009.
- [303] E. M. Godfrey, A. J. Patterson, A. N. Priest, S. E. Davies, I. Joubert, A. S. Krishnan, N. Griffin, A. S. Shaw, G. J. Alexander, M. E. Allison, W. J. Griffiths, A. E. Gimson, and D. J. Lomas, "A comparison of MR elastography and ³¹P MR spectroscopy with histological staging of liver fibrosis," *Eur Radiol*, vol. 22, no. 12, pp. 2790–7, 2012.
- [304] J. A. Talwalkar, D. M. Kurtz, S. J. Schoenleber, C. P. West, and V. M. Montori, "Ultrasound-based transient elastography for the detection of hepatic fibrosis: Systematic review and meta-analysis," *Clinical Gastroenterology and Hepatology*, vol. 5, no. 10, pp. 1214–1220, 2007.
- [305] A. A. M. Shaheen and R. P. Myers, "Diagnostic accuracy of the aspartate aminotransferase-to-platelet ratio index for the prediction of hepatitis c related fibrosis: A systematic review," *Hepatology*, vol. 46, no. 3, pp. 912–921, 2007.

- [306] B. E. Van Beers, S. Doblas, and R. Sinkus, "New acquisition techniques: fields of application," *Abdom Imaging*, vol. 37, no. 2, pp. 155–63, 2012.
- [307] S. S. Doblas, P. Garteiser, N. Haddad, J. L. Daire, M. Wagner, H. Leitao, V. Vilgrain, and R. Sinkus, "Magnetic resonance elastography measurements of viscosity: a novel biomarker for human hepatic tumor malignancy." Proc. 19th Annu. Meeting of ISMRM, 2011, Conference Proceedings, p. 389.
- [308] M. R. Engelbrecht, G. J. Jager, and R. J. Laheij, "Local staging of prostate cancer using magnetic resonance imaging: a meta-analysis," *Eur Radiol*, vol. 12, pp. 2294–2302, 2002.
- [309] W. Pegios, W. Bentas, and L. Wittmann, "Kernspintomographisches Staging des Prostatakarzinoms mittels kombinierter endorektal-body-phased-array-Spule und histopathologischer Korrelation," *Fortschr Roentgenstr*, vol. 175, pp. 1660–1666, 2003.
- [310] A. Kolipaka, K. P. McGee, A. Manduca, A. J. Romano, K. J. Glaser, P. A. Araoz, and R. L. Ehman, "Magnetic resonance elastography: Inversions in bounded media," *Magn Reson Med*, vol. 62, no. 6, pp. 1533–42, 2009.

Appendices

Technical Evaluation A

This appendix includes additional data of the acceleration and force measurements of the passive turbine as referred to in Sec. 4.1.1.

Table A.1 – Additional parameters acquired during acceleration measurements (Sec. 4.1.1) for the small and large unbalance.

Frequency	FWHM _s (Hz)	FWHM _l (Hz)
30 Hz	0.84	0.81
40 Hz	0.58	1.60
50 Hz	0.86	0.89
60 Hz	0.71	1.50
70 Hz	1.17	0.24
80 Hz	2.07	1.06
90 Hz	2.16	0.73

Average exerted force

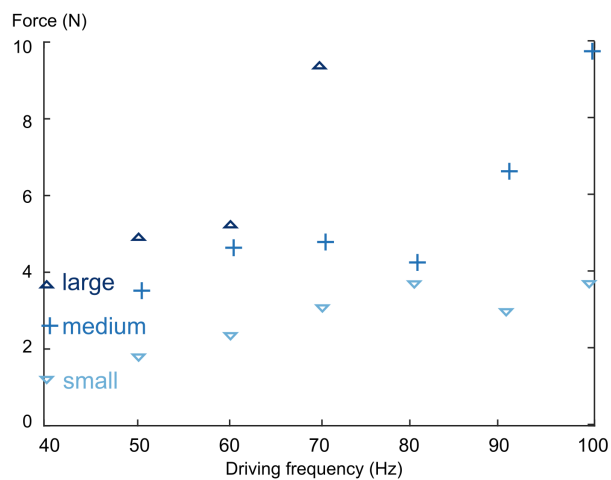
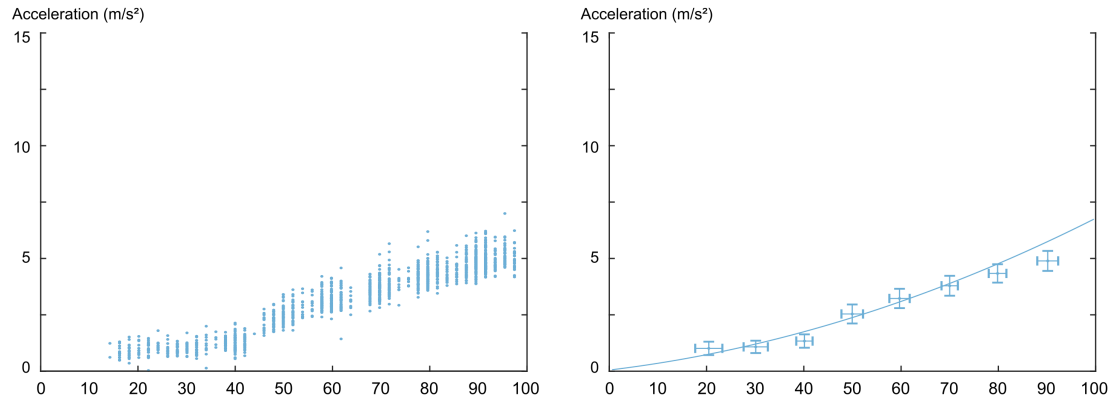


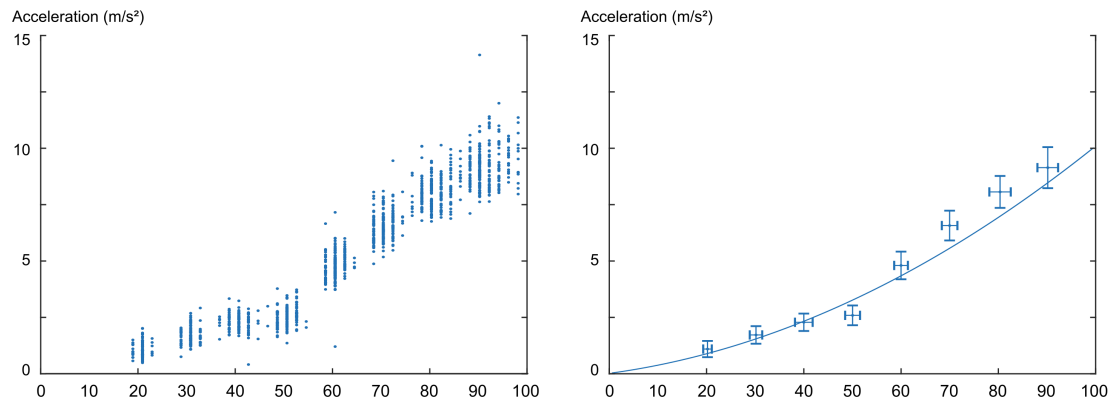
Figure A.1 – Diagrams of average force measurements of the passive driver. Three weights of the unbalance were evaluated.

Acceleration measurements of the turbine

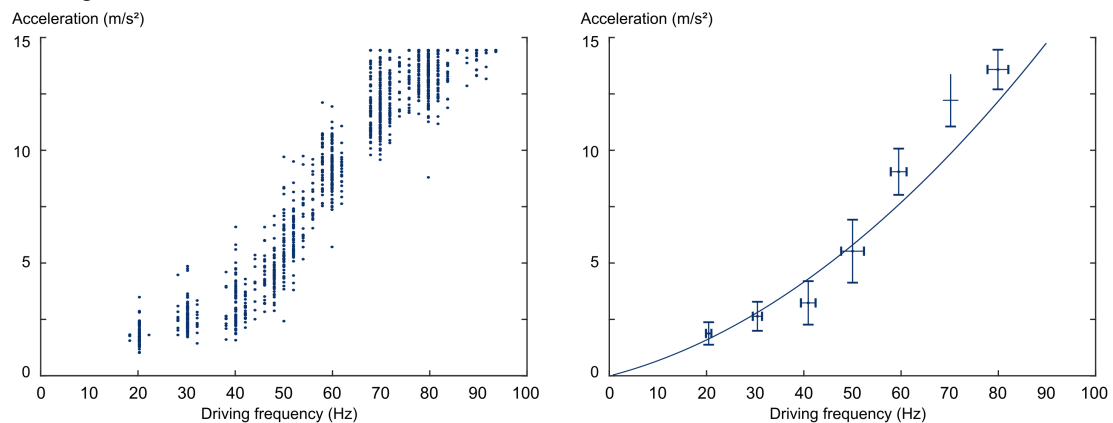
A Small unbalance



B Medium unbalance



C Large unbalance



Acquired data points

Fitted data

Figure A.2 – Diagrams of acceleration measurements of the passive driver. Data points are displayed (left) as well as a fit (right) with average acceleration values and standard deviation in x and y direction. Three weights of the unbalance were evaluated. **A:** Small unbalance. **B:** Medium unbalance. **C:** Large unbalance. The range of the acquired data was restricted to values $< 15 \frac{m}{s^2}$.

Technical Documentation **B**

Selected documents of the technical documentation printed in bold (Sec. 4.1.3) are appended in the following. They include the sections of the product specifications, namely the design documentation:

IV Product specifications

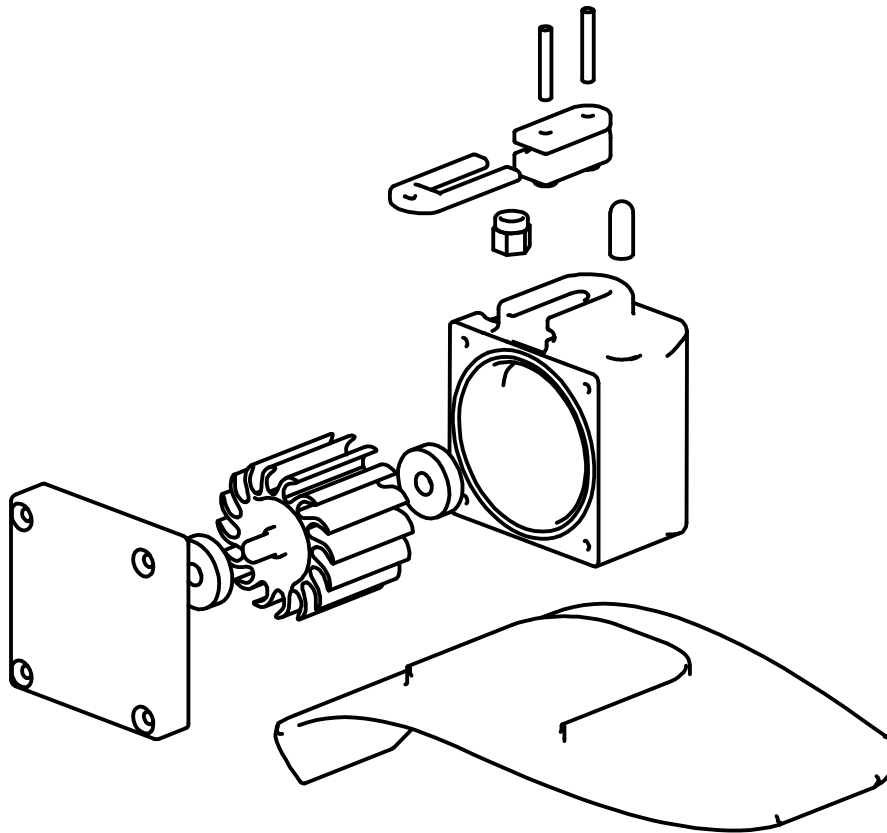
a) Design documentation - Passive Driver

- i. CAD - Overview turbine model V4
- ii. CAD - Housing
- iii. CAD - Side housing
- iv. CAD - Turbine medium unbalance
- v. CAD - Turbine small unbalance
- vi. CAD - Turbine fillable unbalance
- vii. CAD - Light sensor mounting

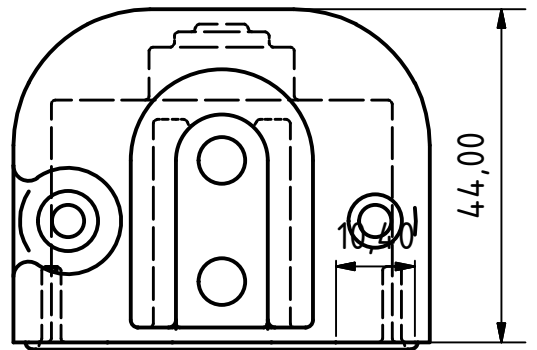
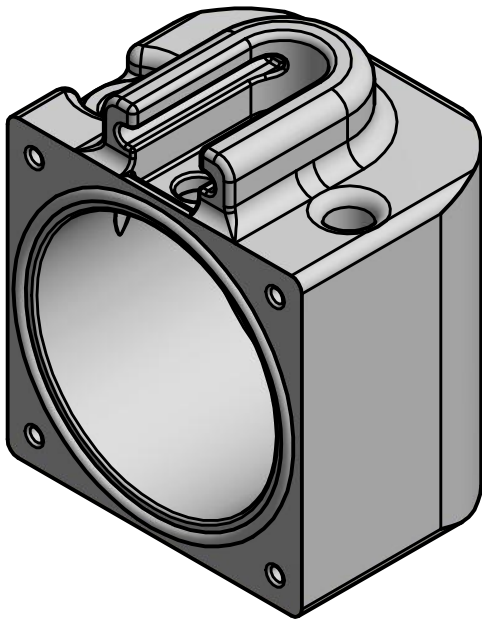
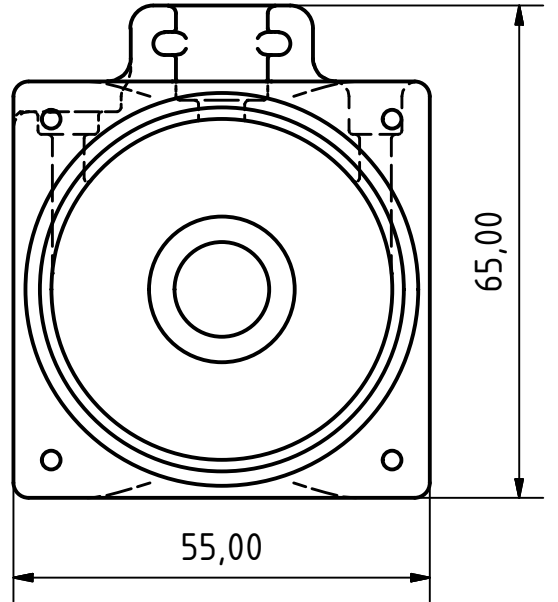
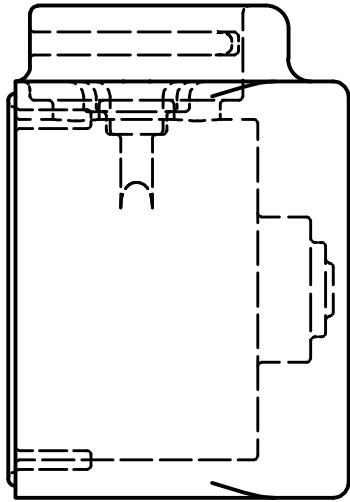
b) Design documentation - Active Driver

- i. Description of function implemented in the micro controller software
- ii. Pin settings and ports of the control unit of the active driver
- iii. List of data sheets of the components of the active driver
- iv. Design of the printed circuit board of the control unit of the active driver

All others documents are included in the electronic version of this thesis or are accessible in the Department of Computer Assisted Clinical Medicine, Medical Faculty Mannheim, Heidelberg University.

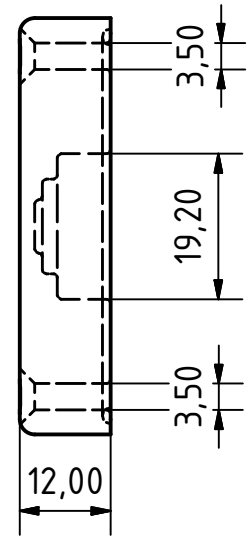
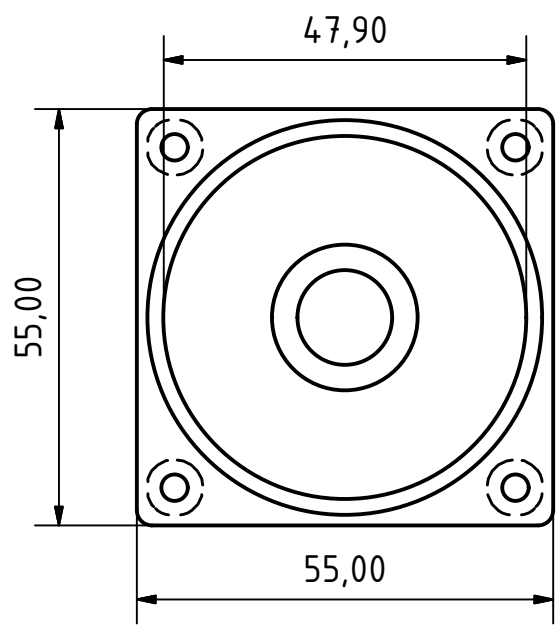
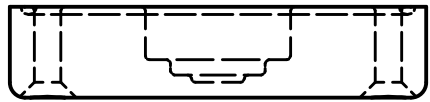
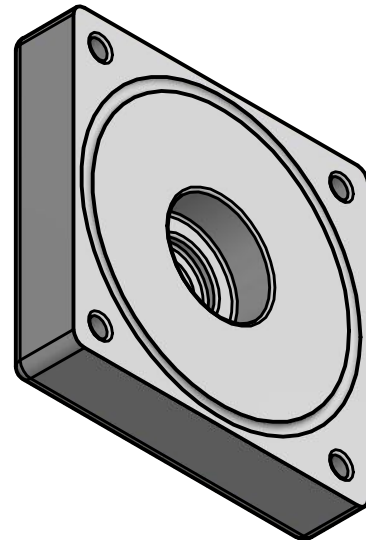


DRAWN	20.02.2018	TITLE Overview turbine model V4 with liver adaptor plate		
wn4				
CHECKED				
QA				
MFG				
APPROVED		SIZE	DWG NO	REV
		A4	V4_assembly_explosion_201802	
		SCALE	1 / 2	SHEET 1 OF 1



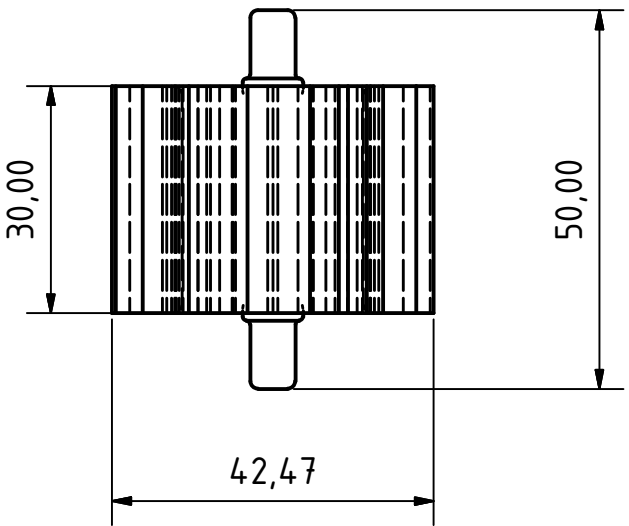
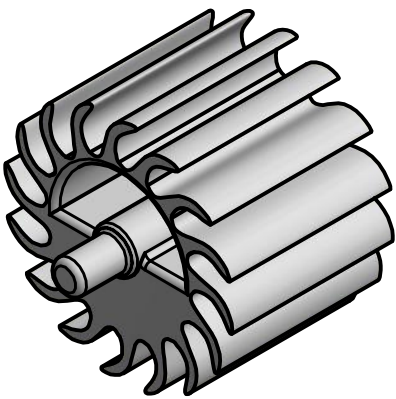
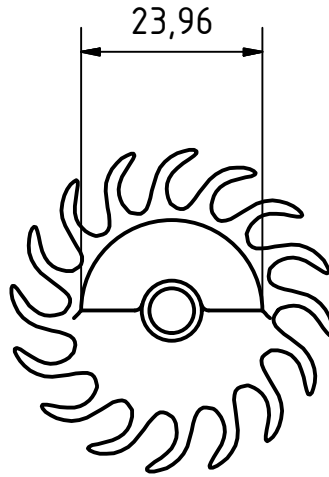
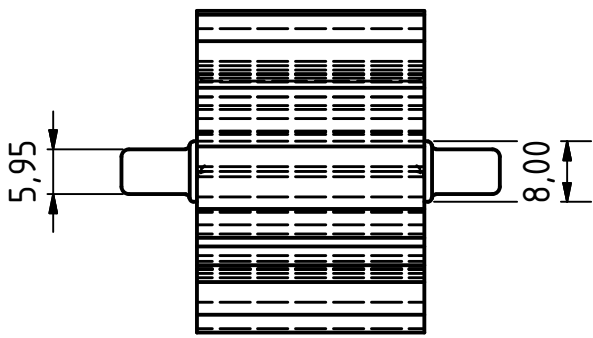
Date	Name
27.02.2018	wn4
Scale	
1 : 1	

V4_housing



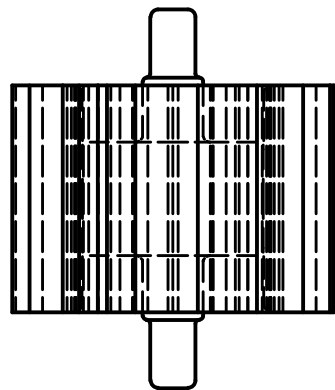
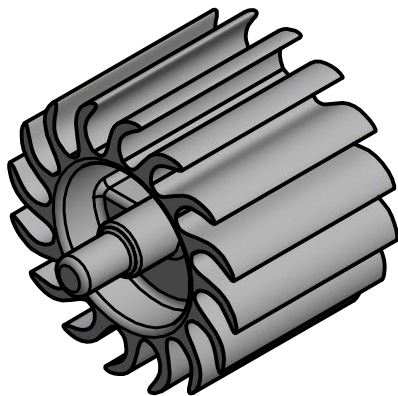
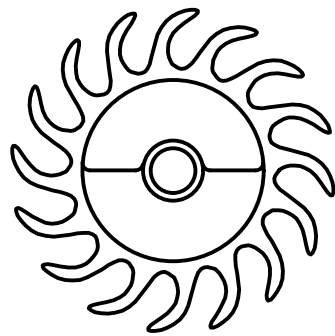
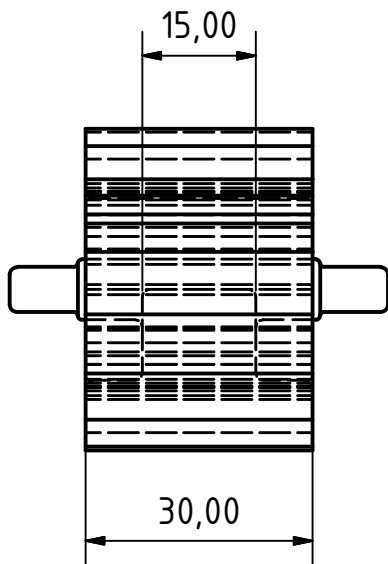
Date	Name
27.02.2018	wn4
Scale	
1 : 1	

V4_housing_side



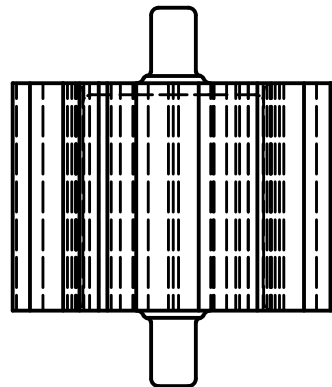
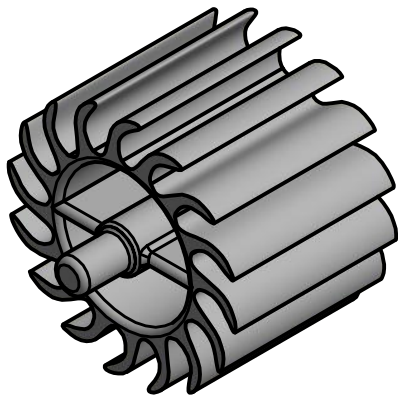
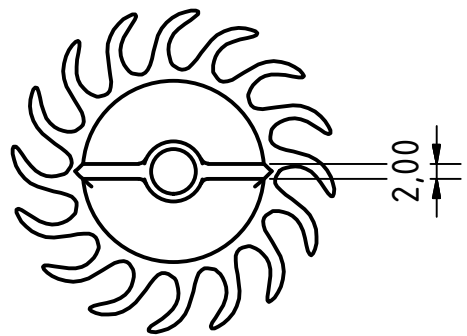
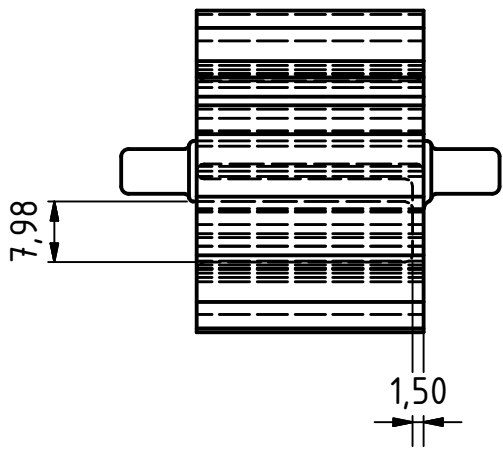
Date	Name
27.02.2018	wn4
Scale	
1 : 1	

V4_turbine



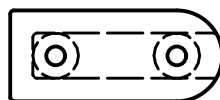
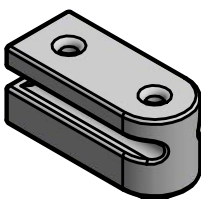
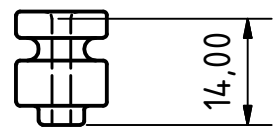
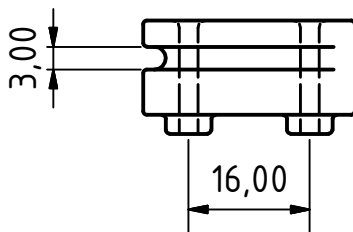
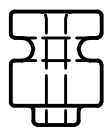
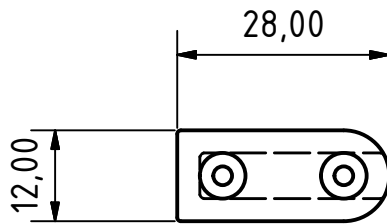
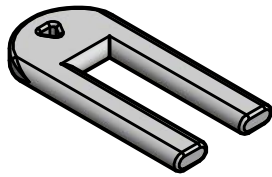
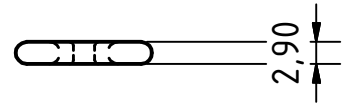
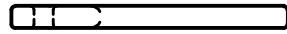
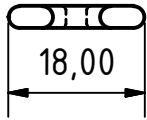
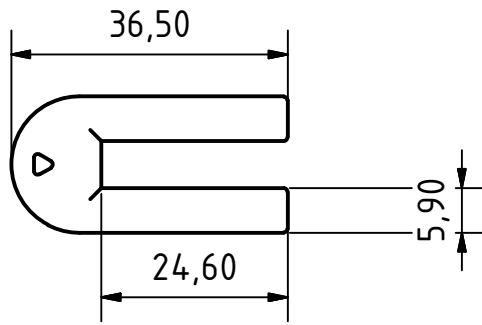
Date	Name
27.02.2018	wn4
Scale	
1 : 1	

V4_turbine_half_unbalance



Date	Name
27.02.2018	wn4
Scale	
1 : 1	

V4_turbine_fillable_unbalance



Date	Name
27.02.2018	wn4
Scale	
1 : 1	

V4_mounting_light_sensor

Technische Dokumentation
Magnetresonanz-Elastographie Wellengeber
Dokument 4.2
Version 1.0
Datum: 06.04.2018

4. Datenblätter und Konstruktionsunterlagen

4.2.1 Steuerungsprogramm der Steuereinheit CKM_EVA

Anwendung

EVA_RED_PIC_Programm_AS ist ein primäres Steuerungsprogramm für **CKM-EVA** System.

Das Programm besteht aus drei Modi:

- **Automatischer Modus:** Der Benutzer gibt die gewünschte Frequenz (Soll-Frequenz) an und das Programm stellt die Frequenz der Wellengeber über die **setDutyValue()**- Funktion automatisch ein.
- **Manueller Modus:** Der Benutzer gibt direkt die Größe von Duty Cycle des PWM-Signals und somit eine Spannung am Ventil ein. Die Frequenz des Wellengebers wird proportional zu Spannung eingestellt.
- **Evaluierungsmodus:** Eine erweiterte Funktion um mit der Hilfe von einem angeschlossenen Beschleunigungssensor die maximale Beschleunigung des Wellengebers pro Sekunde anzeigen zu lassen.

Für Datenspeicherung und besseres Bedienung gibt es ein extra dazu entwickeltes Programm: **EVA_RED_onlySD.X**

Das Programm läuft immer in einer drei Modi. Die Funktionen wie die Frequenzberechnung, Tastenabfrage und Beschleunigungsberechnung arbeiten im Hintergrund.

Dateien

Das Programm besteht aus mehreren Datei-Paare: Header und C-Code Datei und ein **main.c** Datei. Jedes Paar enthält Funktionsdefinitionen und Deklarationen zu einem bestimmten Aspekt des Programms.

functions.c

Die Datei **functions.c** enthält alle selbsterstellte Funktionen und dazu nötige Variablen, die fürs Hauptprogramm nötig sind. Dazu zählen die Funktionen für Frequenzbestimmung, Modi-Funktionen, und Ventilsteuerungsfunktionen.

<ul style="list-style-type: none"> • inkTime() • getTime() • resetTime() 	time-Variable inkrementieren time-Variable zurückgeben time-Variable zurücksetzen
<ul style="list-style-type: none"> • setDutyValue() 	DutyValue anpassen (verschiedene Schrittweiten) → ist_f an soll_f angleichen
<ul style="list-style-type: none"> • inkCount() 	Zähler erhöhen → Frequenz
<ul style="list-style-type: none"> • countFrequenzy() • inkFrequenzy() • dekFrequenzy() 	count-Wert ins ist_f umrechnen(von der Zeitinterval und Flankenanzahl abhängig) soll_f erhöhen wenn S2-Taste gedrückt ist soll_f verringern wenn S1-Taste gedrückt ist
<ul style="list-style-type: none"> • changeMode() 	Betriebsmodus ändern (A→M→E), soll_f und DutyValue (ist_f) zurücksetzen
<ul style="list-style-type: none"> • inkVoltage() • dekVoltage() • getVoltage() • getMaxAcc() 	Spannung/Duty-Cycle erhöhen wenn S2-Taste gedrückt ist Spannung/Duty-Cycle → verringern wenn S1-Taste gedrückt ist Spannungswert zurückliefern aus Duty-Cycle-Wert → an LCD-Ausgabe Beschleunigung in x-Richtung abfragen, größten Wert speichern (1 pro s)
<ul style="list-style-type: none"> • autoMode() • ManMode() • evaMode() 	Anzeige: soll_f & ist_f mode=0 Soll_f über Tasten einstellen Anzeige: Spannung (Duty-Cycle) & Frequenz (ist_f) mode=1 Direkte Eingabe von DutyCycle Anzeige: Beschleunigung [mG] & soll_f, ist_f mode=2 Soll_f über Tasten einstellen

Liste der Funktionen

Die Funktionen werden meistens in Rahmen von Interrupt Service Routine von jeweiligem Peripherie-Modul ausgeführt.

Die Funktionen setDutyValue() und allgemeine Mode-Funktion(passt für alle drei Funktionen) werden hier grafisch dargestellt

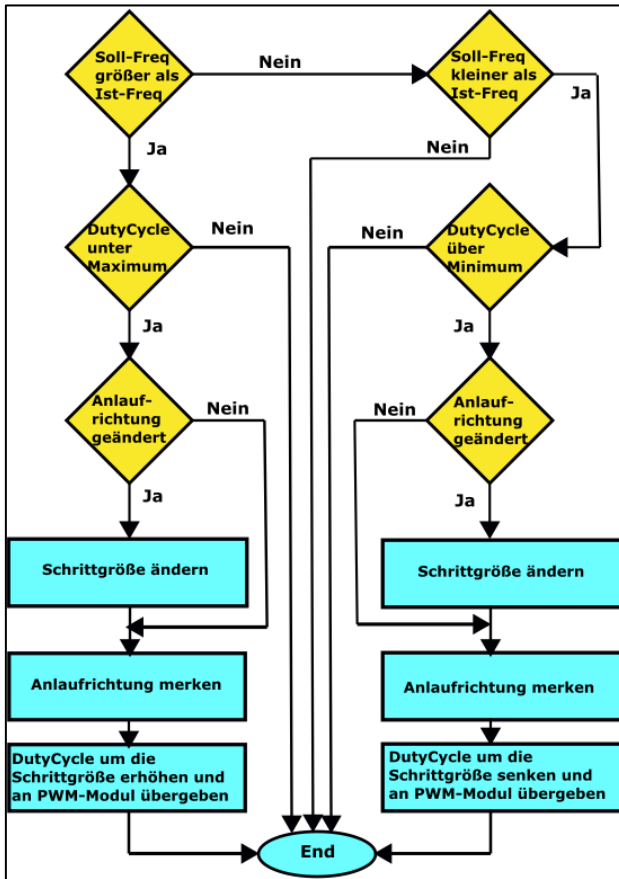


Abb.1: setDutyValue() Funktion

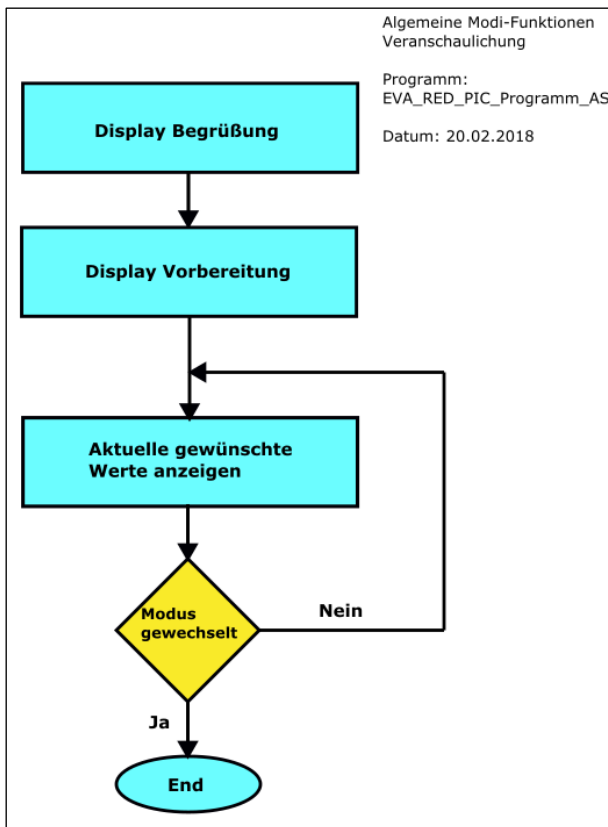


Abb. 2: Mode-Funktion

mcc.c : System Initialisierung

mcc.c enthält die Initialisierung und Grundeinstellungen die der Mikrokontroller beim Einschalten übernimmt. Die Funktion **SYSTEM_Initialize()** enthält alle Initialisierungsfunktion des Mikrokontrollers und seiner Peripherie.

OSZILLATOR_Initialize() stellt den Oszillator ein. Dieser Datei so wie die folgenden wurden mit Hilfe von der Erweiterung MCC (Microchip Code Configurator) erstellt.

tmr0.c : Timer0 Funktionen

tmr0.c erhält die Funktionen, die für die Steuerung von Zähler-Modul notwendig sind. Alle 5ms unterbricht Timer0 den Programmablauf und startet sein Interrupt Service Routine, hier als eigene Funktion **TMR0_DefaultInterruptHandler()** benannt. InterruptHandler zählt die Unterbrechungen mit Hilfe der **inkTime()** und nach gewünschter Zeitperiode (count=200, entspricht 1 sek) startet die Funktion **countFrequency()**.

tmr1.c : Timer1 Funktionen

Timer 1 ist der Zähler, mit denen die Abfrage der Knöpfe realisiert wurde. Alle 30ms wird abgefragt, ob einer der zwei Knöpfe oder beide gleichzeitig gedrückt wurden. Gleichzeitiges Drücken startet die Funktion **changeMode()**, sonst werden je nach Modus werden die Werte für die Spannung und Soll-Frequenz inkrementiert oder dekrementiert.

tmr2.c : Timer2

Timer 2 wird nicht direkt benutzt, sondern wird für die Funktion von PWM3- Modul benötigt.

pwm3.c : PWM3-Modul

PWM-Modul wird benötigt um ein regelbaren Spannungssignal für Druckluftventil zu erzeugen.

Die Datei enthält eine Funktion zum Initialisieren und eine um den DutyCycle-Wert (Spannung) zu ändern.

tmr4.c : Timer4

Timer 4 wird zurzeit nicht benutzt.

pin_manager.c: Pin-Belegung und Pin-Interrupt(IOC)

Die Datei enthält die Funktion, die alle benötigte Pins und deren Eigenschaften festsetzt (**PIN_MANAGER_Initialize()**), sowie Funktionen für IOC(Interrupt On Change).

Hier, wie auch beim Timer0 und 1, gibt es ein **DefaultInterruptHandler()**, der die Funktionen enthält bei welchem der Interrupt ausgeführt werden sollen.

Pin C0 bekommt ein Signal von der Lichtschranke, jede Flanke (positiv und negativ) löst den Interrupt worauf die **inkCount()** ausgeführt wird. Somit dienen diese Funktion und der Timer0, um die Ist-Frequenz zu bestimmen.

In den zusätzlichen Evaluierungsmodus wird auch nach jeden dritten Interrupt die Funktion **getMaxAcc()** ausgeführt.

interrupt_manager.c

Enthält die Funktion, die Interruptsabläufe regelt.

spi.c: Kommunikation zwischen Mikrocontroller und Beschleunigungssensor

Die Kommunikation zwischen Mikrocontroller und Beschleunigungssensor ADXL345 wird mit Hilfe von SPI(Serial Peripheral Interface) realisiert. Dabei spielt die zentrale Rolle die Funktion **SPI_Exchange8bit(uint8_t data)**. Die Funktion wird benutzt um die Befehle zu schicken und Daten von ADXL345 abzulesen (die ausführliche Bezeichnung enthalten die Datenblätter von PIC18F1719 und ADXL345).

Lcd_mini.c: Anzeige-Funktionen

Hier werden die Funktionen für die Bedienung von LCD-Modul definiert. LCD wird nur im Write- Modus betrieben.

WriteLcdMiniCommand(uint8_t cmd)	Ein Befehl an LCD schicken (Befehl-codes im Datenblatt)
LcdMiniInitialization ()	8-bit-Betrieb Initialisierung (Beispiel im Datenblatt)
WriteLcdMiniByte(uint8_t data)	Ein Zeichen auf dem Bildschirm schreiben
WriteLcdMiniString(char *data)	Ein String schreiben
LcdMiniGoto(uint8_t row, uint8_t column)	Cursor verschieben
LcdMiniClear()	Anzeige löschen

adxl345.c: Beschleunigungssensor- Funktionen

Die Funktionen benutzen SPI-Funktionen. Mit deren Hilfe werden die Befehle an den Sensor übergeben und Daten von dem Sensor gelesen. Die Befehle werden ausführlich im Datenblatt beschrieben.

ADXL345Init()	Arbeitsmodus der Sensor einstellen
getX/Y/Z()	Die jeweiligen Achsenwerte auslesen
setOffset(int8_t x,int8_t y,int8_t z)	Offset einstellen (Kalibrierung der Sensor)

main.c

Die main-Funktion initialisiert und regelt den Programmablauf.

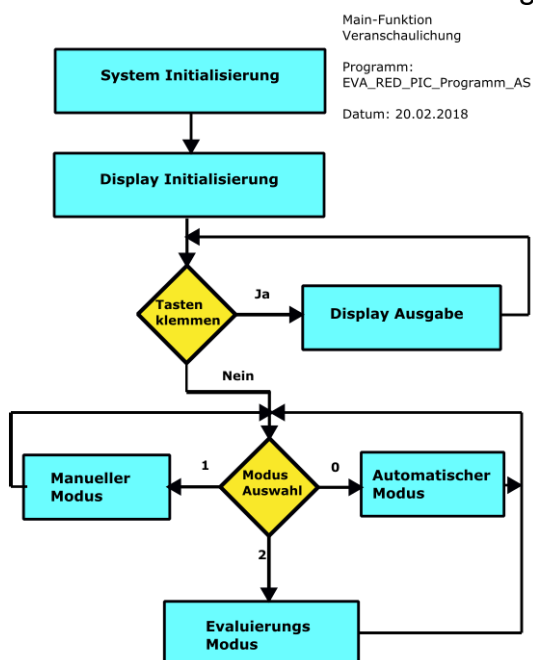


Abb. 3: Veranschaulichung der main-Funktion

4.2.2 Pin-Belegung und Anschlüsse der Steuereinheit CKM_EVA

Anschlüsse vom EVA RED zum SVVS-board v.1

Datum: 06.12.2017

Programm: EVA_RED_ADXL_b.1.0.X *Bemerkung: enthält Eva-Modus*

Verweis: G:\CKM_Ressourcen\Elastography\PIC Project\PIC Programme\EVA_RED_ADXL_b.1.0.X

Rotes Kabel von EVA RED an 5VSUPPLY auf dem SVVS

Grünes Kabel von EVA RED an GND auf dem SVVS

Ein Kabel zwischen **LSON** auf dem SVVS und **RC0**-Pin auf der EVA RED

Ein Kabel zwischen **PWMOUT** auf dem SVVS und **RB0**-Pin auf der EVA RED

LCD-Anschluss

16 Pins Bandkabel: **Orange ist Pin1, grau ist Pin16**

Versorgungsspannung Pin1 (orange)->GND Pin2 (rot)->5V(Vdd) Beleuchtung Pin16 (grau)->GND Pin15 (weiß)-> über ein 10Ω Widerstand(!) auf 5V(Vdd)	Steuersignale Pin3 (braun)->RA0 (Kontrast über Poti) Pin4 (schwarz)->RE1(RS) Pin5 (weiß)->GND(RW) Pin6 (grau)->RE0(E) Pins7-14 ->auf RD0-RD7(Data bus)
---	---

Bemerkung: Es sind die Anschlüsse neben dem Mikrocontroller zu benutzen, ein **10Ω Widerstand** gibt es als extra Draht mit Pins.

Weitere Anschlüsse für beide Varianten:

4-pin-Anschluss für die Lichtschranke: Pin1 (blau) an GND auf dem SVVS Pin3 (schwarz) an LSOUT auf dem SVVS Pin4 (braun) an 24VSUPPLY auf dem SVVS	6-pin-Anschluss für das Ventil: Pin1 (braun) an 24VSUPPLY auf dem SVVS Pin4 (gelb) an VENTILIN auf dem SVVS Pin5&6 (grün&blau) an GND auf dem SVVS
--	--

Innere Anschlüsse und Pinbelegung CKM-EVA-2

Datum: 11.12.2017

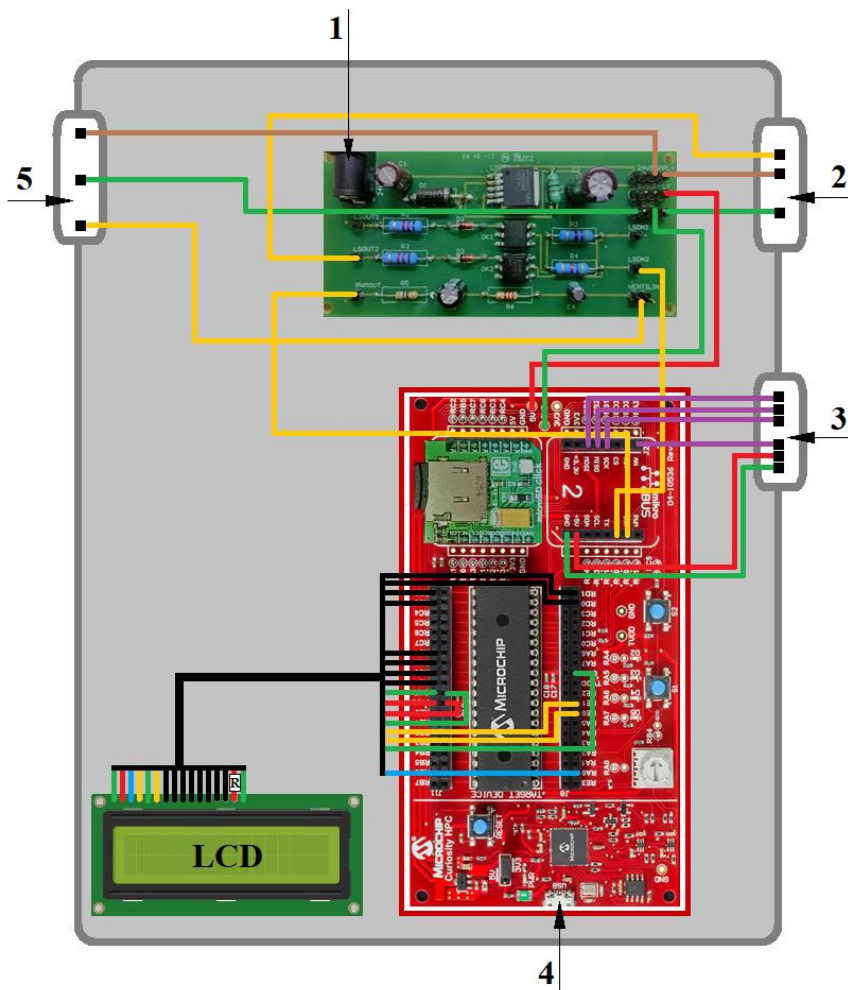
Steuerungsprogramm: EVA_RED_ADXL_b.1.0.X *Mit Eva-Modus ohne SD-Karte*

Verweis: G:\CKM_Ressourcen\Elastography\PIC Project\PIC Programme\EVA_RED_PIC_Programm_AS

Evaluierung-Programm: EVA_RED_onlySD.X *Nur Eva-Modus mit Sd-Karte*

Verweis: G:\CKM_Ressourcen\Elastography\PIC Project\PIC Programme\EVA_RED_onlySD.X

1. 24V Anschluss für die Netzteil
2. Lichtschranke- Anschlusssockel
3. Accelerometer-Anschlusssockel
4. mikroUSB-Anschluss
5. Ventil-Anschlusssockel



- Farblegende:**
Braun: 24V Versorgungsspannung
Grün: Ground
Rot: 5V/Vdd
Gelb: Steuerungssignale
Schwarz: Datenbus
Violett: SPI-Steuerungssignale

Die Farben entsprechen **nicht** den tatsächlichen Draht-farben! (siehe weitere Anschlussbeschreibungen)

LCD Anschluss an CKM-EVA

16 Pins Bandkabel: **Orange ist Pin1, grau ist Pin16**

Versorgungsspannung Pin1 (orange)->GND Pin2 (rot)->5V(Vdd) Beleuchtung Pin16 (grau)->GND Pin15 (weiß)-> über ein 10Ω Widerstand(!) auf 5V(Vdd)	Steuersignale Pin3 (braun)->RA0 (Kontrast über Poti) Pin4 (schwarz)->RE1(RS) Pin5 (weiß)->GND(RW) Pin6 (grau)->RE0(E) Pins7-14 ->auf RD0-RD7(Data bus)
---	---

Bemerkung: Es sind die Anschlüsse neben dem Mikrocontroller zu benutzen, ein **10Ω Widerstand** gibt es als extra Draht mit Pins.

Anschluss von an CKM-EVA-Red auf SVVS

Rotes Kabel(5V) von **EVA RED** an **5VSUPPLY** auf dem **SVVS**

Grünes Kabel(GND) von **EVA RED** an **GND** auf dem **SVVS**

Ein Kabel(**orange**) zwischen **RC0**-Pin auf der **EVA RED** und **LSON2** auf dem **SVVS**

Ein Kabel(**orange**)zwischen **RB0**-Pin auf der **EVA RED** und **PWMOUT** auf dem **SVVS**

Sockelanschlüsse auf SVVS

Lichtschranke- Anschlusssockel: Pin1 (blau) an GND auf dem SVVS Pin3 (schwarz) an LSOUT2 auf dem SVVS Pin4 (braun) an 24VSUPPLY auf dem SVVS	Ventil-Anschlusssockel : Pin1 (braun) an 24VSUPPLY auf dem SVVS Pin4 (gelb) an VENTILIN auf dem SVVS Pin5&6 (grün&blau) an GND auf dem SVVS
--	---

Accelometer-Anschlusssockel auf EVA-RED

Pin-Belegung	Funktion
Pin1 (braun) auf 5V	Versorgungsspannung
Pin3 (rot) auf GND	Ground
Pin4 (gelb) auf RA2	Chip-Select(CS)
Pin7 (violett) auf RB2	MISO(Master In Slave Out) ADXL->EVA
Pin8 (grau) auf RB3	MOSI(Master Out Slave In) EVA->ADXL
Pin9 (weiß) auf RB1	SCK (Takt)

Hinweis: Pins **2** und **5** sind nicht belegt, Pin 6 ist leer. Die Anschlüsse des 2. Mikro-bus haben alle nötige Pins und sind zusätzlich mit Funktionen beschriftet.

Für EVA-3 werden die D-Sub-Standard-Steckverbinder benutzt und farbige Verbindungsdrähte mit male/female Pins. Der nicht benutzte Pin wird abgeschnitten und abisoliert (etwa 5mm). Ein Schrumpfschlauch (etwa 10mm) aufbringen und zuerst nach hinten weg von der Lötstelle bringen. Das abisolierte Kabel in gewünschten Pin der Steckverbinder reinstecken und anlöten. Die Schrumpfschläuche auf die Lötstellen ziehen und mit Heißluftfön aufwärmen bis sie festsitzen (**!Vorsicht!** der Stecker werden davon auch heiß).

Sensoranschluss

Gehäuse		Kabel	
Steckverbinder: female 25-Pin Bunte Kabeln mit male -Pin		Steckverbinder: male 25-Pin Kabel: Regenbogen-Bandkabel	
1-Pin ->	brauner Draht	1-Pin ->	brauner Draht
3-Pin ->	roter Draht	3-Pin ->	roter Draht
5-Pin ->	orangener Draht	5-Pin ->	orangener Draht
8-Pin ->	gelber Draht	8-Pin ->	gelber Draht
11-Pin ->	grüner Draht	11-Pin ->	grüner Draht
16-Pin ->	blauer Draht	16-Pin ->	blauer Draht
19-Pin ->	violetter Draht	19-Pin ->	violetter Draht
22-Pin ->	grauer Draht	22-Pin ->	grauer Draht
25-Pin ->	weiser Draht	25-Pin ->	weiser Draht

Ventilanschluss

Gehäuse		Kabel	
Steckverbinder: female 15-Pin Bunte Kabeln mit female -Pin		Steckverbinder: male 15-Pin Kabel: M8-Kabel	
1-Pin ->	brauner Draht	1-Pin ->	brauner Draht
5-Pin ->	orangener Draht	5-Pin ->	gelber Draht
15-Pin ->	grüner Draht	15-Pin ->	grüner&blauer Draht

Lichtschrankenanschluss

Gehäuse		Kabel	
Steckverbinder: female 9-Pin Bunte Kabeln mit female -Pin		Steckverbinder: male 9-Pin Kabel: M4-Kabel	
1-Pin ->	brauner Draht	1-Pin ->	brauner Draht
3-Pin ->	orangener Draht	3-Pin ->	roter Draht
9-Pin ->	grüner Draht	9-Pin ->	blauer Draht

Hinweise zu SVVS-2:

Design

Obere Reihe beinhaltet Komponenten der Spannungsversorgung

Untere Reihe: PWM-Signalglättung (Tiefpass)

Zwei mittleren Reihen: Lichtschrankensignal-Verarbeitung (24V->5V)

Layer-Anzahl: 2

Bottom-Layer: Ground-Netz

Top-Layer: Signal- und Spannungsleitungen

Leitungsdicke: 0,508mm

Vias bei Spannungsregler LM2596S, Durchmesser: 1mm

Montage-Bohrungen: 3mm

Hinweise zu Bestückung

1. Die Durchkontaktierungen bei Vias schaffen mit Hilfe von passenden Draht und Lötzinn.
2. LM2596S fest positionieren, z.B. mit Hilfe von Kreuzpinzette
3. Anbringen aller verbleibenden Bauteilen.



Abb. 5: Bestückung der Schaltplatine SVVS-2

This appendix includes additional data of the rheometric evaluation of silicones as referred to in Sec. 4.3.1.

Elasticity changes of the silicones after four months

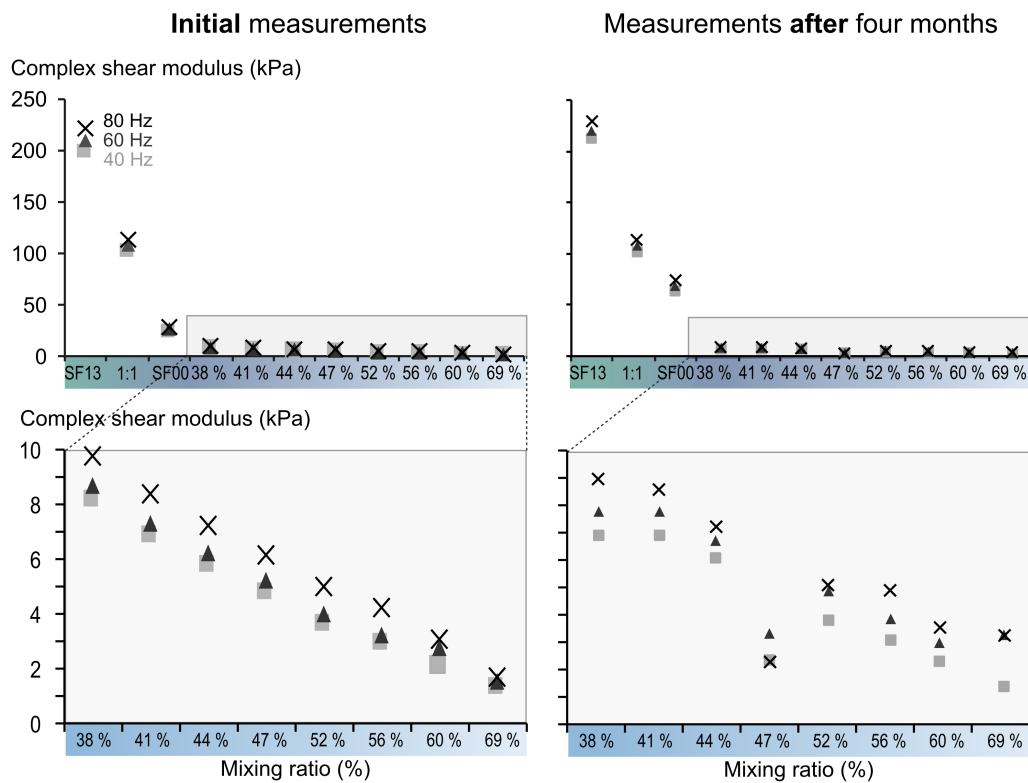


Figure C.1 – Diagram of elasticity changes of silicone samples after four months. Upper row shows selected samples covering the minimum and maximum range of shear moduli of the evaluated silicon samples. The lower row shows samples diluted with silicone oil in the range of human soft tissue elasticity.

Elasticity variations due to **A** long term storage and **B** batch variations

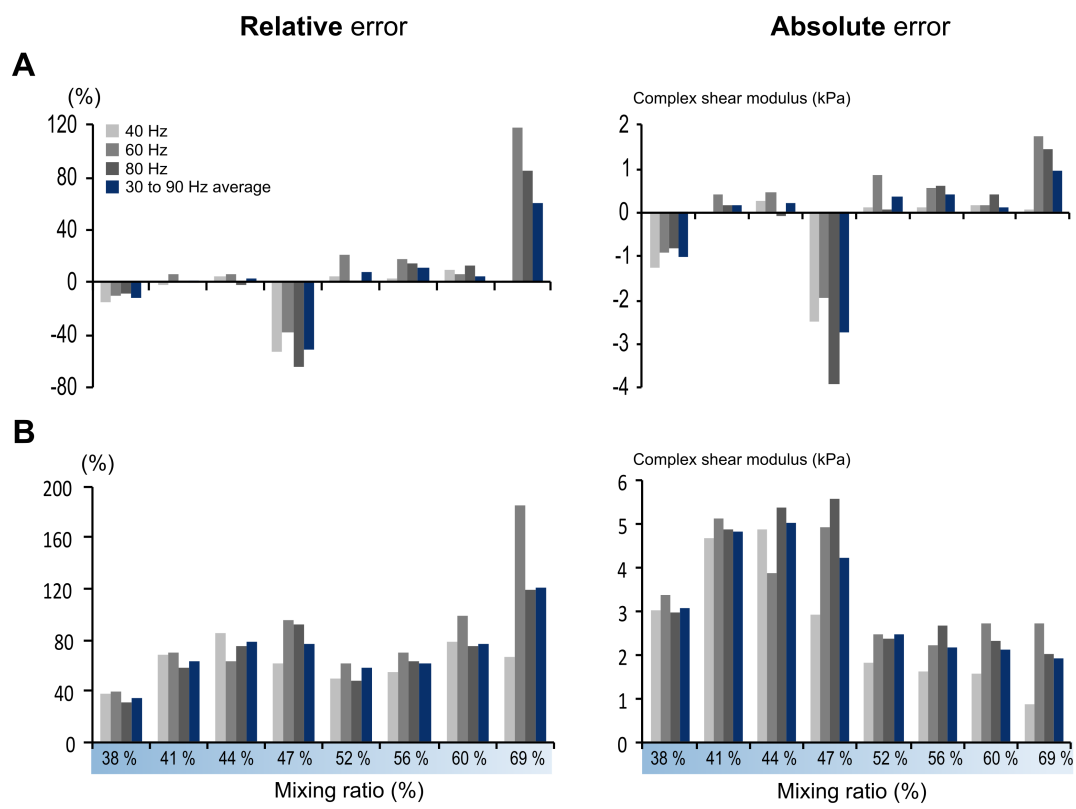


Figure C.2 – Diagram of relative (left) and absolute (right) error of the shear modulus due to **A**: long term storage and **B**: batch variations.

The elasticity varied between batches of raw materials

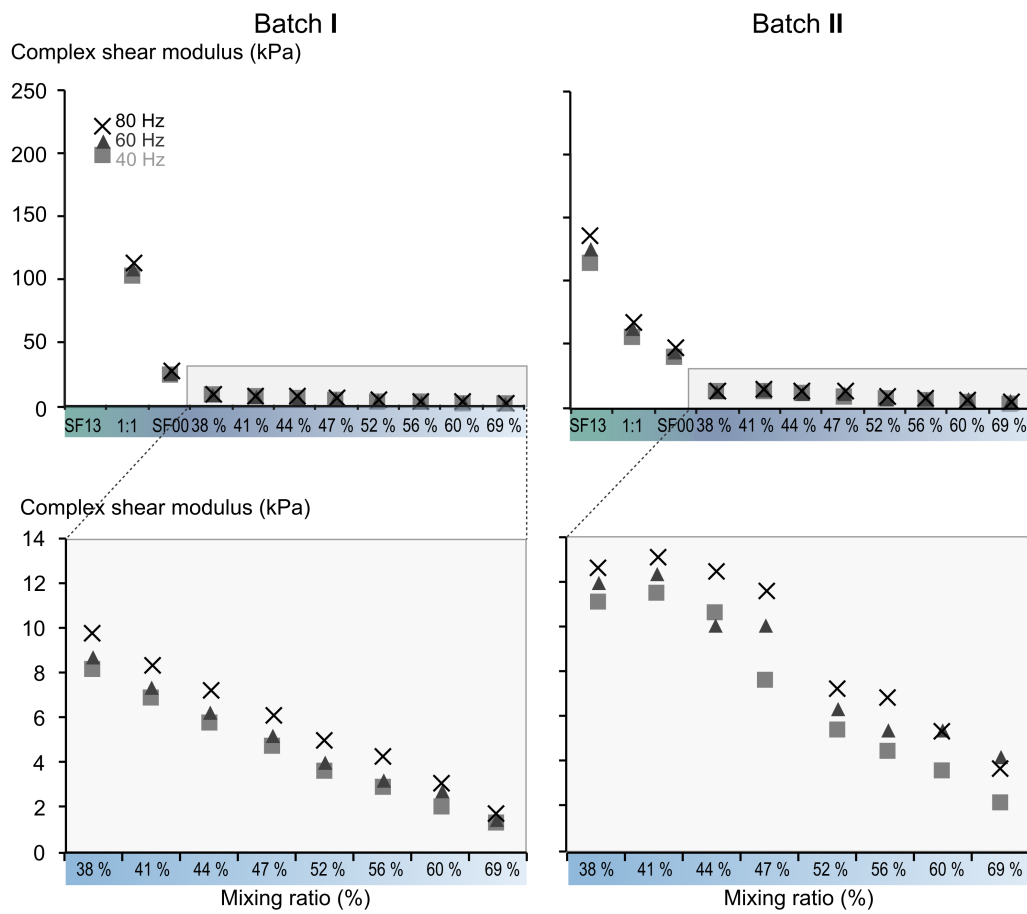


Figure C.3 – Diagram of elasticity changes of silicone samples due to different batches of raw material. Upper row shows selected samples covering the minimum and maximum range of shear moduli of the evaluated silicon samples. The lower row shows samples diluted with silicone oil in the range of human soft tissue elasticity.

The shear modulus depends on the sample's height and diameter

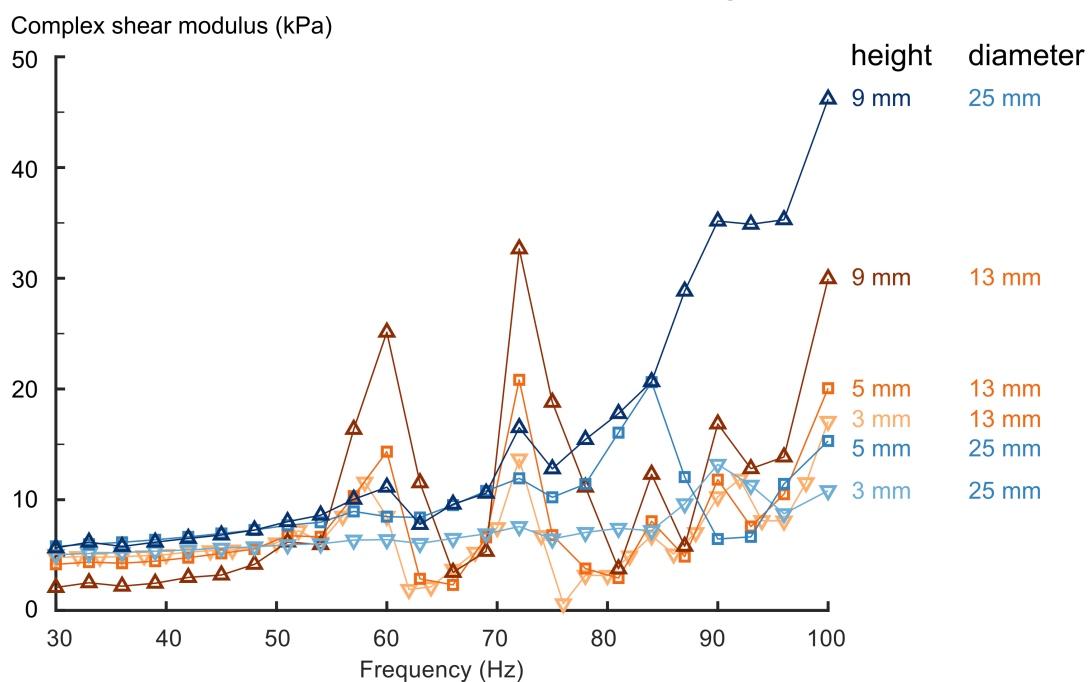


Figure C.5 – Diagram of elasticity curve of samples with two different diameters (13 mm in orange and 25 mm in blue) and three different sample heights.

Scatter particles increase the shear modulus of the silicone sample

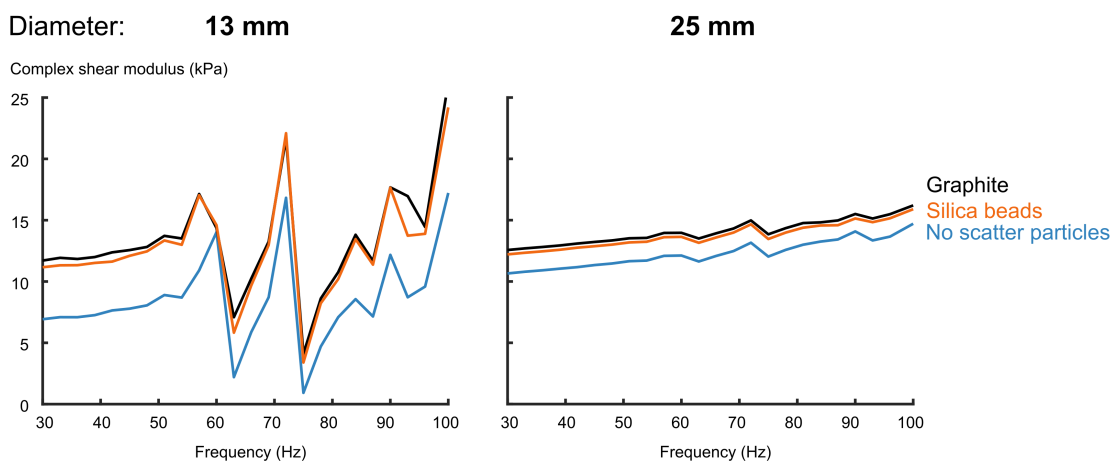


Figure C.6 – Diagram of elasticity curve of silicone samples with scatter particles evaluated with two different diameters (left: 13 mm, right: 25 mm). Silica beads (orange) and graphite (black) were added and compared to a sample without additional particles.

MR Elastography **D**

This appendix includes additional data acquired during MRE imaging with the developed SE-EPI sequence of the abdominal phantom as referred to in Sec. 4.3.3.

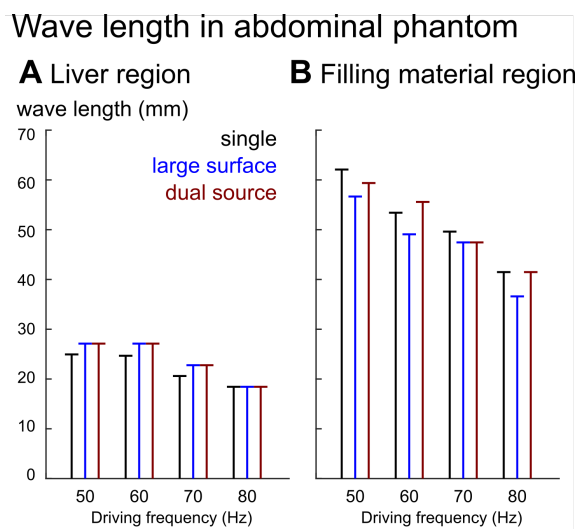


Figure D.1 – MRE - measured wave lengths in mm in the abdominal phantom. **A**: The wavelength in the central liver region. **B**: The wavelength in the filling material. The mechanical actuation frequency was iterated from 50 Hz to 60 Hz, 70 Hz, and 80 Hz. The three actuation set-ups showed no noteworthy differences in the wave lengths. As expected, the wave lengths shortened with increasing actuation frequencies.

Phase images of abdominal phantom with varying MEG amplitude

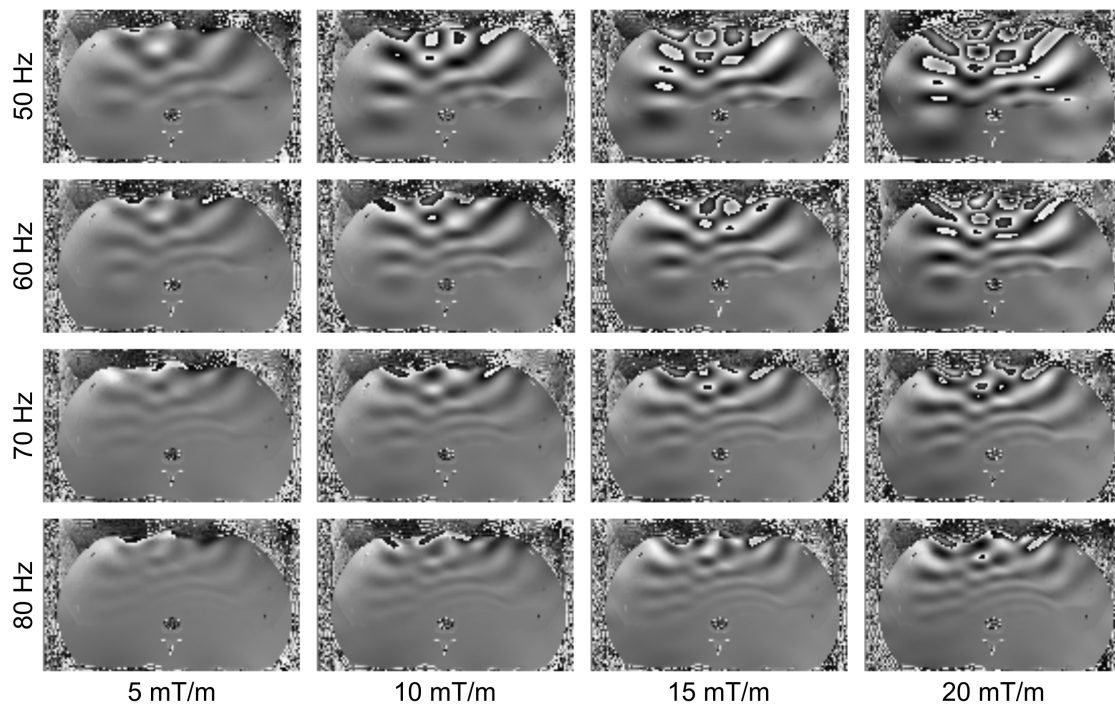


Figure D.2 – MRE - results of abdominal phantom with SE-EPI sequence and **large surface** actuation. The amplitude of the MEG was increased from $5 \frac{\text{mT}}{\text{m}}$ to $20 \frac{\text{mT}}{\text{m}}$ with a step width of $5 \frac{\text{mT}}{\text{m}}$ (left to right). The mechanical actuation frequency was iterated from 50 Hz to 60 Hz, 70 Hz, and 80 Hz (top to bottom).

Phase images of abdominal phantom with varying MEG amplitude

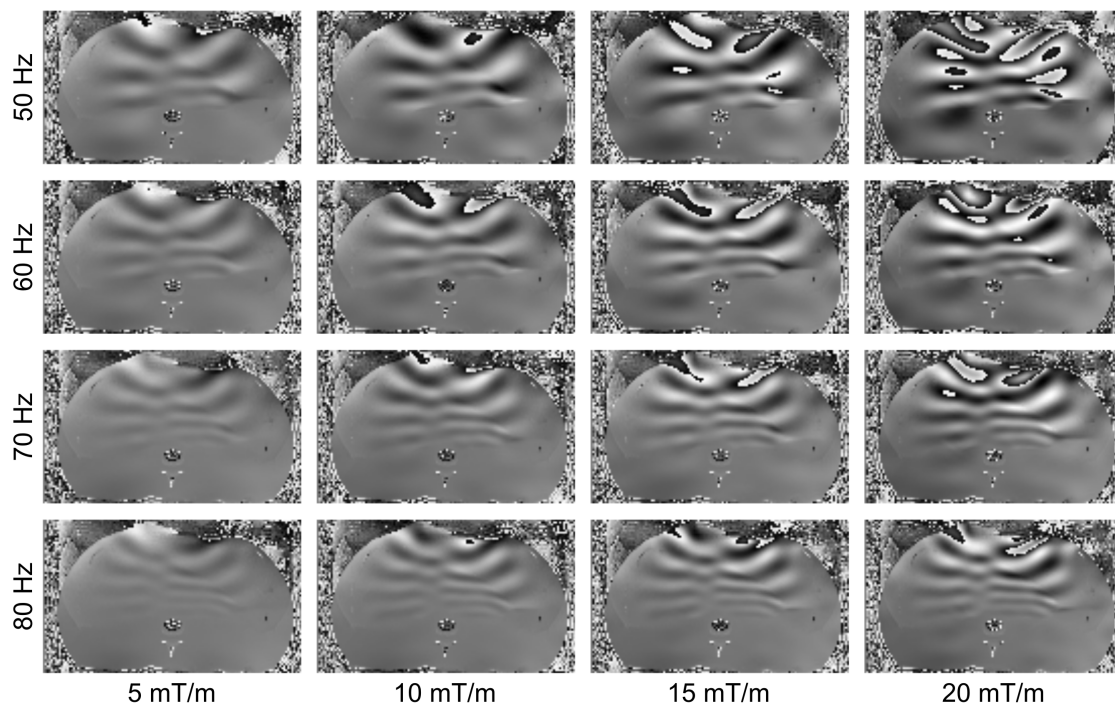


Figure D.3 – MRE - results of abdominal phantom with SE-EPI sequence and **dual source** actuation. The amplitude of the MEG was increased from $5 \frac{\text{mT}}{\text{m}}$ to $20 \frac{\text{mT}}{\text{m}}$ with a step width of $5 \frac{\text{mT}}{\text{m}}$ (left to right). The mechanical actuation frequency was iterated from 50 Hz to 60 Hz, 70 Hz, and 80 Hz (top to bottom).

Publications

Parts of this thesis were published as a peer-reviewed journal article, patent, or as conference contributions.

Patent

W. Neumann and F. Zöllner. A Mechanical Actuator and a Method for Magnetic Resonance Elastography Using Centrifugal Force.17000576.3. Filed 5. Apr. 2017.

Journal Article

W. Neumann, A. Bichert, J. Fleischhauer, A. Stern, R. Figuli, M. Wilhelm, L. Schad and F. Zöllner. A novel 3D printed mechanical actuator using centrifugal force for magnetic resonance elastography: initial results in an anthropomorphic prostate phantom. PlosOne. 2018. DOI [10.1371/journal.pone.0205442](https://doi.org/10.1371/journal.pone.0205442).

W. Neumann, V. Lehnart, Y. Vetter, A. Bichert, L. Schad and F. Zöllner. Coupled actuators with a mechanically synchronized phase during MR elastography: a phantom feasibility study. 2018. *submitted to Concepts in Magnetic Resonance Part B on 21.08.2018*.

W. Neumann, T. P. Pusch, M. Siegfarth, L. Schad and J. Stallkamp. CT and MRI compatibility of flexible 3D printed materials for soft actuators and robots used in image-guided interventions. 2018. *submitted to Journal of 3D printing and Additive Manufacturing Robotics on 16.10.2018*.

W. Neumann, T. Uhrig, M. Malzacher, V. Kossmann, L. Schad and F. Zöllner. Risk assessment of copper containing contraceptives: The impact for women with implanted intrauterine devices during clinical MRI and CT examinations. European Radiology. p. in press. 2018. DOI [10.1007/s00330-018-5864-6](https://doi.org/10.1007/s00330-018-5864-6)

N. Paschke, **W. Neumann**, T. Uhrig, M. Winkler, E. Probst, M. Fatar, L. Schad and F. Zöllner. Influence of Gadolinium-Based Contrast Agents on Tissue Sodium Quantification in Sodium Magnetic Resonance Imaging. *Investigative Radiology*, p. in press, 2018.

W. Neumann, L. Schad and F. Zöllner. A Novel 3D-Printed Mechanical Actuator Using Centrifugal Force for Magnet Resonance Elastography. *Engineering in Medicine and Biology Society (EMBC), 39th Annual International Conference of the IEEE 2017*, pp. 3541 - 3544. DOI 10.1109/EMBC.2017.8037621

W. Neumann, F. Lietzmann, L. Schad and F. Zöllner. Design of a Multimodal ($^1\text{H}/^{23}\text{Na}$ MR/CT) Anthropomorphic Thorax Phantom. *Z Med Phys*, 2017.

T. Gaa, **W. Neumann**, S. Sudarski, S. Schönberg, L. Schad and F. Zöllner. Comparison of perfusion models for quantitative T_1 weighted DCE-MRI of rectal cancer. *Scientific Reports*, p. 12036, 2017.

Conference Contributions

W. Neumann, A Bichert, L. Schad and F. Zöllner. In-Phase Anregung eines dualen Aktors für die MR-Elastographie mittels zentrifugaler Kraft. Jahrestagung der Deutschen Gesellschaft für Medizinische Physik und der Deutschen Sektion der ISMRM, Nürnberg, Deutschland, 2018. *poster presentation*.

W. Neumann, A. Bichert, J. Fleischhauer, L. Schad and F. Zöllner. Feasibility of Multi-Frequency Wave Actuation for Magnetic Resonance Elastography of a Novel Actuator using Centrifugal Force. 3rd Conference on Image-Guided Interventions & Focus Neuroradiology 2017, p. 20. *oral presentation*.

W. Neumann, L. Schad and F. Zöllner. Two Novel Low-Cost 3D-Printed Mechanical Actuators for MR Elastography Using Exact End-To-End Motion and Centripetal Force. *Proc. Intl. Soc. Mag. Reson. Med., Honolulu, HI, USA, 2017, 25, p. 1380. poster presentation*.

N. Paschke, **W. Neumann**, T. Gaa, A. Neubauer, L. Schad and F. Zöllner. Influences of MRI Proton Contrast Agent on Sodium MRI at Clinical 3T Field Strengths. *Proc. Intl. Soc. Mag. Reson. Med., Honolulu, HI, USA, 2017, 25, p. 2962. poster presentation*.

T. Gaa*, **W. Neumann***, M. Malzacher, L. Schad and F. Zöllner. Safety Assessment of Copper Containing IUDs at 1.5 T, 3 T and 9.4 T. *Magn Reson Mater Phys*, 2017, 30, Suppl. 1, p. S258. *shared first-authorship. *lightning talk and poster presentation, Award: Certificate of Merit*.

W. Neumann, A. Bitz, L. Schad, F. Zöllner, M. Ladd, A. Nagel and J. Lommen. Metallic Taste Perception at 7 Tesla: Influences of Jaw Position and Ionic Composition of Saliva. Proc. Intl. Soc. Mag. Reson. Med., Honolulu, HI, USA, 2017, 25, p. 2619. *poster presentation, Award: Magna Cum Laude Merit Award.*

W. Neumann, F. Lietzmann, L. Schad and F. Zöllner. Design of a Multimodal (1H MRI/23Na MRI/CT) Anthropomorphic Thorax Phantom: Initial Results at 3 T. Proc. Intl. Soc. Mag. Reson. Med. , Singapur, 2016, 24, p.1631. *poster presentation, Award: Magna Cum Laude Merit Award.*

W. Neumann, F. Lietzmann, L. Schad and F. Zöllner. Design and Validation of a CT and MRI Compatible Anthropomorphic Thorax Phantom. 2nd Imaged-Guided Intervention Conference, Mannheim, 2015. *poster presentation.*

Supervised Theses

Master's thesis. Developement of a motion encoding sequence for magnetic resonance elastography. 2018. *Yannik Vetter.*

Bachelor's thesis. Technische Entwicklung einer Schnittstelle zur Trigger-Signalübertragung zwischen Aktuator und Aufnahmesequenz für die Magnetresonanz-Elastographie. 2018. *Andreas Bichert.*

Bachelor's thesis. Realisierung zweier parallel betriebener Turbinenvibratoren für die Magnetresonanz-Elastographie. 2018. *Vanessa Lehnart.*

Bachelor's thesis. MRT-Sicherheitsbewertung kupferhaltiger Intrauterinpressare in vitro bei 1,5 T, 3 T und 9,4 T. 2018. *Verena Kossmann.*

Bachelor's thesis. Zertifizierung eines Wellengebers für die MR-Elastographie - Risikomanagement nach DIN EN ISO 14971:2013-04. 2018. *Katharina Knossalla.*

Bachelor's thesis. Gewebeelastizitäts-imitierendes Adomen Phantom für MRE. 2017. *Jonas Fleischhauer.*

Practical internships with a duration of five months each: Verena Franke (2017), Andreas Bichert (2017), Antonia Stern (2018), Patrick Kögel (2018), Mike Kankeu (2018).

Wiebke Neumann

Curriculum Vitae

* 23rd March 1989 in Berlin

Education

- since 07/2016 **Doctoral candidate**, *Heidelberg University, Medical Faculty Mannheim, Computer Assisted Clinical Medicine, Mannheim.*
Research focus: Magnetic Resonance Elastography
- 9/2013 – 8/2015 **Master of Science**, *Heidelberg University, Heidelberg, grade: A.*
Major: Biomedical Engineering, Minor: Radiotherapy, Imaging
- 9/2012 – 7/2013 **One-Year-Exchange-Program**, *Waseda University, Tokyo, Japan.*
School of International Liberal Studies
- 10/2009 – 8/2013 **Bachelor of Science**, *Hamburg University of Technology, Hamburg, grade: 1.8 (A).*
Major: General Engineering Science, Minor: Biomedical Engineering
- 6/2008 **Abitur**, *Dietrich-Bonhoeffer-Gymnasium, Quickborn, grade: 1.3.*

Theses

- Master's Thesis **Design and Validation of a CT and MRI Compatible Anthropomorphic Thorax Phantom**, *grade: 1.0.*
Supervisors: Prof. Frank G. Zöllner & Prof. Lothar R. Schad
- Bachelor's Thesis **Overload of the Head-Stem Taper Junction in Monoblock Hip Implants**, *grade: 1.0.*
Supervisors: Prof. Michael M. Morlock & Dr.-Ing. Florian Witt

Scholarships

- 6/2018 Erasmus Plus for the 26th Annual ISMRM Meeting (France)
- 10/2017 ESMRMB Student Support Programme for the 34th Annual ESMRMB Meeting (Spain)
- 8/2017 DAAD conference travel programme for the IEEE EMBC'17 (South Korea)
- 4/2017 ISMRM Student Support Programme for the 25th Annual ISMRM Meeting (USA)
- 5/2016 ISMRM Student Support Programme for the 24th Annual ISMRM Meeting (Singapore)
- 2009 – 2015 German National Academic Foundation (Studienstiftung des deutschen Volkes) scholarship
- 2012 – 2013 Dr. Jürgen Ulderup foreign exchange scholarship

Awards

- Abstract **Safety Assessment of Copper Containing IUDs at 1.5 T, 3 T and 9.4 T**, *T. Gaa**, **W. Neumann***, *M. Malzacher, L. Schad and F. Zöllner*, *Magn. Reson. Mater. Phys.*, 2017, 30, Suppl. 1, p. S258.
Poster, *shared authorship, Certificate of Merit
- Abstract **Metallic Taste Perception at 7 Tesla: Influences of Jaw Position and Ionic Composition of Saliva**, **W. Neumann**, *A. Bitz, L. Schad, F. Zöllner, M. Ladd, A. Nagel and J. Lommen*, *Proc. Intl. Soc. Mag. Reson. Med.*, Honolulu, HI, USA, 2017, 25, p. 2619.
Poster, Magna Cum Laude Merit Award
- Abstract **Design of a Multimodal (¹ MRI/²³Na MRI/CT) Anthropomorphic Thorax Phantom: Initial Results at 3 T**, **W. Neumann**, *F. Lietzmann, L. Schad and F. Zöllner*, *Proc. Intl. Soc. Mag. Reson. Med.*, Singapore, 2016, 24, p.1631.
Poster, Magna Cum Laude Merit Award

Additional Work Experience, Training and Interests

- 12/2014 – 10/2015 **Research assistant**, *Fraunhofer Project Group for Automation in Medicine and Biotechnology*, Mannheim.
- 1/2014 – 7/2014 **Research assistant**, *Heidelberg University, Institute of Experimental Radio Oncology*, Heidelberg.
- since 3/2016 **Training on Medical Physics for Physicists**, *Heidelberg University*.
Advanced education for medical physics expert certification
- since 9/2015 **Kung Fu** *Kung Fu Course Instructor at University Mannheim Institute of Sports*
1st Place, WKC World Championship 2016, Category Women Chinese Soft Style
2nd Place, WKC World Championship 2014, Category Women Chinese Soft Style

Danksagung

Ich möchte mich bedanken bei meinen Lehrern, die ihr Wissen und ihre Erfahrung mit mir geteilt haben, bei meinen Schülern, mit denen ich mein Wissen teilen durfte und von denen ich oft mehr gelernt habe als sie von mir und bei meiner Familie, die mich bedingungslos unterstützt.

Insbesondere gilt mein Dank

Prof. Dr. Lothar Schad für die Möglichkeit an seinem Institut eine Doktorarbeit zu beginnen.

Prof. Dr. Frank Zöllner für die umfassende Unterstützung und Betreuung dieser Arbeit.

Dr. Florian Lietzmann, der mich während meiner Masterarbeit betreute und den Weg zur Promotion am CKM ebnete.

Tanja Uhrig für die Aufrechterhaltung des besten Büroklimas, nach quantifizierbaren Maßstäben mit $T_{\text{opt}} > 25^\circ\text{C}$ sowie qualitativer Natur durch $\text{AIF}_{\text{Ayrer}} > 2.0 \frac{\text{cl}}{\text{h}}$, und für die schöne Zusammenarbeit bei Articles, Abstracts und Abschlussarbeiten.

Dr. Jorge Chacón-Caldera, Matthias Malzacher, Nadia Paschke, Ruomin Hu und Tanja Uhrig für das Korrekturlesen dieser Arbeit.

Meinen Studenten Verena Franke, Jonas Fleischhauer, Andreas Bichert, Antonia Stern, Katharina Knossalla, Patrick Kögel, Vanessa Lehnart und Verena Kossmann, die ich betreuen durfte und einen großen Anteil an dieser Arbeit haben.

Dem M²olie Haus 8 Team Gordian Kabelitz, Barbara Waldkirch, Khanlian Chung, Alena Schnurr, Tom Russ und Dominik Bauer.

Allen weiteren CKM'lern für die wertschätzende Atmosphäre am Institut.

Außerdem möchte ich mich bei Kayhan Gülmez und Tim Otte bedanken, die mir als Kung Fu Trainer weit mehr als nur Formen und Techniken vermittelt haben.

Vielen Dank an Constantin, natürlich für's Korrekturlesen, aber eigentlich einfach für's da sein und an seine Familie.

Vielen Dank an meinen Bruder Niels mit Lidia und Paul und an meine Eltern. Danke, dass ihr immer für mich da seid.